FUNDAMENTALS OF MECHANOCATALYSIS FOR LIGNIN VALORIZATION

A Dissertation
Presented to
The Academic Faculty

by

Andrew Wheeler Tricker

In Partial Fulfillment
of the Requirements for the Degree
Doctor of Philosophy in the
School of Chemical & Biomolecular Engineering

Georgia Institute of Technology
August 2021

FUNDAMENTALS OF MECHANOCATALYSIS FOR LIGNIN VALORIZATION

Approved by:

Dr. Carsten Sievers, Advisor
School of Chemical & Biomolecular Engineering
Georgia Institute of Technology

Dr. Andrew J. Medford
School of Chemical & Biomolecular Engineering
Georgia Institute of Technology

Dr. Matthew J. Realff, Advisor
School of Chemical & Biomolecular Engineering
Georgia Institute of Technology

Dr. Marta C. Hatzell
The George W. Woodruff School of Mechanical Engineering
Georgia Institute of Technology

Dr. Valerie M. Thomas, Advisor
H. Milton Stewart School of Industrial and Systems Engineering
Georgia Institute of Technology

Date Approved: June 04, 2021

“Let the scientific man realize that he must be a good first-hand observer of things in their native haunts, if he is to stand in the first rank of his profession. Let him also remember that it is his business to write well!”

Theodore Roosevelt[1]

ACKNOWLEDGEMENTS

I must first thank Dr. Carsten Sievers for his mentorship over the last five years. Your confidence in me has been crucial in developing confidence in myself and I do not believe I could have had a better Ph.D. advisor or thesis topic. Your passion and excitement for research still amazes me, and your many, many ideas have certainly kept me busy.

I cannot overstate how critical the input and guidance from Dr. Matthew Realff, Dr. Valerie Thomas, Dr. AJ Medford, and Dr. Marta Hatzell has been in the completion of this thesis and the success of so many diverse research projects. Being able to call each of you a co-author is one of my proudest accomplishments.

My time here would certainly have been far less enjoyable without the comradery of Dr. Mike Stellato, Dr. Nick Kruyer, and Dr. Thomas Kwok and our Lignin Group. Without you three, our lignin characterization paper would certainly not be. In addition, I would like to thank Nasreen Kahn and the entire TAPPI Student Chapter leadership board for all their hard work. I would also like to thank Virginia Howell and the staff of the Robert C. Museum of Papermaking for helping TAPPI put on so many paper making events. I want to also express my great appreciation to Dr. Chris Luettgen for being an excellent mentor with respect to TAPPI, educator with respect to pulp, paper, and forestry products, and an all-around great guy.

I want to thank Sean Najmi and Dr. Yimeng Lyu for their patience with my many seemingly random questions and our many insightful and fruitful afternoon discussions. I also want to thank the entire Sievers Research Group for their unquantifiable assistance over the years - Lisa Wiest, Dr. Qandeel Almas, Dr. Giada Innocenti, Bryan Hare, Olivia Williams, Dr. Sireesha Aluri, Dr. Chuck Okolie, Dr. Jungseob So, Dr. Jenn Jocz, and Dr. Ray Xu. It has been a pleasure

to work with George Chang, Anu Osibo, and Erin Phillips these past few months and I can tell I am leaving my mills in great hands.

I would like to thank Dr. Xu Du for his assistance and guidance early during my Ph.D. From fixing the GC/MS (or at least trying to) to helping me get my bearing with lignin, you helped me get a strong footing. I sincerely want to thank you for being such a great friend as well. I want to also acknowledge all the assistance I received from Dr. Wei Liu and the Deng Research Group.

The opportunity to work with some amazing undergraduate students has been one of the highlights of my research experience. So, I would like to thank Rohan Kadambi, George Samaras, and Jason Kang for all their help and input. I must also point out that George Samaras, who is really better described as a colleague, deserves a lot of credit for the success of the hot spot paper with his work modeling the ball deformation.

Dr. Eli Stavitski deserves a special thank you for his assistance in running experiments at the beamline and for always keeping things interesting.

I want to thank Nima Ronaghi, Arvind Ganesan, and William Bradley for their teamwork on PET recycling.

Funding for this thesis was provided by the Renewable Bioproducts Institute through the Paper Science and Engineering fellowship. I would like to thank Lloyd Williams, Dione Morton, and the whole RBI staff as well for creating a real sense of community. RBI also played a critical role in the success of the Lignin Group and the TAPPI Student Chapter. Our trip to the Inaugural lignin Gordon Conference and the TAPPI Seminar Series could not have happened without their financial support. I must also thank the PTB facilities team for holding the building together long

enough for me to graduate. I especially want to acknowledge Mary Williams for all her help during my time in PTB.

Of course, none of what I have accomplished so far could have been achieved without the unwavering support of my entire family. They might not understand what I am doing or why, but at least that is something we have in common.

If there is one person who truly deserves credit for this thesis, it is Karoline Hebisch. The ammonia work was only completed thanks to your sheer force of will. You are a daily inspiration to me, both by how impressive you are as a researcher and as a person and by being my greatest cheerleader. By having you as my lab partner, best friend, and more, I know that pursuing this degree has been the best decision I have made yet.

Finally, this dissertation rounds out nearly a decade as a member of the ChBE and Georgia Tech community. To all those who have made these past ten years so memorable and special, I thank you.

TABLE OF CONTENTS

LIST OF TABLES

LIST OF FIGURES

LIST OF SYMBOLS AND ABBREVIATIONS

Symbols

C_p	Heat Capacity	J kg^{-1} K^{-1}
C_{visc}	Coefficient of Viscosity	kg $m^{-1/2}$ s^{-1}
D	Ball Deformation	m
dD/dt	Rate of Deformation	m s^{-1}
D_{max}	Maximum Ball Deformation	m
DoP	Degree of Polymerization	
E	Young's Modulus	Pa
E_a	Activation Energy	J mol^{-1}
E_E	Elastic Energy	J
E_v	Dissipated Energy	J
F_{CB}	Fraction of Cleavable Bonds	
f_E	Restorative Force	N
f_{rate}	Reaction Rate Function	mol s^{-1} m^{-3}
f_v	Dissipative Force	N
g	Gravitational Acceleration	m s^{-2}
h	Heat Transfer Coefficient	W m^{-2} K^{-1}
K	Effective Spring Constant	kg $m^{-1/2}$ s^{-2}
k_C	Coke Rate Constant	s^{-1}
k_D	Deactivation Rate Constant	s^{-1}
k_H	Hydrogenolysis Rate Constant	s^{-1} g^{-1}_{Ni}
k_{mt}	Effective Mass Transfer Coefficient	m^3 s^{-1}
k_{rxn}	Pre-exponential Factor	s^{-1}
l	Powder Bed Height	m
m_{ball}	Mass of the Ball	kg
M_{CaCO3}	Molar Mass of Calcium Carbonate	g mol^{-1}
M_{CaO}	Molar Mass of Calcium Oxide	g mol^{-1}
M_N	Number Average Molecular Weight	Da
m_{Ni}	Mass of Nickel	g
m_{powder}	Mass of Collided Powder	kg

M_W	Weight Average Molecular Weight	Da
n_r	Moles of Reactant	mol
p	Ball Position	m
p_0	Standard Pressure	Pa
p^*_{CO2}	Partial Pressure of CO_2 in Powder Bed	atm
p_{CO2}	Partial Pressure of CO_2	atm
PD	Polydispersity	
p^r_{CO2}	Partial Pressure of CO_2 in Bulk Reactor	atm
$\dot{p}_0$	Initial Ball Velocity	m s^{-1}
$\dot{p}$	Ball Velocity	m s^{-1}
$\ddot{p}$	Ball Acceleration	m s^{-2}
Q_u	Useful Heat	J
R	Gas Constant	J mol^{-1} K^{-1}
r_0	Carbonate Particle Size	m
R_2	Gas Constant	m^3 atm K^{-1} mol^{-1}
$Rate_{node}$	Nodal Reaction Rate	mol s^{-1}
R_{ball}	Ball Radius	m
R_{def}	Radius of Deformation	m
r_{node}	Nodal radial position	m
S_{NH3}	IR signal for Ammonia	ppm
T	Temperature	K
T_{node}	Nodal Temperature	K
T_{rm}	Room Temperature	K
T_{rxn}	Reaction Temperature	K
V^*	Void Space of Powder	m^3
v_{col}	Collision velocity	m s^{-1}
V_{node}	Nodal Volume	m^3
V^r	Volume of Reactor	m^3
v_x	Velocity in x-direction	m s^{-1}
$\dot{V}(N_2)$	Volumetric flow rate of N_2 at standard conditions	L s^{-1}
$\dot{v}$	Gas Volumetric Flow Rate	m^3 s^{-1}

X_{BPE}	Conversion of benzyl phenyl ether	
Y_{Tol}	Yield of Toluene	
γ	Pressure Conversion Factor	Pa atm^{-1}
Δr	Step Size in Radial Direction	m
$\Delta_r H^0_T$	Enthalpy of Reaction	J mol^{-1}
$\Delta_r S^0_T$	Entropy of Reaction	J mol^{-1} K^{-1}
ΔT	Change in Temperature	K
Δt	Time Step	s
Δz	Step Size in Vertical Direction	m
$\eta_{product}$	Product Efficiency	
$\eta_{thermal}$	Thermal Energy Efficiency	
η_{total}	Total Energy Efficiency	
κ	Thermal conductivity	W m^{-1} K^{-1}
ν	Poisson's Ratio	
ξ	Extent of Reaction	mol
ξ_{50ms}	Extent of Reaction at 50 milliseconds	mol
ξ_{col}	Extent of Reaction per Collision	mol
ξ_{node}	Nodal Extent of Reaction	mol
ρ	Density	kg m^{-3}
σ	Intermediate Material Property Parameter	
φ	Thermal Dissipation Factor	
$n(NH_3)$	Molar Flow Rate of Ammonia	mmol s^{-1}

Abbreviations

BET	Brunauer-Emmet-Teller theory
BTU	British Thermal Unit
CHNOS	Carbon, Hydrogen, Nitrogen, Oxygen, and Sulfur
DoC	Degree of Condensation
DRIFTS	Diffuse Reflectance Infrared Spectroscopy
DTGA	Derivative Thermogravimetric Analysis
EDS	Dispersive X-ray Spectroscopy

EXAFS	Extended X-ray Absorption Fine Structure
FID	Flame Ionization Detector
G	Guaiacyl Monomeric Unit
GC	Gas Chromatography
GPC	Gel Permeation Chromatography
HPLC	High Performance Liquid Chromatography
HSQC	Heteronuclear Single Quantum Coherence
HWBuOH	Hardwood Butanol Fractionated Lignin
HWK	Hardwood Kraft Lignin
HWSCW	Hardwood Super Critical Water Fractionated Lignin
HWSEW	Hardwood SiO_2/Ethanol/Water Fractionated Lignin
IC	Ion Chromatography
ICP-OES	Inductively Coupled Plasma Optical Emission Spectroscopy
IR	Infrared Spectroscopy
MeO	Methoxy Group
MS	Mass Spectrometry
MWL	Milled Wood Lignin
NMR	Nuclear Magnetic Resonance
PIXE	Proton Induced X-ray Emission
RCF	Reductive Catalytic Fractionation
S	Syringyl Monomeric Unit
SCCM	Standard Cubic Centimeters per Minute
STEM	Scanning Transmission Electron Microscopy
SWBuOH	Softwood Butanol Fractionated Lignin
SWK	Softwood Kraft Lignin
TEM	Transmission Electron Microscopy
TGA	Thermogravimetric Analysis
TPD	Temperature Program Desorption
XANES	X-ray Absorption Near Edge Structure
XAS	X-ray Absorption Spectroscopy

XPS	X-ray Photoelectron Spectroscopy
XRD	Powder X-ray Diffractometry

SUMMARY

The valorization of lignocellulosic biomass is a promising approach for replacing petroleum as the dominant source of chemicals. Lignin, one of the three main components of lignocellulose, has often been viewed as a by-product during cellulose valorization. However, as the largest natural source of aromatics, lignin is an appealing sustainable feedstock for many chemicals and materials, such as plastics, pharmaceuticals, and herbicides (just to name a few). The depolymerization to mono-aromatics has remained challenging and industrial applications have remained elusive. A promising approach to biomass valorization and deconstruction is mechanocatalysis. This approach uses mechanical energy, often supplied in ball mill reactors, to drive reactions under solvent free and nominally ambient conditions. However, fundamental understanding of mechanochemistry and mechanocatalysis remains enigmatic, presenting its own set of challenges. The aim of this thesis is to lay fundamental groundwork to better understand mechanocatalytic systems and how these systems can be applied for depolymerizing and valorizing lignin.

Chapter 2 compares the structure of industrially isolated lignin samples from kraft pulping and three alternative processes: butanol organosolv, super-critical water hydrolysis, and sulfur dioxide/ethanol/water fractionation. It is known that kraft processes produce highly condensed lignin, with reduced potential for catalytic depolymerization, while the alternative processes have been hypothesized to impact the lignin less. Structural properties most relevant to catalytic depolymerization are characterized by elemental analysis, nuclear magnetic resonance (NMR) spectroscopy, gel permeation chromatography (GPC), and thermogravimetric analysis (TGA). Quantification of the β-O-4 ether bond content shows partial depolymerization, with all samples having less than 12 bonds per 100 aromatics. This results in a theoretical monomer yields less than

5%, strongly suggesting the alternative fractionation processes generate highly condensed lignin structures that are no more suitable for catalytic depolymerization than kraft lignin. However, the different thermal degradation profiles suggest there are physicochemical differences that could be leveraged in other valorization strategies.

In Chapter 3, a bottom-up modeling approach to describe the reactive conditions in a mechanochemical reactor is presented. The approach is focused on the creation of hot spots as the mechanism of enhanced reaction. Here, energy dissipated during a collision is converted to heat in the milling media, and the reaction proceeds thermochemically. The first step of the model, determining the energy dissipated during the collision, is done by treating the ball and powder bed as viscoelastic materials and using a Kelvin Voigt model. The energy dissipation profile from the collision model is imported into a COMSOL® simulation. The heat transfer through the powder bed, treated as a continuous media, is calculated, providing the temperature, volume, and time profiles needed to calculate reaction rates. The final result of the model is the extent of reaction over a single collision. To verify the approach, the mechanochemical decomposition of calcium carbonate is studied. The real-time CO_2 production under varying milling frequencies is measured using an in-line mass spectrometer. The ball and mill velocities, as well as, collision frequencies is determined by analyzing high speed video of a transparent milling vessel. The model describes hot spots with temperatures exceeding 1000 K that persist for tens of milliseconds.

In Chapter 4, novel behavior of catalysts under mechanocatalytic conditions is explored by introducing a new approach for ammonia production at nominally ambient conditions. As proof of concept, ammonia is synthesized mechanocatalytically by ball milling titanium in a continuous nitrogen and hydrogen gas flow. The ammonia synthesis reaction is proposed to follow a transient Mars-van Krevelen mechanism under mechanically activated conditions, where molecular

nitrogen incorporation into the titanium lattice and titanium nitride hydrogenation occur in thermodynamically distinct environments. X-ray powder diffraction and X-ray absorption spectroscopy confirm the formation of titanium nitride from titanium and N_2. The reactivity of nitrided titanium supports that lattice nitrogen plays a role in ammonia formation. The *in situ* formed titanium nitride is catalytically active, and the nitride regeneration reaction is determined to be the rate-limiting step. A preliminary technoeconomic analysis shows that this approach could be feasible for distributed ammonia production.

In Chapter 5, the mechanocatalytic hydrogenolysis of benzyl phenyl ether (BPE), a model lignin ether, is demonstrated over supported nickel catalysts at nominally room temperature and atmospheric hydrogen pressure. The hydrogenolysis reaction network closely follows those of solution-based thermocatalytic reactions. The mechanical energy during milling not only drives the chemical reactions, but also activates the nickel and exposes fresh metallic surfaces. Recycle experiments using a commercial high nickel loading catalyst (53 wt% Ni on silica-alumina) shows continual deactivation over three reaction cycles and the formation of polyaromatic coke species. The formation of the carbon deposits appears to be the primary cause of deactivation. The reaction over low nickel loading catalysts (~5 wt%) with varying support properties shows that the hydrogenolysis rate is largely independent of the support properties, but the enhanced reactivity of the oxide supports during milling contributes to the carbon loss.

Finally, Chapter 6 summarized the key finding of each chapter and outlines future work to further utilize mechanocatalysis for lignin valorization and sustainable processes.

CHAPTER 1
INTRODUCTION

1.1 The Bioeconomy and Lignocellulosic Biomass

1.1.1 Transition to a Bioeconomy

With the ever-growing threat of climate change, society must move away from utilizing fossil resource and develop sustainable sources for fuels and chemicals. In 2019, the United States consumed 80 quadrillion BTUs of fossil fuels (500 million tons of coal, 32 trillion cubic feet of natural gas, and 6.3 billion barrels of oil), making up approximately 80% of the US energy portfolio. Of this, 520 thousand tons of coal (0.3 million tons of carbon), 1.1 trillion cubic feet of natural gas (18 million tons of carbon), and 1.2 billion barrels of oil (1.5 billion tons of carbon) were used in the production of chemicals and materials.[2] While installation of additional non-emitting energy sources (wind, solar, nuclear, etc.) and electrification will be able to replace much of the fossil resources used for energy, a renewable source of carbon is necessary for producing sustainable chemicals, especially if these chemicals become less available as a by-product of fuels. Terrestrial biomass (*i.e.* plants), which has a global annual growth rate of 56 billion tons of carbon,[3] offers such a renewable, concentrated source of carbon.

The aromatic compounds benzene, toluene, and xylene (commonly known as BTX) are some of the most important petrochemicals currently produced.[4] These compounds consist of a conjugated 6-member carbon ring (aromatic ring) with either all hydrogen bound to the carbon (benzene), a single methyl group substitution (toluene), or two methyl group substitutions (xylene). BTXs serve as the basic building blocks for many important chemicals (*e.g.* dyes and insecticides) as well as many of the most prevalent plastics (*e.g.* nylon, poly(ethylene terephthalate), and polystyrene).[5] Since many of these are functionalized, phenol serves as an important platform

molecule from BTX to the final product.[6-7] Due to this widespread importance of aromatic structures, utilizing an existing, natural source of aromatic compounds would be appealing for producing sustainable chemicals and materials.

1.1.2 Components of Lignocellulose and Structure of Lignin

Lignocellulosic biomass, especially woody biomass (*i.e.* trees), is an appealing feedstock for green chemicals. Lignocellulosic biomass is constructed of three primary components: cellulose (40-60 wt%), hemicellulose (10-40 wt%), and lignin (15-30 wt%).[8] Cellulose provides the structure and rigidity to the plant cell walls and is a crystalline, linear polymer made of only glucose units.[9] As a well-defined, regular polymer, breaking down cellulose into glucose is currently the primary target for most biorefining processes. The glucose can then be converted into fuels such as ethanol or platform chemicals such as lactic acid or succinic acid.[10] Hemicellulose, an ill-defined, amorphous polysaccharide comprised of various hexoses (C-6 sugars) and pentoses (C-5 sugars), acts as the cross-linker between cellulose fibers as well as between the cellulose and lignin.[9] Finally, lignin acts as the glue of the cell wall, providing strength and resilience, as well as protects the plant from degradation.

Lignin, the largest natural source of aromatic carbon, is a random, amorphous polymer comprised of three primary phenylpropanoid monomeric units (or monolignols): *p*-coumaryl alcohol (H units), coniferyl alcohol (G units), and sinapyl alcohol (S units) (Figure 1).[11] While these three represent the majority of monolignol group in the polymer, numerous other phenylpropanoids have been observed as well. The polymerization occurs through radical coupling, which produces random linkages between random monolignols.[12] The most prevalent linkage in native lignin is the β-aryl ether (β-O-4), which can make up between 40% and 60% of all linkages. Other prevalent linkages include the resinol (β-β) linkage and the phenylcoumaran

(β-5) linkages. In woody biomass, there are broadly two types of lignin: softwood lignin, which is primary composed of G units and has no S units, and hardwood lignin, which is composed of both G and S units.

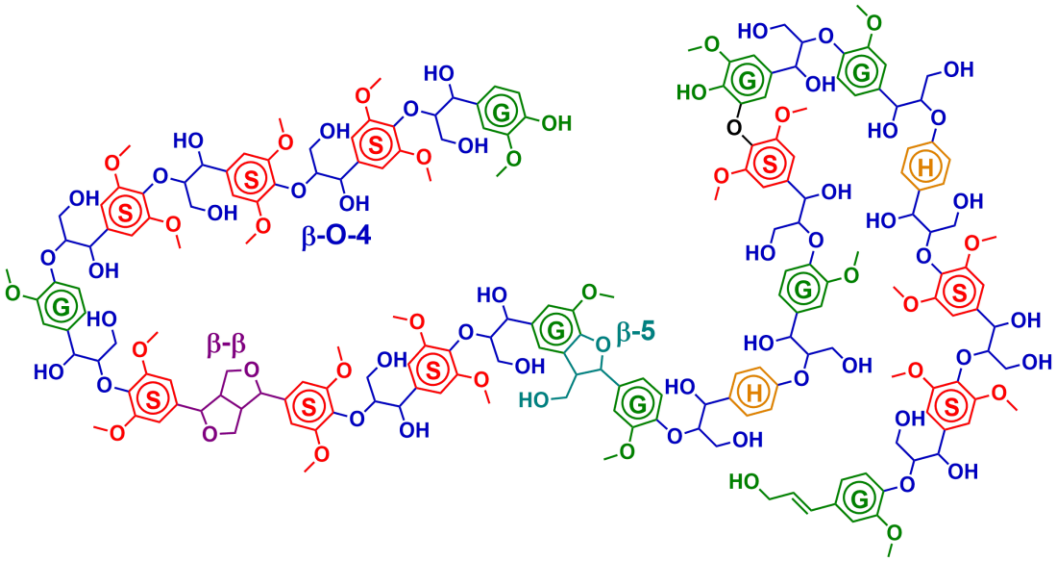

Figure 1: Model hardwood lignin structure. Adapted from *Ralph, J. et al.*[12]

1.2 Strategies and Challenges to Lignin Valorization

1.2.1 Current and Historic Uses of Lignin

The industrial use of lignin has been tied to the pulp and paper industry for the entirety of its history.[13] A key step in paper manufacturing is pulping woodchips. During chemical pulping, the lignin within the woodchips is dissolved and removed, leaving pristine cellulose fibers behind for papermaking. Kraft pulping is the most prevalent chemical pulping method and is used to produce 90% of the global supply of pulp. Here, the woodchips are treated in an aqueous solution of NaOH and Na_2S to separate the lignin from the cellulose.[14] The resulting lignin stream (known as black liquor) is burned in the recovery boiler to produce energy for the mill and as part of the chemical recovery process. Roughly 65 million tons of lignin are produced annually across all forms of pulping and 98% is burned as a low value fuel.

Lignosulfonates, byproducts of sulfite pulping, account for 90% of commercial lignin-derived materials (the 2% of extracted lignin not used as fuel).[15] They are polymeric lignin structures with functional groups replaced with sulfonate groups and have molecular weights ranging between 1,000 and 150,000 Da.[16] Lignosulfonates are used in a wide array of applications (pesticides, surfactants, plasticizers in concrete, additives in oil drilling, and dust suppressants), but these are still relatively low value application.

The most relevant example of lignin as a feedstock for fine chemicals is its use in the production of vanillin. Vanillin is the key component of vanilla flavor, and an important intermediate for many chemicals and pharmaceuticals.[17] The vanillin is synthesized through the oxidation of lignosulfonates.[18] During the latter half of the 20th century, the vast majority of vanillin was produced from lignin, and, for many mills, vanillin production was as profitable as pulp production.[13] For example, in 1981, a single Canadian pulp mill was producing 60% of the global supply of vanillin. However, today only 15% of vanillin is produced from lignin (3,000 tons/yr or just ~0.2% of commercial lignin), and it is all manufactured from a single plant in Sarpsborg, Norway. The last vanillin from lignin plants in North America closed during 1990s. Three main causes have been attributed to vanillin synthesized from petroleum (which now accounts for 85% of production), the large volumes of process waste, and the decline of sulfite pulping (sulfite pulp production capacity in North America dropped by 96% between 1968 and 2017).[18-20]

1.2.2 Depolymerization and Repolymerization of Lignin

Clearly, producing aromatic chemicals from lignin can add significant value to lignin streams while also creating more sustainable chemicals and materials. Synthesizing aromatic chemicals from lignin requires depolymerizing the lignin polymer down to mono-aromatic units.

The most common methods for catalytic depolymerization are acid and base hydrolysis, hydroprocessing (hydrogenolysis and hydrodeoxygenation), and oxidation. Base catalyzed hydrolysis requires milder conditions than hydroprocessing and oxidation but is not capable of breaking recalcitrant C-C bonds.[21] Hydroprocessing utilizes H_2 or hydrogen donating species to cleave lignin bonds and, particularly hydrodeoxygenation (HDO), is seen as the most effective method to combine lignin depolymerization and upgrading.[21-22] Oxidative depolymerization with O_2 or H_2O_2 has primarily focused on the production of vanillin but is gaining more attention for its ability to cleave carbon-carbon bonds.[23-24] Most of these treatments are solution-phase reactions that are typically performed in autoclaves. These batch reactions are limited by the solubility of lignin and usually require harsh organic or super-critical solvents and high temperatures and pressures. The separation of diverse products and catalysts from these solvents has been a challenge of many of these processes.

A major challenge for the depolymerization of isolated lignin is the condensation of the polymer during extraction.[25] While the β-O-4 linkage is the most prevalent in native lignin, the harsh reaction conditions used to separate lignin and cellulose can readily cleave these bonds. Additionally, during the break down of the lignin, condensation and repolymerization reactions can occur, creating new carbon-carbon linkages (Figure 2), which are significantly more difficult to break than ether bonds. Several different reactive points exist on the lignin polymer, specifically unsubstituted aromatics, alpha carbon hydroxyl groups, and unsaturated sidechains, resulting in a wide and complex array of potential linkages. The loss of labile ether linkages and the formation of recalcitrant condensed linkages can severely limit the monomer yields from technical lignin.

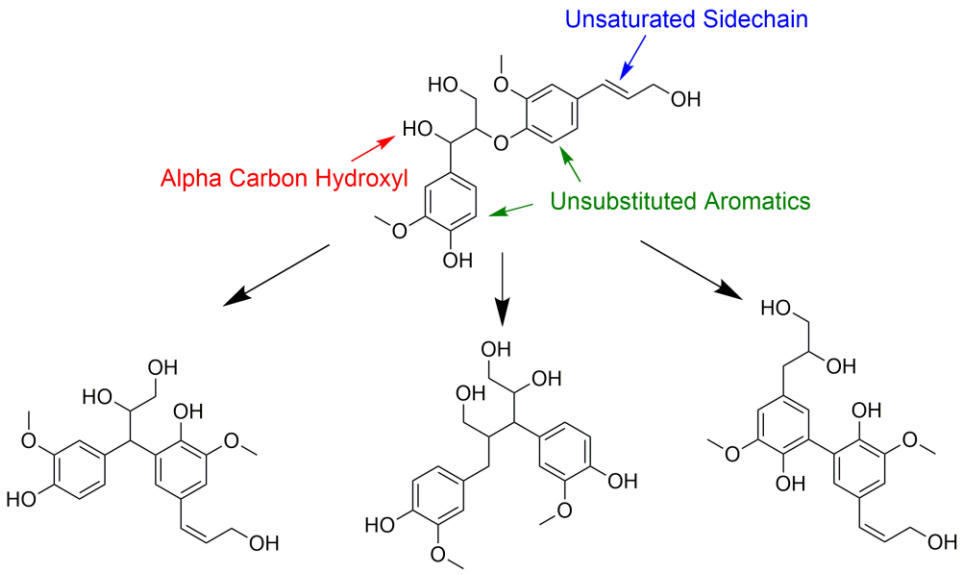

Figure 2: Example of condensed linkages that may form during the repolymerization of lignin.[26]

"Lignin First" biorefining has received much attention in recent years. Here, the valorization of the lignin is emphasized before the valorization of the cellulose, and the most prominent strategies focus on catalytic fraction.[27-28] Catalytic fractionation combines the depolymerization of the lignin with the separation step, going straight to monomers while avoiding an isolated polymeric lignin intermediate. Just as in traditional fractionation, the β-O-4 and other labile linkages are broken, but, critically, a stabilizing agent, such as hydrogen, formaldehyde, or ethylene glycol, is included to block reactive points and prevent repolymerization.[29-31] Notably, these reaction rely on the solvolysis of the lignin using high temperature organic solvents.

1.3 Mechanochemistry and Mechanocatalysis

The popularity of mechanochemistry as a route for green chemicals has increased drastically in recent years.[32] Mechanochemistry relies on the input of mechanical energy to drive chemical reactions, in place of thermal energy. The main advantages of mechanochemistry are that reactions can be performed solvent-free (or with significantly reduced solvent use) and under

nominally ambient conditions (room temperature and atmospheric pressure). These attributes allow for chemical processes that can be more energy efficient and environmentally friendly.[33]

1.3.1 Reactors of Mechanochemistry

The most common machines for performing mechanochemical reactions are ball mills. These devices rely on collisions between the balls and the wall as well as between balls to supply the energy to drive reactions. The work done on the milled material occurs through either compression, shear/friction, or impact, and the style and geometry of a mill will change contribution of each interaction.[34] At lab scale, the most common types of mills are mixer mills and planetary mills. Mixer mills (Figure 3a) shake a vessel filled with the milling media and substrate back and forth at high frequency. Planetary ball mills (Figure 3b) spin a base plate and vessels in opposite directions, creating centrifugal forces that throw the balls across the vessel (impacts) and push the ball along the walls (friction). At larger and industrial scales, horizontal rotating mills (Figure 3c-e) become the most common. Here, the vessel is rotated about its horizontal axis and the type of mechanical energy delivered depends on the speed of rotation.[35] At low rotational speeds, the balls roll over each other with shear being the dominant mode, while at faster rotation, the balls can enter free call and impact collisions become dominant. Eventually, as the mill rotates faster, a critical speed is reached where centrifugal forces pin the balls against the vessel wall and grinding effectively stops.

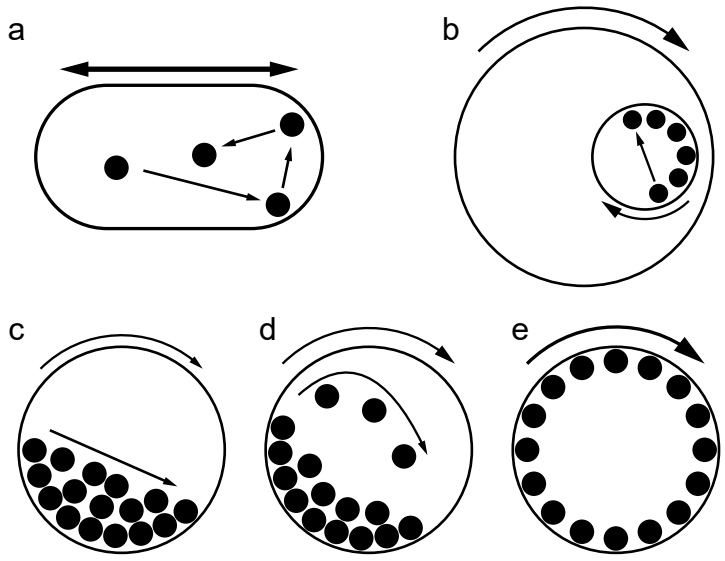

Figure 3: Diagrams of common ball mill reactors. (a) Mixer mill and (b) Planetary ball mill. Rotating ball mill at (c) low rotational speed and (d) high rotational speed. (e) Rotating ball mill above the critical speed. Adapted from *Baláž, P.*[34]

Other common mechanochemical devices are disk mills and extruders. Disk mills consist of two disks with interlocking pins, with one disk spinning. The reagents are fed at the center and centrifugally force outward.[35] As the material moves outward, friction occurs between the particles and the pins, causing size reduction and reaction. Extruders force intimidate contact between reagents by conveying the materials between screw extruders instead of using grinding and collisions like mills.[36] This process creates large amounts of shear and compressive forces. Twin screw extruders are becoming more popular due to the perceived improvements for controllability and scalability, compared to ball mills.[37]

1.3.2 Phenomena of Mechanochemistry

There are various ways how mechanical energy can drive the chemical reaction, which strongly depend on the materials being milled and the reaction being performed.[38] During mechanochemical reactions with inorganic materials (primarily metals or ceramics), the impacts and friction between the hard, brittle materials are expected to create highly localized heating (hot

spots), that can exceed several hundreds of degrees but last only milliseconds. Additionally, amorphization and the production of defects within the materials can increase their reactivity.[34]

Organic reactions are believed to propagate primarily through enhanced molecular transport between the organic crystals, the formations of liquid phases between the reactant particles, or the formation of amorphous intermediate phases.[39] In softer materials, the intense local heating proposed for inorganic reactions is not expected to occur. Additionally, the direct mechanical forces on chemical bonds can increase or alter the reactivity of the reagents.[40] In heterogeneous mechanocatalysis, the mechanical energy can play a critical role in altering the activity of the catalyst. Fracturing or deformation of the surfaces can create unstable and uncoordinated sites.[41-42] While these sites will eventually return to a stable configuration, they can exhibit heightened catalytic activity during their limited lifespan.

1.3.3 Mechanocatalytic Depolymerization of Lignocellulose

Mechanical pretreatment of woody biomass for size reduction in biorefining has long been established to increase the accessibility of cellulose for subsequent chemical and biological treatments, but mechanocatalytic biomass conversion is relatively new.[43-54] Mechanocatalytic conversion of cellulose and lignocellulose impregnated with HCl or H_2SO_4 provided quantitative yields of water soluble sugar oligomers within a few hours of milling and, in the case of lignocellulose, efficient sulfur-free lignin fractionation.[55-56] Solid acids, such as delaminated kaolinite, can also depolymerize cellulose, but to a lesser degree than HCl and H_2SO_4.[57] While most reactions have been conducted on the gram scale, water-soluble oligosaccharides were also produced with more than 90% yield on the kilogram scale with increased energy efficiency.[58] Even on the short time scale of 10 min, mechanochemical treatment of lignocellulose substantially increases glucose yields from subsequent hydrolysis.[59]

Studies of mechanically driven lignin depolymerization have been limited. Sumimoto *et al.* published a series of papers on mechanochemical conversion of model compounds, focusing on homolytic cleavage during mechanical pulping, but their work did not include actual lignin.[60-65] Aromatic products from lignin have been detected during the mechanocatalytic deconstruction of lignocellulose with solid acids.[43] During the mechanocatalytic conversion of acid impregnated lignocellulose, the fractionated lignin was shown to have increased higher molecular weights but lower abundance of β-O-4 linkages compared to organosolv lignin, demonstrating mechanocatalytic ether cleavage and repolymerization.[56, 66] Kraft lignin mechanochemically pretreated with KOH showed increased reactivity during oxidative depolymerization.[67] Direct depolymerization of lignin was first demonstrated using NaOH in a planetary ball mill where 76% of β-O-4 linkages in organosolv lignin were cleaved within 12 h.[68] The addition of methanol during the mechanochemical hydrolysis of organosolv lignin with NaOH increased both the rate and extend of depolymerization by quenching reactive intermediates.[69] Finally, the oxidative mechanocatalytic depolymerization of lignin has also been demonstrated with HO-Tempo, KBr, and Oxone using a mixer mill, mortar mill, and disc mill.[70]

1.4 Outline of this Dissertation

This thesis work primarily focuses on laying the groundwork for using mechanocatalysis to depolymerize and valorize lignin. Chapter 2 highlights the inherent recalcitrance of the lignin polymer due to isolation and the need for novel approaches for lignin valorization. Chapter 3 introduces a bottom-up modeling approach for describing mechanochemical reactions and reaction environments using traditional chemical and physical concepts. Chapter 4 presents a study of mechanocatalytic ammonia synthesis, emphasizing unique reaction paths and catalyst behaviors in mechanocatalytic environments. Chapter 5 demonstrates the feasibility of the necessary

chemistry for hydrogenolysis of lignin using mechanocatalysis. Finally, Chapter 6 summarizes the key conclusions from the previous chapters and outlines potential future routes to further expand on this thesis and generate deeper understanding of mechanocatalysis and lignin valorization.

CHAPTER 2
RECALCITRANT STRUCTURES OF INDUSTRIAL LIGNIN

2.1 Introduction

As the only large-scale renewable source of natural aromatics, the potential value of lignin as an alternative feedstock for petroleum-derived chemicals has sparked much interest.[8, 71-73] The role of lignin in the plant is to protect the cellulose fibers while providing strength, rigidity, and degradation resistance.[74] Lignin extraction has historically required harsh treatments that reduce important chemical moieties and lead to severe condensation of the lignin structure.[25] These recalcitrant lignin polymers are typically burned as a low value fuel to generate steam and electricity. In the pulp and paper industry alone, over 50 million tons per year of lignin are burned at a nominal value of $100 per ton.[75] However, developing of higher value products from lignin requires new upgrading pathways.

Kraft pulping, using sodium hydroxide and sodium sulfide, is the predominant industrial processes to fractionate lignocellulose into cellulose, hemicellulose, and lignin.[76] Removing lignin from the recovery process at a pulp mill is economically attractive because it can increase pulp throughput and create a new revenue streams.[77] Commercial technologies have emerged to precipitate lignin from black liquor using acids or carbon dioxide,[78] with the LignoBoost™ process as one of the predominant technologies.[79] However, high severity kraft cooks have been reported to produce condensed lignin with high sulfur content, which may present problems with downstream processing.[80] Lignin extracted from black liquor has been primarily used as a polymeric additive in carbon fiber composites, activated carbon, polyurethanes, and adhesives. These lignin-infused materials tend to have inferior performance compared to the original.[81] It is plausible that better understanding and control of the depolymerization process will allow for the incorporation of renewable carbon without sacrificing final material properties.

The predominant pathway to chemicals from lignin is catalytic depolymerization. Catalytic depolymerization (acid/base hydrolysis, oxidative depolymerization, and hydroprocessing) can produce a relatively narrow product distribution of mono-aromatics, compared to other strategies such as pyrolysis, that can be more readily funneled into value-added chemicals.[71] A major hurdle for this process is the recalcitrant bonds formed during fractionation. Isolated lignin tends to have fewer labile ether linkages (β-O-4, α-O-4) and more aliphatic and condensed linkages (β-5, β-β, 4-O-5, 5-5').[25] Most depolymerization strategies only cleave labile ether bonds, so monomer yields are severely diminished (just 5% - 15% for kraft lignin).[72] Additionally, many depolymerization strategies still produce too wide a distribution of mono-aromatic products. The combination of low yield and low selectivity makes the economics of converting isolated lignin to chemicals currently unappealing.[8]

Many new biorefineries, focused on producing renewable fuels and chemicals, isolate lignin using milder solvents and reaction conditions. Commonly, these fractionation processes utilize organic solvents, such as alcohols, to solubilize lignin and hemicellulose.[82-84] Other delignification techniques dissolve the carbohydrates but keep the lignin as a solid through the fractionation process.[85] These alternative solvent processes lead to a variety of different lignin types, many of which retain a majority of native β-ether linkages at laboratory scale.[86] While many biorefineries are producing supposedly less recalcitrant lignin at industrial scales, these lignin structures have yet to be thoroughly characterized.

The aim of this chapter is to comparatively characterize the depolymerization-related structural characteristics of eight lignin samples from four different industrial scale fractionation processes (kraft pulping, butanol organosolv fractionation, super critical water hydrolysis, and SO_2/Ethanol/Water fractionation). These eight samples represent the most comprehensive

characterization of industrial lignin produced via different processes within a single study, known to date. Numerous lignin depolymerization studies have identified that molecular weight, degree of condensation, and abundance of β-O-4 bonds are key characteristics that influence monomer yields.[25, 87-88] These structures in each lignin sample are compared based on a combination of elemental analysis, gel permeation chromatography (GPC), quantitative ^{13}C nuclear magnetic resonance (^{13}C NMR) spectroscopy, ^{1}H-^{13}C 2D heteronuclear single quantum coherence (HSQC) NMR spectroscopy, and thermogravimetric analysis (TGA). These results are used to provide guidance for future valorization routes that start with these lignin feedstocks.

2.2 Materials and Methods

2.2.1 Lignin Sources

All lignin samples were obtained from pilot-scale to industrial-scale process streams (Table 1). The samples were derived from different wood sources, and the operating conditions of the same process (performed by different companies) most likely differed between samples. The initial native structures of these lignin samples and many of the operating conditions, such as total lignin yields, are not knowable. However, these samples truly represent commercially isolated lignin streams and constitute a practical starting point for a lignin to chemicals process. All lignin samples were dried and sieved between 40-mesh and 80-mesh screens. The final particle size was between 185 μm and 425 μm. No additional treatment occurred prior to characterization unless otherwise stated.

Table 1: Source and preparation method of industrial lignin samples.

Lignin Sample Name	Acronym	Sample Preparation
Softwood Kraft 1	SWK1	Southern pine was treated in a standard kraft cook for a bleachable grade pulp. The kraft lignin was isolated by acidification with CO_2 to a pH of 9, followed by additional acidification and wash to a pH of 3.
Softwood Kraft 2	SWK2	Southern pine was treated in a standard kraft cook for linerboard production. The kraft lignin was separated from the resulting black liquor. The lignin was filtered and washed extensively.
Softwood Kraft 3	SWK3	An industrial grade research sample from Southern Pine based on acid-precipitated kraft lignin.
Softwood Butanol	SWBuOH	Mixed softwoods were treated using an n-butanol organosolv processes. After fractionation, the dissolved lignin was recovered by evaporating the solvent.
Hardwood Kraft	HWK	Mixed hardwoods were treated in a standard kraft cook. The lignin was precipitated from the industrial black liquor in house following the procedure described by Zhu and Theliander.[89] The black liquor was heated to 65 °C in a water bath. 6 M sulfuric acid was added until the liquor achieved a pH of approximately 10. The mixture was stirred for an additional hour, and then the lignin precipitate was recovered by vacuum filtration. The lignin was washed with dilute sulfuric acid (pH 3).
Hardwood Super Critical Water	HWSCW	Mixed hardwoods were hydrolyzed with supercritical water. The dissolved cellulose was filtered away from the solid lignin. The lignin was washed with water during the filtration process.
Hardwood SEW	HWSEW	Mixed southern hardwoods were treated with a mixture of sulfur dioxide, ethanol, and water (SEW) at 150 ˚C. The resulting liquor was distilled to remove ethanol and sulfur dioxide, which resulted in lignin precipitation. The precipitate was separated, and water washed (separation by centrifugation) to produce the lignin sample at 60% moisture content.
Hardwood Butanol	HWBuOH	Mixed hardwoods were treated using an n-butanol organosolv processes. After fractionation, the dissolved lignin was recovered by evaporating the solvent.

2.2.2 Chemicals

Stabilized tetrahydrofuran (THF, HPLC Grade, 99.7+%, stab. with 250 ppm BHT) was purchased from VWR (Radnor, PA). Sulfuric acid (ACS reagent, 95.0-98.0%), glacial acetic acid (ReagentPlus®, ≥99%), acetyl bromide (99%), deuterated dimethyl sulfoxide (DMSO-d_6, 99.8%),

chromium (III) acetylacetonate (99.99% trace metals basis) (Cr (III) acac,), trioxane (≥99%), and tetramethyl silane (TMS, ≥99.0%) were purchased from Sigma Aldrich (St. Louis, MO).

2.2.3 Sugar Composition, Ash Content, and Elemental Analysis

Sugar analysis was performed with a modified version of the method by *Sluiter et al*.[90] Dry and milled (0.425 mm to 0.185 mm) samples (0.175 g ± 0.005 g) were treated with 72% (v/v) sulfuric acid at 30 °C for 1 h. Each sample was diluted and heated for 2 h at 121 °C. The samples were then filtered, and the filtrate was analyzed for the concentration of different sugars by high-performance anion-exchange chromatography with pulsed amperometric detection (HPAEC-PAD). Results from the sugars composition analysis are listed in Table A1.

Ash content was determined by heating dried lignin samples at 525 °C in air for 2 h. Results of the ash content analysis are listed in Table A1.

C, H, N, S, and O elemental analysis was performed by Midwest Microlab (Indianapolis, IN, midwestlab.com). C, H, and N contents were determined by high temperature combustion in pure oxygen. The S content was determined via flask combustion and subsequent titration. The O content was determined gravimetrically by pyrolysis at 1200 °C (Unterzaucher Method[91]). The concentration of other elements was determined with proton-induced X-ray emission (PIXE) analysis by Elemental Analysis Inc (Lexington, KY, elementalanalysis.com). Results from the CHNOS elemental analysis are list in Table A2 and results from the PIXE analysis are listed in Table A3.

2.2.4 Gel Permeation Chromatography (GPC)

The lignin samples were derivatized via acetobromination.[92] Dried lignin (10 mg) was added to a 9:1 v/v mixture of glacial acetic acid and acetylbromide. The sample was heated to

50 °C and stirred for 2 h. The sample was then dried using a rotary evaporator at 60 °C. The precipitated lignin was dissolved in 2 mL of THF and filtered with a 0.1 µm PTFE syringe filter.

GPC was performed on an Agilent 1260 Infinity II HPLC with two Agilent PLgel Mixed-B polystyrene-divinylbenzene columns and a 10 µm guard column. A calibration curve was generated using polystyrene standards with M_P ranging from 162 to 6,570,000 g/mol. Solvent (stabilized THF) flowrate was set to 1 mL/min and data was collected using a UV detector (280 nm). Data analysis was conducted using Cirrus software.

2.2.5 Nuclear Magnetic Resonance (NMR) Spectroscopy

Quantitative ^{13}C NMR spectroscopy experiments were conducted following the procedure described by *Crestini et al.*[93] Prior to analysis, lignin samples were dried overnight in a low-pressure desiccator at room temperature to remove excess water. Lignin samples were dissolved in DMSO-d_6 (200 mg/mL). Approximately 100 µL of 1,3,5-trioxane (17 mg/mL), Cr (III) acac (1.8 mg/mL), and TMS (10 mg/mL) in DMSO-d_6 were added to the lignin samples. ^{13}C NMR spectra were collected on a Bruker Avance IIIHD 700 MHz NMR instrument. An inverse-gated proton decoupling pulse sequence was applied with a 90° pulse width and an acquisition time of 1.4 s. A delay of 4.5 s was used to produce a quantitative spectrum. A total of 3 K scans were collected for each spectrum. Spectra were calibrated to the TMS peak at 0.0 ppm.

^{1}H-^{13}C 2D Heteronuclear Single Quantum Coherence (HSQC) NMR spectroscopy experiments were conducted following the procedure described by *Mansfield et al.*[94] Prior to analysis, lignin samples were dried overnight in a low-pressure desiccator at room temperature to remove excess water. The lignin (50 mg) was dissolved in 1 mL DMSO-d_6. HSQC NMR spectra were collected on a Bruker Avance IIIHD 700 MHz NMR instrument using the standard

"hsqcetgpsisp2.2" pulse program (acquisition time: 0.113 s, recycle delay: 1 s). The number of time increments recorded in the ^{13}C direction was 512. The number of points collected in the ^{1}H direction was 1024, with 8 scans per increment. Spectra were calibrated to the DMSO peak at δ_C/δ_H = 39.5/2.49 ppm.

2.2.6 Thermogravimetric Analysis (TGA)

Thermogravimetric analysis was performed in a simultaneous DSC-TGA Q series 600 instrument. Prior to analysis, lignin samples were dried overnight in a low-pressure desiccator to remove excess water. Samples between 5 and 10 mg were loaded into alumina crucibles and heated from room temperature to either 650 °C in air or 1000 °C in nitrogen at a heating rate of 10 °C/min. Gas flows were kept constant at 20 mL/min.

2.3 Results and Discussion

2.3.1 Gel Permeation Chromatography

The number average molecular weight (M_N), weight average molecular weight (M_W), and polydispersity (PD) of the lignin samples were determined by GPC (Figure 4, Table 2). The softwood kraft lignin samples (SWK1-3) had similar molecular weight distributions and polydispersity, but the softwood butanol organosolv lignin (SWBuOH) had a significantly lower average molecular weight. A peak at approximately 180 Da in the trace of SWBuOH resulted in a greater polydispersity compared to the other samples. This peak also corresponded to a typical molecular weight of a mono-aromatic species, suggesting significant depolymerization occurred during fractionation. The hardwood kraft (HWK), hardwood super critical water hydrolysis (HWSCW), and hardwood SO_2/Ethanol/Water organosolv (HWSEW) lignin samples had similar molecular weights, which were lower than the softwood kraft samples. Similarly, the hardwood

butanol organosolv lignin (HWBuOH) had a much lower molecular weight than the other hardwood lignin samples.

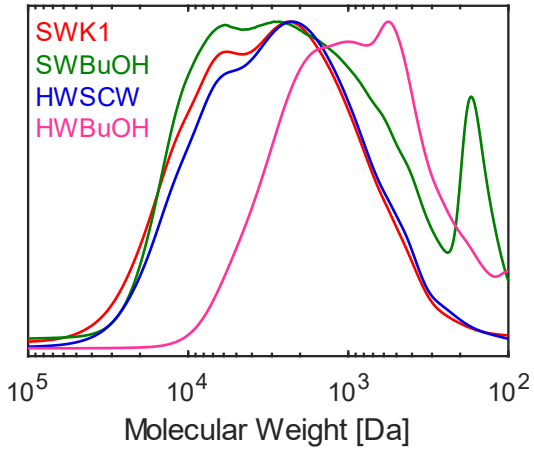

Figure 4: GPC traces of select lignin samples. All GPC traces of the lignin samples can be found in Figure A1.

Table 2: Molecular weight and polydispersity of lignin samples.

Sample	M_N [g mol^{-1}]	M_W [g mol^{-1}]	Polydispersity
SWK1	1590	5270	3.32
SWK2	1540	5060	3.28
SWK3	1610	6040	3.76
SWBuOH	860	3990	4.62
HWK	1400	4060	2.90
HWSCW	1400	4520	3.23
HWSEW	1070	3610	3.38
HWBuOH	650	1460	2.24

2.3.2 ^{13}C NMR Spectroscopy

Quantitative ^{13}C NMR spectroscopy provides direct measurement of different carbon species in the lignin structure. Analysis of the NMR spectra was limited to the aromatic carbons (162 – 102 ppm) and methoxy carbons (MeO) (58 – 54 ppm) (Figure 5).[95] The aromatic region can be further divided into aromatic carbons bonded to oxygen (C_{ArO}) (162 - 142 ppm), aromatic carbons bonded to carbon (C_{ArC}) (142 - 125 ppm), and aromatic carbons bonded to hydrogen

(C_{ArH}) (125 – 102 ppm).[95] Carbon species in conjugated double bonds were also present in the aromatic region, but these moieties are expected to account for less than 5% of the signal area.[93] Integral values are listed in Table S4, and the peak areas were normalized such that the combined aromatic carbon region equaled 6. The normalized area for the methoxy peak provided direct quantification of the methoxy content relative to aromatic carbon nuclei (Table 3). The degree of condensation (DoC) for the samples was calculated as the difference between the theoretical number of C_{ArH} per aromatic, based on the guaiacyl (**G**) and syringyl (**S**) fractions in the lignin, and the measured number of C_{ArH} from ^{13}C NMR spectra (Equation 1,Table 3).[96] An uncondensed **G** unit will contribute 3 C_{ArH} while an uncondensed **S** unit will contribute 2 C_{ArH} per aromatic. The softwood samples were assumed to be comprised solely of guaiacyl units (**G** = 1 and **S** = 0), and the **G** and **S** fractions of the hardwood lignin samples were determined from HSQC NMR spectroscopy (*see below*).

$$DoC\ [\%] = (3G + 2S - C_{ArH}) \times 100 \qquad (1)$$

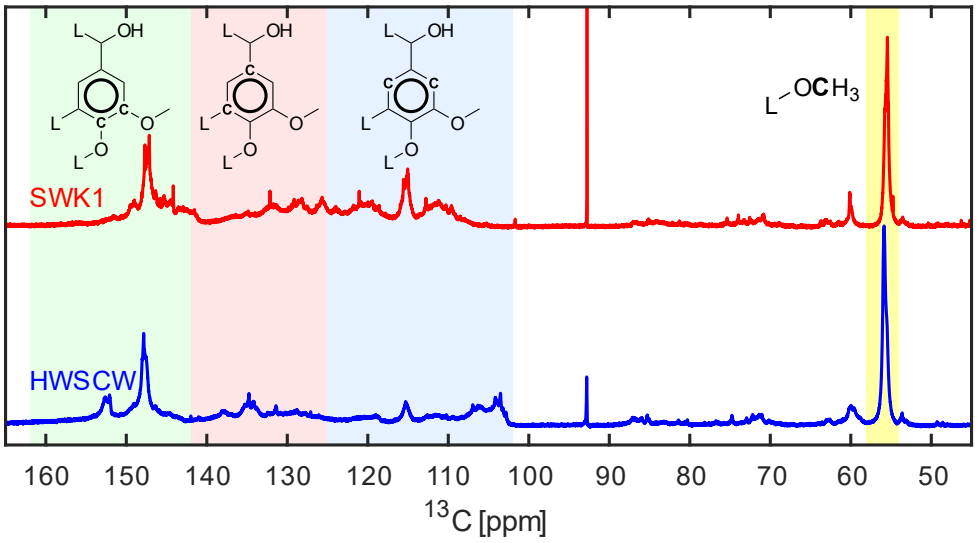

Figure 5: ^{13}C NMR Spectra of select lignin samples. Highlighted regions depict integral bounds for aromatic carbons bonded to oxygen (C_{ArO}) (green), aromatic carbons bonded to carbons (C_{ArC}) (red), aromatic carbons bonded to hydrogen (C_{ArH}) (blue), and methoxy carbons (yellow). Spectra for all lignin samples are shown in Figure A2.

Table 3: S/G ratio, methoxy and inter-aromatic linkage content, and degree of condensation of the lignin samples from this work and of technical lignin and milled wood lignin (MWL) samples from literature.[80, 95-98]

Sample	S/G	MeO [per 100 aromatics]	β5 [per 100 aromatics]	Bβ [per 100 aromatics]	βO4 [per 100 aromatics]	DoC [%]
SWK1	-	91[b]	1.7[c]	1.5[c]	5.1[c]	73[b]
SWK2	-	87[b]	2.2[c]	1.8[c]	8.4[c]	68[b]
SWK3	-	85[b]	1.6[c]	1.5[c]	4.5[c]	64[b]
SWBuOH	-	73[b]	4.9[c]	1.2[c]	4.0[c]	59[b]
Pine Kraft[80]	-	63[b]	1.6[c]	6.0[c,f]	2.2[c]	71[b]
Pine Kraft[80]	-	68[b]	1.1[c]	4.6[c,f]	8.2[c]	68[b]
Spruce MWL[95]	-	100[b]	n.r.[d]	6[b]	45[b]	38[b]
Loblolly Pine MWL[97]	-	99[b]	n.r.	n.r.	n.r.	43[b]
HWK	2.67[a]	115[b]	0.4[c]	2.1[c]	2.5[c]	36[c]
HWSCW	1.91[a]	128[b]	4.3[c]	4.2[c]	11.1[c]	41[c]
HWSEW	1.97[a]	107[b]	0.6[c]	2.1[c]	4.3[c]	61[c]
HWBuOH[e]	2.45[a]	74[b]	3.0[c]	1.7[c]	4.1[c]	30[c]
E. Grandis MWL[96]	1.72[b, f]	160[b]	3[b]	3[b]	61[b]	21[b]
Cottonwood MWL[98]	1.41[b]	151[b]	4[b]	8[b]	52[b]	13[b]
Silver Birch MWL[98]	3.02[b]	177[b]	3[b]	9[b]	66[b]	15[b]
Red Maple MWL[98]	1.20[b]	160[b]	5[b]	10[b]	58[b]	21[b]
Red Alder MWL[98]	1.37[b]	160[b]	3[b]	7[b]	59[b]	24[b]

[a] Determined from HSQC NMR. [b] Determined from ^{13}C NMR. [c] Determined by combination of HSQC NMR and ^{13}C NMR. [d] n.r. = not reported. [e] G_6 peak used to determine S/G ratio. [f] Calculated from reported values.

A major hurdle for high monomer yields is the condensation of the lignin structure during fractionation.[25] In the context of this work, a condensed structure is defined as one containing any additional, non C-H bond on the aromatic ring. Other condensed linkages exist, such as bonds between the propyl tails of monolignols, but those could not be rigorously detected with the utilized characterization techniques. Additionally, condensed moieties are found naturally in the lignin structure and do not solely arise from fractionation and isolation.[99] The DoCs of milled wood lignin have been reported between 38% and 43% for softwoods[95, 97] and between 15% and 24% for hardwoods.[96, 98] The softwood kraft lignin samples measured here had similar DoCs as reported in literature, which were also determined by ^{13}C NMR spectroscopy (Table 3).[80] Aside from simply having more reactive sites, the absence of syringyl units results in higher DoCs in both native and technical softwood lignin because the 5-position on the aromatic ring is more susceptible to condensation reactions.[100] All four fractionation processes resulted in lignin samples that had DoCs higher than native lignin, so diminished monomer yields and selectivities would be expected during depolymerization, especially using techniques which focus on breaking labile ether bonds. Despite the diverse lignin sources and process environments, these fractionation methods resulted in lignin streams with similarly condensed structures.

2.3.3 HSQC NMR Spectroscopy

The aromatic region of the HSQC NMR spectrum (δ_C/δ_H = 131/8.1 - 99/5.9 ppm)[101] has information about the lignin monomer unit composition (Figure 6). For softwood lignin, the spectrum was dominated by three peaks from guaiacyl units (G) at 111.4/7.0, 115/6.7, and 119.5/6.9 ppm, which correspond to the C-H bond at the 2 (G_2), 5 (G_5), and 6 (G_6) position, respectively. For hardwood lignin, additional peaks appeared due to the presence of syringyl units (S). The dominant peak at 103.3/6.6 ppm corresponds to the C-H bond at the 2 and 6 positions

($S_{2/6}$). The smaller peak around 106.5/7.0 ppm corresponds to S with an oxidized C_α position ($S'_{2/6}$).[101] For determining the G and S content (Table 3), the volume integral of the G_2 peak was measured and volume integrals of the $S_{2/6}$ and $S'_{2/6}$ peaks were measured and halved to account for the symmetric C-H bonds. Due to the presence of an unidentified species at δ_C/δ_H 110.3/6.36 ppm in HWBuOH, which interfered with the G_2 peak, the G_6 peak value was used in the calculations. A clear discrepancy is observed between the abundance of methoxy groups and the G and S content of each lignin sample. Demethoxylation of the lignin is expected during fractionation and is well known to occur during kraft pulping.[100] However, the higher levels of demethoxylation for SWBuOH and HWBuOH are notable.

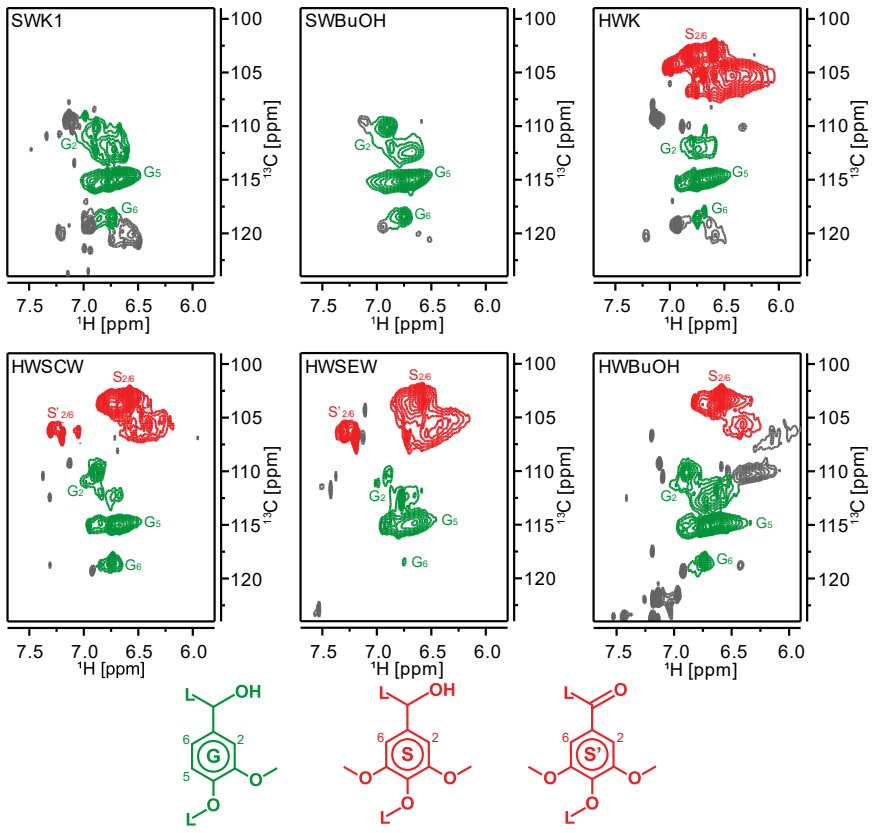

Figure 6: Aromatic region of HSQC spectrum for select lignin samples and key structures. Peak corresponding to guaiacyl (G) units are colored green and peaks corresponding to syringyl (S) units colored red. All aromatic regions from HSQC NMR spectra of the lignin samples and integration boundaries can be found in Figure A3.

The aliphatic region (δ_C/δ_H = 91/5.9 - 48/2.5 ppm)[101] has information about key inter-aromatic linkages (Figure 7). The predominant linkages that can be analyzed in the aliphatic region are the β-O-4 ether bond, the phenylcoumaran bond (β-5), and the resinol bond (β-β).[101] Each linkage has peaks corresponding to C-H bonds at the C_α, C_β, and C_γ positions. For comparisons, the volume integral for the C_α-H signal for the β-O-4 (71/4.8 ppm), β–5 (87.5/5.6 ppm), and β–β (85.7/4.5 ppm) was measured to determine the abundance of the inter-aromatic linkages. The volume of the $\beta-\beta_\alpha$ peak was halved to account for symmetry of the bond. The broad peak at 56.2/3.6 ppm arises from the methoxy groups in the lignin. The volume integral of the methoxy group peak was used as an internal standard to quantify the abundance of the linkages on a per aromatic basis (Table 3).[80] Since significant demethoxylation of the lignin samples occurred, the volume integral of the methoxy peak was calibrated to the methoxy content directly quantified by ^{13}C NMR spectroscopy.

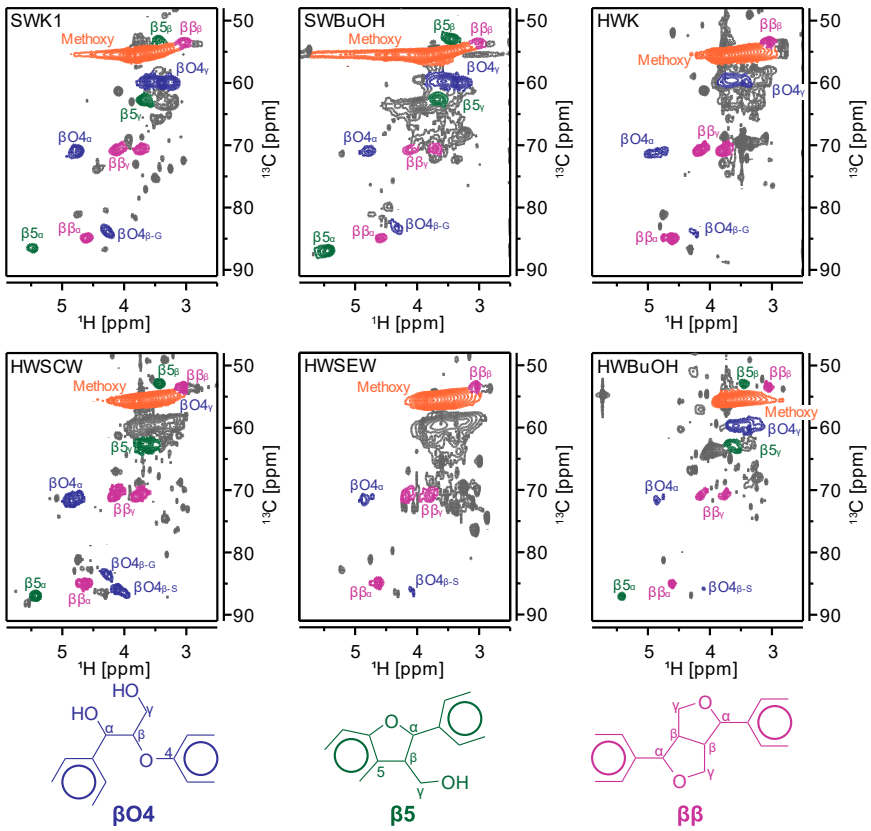

Figure 7: Aliphatic region of the HSQC NMR Spectra of select lignin samples and key structures. Peaks corresponding to methoxy groups are colored orange, peaks corresponding to the β-O-4 linkage are colored blue, peaks corresponding to the β-5 linkage are colored green, and peaks corresponding to the β-β linkage are colored purple. All aliphatic regions from HSQC NMR of the lignin samples and integration boundaries can be found in Figure A4.

The low abundance of the three measurable linkages in all the lignin samples showed that extensive depolymerization occurs during fractionation (Table 3). In native lignin, the β5 linkage was present in concentrations of between 9-12 for softwoods and 3-6 for hardwoods per 100 aromatic units, and the β-β linkages was present in concentrations of between 2-4 for softwoods and 3-7 for hardwoods.[98, 102] Of these two linkages, only HWSCW and HWBuOH exhibit concentrations that fall into the native range, while the rest were present in lower than expected concentrations. Only the ether bonds in the β-5 and β-β structure are expected to be cleaved during fractionation, so carbon-carbon linkages persist even with the disappearance of these bonds.[93] The β-O-4 bond is the most prevalent linkage in native lignin, typically ranging from 40 - 60% of

linkages. The β-O-4 content of even the most preserved lignin samples was reduced to 11.2 (HWSCW) and 8.4 (SWK2) per 100 aromatics, with the rest of the samples having roughly 5 or less. With the significant reduction of these linkages in the lignin samples, the vast majority of remaining linkages in both the softwood and hardwood samples are irregular and, most likely, uncleavable using traditional methods.

2.3.4 Theoretical Monomer Yields

While β-O-4 content is usually the best predictor for the potential monomer yield,[87] the size of the polymer can play a role as well. It has been shown that the depolymerization of lower molecular weight lignin results in higher monomer yields.[103-104] As such, comparing the theoretical monomer yields for the lignin samples allows for discussion based on a greater set of structural information. Theoretical monomer yields of the lignin samples, assuming the lignin polymers are linear, can be calculated (Equation 2) using the degree of polymerization (DoP) and the fraction of cleavable bonds (F_{CB}).[105-106] Equation 2 describes the probability that a monomer unit is linked on both sides by labile bonds or that the monomer unit is a terminal unit linked by a labile bond. The DoP can be calculated from the M_N from GPC (Table 2) and an empirical monomeric molecular weight, based on the elemental composition (Table A2), the methoxy group content (Table 3), and assuming a C_9 basis (Equations A1-A5). The F_{CB} was calculated as the number of β-O-4 bonds per linkage, where the total number of linkages per polymer is one less than the DoP (Equation A6). Most catalytic depolymerization processes focus on the ether linkages, while the aliphatic linkages are considered uncleavable. Other labile bonds do exist, such as the α-O-4, but these are typically present at low concentrations in the native lignin (< 10 per 100 aromatics)[102] and, due to similar bond dissociation energies,[107] can be expected to be significantly cleaved during

fractionation as well. Therefore, the assumption that β-O-4 content represents all cleavable bonds is reasonable.

$$Theoretical\ Yield\ [\%] = \frac{(DoP-2)\times F_{CB}^{2}+(2\times F_{CB})}{DoP} \times 100 \qquad (2)$$

In general, the hardwood lignin samples had lower DoP, which is to be expected from the comparable reductions of native linkages and lower DoCs. However, the theoretical monomer yields for all the lignin samples were similar and were all less than 5% (Table 4). The non-kraft lignin samples had higher expected monomer yields than the kraft lignin samples, except for SWK2, but the yields showed only marginal improvements. While this calculation presents a lower bound for monomer yields, from the linear polymer assumption, clearly the non-kraft lignin samples would produce similar actual monomer yields as kraft lignin. From the structural changes in the lignin samples from fractionation, also evidenced by the higher DoC and lower number of native linkages, it would be reasonable to expect that the monomer selectivity from the non-kraft lignin would be as low as from kraft lignin too. From this data, super-critical water, SEW, and butanol fractionation, when performed at industrial scale, produce a lignin that is no more viable than kraft lignin as a feedstock for valorization via catalytic ether depolymerization.

Table 4: Degrees of Polymerization, Fraction of Cleavable Bonds, and Theoretical monomer yields for the lignin samples.

Sample	Empirical Formula[a]	Monomeric Molar Mass[a] [g mol^{-1}]	Degree of Polymerization[b]	Fraction of Cleavable Bonds[c]	Theoretical Monomer Yield[d] [%]
SWK1	$C_9H_{7.7}O_{2.3}(OCH_3)_{0.91}$	181	8.8	5.8	1.6
SWK2	$C_9H_{8.1}O_{2.6}(OCH_3)_{0.87}$	185	8.7	9.5	2.9
SWK3	$C_9H_{8.0}O_{2.3}(OCH_3)_{0.85}$	180	8.6	5.0	1.4
SWBuOH	$C_9H_{8.6}O_{2.0}(OCH_3)_{0.73}$	171	5.0	5.0	2.1
HWK	$C_9H_{7.4}O_{2.0}(OCH_3)_{1.15}$	183	7.6	2.9	0.8
HWSCW	$C_9H_{7.1}O_{2.6}(OCH_3)_{1.28}$	196	7.1	12.9	4.8
HWSEW	$C_9H_{8.1}O_{3.4}(OCH_3)_{1.07}$	203	5.3	5.3	2.2
HWBuOH	$C_9H_{9.5}O_{2.1}(OCH_3)_{0.74}$	174	3.8	5.6	3.2

[a] Determined from elemental analysis and ^{13}C NMR (Equations A1-A4). [b] Determined from empirical formula and GPC (Equation A5). [c] Determined from DoP and βO4 content (Equation A6). [d] Calculated from Equation 2.

2.3.5 Thermogravimetric Analysis

Dried lignin samples were heated at 10 °C/min in a flow of nitrogen to 1000 °C. (Figure 8) This process is roughly analogous to pyrolytic depolymerization, which one may use to access value added organic molecules.[108-110] The butanol organosolv lignin samples (SWBuOH and HWBuOH) clearly showed faster decomposition at lower temperatures than any of the other samples. The remaining hardwood samples tended to decompose next, followed by the softwoods. It should also be noted that the butanol extracted lignin samples, as well as the super critical water extracted hardwood, did not fully pyrolyze and instead formed a thermally stable carbon residue. Unfortunately, it is impossible to rigorously deconvolute the influence of processing condition and wood source in this study. Additionally, ash is known to affect the thermal stability of lignin,[111] but no correlations were observed between the degradation rate and the ash content (Table A1, Table A3).

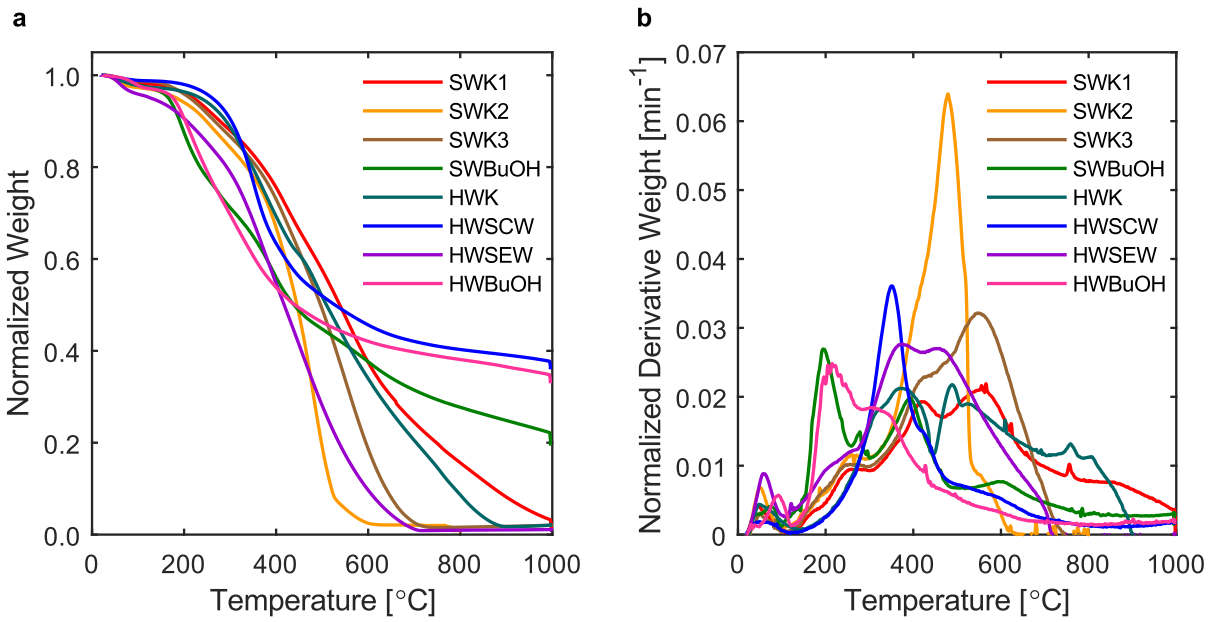

Figure 8: (a) Thermogravimetric analysis (TGA) and (b) derivative thermogravimetric analysis (DTGA) of all industrial lignin samples heated in 20 mL/min of N2 from ambient to 1000 °C at a rate of 10 °C/min.

It is important to note, though, that catalytic ether cleavage is not the only method for lignin depolymerization. Several studies have reported on lignin pyrolysis and gasification as a means of producing mixtures of volatile organic compounds (VOCs) and syngas.[108-109, 112] *Shen et al.* showed that different volatile compounds evolve at different temperatures, with aromatics favored at low temperatures and permanent gasses (CO, CO_2, H_2, and CH_4) favored at higher temperatures.[112] The fact that the measured DTGA profiles observed in this study (Figure 8b) showed so much variation likely indicates that the fast pyrolysis products of these lignin samples would also show considerable variation in quantities evolved. Among the kraft lignin samples, HWK and SWK1 both show some decomposition in the 500-800 °C range, while SWK2 and SWK3 both fully decompose below 700 °C. According to results from *Yang et al.*, this indicates that SWK2 and SWK3 will produce more light hydrocarbons and hydrogen and less CO and CO_2 compared to HWK and SWK1.[109] However, SWBuOH and HWBuOH both showed significant decomposition at 200 °C, and all the non-kraft lignin showed increased decomposition below

400 °C compared to the kraft lignin. This would imply the non-kraft processes create lignin that, while also exhibiting low either bond content as measured by NMR, generate more volatile aromatics than kraft lignin.

2.3.6 Implications for Future Biorefining

As biorefineries continue to grow in number and scale, with some projecting solid lignin production to reach 225 million tons annually by the year 2030 as a consequence of biofuels production,[75] effective methods for characterizing and valorizing lignin, through catalytic depolymerization, pyrolysis, or composite materials, will become more critical than ever. If catalytic depolymerization is the desired pathway, the structural characterization in this work clearly shows that research on novel depolymerization catalysts and processes must focus on cleaving C-C linkages as these are limiting high aromatic monomer yields from technical lignin streams. Importantly, there appear to be complexities in translating promising lab scale results to a larger scale that are not fully understood. Moreover, in all cases, downstream processes will require a consistent feedstock. Here, even the kraft lignin samples would be expected to have different physicochemical properties as significant variability is observed in the thermal degradation profiles. Therefore, developing rigorous structure-property relationships based on facile characterization methods, such as decomposition temperature and product distributions, to determine *a priori* how industrially derived lignin will perform in any given process would be immeasurably helpful in matching lignin streams and valorization pathways.

2.4 Conclusions

In this study, eight industrially sourced lignin samples were collected, and key structural properties relevant to catalytic depolymerization were characterized. NMR spectroscopy revealed heightened degrees of condensation and partial depolymerization due to fractionation in all lignin

samples, showing most of the aromatics were linked together with irregular and recalcitrant bonds. Based on NMR, GPC, and elemental analysis, the theoretical monomer yields for all lignin samples were calculated to be less than 5%. This suggests that solid lignin industrially extracted by any currently available methods will have low monomer yields and would be a poor feedstock for processes intended to take advantage of residual labile ether bonds for depolymerization. Thermogravimetric analysis showed stark differences in the thermal decomposition profiles of the lignin samples, suggesting differences in physicochemical properties and pyrolysis products. These differences may be leveraged in future work to access different types of value-added compounds.

CHAPTER 3
MODELING REACTIVE CONDITIONS IN MECHANOCHEMICAL REACTORS

3.1 Introduction

Mechanochemistry has remained an enigmatic field for much of its history.[113] Analogous to electro- and photochemistry, mechanochemistry utilizes the input of mechanical energy to drive chemical reactions.[114] These reactions are generally performed in ball mills, where the collision between the balls and the vessel supply the mechanical energy. The mechanical action in these reactors is believed to drive the chemical reactions in several ways: the creation of hot spots, enhanced solid-solid mixing and contact area, the creation of meta-stable or unstable structural configurations, or producing reactive surfaces *in situ*. The presence and influence of these different phenomena depend significantly on the media being milled, making a generalized unified theory of mechanochemistry difficult or impossible. None the less, mechanochemistry has seen an increase in popularity over the past several years, with wide applications in metallurgy and inorganic chemistry,[114-116] organic synthesis,[38] materials synthesis,[117-121] environmental protection,[122-126] biomass valorization,[69-70, 127-129] enzymatic catalysis,[130-131] and heterogeneous catalysis,[42, 132] to name a few. The mechanical processes are readily available on an industrial scale as grinding and ball milling are commonly used in manufacturing. But, the scale-up of the chemical aspect remains difficult, compared to traditional chemical processes, due to the lack of general foundational models.[133] A model capable of describing mechanochemical reactions using the existing pool of traditional chemical and physical knowledge would provide a critical step towards elucidating mechanochemistry.

Attempts to understand mechanochemical reactions have focused on a top-down approach by developing kinetic models of the reactions, typically based on energy dose.[134-138] The extent of

reaction or reaction rate have been determined by periodically removing and analyzing the reactants or, preferably, directly measuring their concentrations *operando.*[139] These efforts have highlighted the key parameters of the milling (collision energy and collision frequency)[140] and that the kinetics may follow simple power laws, step-wise kinetics, or require novel mechanisms. The rate of mechanical amorphization of Ni alloys was found to be invariant of milling conditions, but could be wholly described by energy dose.[141] The *in situ* X-ray diffractometry of mechanochemical zni-Zn(**Im**)$_2$ synthesis showed a reaction rate that follows first order kinetics,[142] contrasting earlier, *ex situ* studies, which showed second order kinetics.[143] This discrepancy could have arisen through difficulty in processing the *in situ* data caused by the heterogeneity of the sampling during milling.[144] Through continuous monitoring of gas uptake, the mechanochemical nitridation and hydridation of Hf and Zr powders was shown to follow Johnson-Mehl-Avrami-Kolmogorov kinetics with a rate constant governed by the specific energy dose.[145] The study of the co-crystallization of ibuprofen and nicotinamide, via *in situ* Raman spectroscopy, suggested a mechanism where the reactants were mechanically amorphized but then crystallized thermochemically.[146] Delogu and Takacs were also able to analyze the detailed kinetics of mechanochemical reactions to elucidate several microscopic parameters of the reactions, such as the amount of material impacted within a single collision or minimum impact energies needed to drive a reaction.[147] While the conditions and processes occurring in mechanochemical reactions are complex, their influences often collapse and allow the reaction rate to be described with straightforward kinetic equations, at least over a certain range of parameters.

A second approach, albeit a much less common one, focuses on building bottom-up models of the collision characteristics to describe mechanochemical reactions. Initial attempts to model collision energies focused on understanding the micromechanics of mechanical alloying.[148-149]

These models were based on Hertzian Contact Theory and calculated energies of 10^{-3} to 10^{-2} J per collision and temperatures rises on the order of 500 K in the powder. Kinematic equations for the average motions of balls in a planetary ball mill have also been derived and used to determine the energies of collisions,[150] and has been used to better understand mechanocatalytic reactions.[151] Hashimoto *et al.* developed a model, also based on Hertzian Contact Theory, to calculate collision energies by treating the ball and powder bed as viscoelastic materials.[152] By calculating the forces and deformation over small time steps, the energy dissipated during the collision was determined. Similar equations were used to model the particle-particle interactions instead of the ball-powder interactions. The increase in temperature,[153-154] pressure, and contact area[155] at the points of contact between particles have been modeled. Similarly to Hertzian Contact Theory approach, highly generalized equations, able to describe the localized time, pressure, and temperature conditions, were derived from the theory of glancing collisions of ridged bodies in comminuting devices.[156-157] These models have provided some insights to the microscopic phenomena of mechanochemistry, but their application has been limited. At best, the results have been correlated to macroscopic observations. There is no available model capable of describing mechanochemical reactions or kinetics.

A key difficulty of the bottom-up approach is the lack of understanding for the different phenomena that occur during collisions, but hot spot formation maybe one of the simplest to model. “Hot spots” are one of the oldest theories in mechanochemistry, dating back to Bowden & Yoffe’s works on impact explosives in the 1950s[158-159] and Thiessen & Heinicke’s work on tribochemistry in the 1960s.[160] Research into understanding the conditions of hot spots has continued to the current day.[161-167] Hot spots occur as the kinetic energy is dissipated into the milling medium during a collision, creating a short-lived spot of high temperature. These hot spots

have been proposed to have temperatures greater than 1000 K but last only on the order of microseconds[168] Several mechanisms for hot spot creation have been proposed: viscous heating, localized plastic work, friction between particles, and adiabatic heating of trapped gases,[169-171] but friction and deformation are believed to dominate.[172] The temperatures of these hot spots strongly depend on the material, thermal, and mechanical properties of the milling media.[173] Ultimately, energy will be distributed between heat, comminution, and other chemical and physical processes, but the collision energy provides a good first approximation of the hot spot heating.

Admittedly, the concept of hot spots, as an explanative theory of mechanochemistry, has come under some criticism in recent years. Discrepancies have been demonstrated in the temperature rise of milled metal and metal oxide powders, based on phase transitions.[174] Specific phase transitions were detected in Co (hcp to fcc), TiO_2 (anatase to TiO_2 II to rutile), and ZrO_2 (monoclinic to tetragonal), with the transition of ZrO_2 requiring the highest temperature of 2643 K. However, no changes were detected in Fe, Ti, or Zr, which experience phase transitions between 1100 K and 1200 K. The temperature rises in the Fe, Ti, and Zr powders may not have been as high due to particle malleability, fracturing, or many other physical and dynamic properties that differ between samples. It is also possible that other condition induced by collisions, such as high stress, could influence the phase transitions. The sub-field of organic mechanochemical synthesis has shifted away from using hot spots to describe the reactions.[175] Due to the more malleable nature of organic materials, the enhanced mixing during milling, not localized hot spots, is expected to be the predominant phenomena of the reactions,[36, 143] but reported results have suggested higher than ambient temperatures occurring during collisions.[175-176] Hot spots cannot fully explain all mechanochemical reactions, and the goal of this paper is not to discount the existence of other possible phenomena. The instances where mechanochemical results differ from thermochemical

results are simply too numerous to describe in detail.[177-183] However, at the same time, these works do not provide a definitive refutation of the presence of hot spots in all reactions.

In this chapter, a bottom-up modeling approach to study the reactive conditions in mechanochemical reactors is presented. As a first pass, the approach focuses solely on the creation of hot spots. The heat dissipated into the milling media is calculated as a ball on powder bed collision, followed by the reaction proceeding thermochemically. The mechanochemical calcium carbonate decomposition was selected to validate the modeling approach. Given a collision velocity and material properties, the final result of the model is the extent of reaction over a single collision, which can then be used to scale up to overall reaction rates based on a frequency of collision and velocity distribution.

3.2 Materials and Methods

3.2.1 Chemicals and Materials

Calcium carbonate (ACS reagent grade), silicon dioxide (~99%, 0.5 – 10 μm), and zinc oxide (<5 micron, 99.9%) were purchased from Sigma Aldrich. Calcium Oxide (Reagent grade) was purchased from Alfa Aesar. Sodium Carbonate (anhydrous, 99.5+%, ACS) was purchased from Strem Chemicals. Zinc carbonate basic was purchased from MP Biomedicals, Inc. Argon (ultra high purity grade), nitrogen (ultra high purity grade), and carbon dioxide (bone dry grade) were purchased from Airgas. Poly-methyl methacrylate (PMMA) acrylic rods were purchased from McMaster-Carr. Super Lube® Silicone Heat Sink Compound was purchased from The Home Depot.

3.2.2 Carbonate Characterization

Powder X-ray diffraction (XRD) patterns were collected on a Malvern Panalytical Empyrean diffractometer with a Bragg-Brentano^{HD} source using Cu Kα radiation (λ = 1.5406 Å). Diffractograms were collected between 20° and 100° 2θ with a step size of 0.0131303° and with a scan speed of 0.164129 s^{-1}. Transmission electron microscopy (TEM) images (50,000x magnification) were obtained on a Hitachi-HT7700 with an acceleration voltage of 120 kV and a current of 10 μA. Samples were dispersed on a supported copper mesh with acetone. Nitrogen physisorption measurements were performed using a Micromeritics ASAP 2020 physisorption analyzer. The samples were degassed at 200 °C for 140 min. Surface area was calculated from the adsorption isotherm using the BET method.[184]

3.2.3 Mechanochemical Reactions

Mechanochemical decomposition reactions were conducted using a Retsch MM400 vibratory ball mill with a modified 25 mL stainless steel milling vessel. The vessel was modified with Swagelok connections to allow for continuous gas flow through the vessel during milling. The vessel was loaded with 1.5 g of calcium carbonate ($CaCO_3$) and a single 20 mm diameter stainless steel grinding ball. The flows of argon and nitrogen were controlled by FMA-2604A Omega Mass Flow Controllers. Experiments were conducted once under a gas flow of pure argon (15 sccm) and twice under a gas flow of argon (11 sccm) and nitrogen (1 sccm). The mill effluent was analyzed in-line by a Hiden HPR-20 Mass Spectrometer. The $CaCO_3$ was milled at a specific frequency until a steady state carbon dioxide (CO_2) flow rate was reached. Control experiments were conducted by milling 1.5 g of silicon dioxide (SiO_2), 1.5 g of calcium oxide (CaO), or 1.5 g of sodium carbonate (Na_2CO_3) under similar conditions (30 Hz, one 20 mm grinding ball, 11 sccm argon). No CO_2 production was detected in any control experiment (Figure S1). 1.5 g of zinc

carbonite basic ($Zn_5(CO_3)_2(OH)_6$) was milled under argon (15 sccm) at 30 Hz until a conversion >90% was reached. A calibration curve for CO_2 in argon was used to calculate the flow rate of CO_2 from the mass spectrometer signal.

3.2.4 Thermogravimetric Analysis (TGA)

Thermogravimetric analysis experiments were performed on a Simultaneous DSC-TGA Q Series 600 instrument. Between 10 – 20 mg of the carbonate sample was placed into an alumina crucible. The sample was heated to 30 °C and held at constant temperature for 15 minutes. The temperature was then ramped at 10 °C/min to the final temperature (800 °C for $Zn_5(CO_3)_2(OH)_6$ and 1000 °C for $CaCO_3$) and then held constant for 1 hour. A gas flow of nitrogen was held constant at 50 sccm.

3.2.5 Ball Velocity and Collision Frequency Analysis

A transparent PMMA milling vessel, matching the geometry of the stainless-steel vessel, was manufactured in house. A Chronos 1.4 High Speed camera (2,678 fps) was used to film the transparent vessel with the 20 mm stainless steel grinding ball at the desired frequencies. Video files can be access in the supplementary information. A MATLAB® script, based around the built in *imfindcircles* function, analyzed the video frames to track the positions of the ball and the vessel. Video analysis used the ball diameter as an internal standard to measure distance and the time step was set as the video frame rate. Ball and vessel positions were fit with series of sine functions, as determined by the number of dominant signals from the Fourier transform of the position data. Velocity was calculated as change in position between two frames. Ball velocity was determined as the peak velocity before a collision (change in sign of the velocity vector). Mill velocity was determined as the velocity when the ball velocity is zero.

3.2.6 Coefficient of Viscosity (C_{visc}) Measurements

1.5 g of $CaCO_3$ was evenly distributed over an area of 20.3 cm^2 on a ½" AR500 carbon steel plate and pressed at 0.5 metric tons for 1 minute. The 20 mm grinding stainless steel ball was suspended with an electromagnet at the height necessary to achieve the required impact velocities. Slow motion video (iPhone 6s, 240 fps) was used to capture the ball drop and rebound. Extracted frames were analyzed using GIMP image editing software to measure the rebound height, using the ball diameter as an internal standard. Each impact velocity was measured three times. The coefficient of viscosity (C_{visc}) in the collision model (Section 3.1) was adjusted to match the rebound velocity for each impact velocity.

3.2.7 Powder Bed Heat Transfer Properties

Thermal conductivity (κ) and heat capacity (C_p) of the calcium carbonate powder was measured with a Hot Disk TPS 2500 S Thermal Constants Analyser at room temperature. Calcium carbonate powder was packed into 30 cm^3 pellets (height: 1.4 cm, radius: 2.5 cm) at packing densities between 0.25 and 0.45. The probe was coated in thermally conducting grease (heat sink compound) to remove potential thermal resistance from air between the sensor and the pellet. The sensor was placed between two pellets and values were determined from a heating rate of 10 mW for 40 seconds. Temperature drifts of the sample, collected for 80 seconds, were less than 100 mK before the experiments were collected. Mean temperature deviation for all measurements was below 10^{-3} K.

3.3 Model Description

3.3.1 Collision Model

A Kelvin-Voigt (spring-damper) collision model has been developed in order to determine computationally the energy dissipated during a ball on planar wall collision.[152] Based on Hertz

Contact Theory,[185] the interactions between colliding bodies can be applied to yield the forces on the bodies, where the restorative (spring) force (f_E) [N] is characterized by:

$$f_E = KD^{\frac{3}{2}} \tag{3}$$

$$K = \frac{4}{3(\sigma_{ball}+\sigma_{wall})}\sqrt{R_{ball}} \tag{4}$$

$$\sigma = \frac{(1-\nu^2)}{E} \tag{5}$$

D [m] represents the ball deformation and is calculated as the difference between the initial radius of the ball (R_{ball}) and the distance between the center of the ball and the wall during the collision. The radius of deformation (R_{def}) defines the area of contact between the ball and wall. Figure 9 shows a schematic of the ball-wall collision. K [kg $m^{-1/2}$ s^{-2}] is the effective spring constant of the collision and is determined via the physical properties of the ball and the wall. The properties used are Young's Modulus (E) [Pa] and Poisson's Ratio (ν).[186] σ represents the composite material parameters for either the colliding ball or wall. σ for the ball or the wall is composed of the E and ν for the material of the ball or material of the wall, respectively. For the model and experimental system of this paper, carbonate powder is caught between the grinding ball and vessel wall during a collision. As such, the Young's Modulus of the wall was taken to be that of densely packed $CaCO_3$ powder.[187]

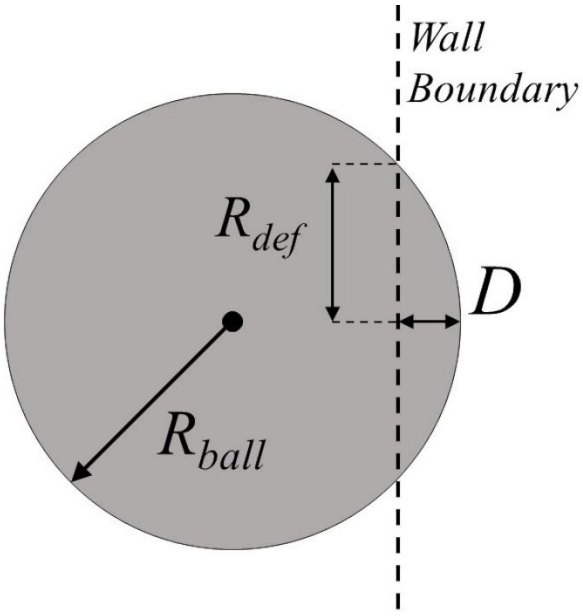

Figure 9: Scheme depicting the physical representation of the collision model with the ball radius (R_{ball}), deformation depth (D), and radius of deformation (R_{def}).

The dashpot or dissipative (viscous) force f_v [N] of the collision reflects the energy not recovered to kinetic energy after the collision and is characterized by:

$$f_v = 1.5 C_{visc} D^{\frac{1}{2}} \frac{dD}{dt} \quad (6)$$

C_{visc} [kg $m^{-1/2}$ s^{-1}], the coefficient of viscosity, is a factor that is dependent on both the ball and the wall materials and the net velocity (sum of ball and wall) of impact. Its value determines the viscous force, and by extension, energy lost through friction.[188] C_{visc} does not have an explicit function that relates it to physical properties, and so it must be determined experimentally for every unique ball and wall combination (Section 3.4.5).

The computation of the above equations is performed in MATLAB® and is based on the approach set forth by Hashimoto *et al.*[152] The collision iteration begins with two initial conditions for the ball: the velocity at the start of the collision right when contact between the ball and the wall begins, and the position of the center of the ball. The former can be set to any desired starting

velocity based on the distribution of velocities in the mill. The latter is exactly one ball radius away from the wall, such that $D = 0$ at the start of the collision and $D < 0$ for its duration. Additionally, the velocity of the wall can also be set as either a constant value or as a function of time. While this velocity does not explicitly appear in the equations of motion (Equations 7 and 8), it affects D by its constant relative motion compared to the ball and therefore f_E and f_v, which do appear in the equations of motion.

$$\ddot{p} = -g + \frac{f_{Ei}}{m_{ball}} + \frac{f_{vi}}{m_{ball}} \tag{7}$$

$$\ddot{p}(0) = -g, \dot{p}(0) = \dot{p}_0, p = 0 \tag{8}$$

The collision forces affect the motion of the ball and are modeled using Equations 3 and 6. The simulation of the differential equations for acceleration, velocity, and position of the ball is carried out by discretizing time into intervals Δt [s], and using a 1st order forward Euler method using the standard equations of discrete particle motion, shown for the acceleration (Equation 7). Initial conditions are given in Equation 6 with the standard definitions for velocity and position (p).

The deformation (D) and the rate of deformation (dD/dt) [m s^{-1}] are available directly from the position and velocity of the ball. These values are updated once every time-step and result in a feedback loop that will eventually halt the motion of the ball into the wall and reverse it. Once the velocity has reversed, the ball moves away from the wall and f_v no longer affects the collision, as plastic deformation has ceased.[188] Once $D \geq 0$, the collision has ceased. A Δt of 1 nanosecond was chosen based on the results of an error analysis to ensure that the dissipated energy during the collision differs negligibly from change in the kinetic energy of the ball before and after the

collision. This is key in order to obtain accurate energy dissipation values, which in turn are used in the calculation of hot spot temperatures, as explained subsequently.

The elastic and dissipative forces are stored for each iteration during the collision, allowing for the calculation of elastic energy (E_E) [J] and dissipated energy (E_v) [J] via trapezoidal rule solutions of the following integrals:

$$E_E = \int_0^D f_E \, dD \tag{9}$$

$$E_v = \int_0^D f_v \, dD \tag{10}$$

The above integrals are solved at every time step, yielding their values up to each individual collision time point during the collision trajectory. Due to the use of a small *dt* of 1 nanosecond, the error accrued due to using the trapezoidal approximation for the integrals is negligible. As a fraction of the dissipated energy is imparted as heat into the collision interface, the change in temperature caused by E_v can be calculated for a progressively larger cylindrical hot spot (Equation 11). The thermal dissipation factor (φ) is the fraction of dissipated energy that contributes to temperature increase, and the mass (m_{powder}) [kg] and specific heat (C_p) [J kg^{-1} K^{-1}] is that of the material trapped during the collision in the progressively larger hot spot.

$$\Delta T = \varphi \cdot E_v \cdot \, m_{powder}^{-1} \cdot C_p^{-1} \tag{11}$$

The radius of the cylindrical hot spot (R_{def}) can be determined at each time-step via a geometric relationship with R_{ball} and D:

$$R_{def} = \sqrt{D(2R_{ball} - D)} \tag{12}$$

The cylindrical radius of the hot spot grows larger as the circular collision interface between the ball and the wall grows larger. With R_{def} and the powder thickness and packing density, the mass

of the cylinder *m* can be calculated. The temperature differences of each progressive iteration are summative, meaning that the innermost cylinder experiences temperature differences equal to the number of iterations, and the outermost only experiences one. As the iteration progresses up to the maximum deformation (D_{max}), isothermal epicycles of decreasing temperature are calculated, thus yielding the temperature gradient formed by the collision. The collision duration is assumed to be much shorter than the timescale of heat conduction, so heat transfer effects are ignored in the collision model. The powder is also assumed to have a uniform temperature as a function of height.

The resulting model allows for a variety of simulation scenarios to be studied. The collision velocity can be adjusted in order to analyze the temperature profiles of average collision velocities that correspond to different milling frequencies.

3.3.2 Heat Decay Model

While the collision model is used to generate the temperature profile of a hot spot based on a collision, it does not take into account the decay of the hot spot due to heat conduction through the powder bed. However, in order to characterize a reaction rate caused by the hot spot, the temporal persistence must be understood. To achieve this, a COMSOL® model was developed that takes, as the input, the radial temperature gradient produced by the collision model, and outputs the decay of the gradient. This yields the time for the temperatures present to fall below the threshold for significant reaction, as well as the profile of the decay up to that point. It should be noted that some of the powder will be moving with the mill, but, in this experimental system, most of the powder is caked to the walls of the vessel and is effectively stationary with respect to the surrounding powder.

Since the duration of the collision falls within 10-100 μs, the conduction that occurs during this time is much lower than the conductive dissipation of the hot spot after the collision, which

occurs on time scales of 10 – 100 ms. Thus, conductive decay of the hot spot during the collision itself is negligible, and so the COMSOL® model can viably utilize the temperature gradient at the end of the collision as the starting point for the hot spot decay.

Geometric assumptions must be made as well. The general layout, as shown below, consists of the inner hot spot cylinder (at the max deformation) surrounded by an outer cylinder that models the powder on the ball mill wall. For computational ease, the model is constructed and computed in two dimensions with radial symmetry. Figure 10 shows a three-dimensional render of the cylinder with a delineation between the two regions of powder. The outer diameter is set such that the temperature decay of the hot spot radially outward does not affect temperatures near the edge during the time scales of interest. This powder bed sits on a second cylinder that represents the metal wall behind the powder bed. While the outer powder cylinder encircling the hot spot serves to conduct heat radially out from the collision, the metal behind serves to characterize conduction through the hot spot into the ball mill wall.

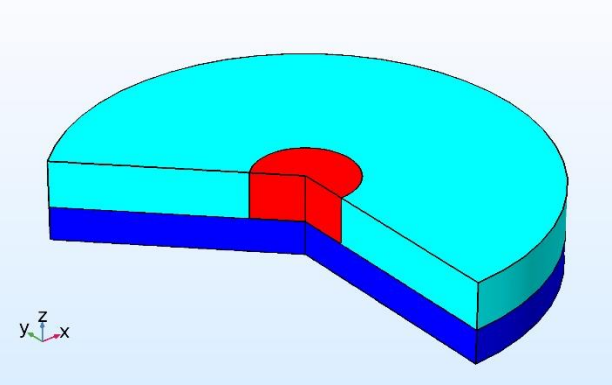

Figure 10: COMSOL render of the hot spot with the collision volume (red), surrounding powder (light blue), and metal wall (dark blue).

The physical parameters required by the model are the heat transfer properties of the powder and the metal (density (ρ) [kg m^{-3}], thermal conductivity (κ) [W m^{-1} K^{-1}], and heat capacity (C_p) [J kg^{-1} K^{-1}]). The initial conditions are set based on the characterization of the hot spot and its

surroundings at the end of the collision. The temperature profile of the hot spot, from its center to its outer radius, is passed into COMSOL® using a fourth order polynomial fit to the data produced by the collision model. The powder surrounding the hot spot and the metal wall are set at ambient conditions (293 K). To reconcile initialization issues within COMSOL® due to the large temperature difference between the hot spot center and the steel wall, a smoothing region is implemented at the bottom of the hot spot powder layer. This smoothing region is small compared to the overall hot spot cylinder height (<1%) and therefore negligibly affects reaction rate. Additionally, as part of the COMSOL® parameterization the 'fraction of initial time step for Backward Euler' is set to 0.00001 (default is 0.001). The boundary conditions of the outer cylinder wall of the powder and the metal, as well as the backside of the metal are set as isothermal (293 K). To account for heat loss through the top of the powder cylinder (hot spot and surrounding powder), convective heat transfer boundary condition was implemented. The heat transfer coefficient (h) was set to 100 W m^{-2} K^{-1} as a typical value.[189]

Finally, the COMSOL® model is run for 50 ms at a time step of 0.2 ms using a physics-controlled mesh with a size setting of 'Fine'. After the model was run, the temperature values of nodes evenly spaced in the r and z directions as a function of time were exported. 500 nodes in the r-direction from ½Δr to $2R_{def}$ – ½Δr and 100 nodes in the z-direction from ½Δz *to* l – ½Δz were used, where Δr and Δz are the step length in their respective directions and l is the powder height.

3.3.3 Batch Reactor Model

The temperature profiles of the nodes (T_{node}) from the two-dimensional COMSOL® model were imported to MATLAB® to calculate the extent of reaction over the duration of the hot spot. Each node represents a concentric volume (V_{node}) [m^3] of the powder bed (Equation 13). The reaction rate for each node ($Rate_{node}$) [mol s^{-1}] is then calculated using Arrhenius law based on

activation energy and pre-exponential factor for the reaction of interest (f_{rate}) (Equation 14). Extent of reaction (ξ_{node}) [mol] is then calculated by the trapezoid rule between time points (Equation 15). The extent of reaction of the hot spot as a function of time can be calculated by summing all ξ_{node} at each time step and the extent of reaction of the hot spot as a function of space can be calculated by summing each ξ_{node} for all time steps. The final result of the model is the extent of reaction for a single collision event.

$$V_{node} = \Delta z \cdot \pi \cdot ((r_{node} + \Delta r)^2 - (r_{node} - \Delta r)^2) \quad (13)$$

$$Rate_{node,t_i} = f_{rate}\left(T_{node,t_i}, C_{A,node}, \dots\right) \cdot V_{node} \quad (14)$$

$$\xi_{node,t_{i+1}} = \left(Rate_{node,t_i} + Rate_{node,t_{i+1}}\right) \cdot \frac{\Delta t}{2} \quad (15)$$

3.4 Results

3.4.1 Calcium Carbonate Characterization

XRD was used to verify the starting material was calcium carbonate and to assess the influence of milling on the crystal structure (Figure B2). The unmilled calcium carbonate consisted of pure calcite. After milling for 11 hours, the calcium carbonate showed a significant presence of aragonite, which forms at pressures greater than 2 GPa.[190] Rietveld refinement determined the crystalline composition to be 52% calcite and 48% aragonite. A significant decrease of the signal-to-noise ratio and peak broadening indicated significant amorphization. No crystalline calcium oxide was detected, as expected from the low overall conversion (<0.5%). TEM imaging (Figure 11) provided a visual tool for assessing the influence of milling, as well as to determine the average particle size needed for the thermal decomposition kinetics (Section 3.4.3). Prior to milling, the calcium carbonate was comprised of relatively small discrete particles with an average particle diameter of 40 nm. After milling, the particles showed high levels of agglomeration, which

demonstrates the formation of highly reactive surfaces, which could be rationalized by dislocation of surface atoms to form high energy surfaces or the formation of melted domains. Either case could make particles adhere to each other. Similar particle agglomeration has been observed in the ball milling of limestone.[191] N_2-physisorption showed an increase in BET surface area from 0.22 m^2g^{-1} before milling to 8.2 m^2g^{-1} after milling (Figure B3), indicating that porous agglomerates were formed during milling.

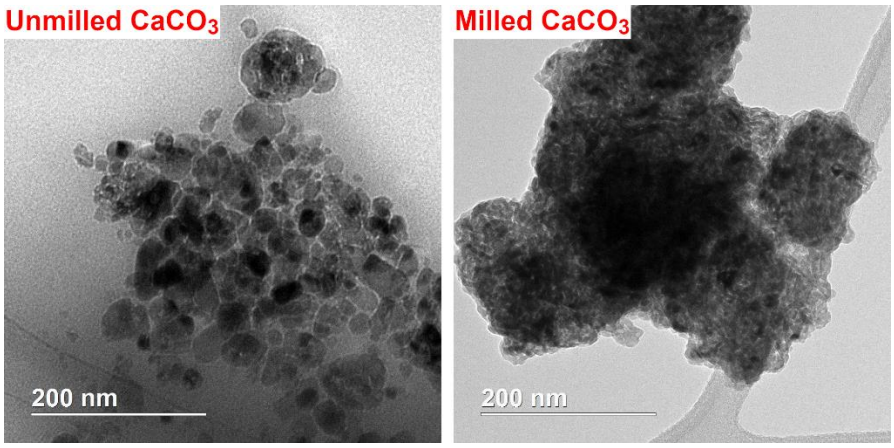

Figure 11: TEM images of the unmilled calcium carbonate and milled calcium carbonate

3.4.2 Mechanochemical Reactions

In-line MS allowed for real time detection of CO_2 in the exhaust stream from the stainless steel ball mill during mechanochemical decomposition of the carbonates. Before delving into hot spot conditions, it is important to acknowledge that simple fracturing of decomposing inorganic particles can produce the volatile products, sometimes through non-thermal processes,[177-180] and this has been observed to contribute to CO_2 formation from $CaCO_3$.[192-193] However, the 93% conversion of $Zn_5(CO_3)_2(OH)_6$ milled at 30 Hz for 6.5 hours (Figure B4a) demonstrates that the detected CO_2 must come from more than fracturing the carbonate particles. The near quantitative conversion of $Zn_5(CO_3)_2(OH)_6$ to zinc oxide (ZnO) is consistent with the XRD trace that only contains diffractions from crystalline ZnO domains (Figure B4b). Comprehensive kinetics could

not be found for $Zn_5(CO_3)_2(OH)_6$, so the decomposition of $CaCO_3$ was selected as the model system to study. The low reaction rate of $CaCO_3$ allows for pseudo-steady state rates to be reach at each milling frequency (Figure 12a). Other runs showed similar signals, but with the milling frequencies in different orders. An 11-point moving average (red) was overlaid on the raw data (black) to highlight the true value of the signal. The highest milling frequency (30 Hz) was dictated by the instrument hardware. For milling frequencies below 22.5 Hz, the signal-to-noise ratio became too low to accurately quantify the CO_2 signal.

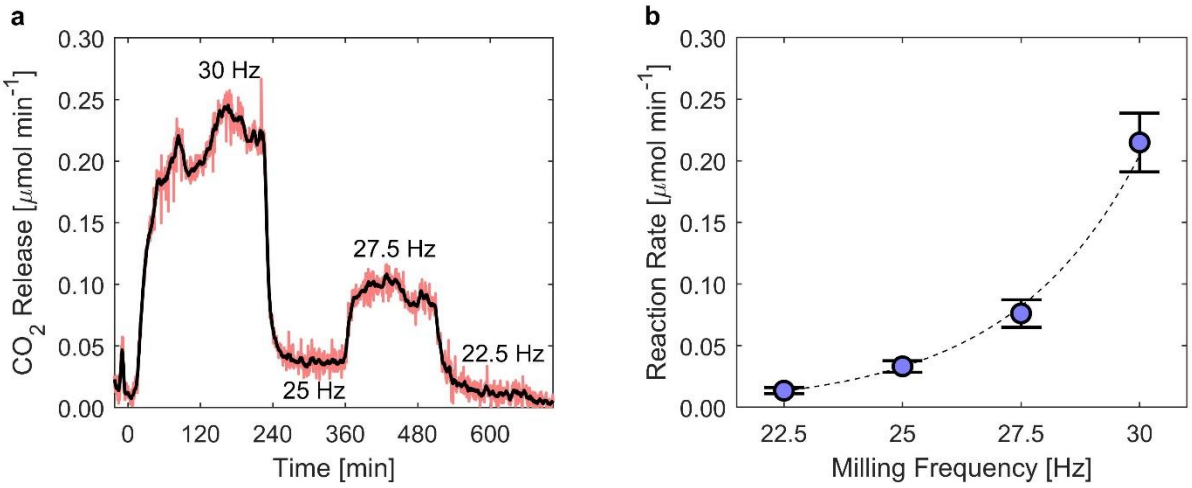

Figure 12: Mass spectrometry results from the mechanochemical decomposition of $CaCO_3$. (a) CO_2 release during the milling of calcium carbonate at frequencies between 22.5 Hz and 30 Hz and (b) average pseudo steady state reaction rate. The raw data (red) was smoothed (black) using an 11-pt moving average to highlight the response to the change in milling frequency.

The pseudo- steady state reaction rates of $CaCO_3$ for the milling frequencies (Figure 12b) ranged from 0.014 to 0.22 µmol min^{-1}. The rates were two to three orders of magnitude lower than the reaction rate of $Zn_5(CO_3)_2(OH)_6$, which is expected due to the higher thermal decomposition temperature of $CaCO_3$ (750 °C versus 258 °C) as determined by thermogravimetric analysis (Figure B5). The reaction rate of $CaCO_3$ increased exponentially with increasing milling frequency (R^2 = 0.998). This exponential trend is a strong indicator that the reaction involves a thermal mechanism. The collision frequency is expected to be linear (Section 3.4.4) and collision energies

are expected to be quadratic with respect to milling frequency. The exponential trend arises from an Arrhenius relationship between the hot spot temperature and reaction rate. While the three trials were conducted using different milling orders, gas phase composition, and gas flow rates, the relatively tight error bars indicate that these parameters have minimal impact on the steady state value.

3.4.3 Partial Pressure of CO_2

As described by the kinetics of carbonate decomposition (Equation 16), the partial pressure of CO_2 (p_{CO2}) around the calcium carbonate particles affects the reaction rate.[194] A series of differential equations, based on the mass balance of CO_2 in the powder bed and reactor bulk, were derived to determine the partial pressure of CO_2 within the powder bed. The reactor is treated as two distinct systems, the void space within the powder bed and the empty bulk space of the vessel, with a single interface between them. Equation 17 describes the change in the partial pressure of CO_2 within the particle bed (p^*_{CO2}) [atm] with a generation term from the decomposition reaction and an outflux term as mass transfer into the bulk reactor. The partial pressure is assumed uniform, both within the powder bed and the bulk reactor, and that individual collisions do not affect the partial pressure within the powder bed. Equation 18 describes the change in the partial pressure of CO_2 in the bulk reactor (p^r_{CO2}) [atm] with an influx term of CO_2 from the powder bed and an outflux term from the carrier gas of the reaction. Here, the transfer of CO_2 from the powder bed to the bulk reactor is governed by the partial pressure differential and a mass transfer coefficient.

$$Rate = \frac{\gamma M_{CaCO_3}}{\rho r_0 (2M_{CaO} R_1 T)^{0.5}} \cdot \frac{1}{p_{CO_2}} \cdot \exp\left(\frac{\Delta_r S_T^o}{R_1}\right) \cdot \exp\left(\frac{-\Delta_r H_T^o}{R_1 T}\right) \cdot n_r \qquad (16)$$

$$\frac{dp^*_{CO_2}}{dt} = \left(k_{rxn} \frac{1}{(T_{rxn})^{0.5}} \frac{1}{p^*_{CO_2}} \exp\left(\frac{-\Delta_r H_T^o}{R_1 T_{rxn}}\right)\right) \frac{R_2 T_{rm}}{V^*} - \frac{k_{mt}}{V^*}\left(p^*_{CO_2} - p^r_{CO_2}\right) \qquad (17)$$

$$\frac{dp_{CO_2}^r}{dt} = \frac{k_{mt}}{V^r}\left(p_{CO_2}^* - p_{CO_2}^r\right) - \frac{\dot{v}}{V^r}p_{CO_2}^r \quad (18)$$

A MATLAB® script was written based on the built-in functions *fmincon* to fit variable or unknown parameters and *ode45* to solve the differential equations. The fitted parameters are the effective reactor temperature (T_{rxn}) [K] under each milling condition, the interspatial volume of the powder bed (V^*) [m^3], the mass transfer coefficient (k_{mt}) [$m^3\ s^{-1}$], and the initial conditions for each partial pressure under each milling condition. The partial pressure of CO_2 in the bulk reactor is known from the mass spectroscopy data (Figure 12a). The actual reactor temperature (T_{rm}) was assumed to be 298 K. The bulk reactor volume (V^r) [m^3] and gas volumetric flow rate ($\dot{v}$) [$m^3\ s^{-1}$] are known from the experimental set-up. R_1 [$J\ K^{-1}\ mol^{-1}$] and R_2 [$m^3\ atm\ K^{-1}\ mol^{-1}$] are the Gas Constants with appropriate units. The partial pressures for each milling frequency for each experiment were solved simultaneously with the same V^* and k_{mt}. Figure 13 depicts the typical fitting results.

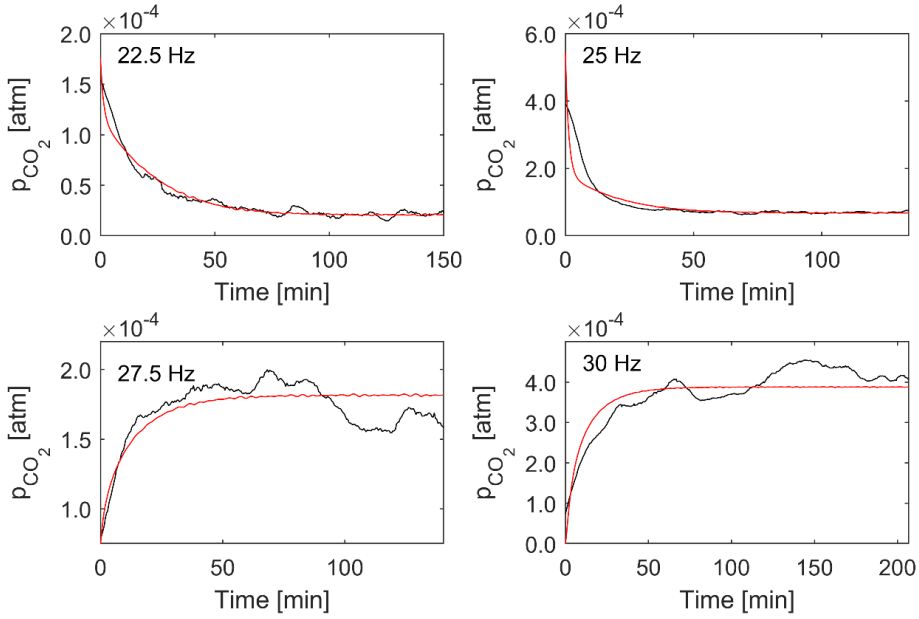

Figure 13: Typical results from fitting the transient partial pressure of CO_2 in the bulk of the reactor based on the differential mass transfer equations. Model results (red) overlaid the experimental measurements (black) from the experiment depicted in Figure 12a.

Figure 14a shows the apparent reactor temperature and Figure 14b the steady state partial pressure of CO_2 in the powder bed as a function of milling frequency. The linear dependence of the apparent reactor temperature ($R^2 = 0.9985$) is expected from the exponential dependence of the reaction rate, and provides support that the fitted parameters are reasonable. The steady state partial pressure increases exponentially with milling frequency ($R^2 = 0.9985$), which is expected as the partial pressure is largely governed by the rate at which CO_2 produced (reaction rate). This in turn is also exponentially dependent on milling frequency. Additionally, the partial pressure of CO_2 within the bed is approximately three orders of magnitude higher than that of the bulk. With this mechanochemical reactor set up, mass transfer of the gaseous chemicals requires a high driving force. From these results it is clear that for mechanocatalytic reactions involving either gaseous reactants or products, mass transfer is an important consideration when studying the kinetics of the system.

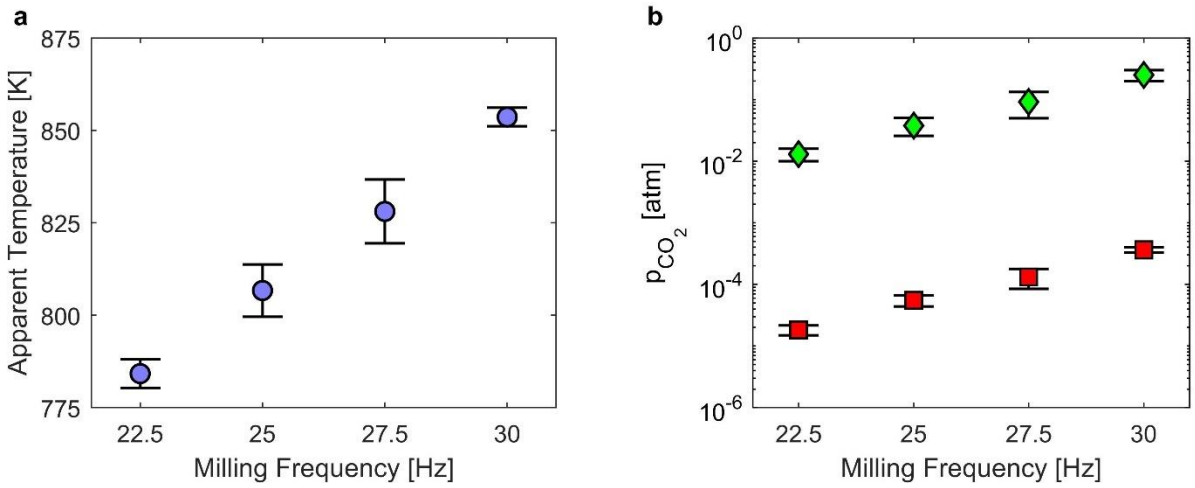

Figure 14: (a) The apparent bulk reactor temperatures required to thermally decompose $CaCO_3$ at the measured rate and (b) steady state partial pressures of CO_2 in the bulk reactor (squares) and within the powder bed (diamonds) based on the results from fitting the differential equations to the mass spectrometer data.

3.4.4 Video Analysis and Collision Velocities

Video analysis of the milling ball in a transparent milling vessel provided the horizontal (x) and vertical (y) positions of the ball and milling vessel over time. Figure 15 shows frames of the video with the ball and mill position identified by the analysis script. The resolution of the circle finding script was not sufficient to extract quantitative information about motion perpendicular to the plane of the video. Qualitative analysis of the ball motion shows a resonance pattern for each mill cycle. For this reason, the x-position and y-position vectors were fit with series of sine functions to smooth the data in place of moving averages. Figure 16a shows a representative portion of the ball velocity in the x-direction ($v_{x,ball}$), the fitted mill velocity in the x-direction ($v_{x,mill}$), and collision events for the 30 Hz milling. The system was dominated by two end-on collisions in the x-direction per cycle. $v_{x,ball}$ remained fairly constant between collisions, suggesting minimal kinetic energy lost from glancing collisions. This was confirmed by the collision events in the y-direction having approximately an order magnitude lower collision velocity.

Figure 15: Frames representing the two dominant collisions in the reactor; backwards (right) and forwards (left). Image identification of the ball (red) and mill position (green) and highlighted as well.

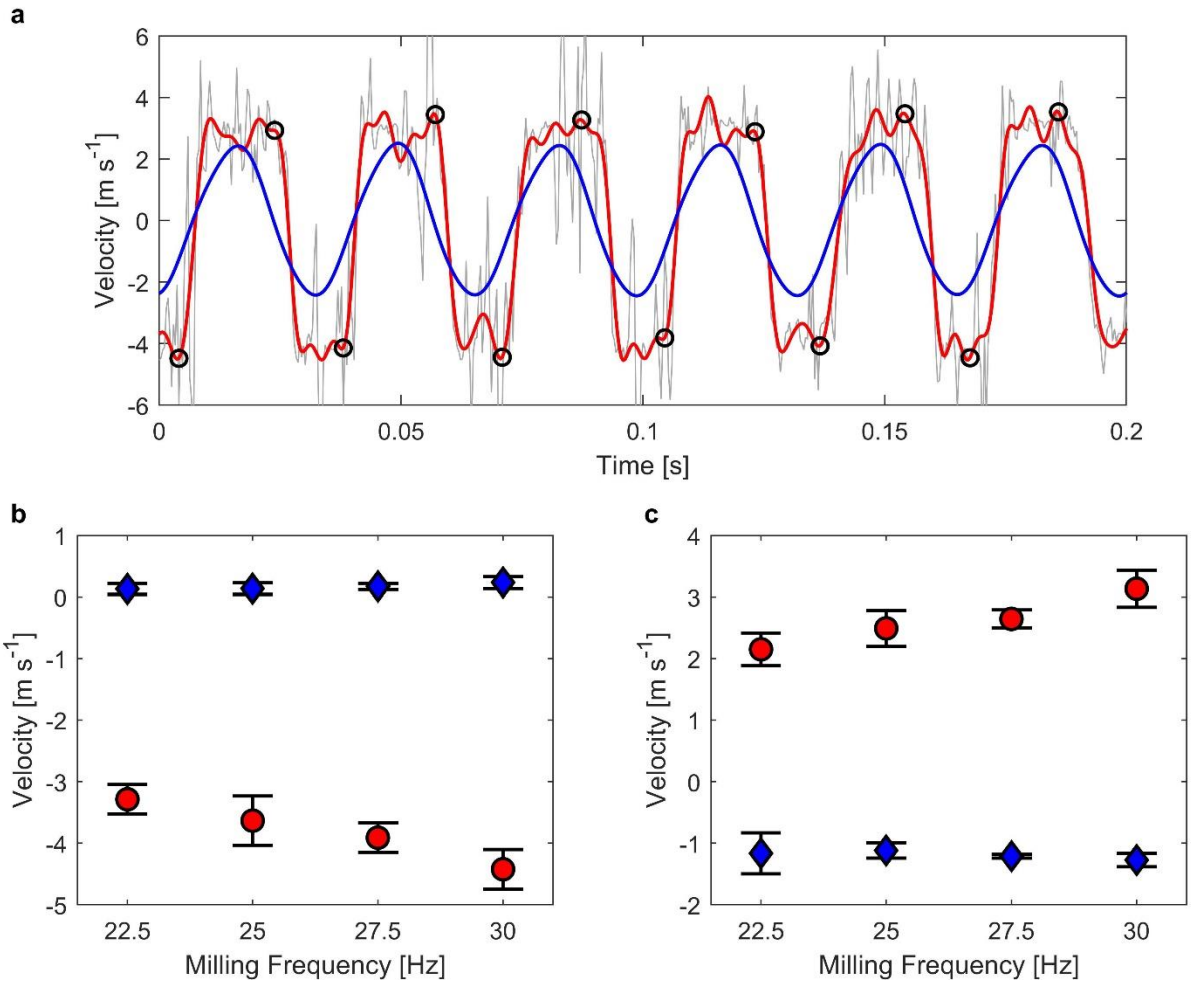

Figure 16: Results from video analysis of milling dynamics. (a) A typical segment of the profiles for the ball and mill velocities during 27.5 Hz milling in the x-direction with the raw ball velocity (light gray), the smoother ball velocity (red), the mill velocity (blue), and collision events (circles). (b) The average ball (circles) and mill (diamond) collision velocities in the backwards (negative x) direction at the relevant milling frequencies. (c) The average ball (circles) and mill (diamond) collision velocities in the forwards (positive x) direction at the relevant milling frequencies.

Somewhat surprisingly, the two end-on collision were asymmetric. For the collision with the ball moving in the negative x-direction, the ball had a higher collision velocity. During the collision with the ball moving in the positive x-direction, the ball had a higher exit velocity than its incoming velocity. These findings are illustrated in Figure 16b and Figure 16c, which shows the negative x-direction collision ball and mill velocities and the positive x-direction collision ball and mill velocities. In both collisions, the velocity of the ball and mill at impact increased linearly

with milling frequency (R^2 = 0.9966, R^2 = 0.9851). The y-intercept of the ball velocities are negative, suggesting the linear relationship may not hold true over the whole space of milling frequencies. Despite the numerous glancing blows, the system is sufficiently described by at most two collisions per cycle.

3.4.5 Determination of C_{visc}

Rebound velocities were measured for impact velocities ranging from 2 to 5 m/s in increments of 0.5 m/s. This is the range was based on velocities from the high-speed video footage. The corresponding C_{visc} values for the velocities are shown in Figure B6. The results were fit with a power function (Equation 19) that allows interpolation of C_{visc}. A power function is deemed most appropriate due to its vertical asymptote at x = 0, which conveys that lower velocities tend towards perfectly inelastic collisions. The data shows a downward trend in C_{visc} with increasing velocity. Therefore a faster collision will contribute a smaller fraction of its kinetic energy to frictional dissipated energy, however that kinetic energy will be higher, and therefore the absolute dissipated energy has a higher value.

$$C_{visc} = 1.94 \cdot 10^6 \, v_{col}^{-0.919} \tag{19}$$

3.4.6 Thermal Properties of the $CaCO_3$ Powder Bed

The thermal properties of the calcium carbonate bed, specifically thermal conductivity (κ) and heat capacity (C_p), play an important role in the temperature and duration of the hot spots. The correlations of the thermal properties of powders and their bulk materials have long been researched, but the correlation rely on powder properties such as particle contact area and knowledge of the conductive, convective, and radiative heat transfer between particles.[195-196] Due to the complexity of the correlations, the thermal properties of the calcium carbonate powder were directly measured. The values of κ of the powder as a function of packing density ranged from

0.10 and 0.17 [W m^{-1} K^{-1}] with a linear increase with packing (R^2 = 0.9609), although this may be a result of a narrow sample space (Figure B7a). The C_p of the powder at packing densities between 0.25 and 0.45 showed to be independent of the packing (Figure B7b). The sum deviation from the average value of 816.8 J kg^{-1} K^{-1} and from the literature value of 834.3 J kg^{-1} K^{-1} for bulk calcite was 156.7 J kg^{-1} K^{-1} and 145.1 J kg^{-1} K^{-1}, respectively.[197] The literature value was used for all conditions in the model.

3.5 Discussion

3.5.1 Model Application and Results

3.5.1.1 Collision Model

The collision model provides various descriptors of the hot spots (Table 5). The inputs are the velocities of the ball and the wall, with the net velocity of the two the driver of dissipated collision energy (E_v). Within the range of net velocities of interest for this experiment (2 to 5 m s^{-1}), energy dissipated ranges between 0.06 and 0.36 J. The pressure values shown below are a result of the elastic force at the maximum deformation applied to the hot spot area. The large force over a small area results in a large pressure value that is experienced by the particles in the powder bed but not necessarily the gas within the bed. Finally, the maximum radius of the deformation, which characterizes the size of the hot spot, has a quadratic relationship with net velocity.

Table 5: Dominant net collision velocities for each milling frequency and corresponding model outputs for each collision condition.

Frequency [Hz]	Net Vel. [m s^{-1}]	Collision Energy [J]	Time to Max Deformation [s]	Total Collision Time [s]	Max Pressure [Pa]	Radius Max Deformation [m]
22.5	3.3140	0.1640	$2.1277 \cdot 10^{-5}$	$6.4998 \cdot 10^{-5}$	$7.2823 \cdot 10^{8}$	$7.3112 \cdot 10^{-4}$
22.5	3.4198	0.1743	$2.1272 \cdot 10^{-5}$	$6.4587 \cdot 10^{-5}$	$7.4196E \cdot 10^{8}$	$7.4486 \cdot 10^{-4}$
25	3.6077	0.1931	$2.1262 \cdot 10^{-5}$	$6.3896 \cdot 10^{-5}$	$7.6589E \cdot 10^{8}$	$7.6878 \cdot 10^{-4}$
25	3.7747	0.2106	$2.1251 \cdot 10^{-5}$	$6.3319 \cdot 10^{-5}$	$7.8669E \cdot 10^{8}$	$7.8956 \cdot 10^{-4}$
27.5	3.8570	0.2194	$2.1245 \cdot 10^{-5}$	$6.3046 \cdot 10^{-5}$	$7.9678E \cdot 10^{8}$	$7.9964 \cdot 10^{-4}$
27.5	4.0832	0.2447	$2.1227 \cdot 10^{-5}$	$6.2333 \cdot 10^{-5}$	$8.2402E \cdot 10^{8}$	$8.2684 \cdot 10^{-4}$
30	4.4082	0.2831	$2.1197 \cdot 10^{-5}$	$6.1391 \cdot 10^{-5}$	$8.6197E \cdot 10^{8}$	$8.6470 \cdot 10^{-4}$
30	4.6585	0.3144	$2.1172 \cdot 10^{-5}$	$6.0723 \cdot 10^{-5}$	$8.9031E \cdot 10^{8}$	$8.9296 \cdot 10^{-4}$

The energy dissipated at each primary collision is shown in Figure 17, which shows a quadratic relationship between net velocity and dissipated energy. In terms of the backward and forward collisions observed, the energy contribution from the floor is higher in the forward collision and lower in the backward collision. However, the ball velocity is lower in the forward collision, yielding a lower overall energy dissipation. For the backward collision, the net velocity is comprised nearly entirely of the velocity of the ball.

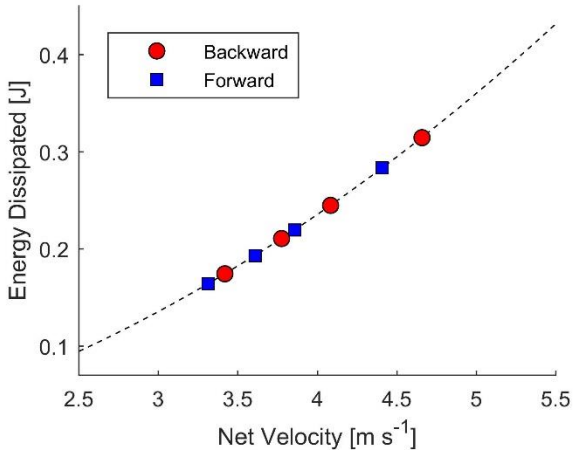

Figure 17: Computed dissipated energy for four experimental milling frequencies (22.5, 25, 27.5, and 30 Hz). Each frequency has two energy dissipated values as the collision on each end of the ball mill has a distinct ball/wall velocity combination.A key insight from the collision model is the

spatial resolution of the collision event. Uniformly distributing the dissipated energy into the collision mass would result in temperature rises of only 120 to 240 K, which would be far too low to produce any noticeable reaction. A cumulative collision energy model sheds light on the distribution of E_v as a function of radial location by describing the amount of dissipated energy contained within any radial location of the hot spot. As seen in Figure 18a, only a very small fraction of the dissipated energy is contained at the very center of the hot spot. However, the temperature is highest there because the volume initially in contact with the ball is miniscule, meaning that even that small amount of energy is enough to cause a large temperature increase. As the deformation radius increases, the hot spot volume increase outpaces the energy increase, such that temperatures are lower radially outward from the center of the hot spot. The temperature profile in Figure 18b demonstrates this and serves as the initial condition for the temperature decay model.

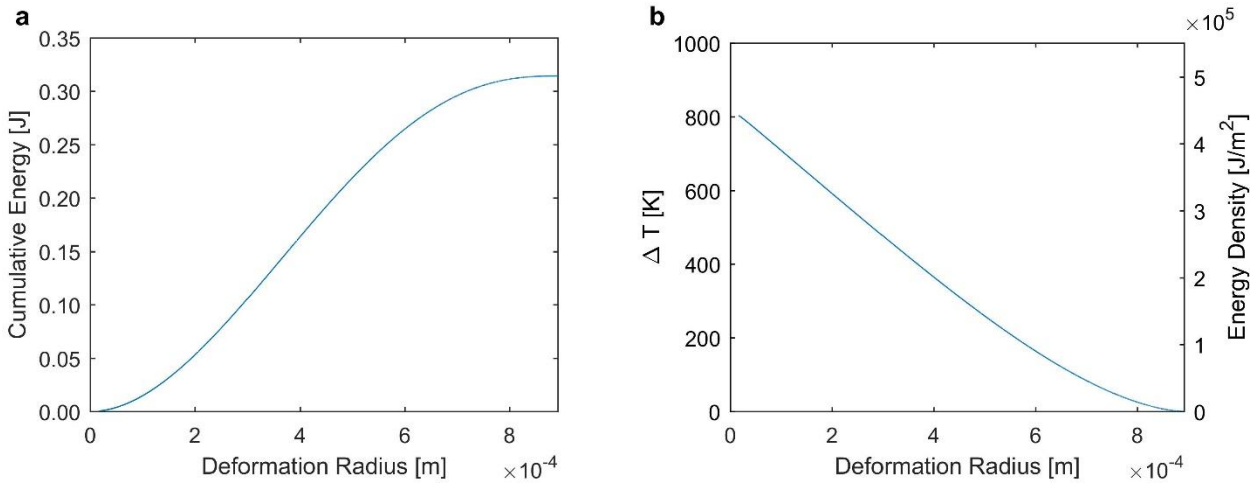

Figure 18: (a) Cumulative energy dissipation profile and (b) temperature rise and energy density profile versus deformation radius of the collision at 30 Hz (4.66 m s^{-1}).

The increasing volume approach and the magnitude of the maximum temperature of the hot spot is supported by literature. There is experimental evidence using infrared sensors in support of high temperature spikes (>1000 °C) at the very beginning of an impact, suggesting that a

stepwise collision process better characterizes hot spot temperature than a bulk approach whereby all collision energy is inserted into the final deformation volume.[198] Indeed, studies that utilize a bulk approach yield much lower temperature changes.[148-149, 199-200] One discrepancy that became apparent is that others report one to two orders of magnitude less energy dissipation compared to this work.[149, 199] This is easily explained by the use of different milling media, which can vary greatly in their elastic properties. The approach presented here remains rigorous as energy dissipation is characterized by the physical ball drop experiment described earlier, and thus is calibrated to accurately characterize the physical system in question.

As mentioned above, the appropriateness of the spatial resolution selected for the model is important to consider. Too little resolution results in temperature insufficient to drive the observed chemical reaction. Conversely, this model treats the powder bed as a continuous medium and sacrifices the individual particle interactions for computational ease and efficiency. This simplification results in a loss of information at the point of particle-particle contact. The discrepancies of the pressures during the collision highlight this loss in information. The model calculates a maximum pressure of 0.89 GPa, whereas as the formation of aragonite, which was detected experimentally, requires a minimum experienced pressure of 2 GPa.[190] The higher pressures arising from the small contact areas in particle deformations have been smoothed out in this model. Similarly, temperatures at the points of contact between particles can be expected to be higher than the bulk during the collision. Due to the large temperature gradient that would exist between the particle surface and core, along with the order of magnitude higher thermal conductivity of the particle ($\kappa_{calcite} \sim 3$ W m^{-1} K^{-1})[201] compared with the powder bed ($\kappa_{powder} \sim 0.2$ W m^{-1} K^{-1}), it can be assumed that the bulk mass of the particle rapidly reaches a pseudo-thermal equilibrium. For mechanochemical reactions that use the bulk material, this state

of intraparticle thermal equilibrium should sufficiently characterize the system. For systems where surface interactions are significant, such as in mechanocatalysis with gaseous reagents, the necessary spatial resolution should be more rigorously addressed.

3.5.1.2 Temperature Decay Model

The heat decay occurs on the order of milliseconds (Figure 19). Since this time frame is significantly longer than that of the collision, heat transfer from the hot spot to the environment during the actual collision event can be neglected. The heat dispersion occurs primarily through heat transfer to the surrounding powder and metal plate. However, due to the high thermal conductivity of the metal and the increasing radial mass of powder around the hot spot, negligible increases in temperature are observed in either component. Due to the low convective heat transfer, the peak temperature persists roughly one fourth the powder height below the surface, but this condition is only noticeable long after the reaction has completed (Section 3.5.4). Finally, the peak temperature drops below 373 K after roughly 400 ms.

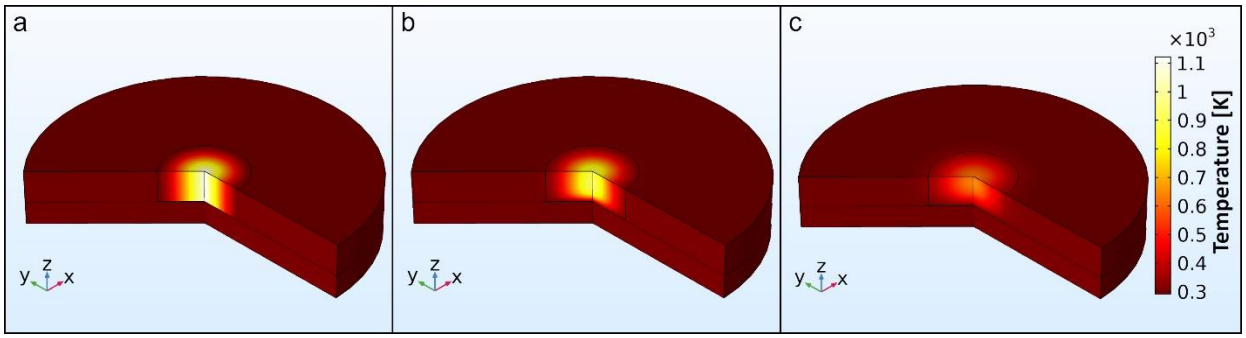

Figure 19: Progression of the temperature profile within in the hot spot and surrounding powder and steel plate. Temperature profiles are shown at (a) 0 ms, (b) 50 ms, and (c) 250 ms after collision.

3.5.1.3 Batch Reactor Model

The temperature decay profile can be treated as a batch reactor in order to determine the extent of reaction as a function of both space and time. For all conditions, the COMSOL model

was run for 50 ms, which fully captures the extent of reaction. Since the extent of reaction will perpetually increase with longer model times, the final extent of reaction (ξ_{col}) was defined as 99.9% of the extent of reaction at 50 ms. To confirm the suitability of this criterion, the COMSOL model for one of the 30 Hz conditions was ran for 500 ms and resulted in only a 0.12% increase in extent of reaction. Figure 9 shows typical results from the reactor model of ξ_{col} as a function of space (a) and of time (b). Qualitatively, the reaction occurs in only a small portion of the hot spot. Due to the exponential nature of the rate, the hot center contributes disproportionately to the overall extent of reaction. The fluctuations along the highest ridge arise from small deviations in the COMSOL® initialization. Similarly, the reaction rate occurs predominately at the beginning of the hot spot and quickly decays, despite the still relatively high temperature. This observation is not surprising considering that reaction rate constants are exponential functions of the temperature.

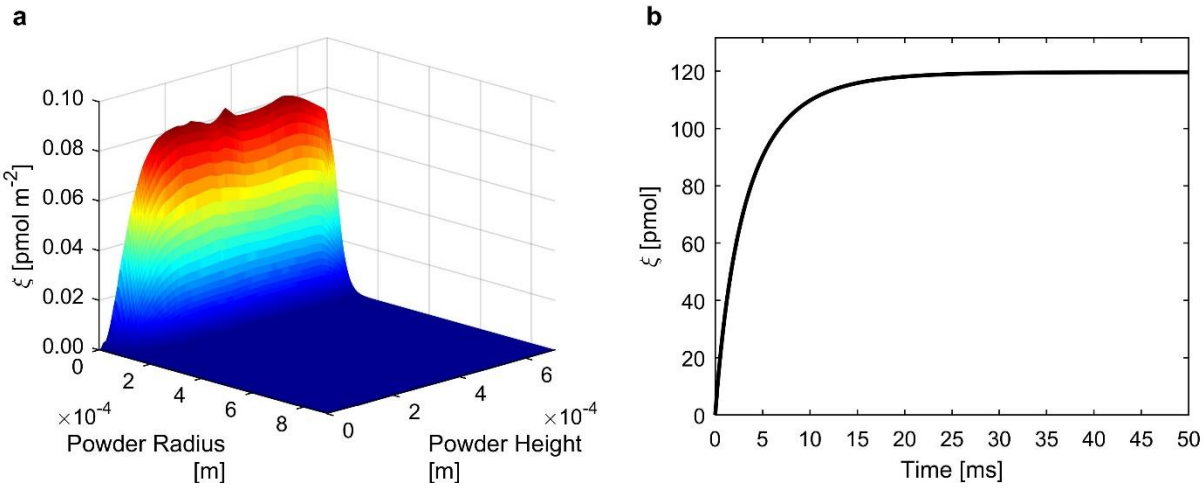

Figure 20: (a) The final extent of reaction per area across the vertical cross section of the hot spot and (b) the extent of reaction over time for the 30 Hz milling condition.

For determining the total extent of reaction, the contributions from both collisions were considered. Since the partial pressure of CO_2 (p_{CO2}) is known for only the mill as a whole, the reactor model was run with the same p_{CO2} for all collisions within the same milling frequency. From this, the slower of the two collision energies produce merely 1% of the ξ_{col} of the higher

velocity collision. As such, only the more energetic of the two combinations is utilized in the calculation of reaction rates at each frequency. This also means that each milling cycle has only a single meaningful collision event. Thus, the extent of reaction per collision for this reaction is simply the steady state reaction rate divided by the milling frequency.

Previous studies of energy dissipation and temperature rise during collisions have assumed that all the dissipated energy is released as heat.[149, 199] When just studying the final temperature, this assumption is acceptable as nearly all the energy does dissipate as heat, and any discrepancies will only result in linear errors in terms of the final temperature. However, when studying chemical reaction rates, the errors will be exponential. Thus, an additional parameter, Thermal Dissipation Factor (φ), is considered to make this correction. The predominant modes of energy dissipation are friction (or heat), particle fracture, and particle kinetic energy,[202] but essentially no research has been performed to understand energy partitioning of a ball collision with a fine powder bed. The energy partition during a collision has primarily been studied in the context of particle breakage, where the particles are only an order or two of magnitude smaller than the ball. The heat generated during the breakage of a single particle from a ball collision was found to be between 30% and 80% of the supplied kinetic energy, but the total dissipated energy was not reported.[203] Since no clear means exist to measure this parameter experimentally, the factor was fit with the model for each milling frequency in order to accurately study the hot spot conditions. Table 6 shows the final results for each milling frequency. At higher net collision velocities, φ decreases, meaning more of the energy is dissipated through other phenomena, such as the kinetic energy of ejected particles.

Table 6: Summary of the primary experimental and modeling results used in final parameters and outputs for each milling frequency.

	Reaction Rate [mol s^{-1}]	p_{CO2} [atm]	Φ	ξ_{col} [mol]	Collision Energy [J]
22.5 Hz	$2.25 \cdot 10^{-10}$	$1.30 \cdot 10^{-2}$	0.9625	$1.00 \cdot 10^{-11}$	0.174
25 Hz	$5.54 \cdot 10^{-10}$	$3.80 \cdot 10^{-2}$	0.9347	$2.22 \cdot 10^{-11}$	0.211
27.5 Hz	$1.27 \cdot 10^{-9}$	$9.13 \cdot 10^{-2}$	0.9159	$4.62 \cdot 10^{-11}$	0.245
30 Hz	$3.58 \cdot 10^{-9}$	$2.50 \cdot 10^{-1}$	0.8712	$1.19 \cdot 10^{-10}$	0.314

3.5.2 Model Sensitivity Analysis

The sensitivity of the model was studied by varying each model parameter for the 30 Hz milling condition by ±10% (even though several parameters can be controlled much more accurately). Figure 10 depicts the change in extent of reaction and maximum temperature at the hot spot for each parameter. A clear division in sensitivity is apparent due to the Arrhenius nature of the chemical reaction. Parameters that contribute to the exponential term of the rate law, or have substantial effect on the hot spot temperature, have a drastic effect on the calculated extent of reaction. Additionally, the ball velocity shows the most asymmetric sensitivity in temperature (and correspondingly extent of reaction). Maximum temperature is proportional to the square root of velocity, so an increase in velocity results in a smaller absolute change in temperature compared to a decrease in velocity. The mass of the collision increases proportionally to the collision velocity, and despite the total dissipated energy increasing quadratically with velocity, the energy dissipated at the center of the collision increases proportionally to the velocity to the power of 1.5. At higher collision velocity, the energy becomes more evenly distributed throughout the collision mass. The asymmetry observed for the extent of reaction and maximum temperature for the thermal dissipation factor, hot spot mass, and heat capacity are simply a result of their mathematical relationships.

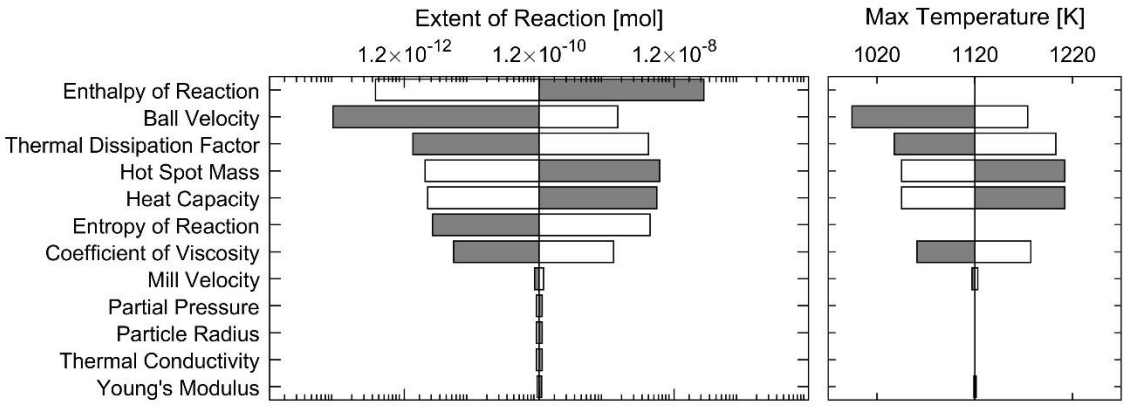

Figure 21: Sensitivity analysis of the hot spot model with respect to the various parameters. Shown are the change in the extent of reaction and maximum temperature for the 30 Hz condition resulting from a 10% increase (white) or 10% decrease (gray) in each parameter.These results additionally highlight the key properties of the milling system that require high levels of accuracy and understanding to fully predict mechanochemical reaction rates. The distribution profiles of collision velocities need to be determined as more energetic collisions will contribute disproportionally more to the reaction rate. This will be an important challenge for systems with multiple balls that can collide with each other, in addition to ball-wall collisions. Methodologies to independently measure how the dissipated energy is partitioned and directly measure the amount of powder caught in the collision are necessary. Finally, accuracy in the pre-exponential factor and activation energy of the thermochemical rate equation is equally important as any one of the mill dependent parameters.

3.5.3 Predictive Capabilities

To explore the predictive capabilities of the model, the error in the expected steady state reaction rate was calculated based on extrapolation and interpolation of a subset of the data. The two parameters that were required are φ and p_{CO2}. φ was predicted based on a linear fit against the milling frequency net collision velocity. p_{CO2} was predicted based on an exponential fit against

milling frequency. A total of seven conditions were analyze: one where all four data points were used in the fit and six where the fit from two milling frequencies were used to predict the remaining two. The errors are shown in Table 7. The fit will all four conditions provides a baseline range for the expected errors. Even with all data, the fit produces error between 5% to 20%. The extrapolation and interpolation of the data will, in general, result in higher errors. However, despite the exponential error relationship between reaction rate and φ, fitting the data with simple linear equations, using two data points, results in a single maximum error of just 63.7% with most of the errors being substantially lower.

Table 7: Errors in predicted $CaCO_3$ decomposition rates based on extrapolation and interpolation of a subset of data. The fitted data was used to predict φ and p_{CO2} for the remaining data in order to calculate the expected reaction rate.

	Reaction Rate Error [%]			
Fitted Data	**22.5 Hz**	**25 Hz**	**27.5 Hz**	**30 Hz**
22.5, 25.0, 27.5, 30.0	-14.5	6.7	-19.8	14.3
22.5, 25.0	-	-	-40.9	-44.6
22.5, 27.5	-	-56.6	-	16.7
22.5, 30.0	-	8.6	-19.1	-
25.0, 27.5	-41.6	-	-	63.7
25.0, 30.0	-22.4	-	-26.5	-
27.5, 30.0	51.6	30.6	-	-

3.5.4 Hot Spot Characteristics – Size, Duration, and Temperature

Application of the model allows for investigation into the characteristic of the hot spot. The three key aspects of the hot spot, in the context of chemical reactions, are duration, size, and temperature (Table 8). As described in Section 3.5.1, the final extent of reaction was taken as 99.9% of the extent of reaction at 50 ms. This provides the definition for the duration of the reactive hot spot. The reactive hot spots exist on the order of 10 ms, and the duration increases at higher milling frequencies. While nearly all of the collision powder experiences temperature increase, most of it remains too cold to significantly contribute to the reaction. Here, the radius of the hot

spot is defined as the radius of material that contributes 99% of the extent of reaction. These radii are an order of magnitude smaller than the collision radius, resulting in only about 1.5% of the collision mass contributing to the reaction. The temperatures in all cases exceed 1000 K, but decrease by only 150 K by the time the reaction has decayed.

Table 8: The reaction conditions within the hot spots generated in under each milling condition.

Milling Frequency [Hz]	Duration[a] [s]	Radius[b] [m]	Initial Max Temperature [K]	Final Max Temperature[c] [K]
22.5	$2.41 \cdot 10^{-2}$	$9.18 \cdot 10^{-5}$	1030	884
25.0	$2.75 \cdot 10^{-2}$	$9.85 \cdot 10^{-5}$	1059	907
27.5	$3.04 \cdot 10^{-2}$	$1.05 \cdot 10^{-4}$	1086	928
30.0	$3.53 \cdot 10^{-2}$	$1.15 \cdot 10^{-4}$	1120	956

[a] Time to reach ξ_{col} ($\xi_{col} \equiv 99.9\%\ \xi_{50ms}$); [b] Radius encompassing 99% ξ_{col}; [c] Maximum temperature at the end of the hot spot

The results of the hot spot temperature highlight the importance that bulk reactor temperature can play in mechanochemical reactions. There is a relatively small difference between the temperatures of each milling frequency. The collision event can be assumed adiabatic, and that bulk temperature will have minimal influence on the dissipated energy. Raising the bulk temperature should translate to an equivalent increase in the hot spot temperature. Therefore, controlling the bulk reactor temperature can allow for effective shifts in milling frequency and result in exponential changes in reaction rate. Conversely, a sufficiently low bulk temperature can effectively quench a reaction. This effect was indirectly demonstrated by Eckert *et al.*, who showed an increasing conversion of mechanocatalytically oxidized CO at lower temperatures because the transient active sites formed from the mechanical impact of the catalyst (Cu/Cr_2O_3) decayed more slowly.[204] Such trends were also observed by Andersen *et al.* when studying the mechanochemical Diels-Alder cycloaddition of several dienes and dienophiles.[175] The milling of benzoquinone and 9,10-dimethylanthracene for three hours at ambient conditions (36 °C) resulted in 100% yield, but a reduction in the reactor temperature to 22 °C resulted in a yield of just 12%. Likewise, the milling

of benzoquinone and anthracene produce no measurable yield after three hours at ambient conditions, but raising the reactor temperature to roughly 90 °C and 100 °C resulted in yields of 35% and 100%, respectively.

Milling vessels and grinding balls have been shown to have high temperature increases (>50 °C) under certain milling conditions.[205-206] Often, reactor temperatures are measured as the outside surface temperature of the mill, but potentially large temperature gradient can exist between the outer wall and the milled powder.[206] The bulk temperature rise during organic mechanosynthesis has been measured *in situ*, with results ranging from 10 to 40 K (largely due to the heat of reaction). This change in temperature can significantly impact the reaction pathway.[207-208] It can be clearly seen that precise controls of reactor temperatures and accurate measurements thereof will be critical in fundamentally understanding and optimizing mechanochemical reactions.

3.5.5 Collision Efficiency

The question of how efficient mechanochemical reactions are have long been pondered by experts in this field.[209-212] The application of the hot spot model allows for the efficiency of single collision events to be assessed. Here, three efficiency are defined: total energy efficiency (η_{energy}), thermal energy efficiency ($\eta_{thermal}$), and product efficiency ($\eta_{product}$). For total energy and thermal energy, an additional parameter is introduced, "useful heat" (Q_u), which is the total heat dissipated into the effective hot spot radius. Total energy efficiency is defined as the fraction of total dissipated energy (E_v) that goes into useful heat. Similarly, thermal energy efficiency is the fraction of the thermal energy ($\varphi \cdot E_v$) that becomes useful heat. Finally, product efficiency is the ratio of the extent of reaction times the activation energy (E_a) to the total dissipated energy. Table 9 shows the efficiency for all four milling frequencies. The total energy efficiencies and thermal energy

efficiencies range between 5.3% and 6.1%, but show opposing trends. At low enough milling frequencies, all dissipated energy will go into heat, and the total energy efficiency and thermal energy efficiencies will be identical. Therefore, a most energy efficient milling frequency exists for this system. It is important to state again that these efficiencies are especially low due to how intensive the carbonate decomposition reaction is, and efficiencies are expected to increase with more facile reactions. The third metric, product efficiency, provides insight to the absolute utility of the dissipated energy. While the total energy efficiency decreases and thermal energy efficiency slightly increases, the efficiency at which energy is converted into product increases exponentially. It is important to note that the efficiencies are dependent on the specific chemical reaction. In terms of whole mechanochemical reactors, the efficiency of individual collision represents a theoretical maximum, as any system will have additional energy losses (motor friction, ineffective collisions, etc.). This ability to describe the collision efficiencies will allow for more direct comparisons of reactions in different ball mills and provide guidance in optimizing mechanochemical reactors.

Table 9: Total Energy, Thermal Energy, and Product Efficiencies for the single collision hot spots at each milling frequency.

Milling Frequency [Hz]	Total Energy Efficiency[a]	Thermal Energy Efficiency[b]	Product Efficiency[c]
22.5	$5.50 \cdot 10^{-2}$	$5.71 \cdot 10^{-2}$	$2.81 \cdot 10^{-5}$
25.0	$5.45 \cdot 10^{-2}$	$5.83 \cdot 10^{-2}$	$5.15 \cdot 10^{-5}$
27.5	$5.46 \cdot 10^{-2}$	$5.96 \cdot 10^{-2}$	$9.24 \cdot 10^{-5}$
30.0	$5.33 \cdot 10^{-2}$	$6.12 \cdot 10^{-2}$	$1.86 \cdot 10^{-4}$

[a] $\eta_{total} \equiv Q_u/E_v$; [b] $\eta_{thermal} \equiv Q_u/\varphi \cdot E_v$; [c] $\eta_{product} \equiv \xi \cdot E_a/E_v$

3.6 Conclusions

Herein, a three-part model to determine the energy release, thermal conditions present, and extent of reaction during a collision of a milling ball with a mill wall was developed. Such a model requires knowledge of the physical and thermal properties of the milling media and understanding the dynamics and kinematics of the ball mill system. The model was verified with the

mechanochemical decomposition of calcium carbonate. It shows that the collisions last for tens of microseconds and dissipate on the order of a hundred millijoules of energy into the milling media. These collisions create reactive hot spots that exceed 1100 K and persist for tens of milliseconds. Additionally, for this very energy intensive reaction, a per-collision energy efficiency of roughly 5% is seen. The model is highly sensitive to parameters that exist in the exponential term in the rate kinetics. And yet, it is capable of predicting reaction rates within a 65% error. The methodology of this model need not be limited to the phenomena of hot spots but should be generalizable as long as physical and chemical laws relating energy and reaction rates are available. While refinements, revisions, and additions will be necessary for broader application, this model marks an important step forward in understanding the fundamental phenomena in mechanochemical reactions.

CHAPTER 4
DEMONSTRATING NOVEL MECHANOCATALYST BEHAVIOR VIA AMMONIA SYNTHESIS

4.1 Introduction

The fixation of N_2 to ammonia, a key precursor for fertilizers, is one of the most significant chemical reactions to the modern world,[213-214] fueling the explosive global population growth over the past century. However, ammonia synthesis is burdened by two competing factors: the N_2 triple-bond is very stable (bond energy = 945 kJ mol^{-1}), but ammonia formation is thermodynamically favored at low temperature. Currently, ammonia is obtained almost exclusively through the Haber-Bosch process, which operates at high temperatures (>400 °C) and pressures (>100 atm) in order to achieve sufficient rates and conversion.[215] These harsh reaction conditions require specialized facilities and centralized plants, which inhibit local ammonia production in developing regions, restricting access to fertilizers and limiting agricultural output.[216] This process also accounts for ~2% of global energy consumption and ~1% of global CO_2 emissions, mainly from hydrogen production via methane reforming.[217-218] New industrial processes that operate under mild conditions, with renewable energy sources, and near end use would facilitate both distributed fertilizer production[219] and a decarbonized ammonia industry.[220] Novel catalytic approaches have utilized electrons,[221-222] photons,[223-225] and non-thermal plasmas,[226-227] as well as looping system conditions,[228-230] to synthesize ammonia closer to ambient conditions. Such processes could produce ammonia directly from nitrogen and water using solar power or operate at scales where water electrolysis is competitive with methane reforming. However, none of these alternative approaches are used industrially, so the need for small scale ammonia synthesis remains unresolved.

Mechanochemistry offers a novel platform for distributed chemical production. Lab scale applications exist in a plethora of research areas (*e.g.* organic synthesis,[38, 231-232] materials synthesis,[233-234] heterogeneous catalysis,[235-236] biomass valorization[69, 128, 237]). In these approaches, mechanical energy is applied to the system to drive the reaction, often in ball mills.[113] The energy released during the collisions between grinding balls, reactor walls, and catalyst particles can create transient thermal hot spots,[238] fresh reactive surfaces,[239] and highly active transient defect sites.[42, 132] Due to this localized energy input, reactions that traditionally require elevated temperatures and pressures can operate in reactors at nominally ambient conditions. Mechanochemical approaches to chemically bind nitrogen, such as in metal nitrides[240-241] or N-doped graphite,[242] have been reported. However, mechanocatalytic nitrogen fixation to ammonia has been reported only twice before, more than four decades ago, and over iron based catalysts.[243-244] Gaps in documentation and analysis make these experiments nonreproducible, and specific understanding of the catalytic reaction and process design were not provided. Therefore, rigorously demonstrating mechanocatalytically synthesized ammonia with modern analytics opens truly new opportunities for distributed ammonia production.

As proof of concept, ammonia was mechanocatalytically synthesized for the first time over an *in situ* formed titanium nitride (TiN) catalyst under nominally ambient conditions (<50 °C, 1 atm) from N_2 and H_2. Milling titanium powder (Ti) in a vibratory ball mill with a stainless-steel milling vessel modified to allow a steady gas flow of N_2 and H_2 resulted in the simultaneous formation of TiN and the continual synthesis of ammonia without the need for external heating or pressurizing.

4.2 Materials and Methods

4.2.1 Chemicals

The gases Ar, H_2 and N_2 were obtained from AirGas with a purity of UHP, grade 5. Titanium nitride (TiN), anatase titanium dioxide (TiO_2) were obtained from Alfa Aesar in powder form with a purity of 99.7% trace metals basis. Titanium powder (Ti) (100 mesh, 99.7% trace metals basis), iron powder, and iron oxide (Fe_3O_4) were purchased from Sigma-Aldrich. The titanium powder was stored in a desiccator to minimize additional oxidation.

4.2.2 Mechanocatalytic Reactions

Mechanochemical reactions were performed in a Retsch MM400 shaker ball mill with a 25 mL stainless steel reactor vessel and one stainless steel grinding ball (d = 20 mm, m = 32.3 g). The mill runs with a built-in timer, so the start button needed to be manually pushed every 90 min for experiments longer than 90 min. The reactor was modified by adding two 1/8 in NPT outlet tubes to allow for continuous gas flow. A frit was installed at the effluent connection to retain solids. The reactor was neither heated nor pressurized, though the vessel did heat up internally due to the milling action. Reactions were conducted with 2.00 g of either Ti or TiN powder. The catalyst powder and grinding ball were loaded into the vessel, which was then connected to the gas flow. The gasses were allowed to stabilize at the initial condition for at least 30 minutes prior to milling. During gas composition changes, milling was continued. Unless otherwise specified, the reaction was carried out at a milling frequency of 30 Hz, and a total gas flow of 15 standard cubic centimeters per minute (sccm).

After each reaction, the reactor was disassembled, rinsed, and sonicated with water for 30 min to remove residual catalyst powder. Additionally, silica-alumina powder was milled to further remove any remaining powder. The reactor was then rinsed again and sonicated in dilute

sulfuric acid (pH ~3) for 30 min to remove any residual ammonia on the equipment. Afterwards, the reactor was rinsed and sonicated in pure water for 30 min to remove residual sulfuric acid. Finally, the reactor was placed in a convection oven (105 °C) for 10 min and then allowed to cool down to room temperature by sitting in air before being reassembled.

4.2.3 Ammonia Temperature Program Desorption (TPD) and Thermal Ammonia Synthesis

Ammonia synthesis via direct hydrogenation of TiN (Alfa Aesar, <10 micron, 99.7%) was investigated by exposing it to 100 mL min^{-1} of 5% H_2:Ar (AirLiquide, Arcal F5 5% H_2/Ar). The reactor set-up was equipped with a Thermo Scientific Antaris IGS-System for gas analysis. For this experiment, 0.10 g of the catalyst was loaded into a quartz tube, flushed with 5% H_2:Ar at RT. The catalyst was heated from RT to 900 °C with a heating rate of 10 K min^{-1}. The temperature of 900 °C was held for 90 min. The amount of NH_3 in the effluent gas was determined in an IR-cell (Thermo Scientific IGS Analyzer). The total amount of ammonia was calculated by determining the total area of the ammonia signal (Equation 20):

$$n(NH_3) = S_{NH_3} \cdot \dot{V}(N_2) \cdot \frac{p_0}{R \cdot T_0} \cdot 1000 \qquad (20)$$

where $n(NH_3)$ is the molar flow rate of ammonia [mmol s^{-1}], S_{NH_3} is the IR signal for ammoinia (ppm), $\dot{V}(N_2)$ is the volumetric flow rate of N_2 at standard conditions [L s^{-1}], p_0 is standard pressure [Pa], R is the gas constant [J K^{-1} mol^{-1}], and T_0 is standard temperature [K]. The IR-cell was calibrated using 1000 ppm NH_3 in nitrogen and diluting it stepwise with N_2 to obtain seven calibration points. The calibration was implemented in the instrument using a second order approach with the software TQAnalyst, provided by ThermoScientific.

The catalytic activity of TiN was investigated using the same set-up with N_2 and H_2 in a molar ratio 1:3 and a total flow rate of 100 mL min^{-1}.

NH_3-TPD experiments were carried out using the same setup as described above. For this experiment, 0.10 g of the catalyst was loaded into a quartz tube, flushed with N_2 at RT. The catalyst was pretreated with N_2 (AirLiquide, 99.999%) at 600 °C to clean the surface from adsorbed molecules. The cooled catalyst was then flushed with 2% NH_3 in N_2 (Crystal gas mixture, AirLiquide, 99.999%) for 20 minutes. Afterwards the gas is again changed to N_2 and after no ammonia is detected in the effluent gas the catalyst was heated from RT to 900 °C with a heating rate of 10 K min^{-1}. The temperature of 900 °C was held for 90 min. The amount of NH_3 in the effluent gas was determined in an IR-cell (Thermo Scientific IGS Analyzer). The total amount of adsorbed ammonia was calculated by determining the total area of the ammonia signal (Equation 20).

4.2.4 Colorimetry

Qualitative detection of ammonia in the catalyst wash was determined via the Berthelot reaction[245] following the procedure described by Shi *et al.*[246] Detection Solution 1 contained 0.05 M NaOCl (Sigma Aldrich, ACS reagent grade, 4.00-4.99% chlorine) in DI water. Solution 2 was made of 1 wt % sodium nitroprusside (Sigma Aldrich, ACS reagent grade, 99%) in water. Solution 3 was a 1.0 M aqueous NaOH (Sigma Aldrich, >97%) solution containing 5 wt % salicylic acid (Sigma Aldrich, ACS reagent grade, >99%) and 5 wt % sodium citrate (Sigma Aldrich, ACS reagent grade, >99%). 1 mL of the Solution 1, 0.5 mL of Solution 2, and 0.1 mL of Solution 3 were used in each cuvette. The presence of ammonia was indicated by a color change of the final solution from yellow to green.

4.2.5 Mass Spectrometry (MS)

In-line mass spectrometry data of the effluent gas were collected for select experiments using a Hiden Analytical HPR120 RGA mass spectrometer. When measuring *m/z* = 18 and *m/z* =

17, the ionization energy was reduced from 70 eV to 19 eV (Appendix C.1.2.1), and the emission current was reduced from 250 µA to 120 µA. The vessel was loaded, and the initial gas configuration was allowed to stabilize for at least 8 h overnight. Argon gas was included as an internal standard to account for systematic changes in the measure signal intensity over the course of the reaction. Gas flows were 11.25 sccm for N_2, 3.75 sccm for H_2, and 1 sccm for Ar. After the milling portion of the experiment was completed, the gases were allowed to stabilize again overnight, before the hydrogen flow was set to 0 sccm for safety reasons.

4.2.6 Ion Chromatography (IC)

Ammonia quantification by ion chromatography (IC) was performed with a Thermo Scientific Dionex Aquion Ion Chromatography System with an anionic polymer column (Dionex IonPac AS22, cation column). The processing software was Chromelon Chromatography Studio 7. For calibration, an ammonia standard solution of 1.00 mg L^{-1} as NH_3-N by Hach Company was utilized and diluted to the desired concentration. For the catalyst washing, a suspension of 1 mg mL^{-1} catalyst in deionized (DI) water was sonicated for 45 min. The suspension was centrifuged for 20 min at 13000 rpm. Afterwards, the liquid supernatant was filtered using a 0.2 µm pore sized nylon membrane syringe filter. For analysis upon ammonia content, 5 mL of the washing solution were injected into the column. The eluent was 20 mM methanesulfonic acid (Sigma Aldrich, ≥99.0%) in DI water.

4.2.7 X-ray Powder Diffractometry

X-ray powder diffraction (XRD) patterns were obtained using an Empyrean diffractometer by Malvern Panalytical, which operates with CuKα radiation coming from a Bragg-BrentanoHD source with a wavelength of λ = 1.5406 Å. The mask was 4 mm, the divergence slit was fixed at ¼°, the anti-scatter slit was 1°, and the soller slits were 0.04 rad. With this optics, an area of

104.2 mm^2 of the sample was scanned. The generator was operating at a tension of 45 kV and a current of 40 mA. The sample stage was a reflection-transmission spinner, the detector was a PIXcel3D. Diffractograms were measured at incident angles from 2θ = 10 ° to 100 ° with a step size of 0.0131303 ° and a number of steps of 6855. The time per step was set to 20.4 s, the scan speed was chosen to be 0.164129 s^{-1}. The detection limit was 0.5 wt%. Data analysis was performed using HighScore Plus by Panalytical.

XRD patterns of the thermally reacted TiN were collected using a D2-Phaser (Bruker AXS) with CuKα (30 kVA, 10 mA, λ = 1.5406 nm) radiation with 2θ ranging from 20° to 90° and a scanning speed 0.02 °/0.4 s. The sample was rotated during the measurement with 30 rpm.

4.2.8 X-ray Absorption Spectroscopy

X-ray absorption spectroscopy (XAS) experiments were performed at Brookhaven National Laboratory at the National Synchrotron Light Source (NSLSII), beamline inner shell spectroscopy (ISS) 8-ID, in fluorescence mode. A cryogenically cooled Si (111) double crystal monochromator was used. The beam current was 400 mA. Ten runs of each sample were performed for averaging. About 105 mg of boron nitride (BN) and 3.5 to 4.5 mg of the sample were mixed and fixed in a sample holder with Kapton tape. The florescence of a sample was measured against a Ti foil as a reference. The K absorption edge of titanium was calibrated to 4966 eV.[247] Data processing was performed with the program ATHENA in the Demeter package version 0.9.26.

4.2.9 X-ray Photoelectron Spectroscopy

X-ray photoelectron spectroscopy (XPS) analysis was performed using a Thermo Scientific Scanning X-ray photoelectron spectrometer. This device used a focused monochromatic

Aluminum K-Alpha X-ray (1.486 keV) source for excitation and a 180° hemispherical analyzer. The signals were detected by a 128-channel detector. The 72 W X-ray beam was focused onto a 400 μm spot on the sample. The X-ray beam was incident at 60° from the normal to the sample and the photoelectron detector was oriented normal to the sample surface. High-energy-resolution spectra were collected using a pass-energy of 50.0 eV with a step size of 0.10 eV. The powder samples were loosely loaded into 3 mm deep · 3 mm diameter blind holes drilled into a square copper-alloy powder sample plate. That sample holder was then manually placed into the XPS vacuum introduction system, and the pressure in the chamber was lowered to $<4\cdot10^{-7}$ Torr by a vacuum pumping system utilizing a turbomolecular pump. After that, the sample holder was moved into the XPS ultrahigh vacuum analysis chamber. The base pressure in the analysis chamber was maintained at $<2\cdot10^{-8}$ Torr prior to the analysis by using both a turbomolecular vacuum pump and a titanium sublimation pump. During the analysis itself, an integrated charge compensation source was used to minimize sample charging due to the photoelectron current flowing out of the sample. The source used a mixed beam of electrons and Ar^{+1} ions, which raised the analysis chamber pressure to $\sim3\cdot10^{-7}$ Torr of which >90% is due to the introduced Ar. Data analysis was performed using the Avantage software package v.5.957 by Thermo Scientific. The detection limit was ~1mol%.

4.3 Results and Discussion

4.3.1 Ammonia Formation and Proposed Mechanism

Ammonia synthesized by milling Ti in N_2 and H_2 was qualitatively detected by colorimetry (Appendix C.1.1), mass spectrometry (MS) of the reactor effluent, and olfactorily (Appendix C.1.3), with the possibly of contamination ruled out (*vide infra*). Potential contamination of the Ti with iron (the catalyst of choice for industrial ammonia synthesis) from the steel vessel was

considered, but X-ray photoelectron spectroscopy of milled Ti detected no iron (Appendix C.2.2), and neither iron nor iron oxide showed catalytic activity (Table C1). Finally, synthesizing the catalyst, TiN, from Ti and N_2 in the same system as the ammonia demonstrates catalytic formation from *in situ* fixed N_2 rather than depletion of *ex situ* fixed N_2 in the nitride.

The gas phase during a reaction with Ti was analyzed with an *in-line* mass spectrometer (MS) to qualitatively detect ammonia with an additional, orthogonal method and without the necessity to remove the catalyst from the system. The ionization energy of the MS was reduced from 70 eV to 19 eV to avoid the influence of fragmented water (OH) on the ammonia signal (*m/z* = 17). Figure 22 shows the ammonia signal from the MS normalized to the N_2 signal. While the MS signal was recorded for more than 144 h, the catalyst was only in a reactive (*i.e.*, milling) environment for a total of 7.5 h (indicated by the white bar "Mill On").

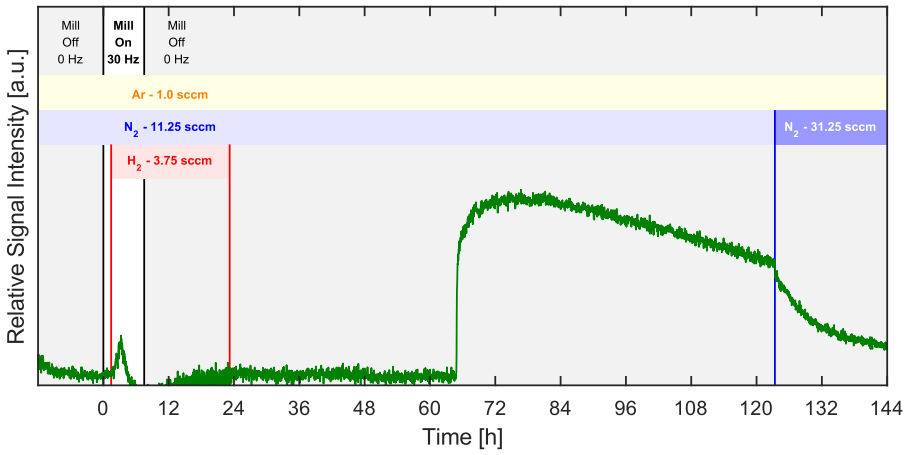

Figure 22: MS signal intensity for ammonia (*m/z* = 17) relative to nitrogen (*m/z* = 28) with an ionization energy of 19 eV. The feed composition at each time point is highlighted with yellow (Ar), blue (N_2) and red (H_2) bars.

The initial feed of N_2 (11.25 sccm) and Ar (1.0 sccm) was left to stabilize over night before the experiment began (defined as t = 0 h when milling started). H_2 (3.75 sccm) was introduced after 1.5 h of milling. The milling experiment ended after an additional 6 h of milling (t = 7.5 h)

and the milling vessel was left idle (0 Hz) for the remainder of the time. The gas flows were then left to stabilize overnight, after which the H_2 flow was stopped (t = 23.2 h). Fluctuations in the ammonia signal between 7.5 h and 23.2 h resulted from the presence of H_2 in the MS (Appendix C.1.2.2). A breakthrough of ammonia was observed 58 h after milling ended (t ~ 65 h), followed by a steady decay. The precise cause of the delay is currently unknown, but it is reproducible and potential explanations are discussed below (Appendix C.1.2.3). Increasing the nitrogen flow rate from 11.25 sccm to 31.25 sccm (t = 123.4 h) resulted in a sudden change in the slope of decay of the ammonia signal, which is explained by dilution of the ammonia stream.

In this mechanocatalytic system, only a small fraction of the catalyst is activated by the ball collision at any given time.[238] The estimated mole fraction of ammonia in the active catalyst void space is 0.06 (Appendix C.3). In a conventional thermochemical reaction at steady state, this mole fraction would only be achievable up to 230 °C, based on the thermodynamic equilibrium (Figure 23a). Notably, collision induced hot spots are expected to greatly exceed this temperature (*e.g.*, 800 °C during the milling of $CaCO_3$), with the exact number dependent on powder properties.[148-149, 198, 238] Additionally, despite nitrides being among the most active catalysts for ammonia synthesis,[248-249] significant thermal catalytic turnovers for TiN were observed only above 600 °C (Appendix C.4.2). Thus, a transient Mars van-Krevelen (MvK) process is proposed for mechanocatalytic synthesis (Figure 23b), where N_2 fixation and ammonia formation occur in thermodynamically distinct regimes. TiN is first mechanically activated, forming an environment where N_2 can be dissociated. Next, the TiN relaxes to conditions where ammonia formation is thermodynamically favorable and kinetically feasible, before returning to an inactive state. Parallel reaction pathways may be present, such as through a TiH_2 intermediate, but TiN is expected to be the dominant catalyst (Appendix C.2.3). This mechanical activation could be a combination of

several phenomena (*e.g.* temperature rise, reactive defect sites and surfaces, lattice strain). For illustrative purposes, the mechanical activation could be explained by localized heating where the peak temperature enables N_2 activation, but ammonia formation is strongly thermodynamically limited. Analogous to dynamic catalysis,[250] the mechanocatalytic reactor creates a constantly transient reaction environment that increases the local reaction rate by three orders of magnitude (Appendix C.4.2) and circumvents steady state thermodynamic and kinetic limitations.

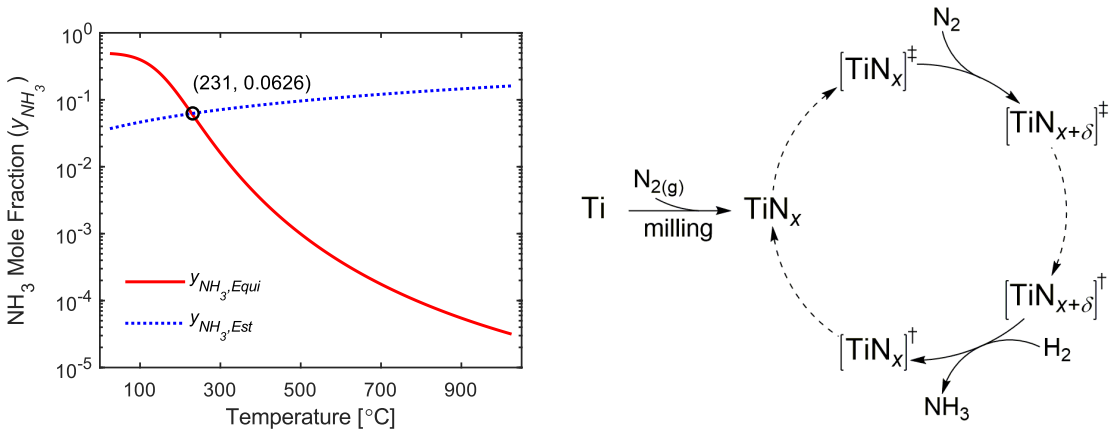

Figure 23: Analysis of local ammonia mole fraction and proposed mechanism for mechanocatalytic ammonia synthesis. (a) Curves of the equilibrium (red) and estimated (blue) mole fraction of ammonia at temperatures between 25 °C and 1025 °C. The intersection of the curves (231 °C) marks the upper temperature limit of surface catalyzed mechanism. (b) Proposed transient Mars-van Krevelen reaction mechanism for ammonia synthesis.

4.3.2 In Situ Synthesis of Titanium Nitride

X-ray Powder Diffraction (XRD) and X-ray Absorption Spectroscopy (XAS) provided complementary evidence for the mechanochemical synthesis of TiN. XRD showed a substantial change in crystal structure from pure Ti to a Ti/TiN mixture within 1.5 h (Figure 24a). By 3 h, TiN becomes the dominant crystal structure. A peak shift of Ti toward lower diffraction angles has been explained by the formation of a solid solution,[251] with dissolved N atoms expanding the Ti crystal lattice. The peak shift to higher angles of TiN indicates a more compact structure, originating from nonstoichiometric TiN_x phases.[252] The peak broadening and a lower signal-to-

noise ratio at increased milling time indicates mechanically induced amorphization.[251-252] Since XRD cannot characterize amorphous phases, XAS measurements of the Ti K-edge were collected. The X-ray Absorption Near Edge Structure (XANES) spectrum of Ti milled in N_2 was dominated by characteristic features of TiN (Figure 24b). The Ti pre-edge peak (4965 eV) disappeared, the white line intensity (4895 eV) increased, and the edge shifted by 3.6 eV to a higher energy. The overall XANES line shape is consistent with TiN. The Fourier Transform of the EXAFS region (Figure 24c) showed that the Ti milled in N_2 had both a Ti-N shell (1.69 Å) and a Ti-Ti shell (2.52 Å). The smaller radial distance of the Ti-Ti shell in the milled Ti, compared to the TiN, supported the observations of a more compact nitride structure. The diminished intensity is caused by amorphization. Thus, XRD and XAS confirmed the near quantitative *in situ* conversion of Ti to stoichiometric TiN.

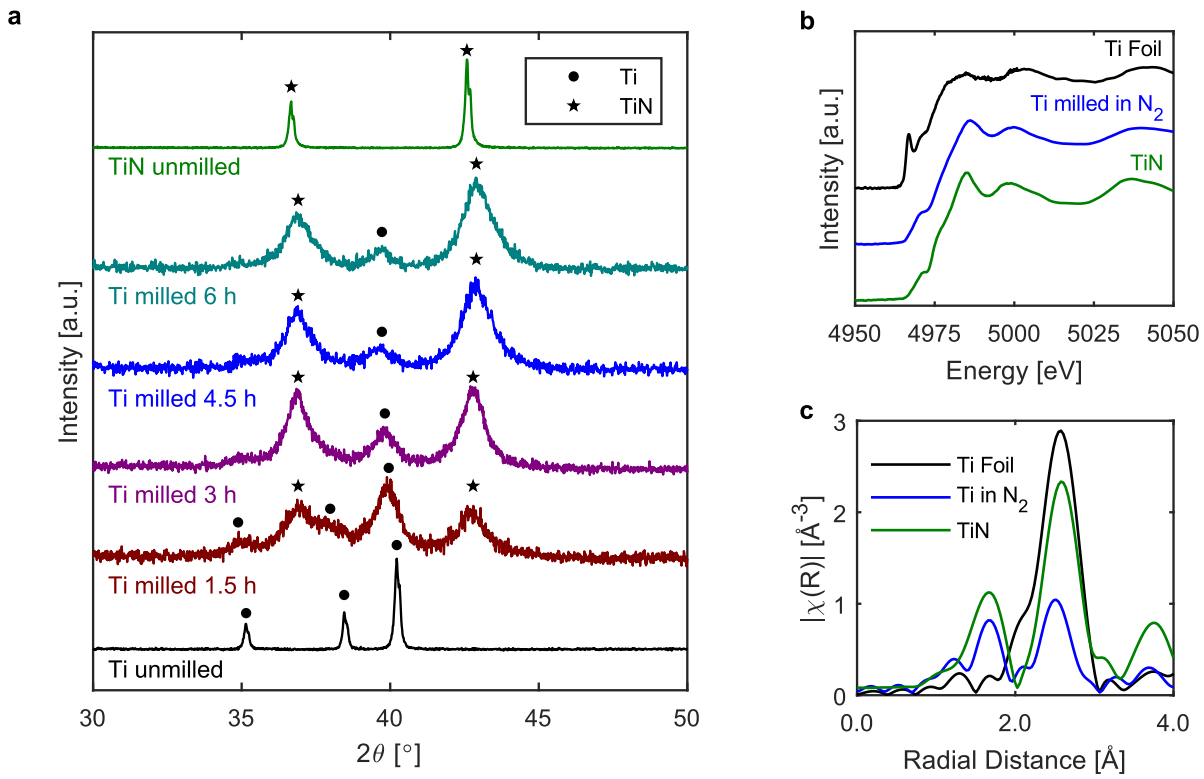

Figure 24: Characterization of milled titanium in N_2.X-Ray diffractograms for unmilled Ti, unmilled TiN and Ti milled for 1.5 h, 3 h, 4.5 h, and 6 h in 15 sccm N_2. Peak assignment was performed according to the unmilled Ti and TiN samples and literature.[253] (b) X-ray absorption spectra of the titanium K-Edge and (c) Fourier Transform of the EXAFS region for Ti foil (black), Ti powder milled in N_2 for 4.5 h (blue), and unmilled TiN (green).

4.3.3 Mechanochemical and Mechanocatalytic Ammonia Synthesis Reactions

During the experiment to qualitatively detect ammonia in the reactor effluent with MS (Ti milled in N_2 for 1.5 h then N_2 and H_2 for 6 h), a significant delay of 58 h between the end of milling and the initial detection of ammonia in the gas phase was observed (Figure 22). Thus, ammonia yields were measured by washing the catalyst after reaction with DI water, and then performing ion chromatography (IC) with the washing solution (Appendix C.1.4). Contamination by ambient ammonia is necessary to consider.[254-256] Negative results (Figure 25a) from milling iron, iron oxide, or titanium dioxide under reactive conditions rule out potential contamination in the gas streams, the reactor system, and the IC sample preparation procedure and demonstrate the necessity of the TiN or Ti for positive ammonia detection. Control experiments with TiN and Ti

rule out initial contamination from these materials as well, and background subtraction of initial present ammonia on the catalyst was deemed unnecessary.

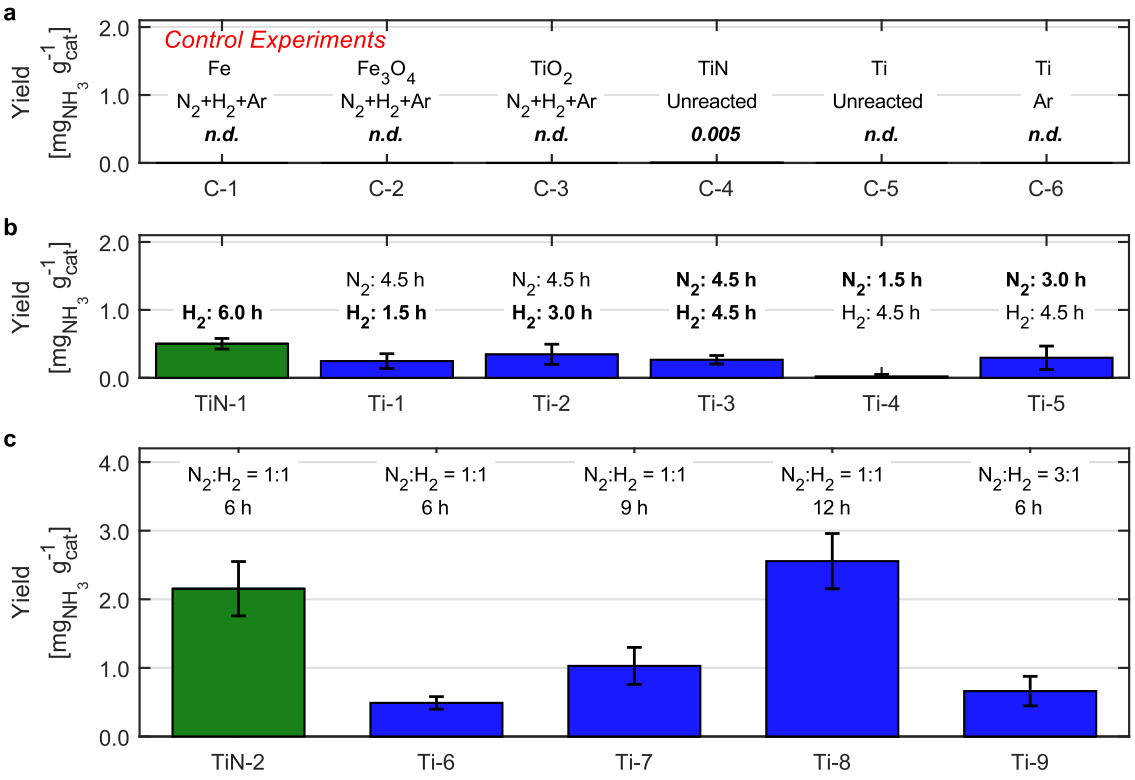

Figure 25: Mechanochemical and mechanocatalytic ammonia yields. (a) Ammonia yields for control experiments. n.d. = not detected. (b) Ammonia yields for TiN milled in H_2 and Ti milled in N_2 followed by H_2, with varying reaction times. Samples were milled at 30 Hz in a pure gas stream (15 sccm). (c) Ammonia yields for TiN and Ti milled in H_2 and N_2 with varying composition and reaction time. Samples were milled at 30 Hz in a mixed gas flow (15 sccm) of both N_2 and H_2. Full experimental conditions and numeric values are reported in Table C1.

The amount of reactive nitrogen in mechanochemical and commercial TiN was studied. Ti samples were first milled in N_2 for 4.5 h, then in H_2 for 1.5, 3.0 or 4.5 h (Figure 25b, Ti-1 to Ti-3). Extending milling time in H_2 did not significantly increase the ammonia loading. Likewise, milling commercial TiN in H_2 (Figure 25b, TiN-1) and thermally reducing TiN in H_2 (Appendix C.4.2) resulted in similar ammonia yields. The slightly higher yield from the commercial TiN may arise from incomplete conversion of Ti to TiN during milling. Thus, titanium nitride contains a certain

amount of inherently reactive nitrogen, regardless of its synthesis method or reaction environment. After depletion, the residual nitride becomes inactive until replenished with a nitrogen source.

The reactivity of titanium with different nitridation degrees was investigated by milling Ti for 1.5, 3.0, or 4.5 h in N_2 followed by 4.5 h milling in H_2 (Figure 25b, Ti-3 to Ti-5). Milling for only 1.5 h resulted in background levels of ammonia, while 3.0 h and 4.5 h had yields similar to TiN milled in H_2. This significant increase in ammonia yield by increasing milling time in N_2 from 1.5 to 3.0 h aligns with the expected nitridation mechanism based on XRD (Figure 24a).[252-253] Initially, nitrogen gradually diffuses into the Ti metal, forming a solid solution. Once a threshold concentration is reached (~32 mol%),[251] a rapid, bulk change to TiN occurs.[252-253] The low ammonia yields at short milling times in N_2 indicates that the dissolved nitrogen is not reactive toward ammonia, but must be incorporated into a nitride crystal lattice, supporting a MvK mechanism during catalytic ammonia formation. Thus, a critical amount of incorporated lattice nitrogen is required for relevant ammonia yields.

The catalytic properties of TiN were investigated under steady state conditions. Commercial TiN milled in N_2 and H_2 (Figure 25c, TiN-2) showed an ammonia yield four times larger than TiN milled in H_2, indicating that TiN has catalytic activity toward ammonia formation. The ammonia yields from Ti milled in a continuous flow of N_2 and H_2 was measured after 6 h, 9 h, and 12 h (Figure 25c, Ti-6 to Ti-8). The samples show a continuous production of ammonia by milling, demonstrating that catalytic activity is sustained for an extended period. An induction period can be inferred before catalytic ammonia production starts, which would be expected from the need to first synthesize the TiN. Notably, for both TiN and Ti as (pre)catalyst, significantly higher amounts of ammonia are achieved under continuous conditions, compared to the experiments with a separate feed (Figure 25b). Thus, the presence of N_2 in the feed allows for

continuous nitride regeneration, and this regeneration ability is sustained for extended times via a fully catalytic process.

The influence of feed composition and nitride content are two key parameters that will control the catalytic behavior of the system. Two Ti samples (Figure 25c, Ti-6 and Ti-9) were milled in different gas compositions, 1:1 and 3:1 N_2:H_2, respectively. The influence of gas composition and nitride content cannot be completely separated as milling Ti in a mixture of N_2 and H_2 results in a mixture of nitride and hydride phases (Appendix C.2.3). However, the nitride to hydride ratio increased with higher N_2 content in the gas phase. The 50% increase of N_2 in the gas phase did show an increase in ammonia yield, though precise discussion is difficult due to the large error bars between Ti-6 and Ti-9. Obtaining higher ammonia yields with a higher N_2 feed and greater nitride content suggests that the ammonia synthesis rate is limited by the nitride regeneration rate. Optimal catalytic activity is expected to require a balance of stability of the nitride, with a more stable nitride than TiN exhibiting higher activity due to greater nitrogen binding and nitride formation energies. By further studying these parameters and more traditional thermal nitride catalysts (*e.g.* MoN,[257-258] Co_3Mo_3N[248, 259]), higher mechanocatalytic ammonia yields should be obtained.

4.3.4 Preliminary Technoeconomic Analysis

When introducing a new approach, addressing the feasibility of the process is valuable to frame its broader significance. Metrics laid out by Comer *et al.* suggests preliminary performance targets for solar powered fertilizer processes of $8.83 \cdot 10^4$ kJ mol_N^{-1} energy consumption and 100 kg_N ha^{-1} yr^{-1} production rate.[219] Other novel approaches for distributed fertilizers (*i.e.* electrocatalysis, photocatalysis, and plasma-assisted catalysis) produce ammonia at energy consumptions of 10^4-10^5 kJ mol_N^{-1}.[219] A small, electric industrial ball mill (1 m^3) would have a

typical mineral (*i.e.* catalyst) loading of 10^3 kg while requiring 10^4 W to operate.[260] A preliminary technoeconomic analysis (Appendix C.5) shows that ammonia could be produced at 10^3 kg yr^{-1} with a solar energy consumption of 10^4 kJ mol_N^{-1} (assuming 20% solar panel efficiency). Such a mill could produce fixed nitrogen equivalent to the necessary amount to fertilize a small to medium sized farm (~10 ha) and be powered onsite with the typical output of 200 solar panels.[219] Future assessments would need to account for nitrogen separation from air, hydrogen production via electrolysis, and upgrading the ammonia to fertilizers (*e.g.* urea or ammonium nitrate). Notably, mechanocatalysis has unique advantages, such as generating catalysts *in situ* from abundant materials and utilizing non-electrical sources of renewable energy (*i.e.* direct mechanical energy from wind or water mills). While this assessment is preliminary, it reveals that mechanocatalysis is clearly competitive with other well-studied alternative systems for distributed ammonia production.

4.4 Conclusions

In summary, a novel approach to ambient ammonia synthesis via mechanocatalysis is introduced, where N_2 and H_2 are catalytically reacted over an *in situ* synthesized nitride catalyst. By creating transient microenvironments, kinetic and thermodynamic limitations are elegantly circumvented. A transient Mars-van Krevelen mechanism is proposed, comprising nitrogen incorporation and titanium nitride hydrogenation steps. The catalytic cycle is rate limited by the nitride regeneration, thus a more stable nitride is expected to yield higher ammonia rates.

This work demonstrates how mechanocatalysis provides fundamentally new opportunities to exploit spatiotemporal variations in thermodynamic driving forces and kinetic phenomena to make difficult chemistry accessible at benign conditions. The mechanocatalytic process shown here could foreseeably be utilized for other reactions with similar kinetic and thermodynamic

mismatches, such as the partial oxidation of methane to methanol[261-262] or the water-gas shift reaction,[263] opening new avenues for a distributed chemical production.

CHAPTER 5
MECHANOCATALYTIC HYDROGENOLYSIS OF A MODEL LIGNIN ETHER

5.1 Introduction

As society strives to shift away from fossil-based fuels and chemicals, the necessity for complete utilization of biomass becomes ever more pressing. Lignin, one of the primary components of woody biomass, is an abundant renewable resource (growth rate of $2 \cdot 10^{12}$ tonnes and production rate of $6 \cdot 10^{7}$ tonnes annually globally) but is practically unutilized as a feedstock for chemicals and materials (< 2% of isolated lignin).[264] This heterogeneous, amorphous polymer is comprised primarily of three propyl-phenolic monolignols (p-coumaryl alcohol, coniferyl alcohol, and sinapyl alcohol) linked together randomly by various C-O (β-O-4, α-O-4, 4-O-5) and C-C (β-β, β-5, 5-5) bonds.[265] As the largest natural source of aromatic carbon, lignin is a promising, sustainable alternative starting point for historically BTX-derived chemicals if the polymer can be depolymerized selectively to mono-aromatics. The fractionation of lignin from the lignocellulosic matrix drastically changes the structure of the polymer and increases the abundance of condensed linkages,[266] resulting in either large product distributions or low monomer yields.

Two of the most promising approaches to depolymerize lignin utilize hydrogen as either a cleaving or stabilizing reagent: hydroprocessing and reductive catalytic fraction (RCF).[8] Hydroprocessing, generally performed with isolated lignin, combines hydrogenolysis of the linkages to produce monomers and hydrodeoxygenation to upgrade monomers simultaneously.[71] These reactions tend to produce monomer yields between 10 and 20 wt%, with harsher reaction conditions increasing monomer yields at the expense of product selectivity.[8] RCF starts with complete lignocellulose and combines the isolation and depolymerization of lignin, where solvolysis formed monomers are stabilized before repolymerization can occur.[29] Most reported

monomer yields from RCF studies range from 10 to 30 wt% for softwood and from 30 to 60 wt% for hardwood feedstocks with very high selectivites of phenolics. Both hydroprocessing and RFC reactions employed noble metals, such as Pt, Pd, Ru, or Rh, or transition metal, primarily Ni and Cu, on either acidic or neutral supports. These reactions often require elevated temperatures (130 - 450 °C), elevated hydrogen pressures (10 – 100 bar), and large quantities of organic solvents, such as methanol, dioxane, or THF.[8] The specialized equipment necessary for the combination of high hydrogen pressures and heated, flammable solvents, along with the energy demands for solvent recovery, currently stand as major barriers to scale up for these processes.[267]

Mechanocatalysis offers a novel approach for green chemical production by performing reactions under solvent-free conditions and at nominally ambient temperatures and pressures.[33, 38] The direct input of mechanical energy, such as collisions in a ball mill, drives the reaction between solid reactants and catalyst. This energy can influence the system in many ways, such as enhancing solid-solid mixing and contact,[39] creating fresh reactive surfaces,[239] creating localized hot spots,[238] and altering reactivity of reagents[40] and catalysts.[42, 268] Mechanical energy, without added chemicals or catalysts, has long been used as a method for pulping wood and pretreating biomass for conversion to fuels and chemicals. In recent years, the use of mechanocatalysis for biomass valorization has seen a rise in popularity, albeit with an emphasis on cellulose or whole lignocellulosic biomass.[269] Works on the degradation of isolated lignin have been limited; for example using mechanochemistry as a pretreatment method[67] or for alkaline[69, 128] and oxidative[70] depolymerization. As of now, reductive mechanocatalytic depolymerization of lignin has not been explored.

While the mechanocatalytic hydrogenation of benzene over nickel in a vibratory ball mill was reported as far back as 1963,[270] studies on reductive mechanocatalysis with gaseous hydrogen

have also been sparse.[271-272] The methanation of CO_2 over Ni/Fe/Ru on MgO catalysts[273] and LaNi alloys[274] and of CO over mixed FeCo and MgNi catalysts[275] have been demonstrated. The hydrogenation of numerous alkynes, alkenes, aromatics, and various functional groups have been reported using a feed of H_2 or splitting water *in situ*.[276-278] Recently, the reduction of N_2 to NH_3 with H_2 was reported using a batch planetary ball mill with an iron catalyst[279] and in a continuous-flow vibratory ball mill using a titanium nitride catalyst.[268]

Herein, the first use of reductive chemistry to mechanocatalytically cleave a model lignin ether is reported. Benzyl phenyl ether (BPE) is often studied as a model compound for lignin because of the similarity in C-O bond strengths between BPE and the β-O-4 linkage in lignin.[280] The hydrogenolysis of BPE was conducted under solvent-free, nominally ambient conditions (room temperature, ~1 bar H_2) using supported nickel catalysts in a vibratory ball mill. The hydrogenolysis occurred at the benzyl ether bond, producing toluene and phenol as primary products. Additionally, the milling generated metallic nickel surfaces *in situ*, circumventing the need for a thermal reduction step. The unique design of the ball mill reactor allowed for the continuous monitoring of the formation of toluene and for a simple kinetic model to be fit to the reactions. Recycle experiments with a commercial 53 wt% Ni on silica-alumina catalyst showed the continuous deactivation of the catalyst during milling, while Raman spectroscopy confirmed the formation of polyaromatic coke. The influence of the support properties on the reaction was also studied. The enhanced reactivity of the oxides during milling was determined to be a key factor for forming chemisorbed species and subsequent carbon loss. These insights will aid further developing processes for the solvent-free and mild depolymerization of lignin via reductive mechanocatalysis.

5.2 Materials and Methods

5.2.1 Chemicals

Benzyl phenyl ether (BPE, 97%) and o-xylene (99%) was purchased from Alfa Aesar. Nickel on silica-alumina ($Ni_{53}SiAl$), silicon dioxide (quartz, ~99%), silica-alumina catalyst support (grade 135), and nickel nitrate hexahydrate ($Ni(NO_3)_2 \cdot 6H_2O$, 99.999%) was purchased from Sigma-Aldrich. Silica gel was purchased from Sorbent Technologies. Methanol (ACS grade) was purchased from VWR. Hydrogen (H_2, UHP, Grade 5) and nitrogen (N_2, UHP, Grade 5) was purchased from Airgas.

5.2.2 Catalyst Synthesis

Three 5 wt% nickel catalysts were synthesized using the amorphous silica-alumina ($Ni_{05}SiAl$), silica gel ($Ni_{05}Si_{High}$), and quartz ($Ni_{05}Si_{Low}$). The catalysts were prepared by incipient wetness impregnation with an aqueous $Ni(NO_3)_2$ solution. The wetted samples were dried at 105 °C in air overnight. The dried samples were reduced in 7% H_2 in Ar at 450 °C (ramp from room temperature at 10 °C/min) for 8 hours. The samples were exposed to and stored in air after returning to room temperature.

5.2.3 Catalyst Characterization

5.2.3.1 Inductively Coupled Plasma Atomic Emission Spectroscopy (ICP-OES)

Acid digestion and inductively coupled plasma atomic emission spectroscopy (ICP-OES) was performed by the Renewable Bioproducts Institute. Sample aliquot was weighed into a predigested beaker. The beaker with sample was placed on a hot plate. After 5ml concentrate nitric acid was added, the contents were reacted for 30 minutes under elevated temperature (not boiling). This was followed by adding another 2.5 ml concentrate HCl, and the mixture was reacted for another 30 minutes. The digested mixture was cooled to room temperature and was filtered through

a grade 40 ashless Whatman filter paper. The filtering assemble was washed with di-ionized water and jointed to the filtrate. The volume of the final aqueous solution was recorded.

Instrument was periodically tested for performance, which includes detector calibration, align view, wavelength calibration. In each batch of sample analysis, the instrument was calibrated with standards for the target elements, and a four-point calibration curve was established for each interested element. The aqueous sample prepared as stated above was used for ICP-OES analysis.

5.2.3.2 Carbon, Hydrogen, and Nitrogen Elemental Analysis

C, H, and N elemental analysis was performed by Atlantic Microlab. C, H, and N contents were determined by high temperature combustion in pure oxygen.

5.2.3.3 N_2 Physisorption

Nitrogen physisorption measurements were performed using a Micromeritics ASAP 2020 physisorption analyzer. The samples (50-100 mg) were evacuated at 50 °C and 10 μmHg for 1 min and subsequently degassed at 110 °C and 100 mmHg for 4 h prior to the measurement. The measurement was performed at 77 K. Surface areas were calculated based on the BET method described elsewhere for a *p/p0* range between 0.025 and 0.30.[184]

5.2.3.4 XRD

X-ray powder diffraction (XRD) patterns were obtained using an Empyrean diffractometer by Malvern Panalytical, which operates with CuKα radiation coming from a Bragg-BrentanoHD source with a wavelength of λ = 1.5406 Å. The mask was 4 mm, the divergence slit was fixed at ¼°, the anti-scatter slit was 1°, and the soller slits were 0.04 rad. With this optics, an area of 138.7 mm^2 of the sample was scanned. The generator was operating at a tension of 45 kV and a current of 40 mA. The sample stage was a reflection-transmission spinner, the detector was a

PIXcel3D. Diffractograms were measured at incident angles from 2θ = 15 ° to 100 ° with a step size of 0.0131303 ° and a number of steps of 6474. The time per step was set to 61.2 s, the scan speed was chosen to be 0.05471 s^{-1}. The detection limit was 0.5 wt%. Data analysis was performed using the HighScore Plus software by Panalytical. The sample was rotated during the measurement with a revolution time of 16.0 s.

5.2.3.5 STEM and EDS

The powder sample was dispersed in ethanol, then dropped on holy carbon coated Cu grids after ultrasonic for 5 minutes. A Hitachi HD2700 aberration-corrected scanning transmission electron microscope was used to record the high-angle annular dark-field (HAADF) STEM images. The electron beam convergent angle α is 27 mrad and the HAADF detector collection angle β=70–370 mrad.

5.2.3.6 Raman Spectroscopy

Visible Raman spectroscopy was performed on a Renishaw Raman spectrometer using an excitation wavelength of λ = 488 nm. The laser power was set to 1-10% of the total power (30 mW), the grating of the filter was 2400 lines/mm. Samples were analyzed with 50x magnification and an acquisition time between 5-20 s. The acquisition software is WiRE 5.2. The spectra were collected using a CCD detector. The acquired spectra were deconvoluted using the peak analyzer function of the OriginPro 2020 (V9.7) software.

5.2.3.7 DRIFTS

DRIFTS spectra were collected using a Nicolet 8700 FT−IR equipped with a liquid nitrogen cooled MCT/A detector and the Praying Mantis (Harrick Scientific) accessory with a high temperature reactor for in-situ studies. Spectra were averaged at 64 scans with a resolution of

4 cm^{-1}. All spectra were treated using the Thermo Scientific Omnic Software. A background of dried potassium bromide at 50 °C was used for all spectra. The sampling cup was filled with spent catalyst and then smoothed across several times to ensure an even layer. The reactor was sealed and flushed with 100 sccm N_2 for 5 min to settle the sample bed. An initial spectrum of the pure milled catalyst was collected at 50 °C for spectral subtraction against the spent catalyst with species adsorbed. Spent catalysts were measured before at 50 °C and then ramped up to 700 °C at 10 °C/min and held for 30 min in 40 sccm N_2 and then cooled back down to 50 °C. All the spectra were collected at 50 °C after the sample had been heated to the respective reaction temperature.

5.2.4 Mechanocatalytic Reactions

5.2.4.1 Hydrogenolysis Reactions

Mechanocatalytic reactions were performed using a Retsch MM400 vibratory ball mill with a 25 mL stainless steel milling vessel. The milling vessel was modified to allow for continuous gas flow. The effluent line was heated to 160 °C and the effluent gas was bubbled through methanol (~ 10 mL with ~0.03 g o-xylene as an internal standard) cooled to 4 °C to trap volatile products leaving the reactor (Figure 26). Unless otherwise specified, reactions were conducted with 1.00 g of catalyst, 0.20 g of BPE, two 15 mm stainless steel grinding balls, and a milling frequency of 20 Hz in a continuous flow of H_2. The vessel was left unheated but milling induced a temperature increase to ~30 °C within the reactor. The vessel was purged with N_2 for 15 min and then with H_2 for at least 15 min before milling began. After milling, the vessel was purged with N_2 for 1 h to remove additional residual volatile products.

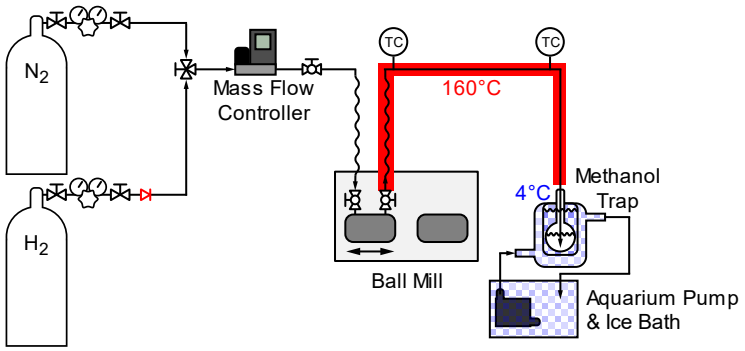

Figure 26: Depiction of flow-through ball mill reactor

Unconverted BPE and non-volatile products were measured after each reaction by removing the product-catalyst mixture from the milling vessel and sonicating in methanol (~10 mL) for 30 minutes. Roughly 90% of the sample mas could be recovered from the vessel. The remaining ~10% remained stuck on the vessel and balls or was in the effluent neck of the ball mill. After sonication, o-xylene was added (~0.03 g) was added as an internal standard. The yield of volatile products over the course of the reaction was measured by taking aliquots (~0.05 mL) of methanol trap. Product yields were determined via gas chromatography using a Varian 450-GC with a fused silica column (Supelco, SPB-1, 60m x 0.25 mm x 1.0 μm) and a flame ionization detector. The GC-FID is equipped with a PolyArc reactor (Activated Research Company), which allowed for calibration-free quantification of the products.

5.2.4.2 Catalyst Recycle Experiments

The long-term stability of the $Ni_{53}SiAl$ catalyst was studied through a series of recycle experiments. The catalyst was milled for 2 h during the first cycle and 4 h for the second and third cycles. After being washed to recover unconverted BPE and non-volatile products, the catalyst was vacuum filtered and dried under vacuum at room temperature. Similar to the mechanocatalytic reactions with the fresh catalyst, 1.00 g of the recycled catalyst was used. The same experimental procedures were used as the reaction with fresh catalyst. After vial transfers and filtration, only

~65% of the spent catalyst mass could be recovered (~0.65 g), so spent catalyst samples of several different runs were combined for each recycle stage. For example, to produce enough sample to run a third cycle, two second cycle run were performed, which required four fresh catalyst runs.

5.2.4.3 Mechanocatalytic Reaction Kinetics

The mechanocatalytic hydrogenolysis reactions were initially fit using a simplified kinetic model:

$$\frac{dX_{BPE}}{dt} = -(k_H(t) \cdot m_{Ni} + k_C)\big(1 - X_{BPE}(t)\big) \quad (21)$$

$$\frac{dY_{Tol}}{dt} = k_H(t) \cdot m_{Ni} \cdot \big(1 - X_{BPE}(t)\big) \quad (22)$$

where X_{BPE} is the conversion of BPE, k_H is the hydrogenolysis rate constant, m_{Ni} is the mass of nickel, k_C is the coking rate constant, and Y_{Tol} is the yield of Toluene in the condenser. Equation 21 and 22 can be integrated for an analytical solution:

$$X_{BPE}(t) = 1 - \exp(-(k_H \cdot m_{Ni} + k_C)t) \quad (23)$$

$$Y_{Tol}(t) = \frac{k_H \cdot m_{Ni}}{k_H \cdot m_{Ni} + k_C}(1 - \exp(-(k_H \cdot m_{Ni} + k_C)t)) \quad (24)$$

Since the X_{BPE} was measured for several time points for fresh $Ni_{53}SiAl$, Equations 23 was fit to solve for $k_H \cdot m_{Ni} + k_C$. For experiments where the full product yields were only measured once and the conversion of BPE is incomplete, $k_H \cdot m_{Ni} + k_C$ can be determined by rearranging Equation 23 and using the final conversion:

$$k_H \cdot m_{Ni} + k_c = -\frac{ln\big(1 - X_{BPE}(t_{final})\big)}{t_{final}} \quad (25)$$

Since $Ni_{53}SiAl$-Cycle 2 had was run only once, but had nearly 100% conversion of BPE, k_c could not be determined directly and was approximated by the k_C of $Ni_{53}SiAl$-Cycle 3. k_H was fit using Solver in Excel to minimize the error between the model and the toluene yield from the condenser. Due to the observed induction period in the condenser yield, a delay term was also fit.

To assess the deactivation of $Ni_{53}SiAl$, a first-order deactivation term was included in the model:

$$\frac{dk_H}{dt} = -k_D \cdot k_H(t) \quad (26)$$

where k_D is the deactivation rate constant. There is no analytical solution to Equations S1, S2, and S6, so the equations were fit numerically. A Matlab script based on the built in functions *fmincon* (error minimization) and *ode45* (differential equation solver) was used to determine k_D and the initial hydrogenolysis rate constant ($k_{H,0}$). An average k_C was used and assumed constant.

5.3 Results and Discussion

5.3.1 Catalyst Characterization

ICP-OES was used to measure the nickel loadings of the catalysts. The commercial nickel on silica-alumina ($Ni_{53}SiAl$) had 53.4 wt% Ni and the synthesized catalysts ($Ni_{05}SiAl$, $Ni_{05}Si_{High}$, and $Ni_{05}Si_{Low}$) had 4.42 wt%, 4.93 wt%, and 4.85 wt% Ni loadings, respectively. The BET surface areas of $Ni_{53}SiAl$, $Ni_{05}SiAl$, $Ni_{05}Si_{High}$, and $Ni_{05}Si_{Low}$ were 85.3 $m^2\ g^{-1}$, 499 $m^2\ g^{-1}$, 515 $m^2\ g^{-1}$, and 6.7 $m^2\ g^{-1}$, respectively. Adsorption and desorption isotherms are shown in Figure D1. XRD of $Ni_{53}SiAl$ showed the presence of both Ni and NiO, while only peaks corresponding to metallic Ni were observed in the diffractograms of $Ni_{05}SiAl$, $Ni_{05}Si_{High}$, and $Ni_{05}Si_{Low}$ (Figure D2). STEM images showed that the nickel particles of $Ni_{53}SiAl$ were encapsulated in NiO (Figure 27a, Figure D3). Similarly, STEM showed outer layers of NiO on the nickel particles for $Ni_{05}SiAl$, $Ni_{05}Si_{High}$,

and $Ni_{05}Si_{Low}$ (Figure 27b-d). $Ni_{05}SiAl$, $Ni_{05}Si_{High}$, and $Ni_{05}Si_{Low}$ had initial particle sizes of 18.7 nm, 15.1 nm, and 46.7 nm, respectively (Figure D4). EDS mapping of $Ni_{53}SiAl$ showed particles uniformly coated in nickel (Figure 27e), while the low nickel loading catalysts had more discrete nickel particles (Figure 27f-g). The abundance of nickel on $Ni_{53}SiAl$ prevented the measurement of enough particles to determine initial particle size.

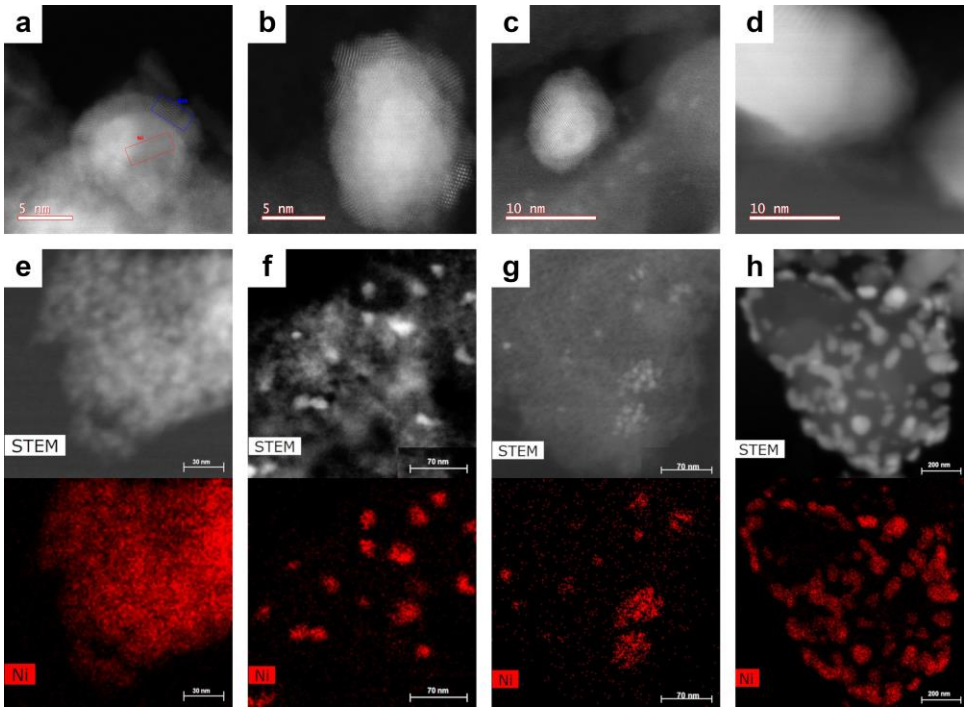

Figure 27: STEM images of individual nickel particles on (a) $Ni_{53}SiAl$, (b) $Ni_{05}SiAl$, (c) $Ni_{05}Si_{High}$, and (d) $Ni_{05}Si_{Low}$. STEM images and EDS mapping of nickel for whole catalyst particles of (e) $Ni_{53}SiAl$, (f) $Ni_{05}SiAl$, (g) $Ni_{05}Si_{High}$, and (h) $Ni_{05}Si_{Low}$.

5.3.2 Hydrogenolysis Reaction Network

Analysis of final products formed over $Ni_{53}SiA$ after various milling times elucidated the mechanocatalytic reaction network of BPE, which closely follows reported pathways during thermally catalyzed hydrogenolysis of BPE (Figure 28).[280-284] At early milling times, the main products were toluene (**1a**) and phenol (**1b**), which are formed by hydrogenolysis of the benzyl ether bond. At longer milling times, a discrepancy between toluene and phenol yields were

observed, and the origins of this break in stoichiometry are discussed below. Benzyl alcohol, a potential product of hydrogenolysis of the phenyl ether bond, was not detected. Cleavage of the benzyl ether bond is the expected dominant reaction pathway since the bond dissociation energy of the benzyl ether (56.4 kJ/mol)[107] is much lower than that of the phenyl ether (95.7 kJ/mol).[285] The formation of methylcyclohexane (**2**) and cyclohexanol (**3**) occurs through the hydrogenation of toluene and phenol, respectively. Hydrogenated ethers (**4** & **5**) were detected, and yields passed through maxima at 60 min, suggesting that hydrogenolysis of these compounds occurred. However, the yields never exceeded 1%, and so these reaction paths are not expected to significantly contribute to the formation of the single-ring products. Phenol hydrogenation to cyclohexanol was established as a reaction path based on the maximum in the phenol yield at 60 min. Methylcyclohexane yields (<1%) were significantly lower than cyclohexanol yields because toluene evaporated and was removed from the reactor prior to be being hydrogenated. Benzene (**6**) and cyclohexane (**7**) were detected after 60 min and 120 min, respectively, from the hydrodeoxygenation (HDO) of phenol and cyclohexanol. Since benzene and cyclohexane were only found in the condenser, benzene is expected to volatilize before hydrogenation can occur. Increased selectivity of benzene to phenol and cyclohexane to cyclohexanol was observed over the low nickel loading catalysts (Figure D5), which should have higher numbers of sites for metal/support interactions. This suggests a direct HDO path since the tautomerization/hydrogenation/dehydration mechanism of phenol to benzene and the dehydration/hydrogenation of cyclohexanol to cyclohexane are catalyzed by the combination of metal and acid sites.[286-287] Alkylation and heavier products have been reported in thermal catalytic systems.[282, 288-289] From the decreasing carbon balance with milling time, similar species might have formed in this system as well (*vide infra*), but specific species could not be identified. Overall,

the nickel catalyst behaves similarly in mechanochemical and thermochemical systems, so the results of other thermocatalytic reactions could be anticipated when performing mechanocatalytic reactions.

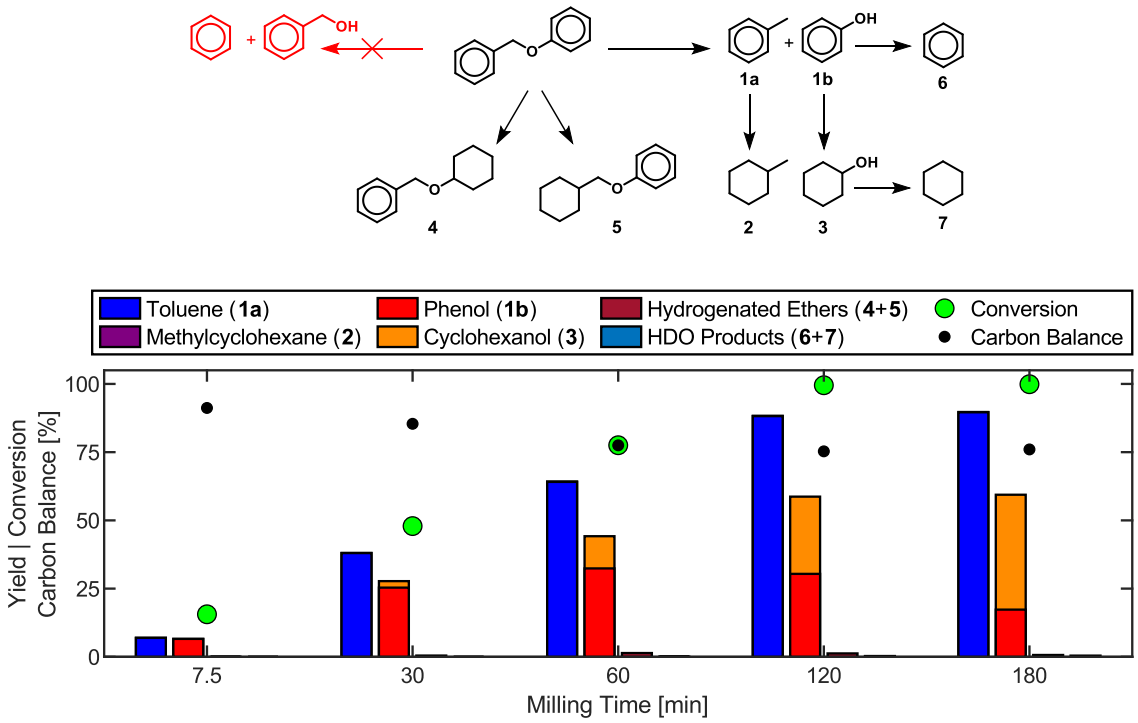

Figure 28: Product yields, conversion of BPE, and carbon balance during the mechanocatalytic hydrogenolysis of BPE with $Ni_{53}SiAl$. 1.00 g $Ni_{53}SiAl$, 0.20 g BPE, 25 mL S.S. vessel, 2x15 mm S.S. grinding balls, 30 Hz, 60 sccm H_2.

Before traditional thermal catalysis, nickel must often be reduced at elevated temperatures to remove oxide layers (*i.e.* activated) *in situ* before reactions. In this system, thermal pretreatment of the nickel is not necessary as milling activates the catalyst. While the nickel particles of the $Ni_{53}SiAl$ catalyst were encapsulated by a layer of NiO (Figure 27a), NiO itself showed marginal catalytic activity (Figure D6). Mechanocatalytic hydrogenolysis of BPE using a fully oxidized $Ni_{53}SiAl$ catalyst (pre-treated in air at 450 °C for 8 h) showed less than 10% yield of hydrogenolysis products within 180 min of milling. Thus, instead of relying on a thermal pre-treatment, the nickel was mechanically activated. Attrition during milling is expected to remove

the nickel oxide layer, liberating the metallic nickel. Particularly when milling hard and brittle material, localized hot spots can be expected for form[238] which may produce temperatures high enough to directly reduce the NiO back to metallic Ni. This mechanochemical reduction of the NiO could explain why the rate of toluene production increased during the course of milling with the oxidized $Ni_{53}SiAl$. Mechanical energy both drives the hydrogenolysis reaction and activates the catalyst, removing the need for high temperature pre-treatments and allowing for a fully ambient system.

5.3.3 Catalyst Recycle and Deactivation

The accumulation of toluene yield in the condenser can serve as a proxy for the hydrogenolysis rate. The profile of the toluene yield in the condenser when milling with fresh $Ni_{53}SiAl$ for 120 min (Figure 29a - Cycle 1) closely matches the progression of toluene yield during the full product analysis (Figure 28). An induction period for the condenser toluene yield of about 10 min is observed, which are traditionally associated with a catalyst activation period. However, at 7.5 min, the full toluene yield was 7% (compared to just 1% for the condenser toluene yield), suggesting the delay is an artifact of the reactor system rather than, for example, a period needed to mechanically activate the nickel.

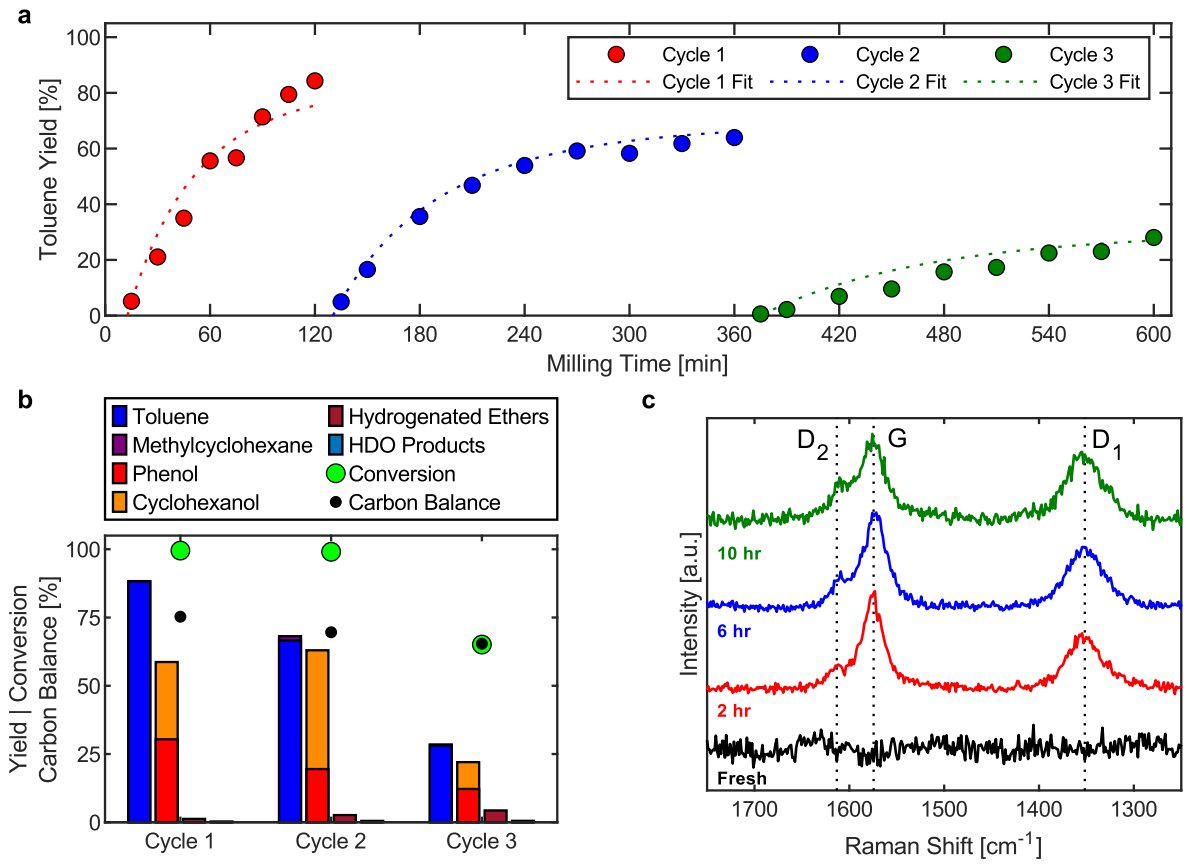

Figure 29: Toluene yields and all product yields from recycle experiments with $Ni_{53}SiAl$, and Raman spectra of spent $Ni_{53}SiAl$ samples. (a) Toluene yield in the condenser during the hydrogenolysis of BPE with fresh $Ni_{53}SiAl$ (Cycle 1) and recycled $Ni_{53}SiAl$ (Cycle 2 and Cycle 3). Fits from the kinetic modeling are overlaid the toluene yields. (b) Full product yields, conversion of BPE, and carbon balance after the hydrogenolysis reaction of BPE with fresh and recycled $Ni_{53}SiAl$. 1.00 g $Ni_{53}SiAl$, 0.20 g BPE, 25 mL S.S. vessel, 2x15 mm S.S. grinding balls, 30 Hz, 60 sccm H_2. (c) Raman spectra of fresh $Ni_{53}SiAl$ (black), $Ni_{53}SiAl$ after 2 h of reaction (after Cycle 1) (red), $Ni_{53}SiAl$ after 6 h of reaction (after Cycle 2) (blue), and $Ni_{53}SiAl$ after 10 h of reaction (after Cycle 3) (green).

To evaluate the longer-term stability of the catalyst under such intense conditions, the $Ni_{53}SiAl$ catalyst was recycled twice. After each reaction, the catalyst was washed with methanol to analyze the complete product profile, and then filtered and dried under vacuum overnight at room temperature. The toluene yields for each run (Figure 29a) show a continuous deactivation of the catalyst. In the second cycle, the toluene yield flattened by the fourth hour, trending towards a maximum toluene yield of 65%. During the third cycle, the toluene yield increased over the whole 4 h experiment, but only a 30% yield was achieved. Similar to the first cycle, an induction period

of about 10 min was observed in the second and third one. As expected from the toluene yield profiles (Figure 29b), the full product profiles showed nearly 100% conversion of BPE by the end of Cycle 2 and incomplete conversion (65%) by the end of Cycle 3. The deactivation of the nickel was also observed in the decreased selectivity of cyclohexanol to phenol between Cycle 2 (69%) and Cycle 3 (45%). Finally, significant carbon loss was observed for each cycle.

The carbon balance suggests carbonaceous deposits form as undesired side reactions with increasing milling time. Raman spectroscopy was performed on the spent catalyst after each cycle to qualitatively detect coke deposits (Figure 29c). Three bands in the Raman spectra of spent catalysts were detected: the G-band (1580 cm^{-1}; ideal graphitic lattice vibrations), the D_1-band (1350 cm^{-1}; vibrations of graphene layer edges), and the D_2-band (1610 cm^{-1}; surface graphene layers). These three bands are indicative of polyaromatic coke.[290] At longer milling times, the relative intensity of the D bands increase (compared to the G band), which is supported by deconvolution and fitting of the bands (Table D2). This increase of the D-bands and the decrease of the G-band suggest that the coke transformed to a more disordered and amorphous structure, which is expected with extended milling times.[291] Suppressing the path for coke formation will be critical in future research.

A simplified kinetic model was developed to provide a more quantitative description of the catalyst activity and deactivation. Here, the system was approximated by two reactions: hydrogenolysis of BPE to toluene (k_H) and the coking of BPE (k_C), both first order with respect to BPE (Equations 21-22). Initially, the conversion of BPE and yield of toluene for each cycle were fit independently to determine k_H and k_C (Figure D7). Both Cycle 1 and Cycle 3 had similar rates of coke formation ($k_{C,1}$ = 0.17 hr^{-1}; $k_{C,3}$ = 0.16 hr^{-1}), suggesting the activity of the catalyst towards coke formation is constant across all three cycles. Due to the high final conversion in Cycle 2,

calculating $k_{C,2}$ directly would result in high uncertainty, so the value for $k_{C,3}$ was used during the fitting. The results of this kinetic modeling confirm the deactivation of the catalyst towards hydrogenolysis with a decrease in the rate constant between each cycle ($k_{H,1}$ = 2.0 h^{-1} g^{-1}_{Ni}; $k_{H,2}$ = 0.89 h^{-1} g^{-1}_{Ni}; $k_{H,3}$ = 0.20 h^{-1} g^{-1}_{Ni}). By the third cycle, the catalyst retained only a tenth of its initial activity. Next, all three cycles were fit simultaneously, using an average k_C of 0.163 h^{-1}, with a first order deactivation term introduce to the hydrogenolysis rate constant (Equation 26). These fits were overlaid on the toluene yields in Figure 3a. This fit shows an initial rate constant ($k_{H,0}$) of 2.5 h^{-1} g^{-1}_{Ni} and that the catalyst deactivated at a rate of 34% per hour of milling (k_D = 0.34 h^{-1}). The good agreement between the observed activity of the catalyst and the deactivation model suggests a continuous mechanism is occurring during milling, instead of discrete deactivation occurring between cycles.

As expected from the carbon balances, the carbon content of the spent catalyst, in general, increased with milling time (Figure D8). Notably, the residual carbon on the catalyst did not close the carbon balance, suggesting some carbon deposits were removed during the sonication/washing step but were not detectable by GC. Agglomeration, attrition, and oxidation of the nickel were also explored as potential sources of deactivation. EDS mapping of the spent catalyst did not show separation of the nickel from the support or agglomeration the nickel particles (Figure D9). Additionally, agglomeration of the nickel particle is not expected to have a significant impact on the observed rate of hydrogenolysis. Large amount of agglomeration was observed for the spent $Ni_{05}SiAl$ and $Ni_{05}Si_{Low}$ and not $Ni_{05}Si_{High}$, but the hydrogenolysis rates were similar between the three catalysts (*vide infra*). Since the nickel is located on the exterior of the support, attrition could lead to a loss of nickel particles during milling. However, elemental analysis showed no significant change in the Ni:Al ratio between the fresh and spent catalysts (Figure D10). Finally, since the

catalyst was exposed to air between cycles, the newly exposed metallic surfaces were expected to oxidize. XRD of the spent catalysts (Figure D11) showed negligible amounts of bulk oxidation, so the new passivating oxide layers are expected to be removed during milling similar to the fresh catalyst. Consequently, the formation of carbon deposits is the most reasonable explanation for the deactivation of the catalyst for now, but future work will be necessary to elucidate the exact mechanism of the deactivation and to identify ways to prevent it.

5.3.4 Influence of Support Properties

Three catalysts were synthesized with low nickel loading (~5 wt%) to explore the influence of the support properties on the reactivity of the system. The support materials were silica-alumina and silica ($Ni_{05}SiAl$ versus $Ni_{05}Si_{High}$) and the surface area of the support was varied between the silica supports ($Ni_{05}Si_{High}$ versus $Ni_{05}Si_{Low}$). The hydrogenolysis of BPE was performed for 180 min with each catalyst. The toluene yield over the course of the reaction (Figure 30a) showed a constant increase for $Ni_{05}Si_{Low}$, while the rate of toluene yield diminished for $Ni_{05}SiAl$ and $Ni_{05}Si_{High}$. The full product profiles of the reactions with $Ni_{05}SiAl$ and $Ni_{05}Si_{High}$ (Figure 30b) showed that the decreasing rate was primarily due to the conversion of BPE to undesirable side products, resulting in large carbon losses. The other major distinction between $Ni_{05}Si_{Low}$ and the high surface area catalysts was the discrepancy between the toluene and phenol/cyclohexanol yield. Similar to the fresh $Ni_{53}SiAl$, $Ni_{05}Si_{Low}$ had a significantly higher yield of toluene than of phenol and cyclohexanol, while $Ni_{05}SiAl$ and $Ni_{05}Si_{High}$ had near stoichiometric amounts. Finally, lower surface area for the support appeared more desirable for an effective catalyst in this system, primarily based on the lower carbon loss.

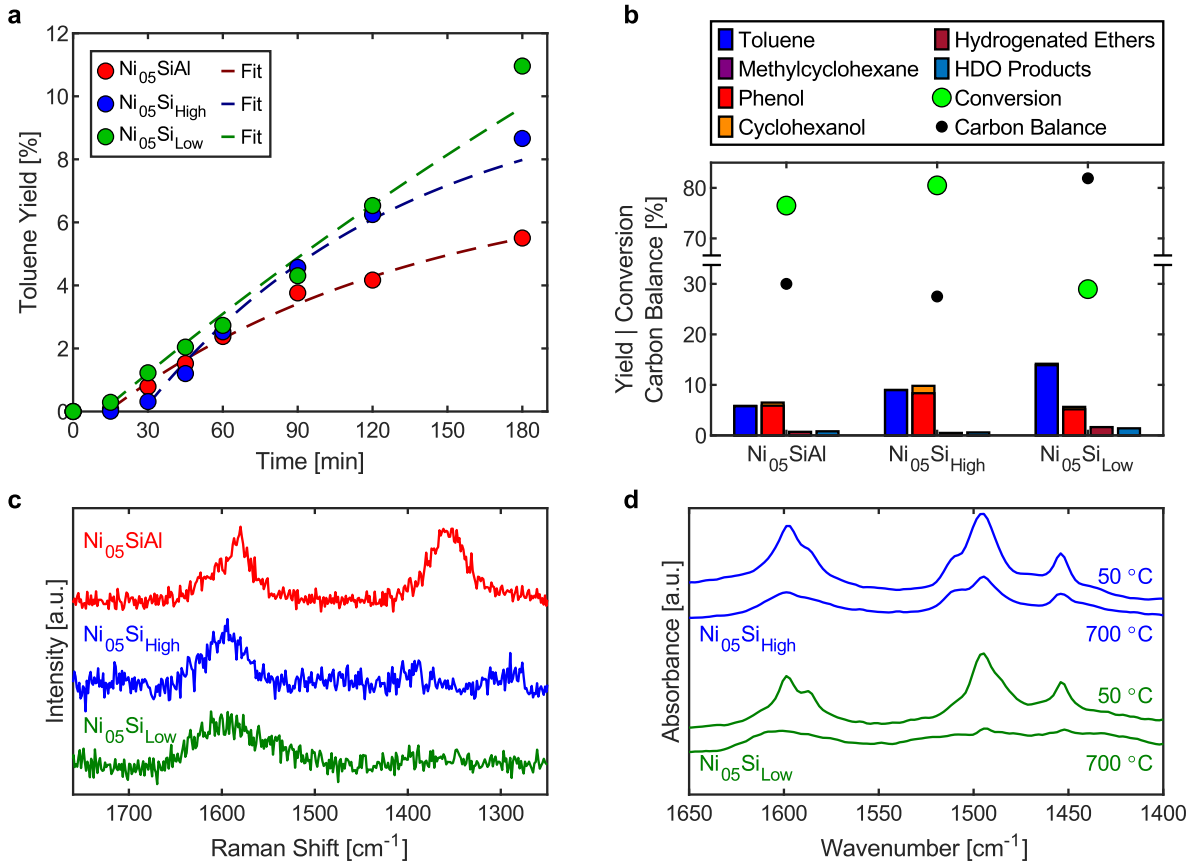

Figure 30: Toluene yields and all product yields from hydrogenolysis reactions with $Ni_{05}SiAl$, $Ni_{05}Si_{High}$, $Ni_{05}Si_{Low}$. Raman spectra and DRIFTS spectra of spent low Ni catalysts. (a) Toluene yields during the hydrogenolysis of BPE with $Ni_{05}SiAl$ (red), $Ni_{05}Si_{High}$ (blue), and $Ni_{05}Si_{Low}$ (green). Fits from the kinetic modeling are overlaid the toluene yields. (b) Full product yields, conversion of BPE, and carbon balance after the hydrogenolysis reaction of BPE with $Ni_{05}SiAl$, $Ni_{05}Si_{High}$, and $Ni_{05}Si_{Low}$. 1.00 g catalyst, 0.20 g BPE, 25 mL S.S. vessel, 2x15 mm S.S. grinding balls, 30 Hz, 30 sccm H_2. (c) Raman spectra of the spent $Ni_{05}SiAl$ (red), $Ni_{05}Si_{High}$ (blue), and $Ni_{05}Si_{Low}$ (green). (d) DRIFTS spectra of the spent $Ni_{05}Si_{High}$ (blue) and $Ni_{05}Si_{Low}$ (green) at 50 °C (top) and 700 °C (bottom).

The three low nickel loading catalysts were analyzed with Raman spectroscopy after the hydrogenolysis reaction to determine the nature of the carbon deposits (Figure 30c). The spent $Ni_{05}SiAl$ exhibited the same characteristics bands for polyaromatic coke (the G band, D_1 band, and D_2 band) as the spent $Ni_{53}SiAl$, which was expected from the low carbon balance after reaction. The D_2 band was much less distinct, and there was only a shoulder of the G band. Additionally, the G band and D_1 band of the deposits on $Ni_{05}SiAl$ increased by about 5 cm^{-1} wavenumbers compared to $Ni_{53}SiAl$. Smaller conjugated π-systems have been observed to have larger

wavenumbers,[292] suggesting the polyaromatics on the spent $Ni_{05}SiAl$ are smaller than those on the spent $Ni_{53}SiAl$. The larger surface area of the $Ni_{05}SiAl$ catalyst may limit the interactions between aromatic species, resulting in these smaller polyaromatics. The spectrum of spent $Ni_{05}Si_{High}$ does not show polyaromatic coke, despite a similar carbon loss as $Ni_{05}SiAl$. Non-polycyclic aromatic systems, such as lignin[293] or adsorbed aromatic thiols,[294] have a dominant Raman band around 1600 cm^{-1} and smaller bands between 1400 cm^{-1} and 1300 cm^{-1}. Only a single band at 1596 cm^{-1} was observed in the two spent silica supported catalysts suggesting that the deposits are predominantly mono-aromatic species. Acidic catalysts and supports, such as silica-alumina, are well known to facilitate coking reactions,[295-296] so the presence of polyaromatic carbon deposits on $Ni_{53}SiAl$ and $Ni_{05}SiAl$ is not surprising. Silica can be reactive during mechanical activation,[41, 297-298] so chemisorbed species, such as phenolates, may be forming during the ball impact. However, silica is essentially inert under relaxed conditions and so may not further catalyze polyaromatic coke formation.

The spent $Ni_{05}Si_{High}$ and $Ni_{05}Si_{Low}$ were subsequently analyzed using *in-situ* DRIFTS (Figure 30d) to further characterize deposits on the surface. The depicted region between 1400 and 1600 cm^{-1} corresponds to ring vibrations of aromatic species. After heating the samples, the extent of aromatics left on the $Ni_{05}Si_{High}$ catalyst was much greater than what was left on the $Ni_{05}Si_{low}$. Similar experiments using fresh catalysts impregnated with BPE showed complete loss of the aromatic features at elevated temperature (Figure D12). This indicates that aromatic species were more strongly adsorbed onto the $Ni_{05}Si_{High}$ surface. This also corroborates the lower carbon balance for $Ni_{05}Si_{High}$ observed in Figure 4b. The exact species that are still adsorbed remain unknown, although it is more likely to be the phenoxy moiety as was shown when BPE was grafted unto SBA-15 and heated to 600 ºC.[299] This possibility is also in line with the Raman spectra that

indicated mono-aromatics are adsorbed on both $Ni_{05}Si_{High}$ and $Ni_{05}Si_{Low}$. The higher surface area of the support can also be responsible for the discrepancy in carbon balances. As a result of milling, the Si-O bonds break creating transient active sites that can catalyze reactions.[41] Due to higher abundance of surface Si-O bonds in the high surface area support, it is plausible that there are more active sites from rupturing than in the low surface area silica support. The higher density of active sites from rupturing can thus be responsible for more adsorbed species and a lower carbon balance on the $Ni_{05}Si_{High}$. Decreasing the intensity of the milling may have a beneficial effect by decreasing the extent the support bonds rupture, but a balance will have to be struck with activating the metal sites and driving the hydrogenolysis reaction. Work on future should focus on mitigating these reactions by either optimizing milling intensity or studying supports that are less prone to rupture. Softer material, like activated carbon, should flex and bend under the mechanical impact, and harder material, like zirconium oxide, should be more resilient to rupture.

The simplified kinetic model (Equations 21 and 22) was applied to these reactions as well, without the deactivation expression, to determine the hydrogenolysis rate constant and the coking rate constant (fits shown in Figure 30a). $Ni_{05}SiAl$ (k_H = 0.81 hr^{-1} g^{-1}_{Ni}) and $Ni_{05}Si_{Low}$ (k_H = 0.83 hr^{-1} g^{-1}_{Ni}) had similar hydrogenolysis rates, which were approximately 33% lower than the rate of $Ni_{05}Si_{High}$ (k_H = 1.21 hr^{-1} g^{-1}_{Ni}). The similarity between the k_H of $Ni_{05}SiAl$ and $Ni_{05}Si_{Low}$ suggests the support material has little influence on the activity of the catalyst. The nickel particle size also had a weak correlation with the activity of the catalyst. Nickel particle on $Ni_{05}SiAl$ and $Ni_{05}Si_{Low}$ agglomerate during milling to a size on the order of 100 nm (Figure 31a-b,e-f), while the size of the nickel particles on $Ni_{05}Si_{High}$ did not appreciably change over the course of the reaction (Figure 31c-d). For a constant mass of particles, a 10-fold increase in particle size corresponds to a 10-fold decrease in surface area. However, the roughly order of magnitude drop in available

nickel surface area only corresponded to a 33% lower rate constant. The agglomeration is indicative of enhanced interaction between the nickel and the mechanical action. As such, the agglomerated particles should have experienced more mechanical activation, resulting in a higher proportion of metallic nickel surface area. So, the agglomerated particles of $Ni_{05}SiAl$ and $Ni_{05}Si_{Low}$ are expected to have fully metallic surfaces, while many of the unaltered particles of $Ni_{05}Si_{High}$ are expected to maintain the inert NiO shell. In a similar vein, the higher activity of $Ni_{53}SiAl$ may result from more efficient mechanical activation due in part to the higher nickel loading. As so, unsupported metal catalysts may be the most promising candidates for future catalyst because any mechanical energy imparted on the catalyst would be used to create additional reactive surfaces and the undesired support interactions would be avoided altogether.

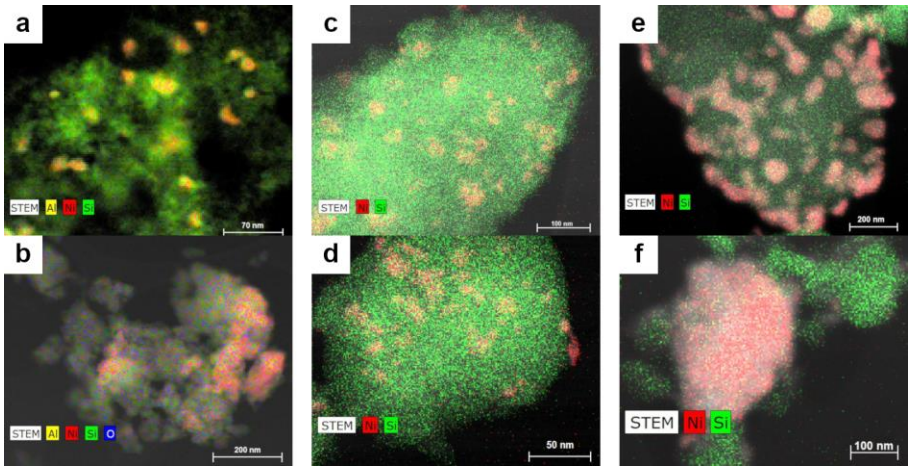

Figure 31: EDS mapping of (a) fresh $Ni_{05}SiAl$ and (b) spent $Ni_{05}SiAl$, (c) fresh $Ni_{05}Si_{High}$ and (d) spent $Ni_{05}Si_{High}$, and (e) fresh $Ni_{05}Si_{Low}$ and spent $Ni_{05}Si_{Low}$.

While the surface area of catalyst had little connection to the hydrogenolysis rate, it had a strong influence on the rate of carbon loss. The coking rate constants for $Ni_{05}SiAl$ (k_C = 0.45 hr^{-1}) and $Ni_{05}Si_{High}$ (k_C = 0.52 hr^{-1}) were nearly an order of magnitude higher than that of $Ni_{05}Si_{Low}$ (k_C = 0.074 hr^{-1}). $Ni_{53}SiAl$ fits this trend well, too (k_C = 0.16 hr^{-1}). This correlation between carbon loss and catalyst surface is expected from the explanation of the origin of the carbon loss for

$Ni_{05}Si_{High}$. The ratio of k_H and k_C from each experiment provide insights to the origin of the discrepancy between toluene yields and phenol/cyclohexanol yields. Excess toluene is observed when k_H is much larger than k_C (Fresh $Ni_{53}SiAl$ and $Ni_{05}Si_{Low}$). When k_H and k_C are closer in magnitude (or k_C is greater than k_H), stoichiometric yields of toluene and phenol/cyclohexanol are observed. What is believed to be happening is that since toluene is produced much more quickly than it could be consumed to form coke or adsorbed species, the toluene will more readily volatilize and leave the reactor before participating in the coking reaction. Since phenol cannot volatilize, the same amount will participate in the coke formation reaction, regardless of how quickly it is produced.

5.4 Conclusions

The mechanocatalytic hydrogenolysis of benzyl phenyl ether was studied over supported nickel catalysts. Hydrogenolysis occurred at the benzyl ether bond, producing toluene and phenol as primary products. The observed reaction network closely matches those for thermal hydrogenolysis of BPE, suggesting similar reactions can be expected to occur between mechanocatalytic and thermocatalytic reactions over metal catalysts. Additionally, the milling liberated active nickel surface *in situ*, side stepping the need for a catalyst reduction step. Catalyst deactivation was observed through recycle experiments, expected to occur predominantly through carbon deposits. Studying the influence of support properties showed that high carbon losses were associated with high catalysts surface areas, even for traditionally insert silica. The enhance reactivity of the support oxide induced by milling is expected to create chemisorbed species, which can further react to form polyaromatic coke and deactivate the catalysts. Less intense milling may diminish these effects, so future work with need to focus on determining optimal conditions for promoting hydrogenolysis while mitigating carbon loss. Importantly, the underlying chemistry

necessary for reductive depolymerization has been demonstrated under mild and solvent free conditions.

CHAPTER 6
SUMMARY AND RECOMMENDATIONS

6.1 Summary

The overarching objective of this thesis is to study the fundamental challenges to lignin depolymerization and phenomena of mechanocatalysis in order to mechanocatalytically valorize lignin. Achieving this goal has focused on understanding the limits of lignin depolymerization imposed by fraction and isolation, developing the means to describe the reaction conditions present in mechanochemical reactors, identifying novel catalyst behaviors due to milling, and demonstrating the chemistry necessary for mechanocatalytic depolymerization. The understanding developed in this thesis lays the foundational groundwork for rationally approaching mechanocatalytic lignin depolymerization and valorization.

In Chapter 2, the structure of lignin from four different industrial fractionation processes are characterized using a suite of analytical techniques. While several of these methods are supposedly less harsh than kraft pulping, all eight lignin streams exhibit extensive depolymerization (loss of labile ether bonds) and repolymerization (formation of condensed carbon-carbon bonds). The largest β-O-4 content was found to be 11.1 linkages per 100 aromatics, far below the expected 40 to 60 linkages in native lignin. The calculated theoretical monomer yields by depolymerization is less than 5% for all the lignin samples. These results suggest that strategies focused on valorizing isolated lignin will face inherently limited monomer yields. Despite the similarities in the structures, stark difference are observed during thermogravimetric analysis, suggesting there still could be exploitable difference between the lignin streams during valorization.

In Chapter 3, a modeling approach is developed to describe mechanochemical reactions using traditional physico-chemical principles. The model uses the kinetic energy dissipated by the

ball during collision to describe the hot spot conditions during the mechanochemical decomposition of calcium carbonate. The kinetic energy is converted to heat, which then dissipates away in the surrounding powder. The described reaction conditions exceed 1000 K and persisted for tens of milliseconds. The reaction rate at these conditions were able to match the experimentally measured decomposition rate. While the model is highly sensitive to the input parameters, due to the exponential term in the reaction rate equation, the model is able to predict experimental rates within a 65% error. While this current approach has limited application, it establishes a valuable tool that can be built upon to describe the conditions present in more complex mechanocatalytic reactions.

In Chapter 4, mechanocatalytic ammonia synthesis is demonstrated over an *in situ* formed nitride catalyst. XRD and XAS confirm that metallic titanium powder milled in N_2 mechanochemically converts to titanium nitride. Milling the metallic titanium in an atmosphere of N_2 and H_2 also results in the formation of titanium nitride, which can mechanocatalytically synthesize ammonia. Assessing the thermodynamics of the reaction shows that a surface catalyzed reaction could not describe the observed reaction rate. Instead, a transient Mars-van Krevelen reaction mechanism is proposed, where the nitrogen is incorporated into the nitride structure, and under different reaction conditions, the nitride is reduced with H_2 to form ammonia. This study exemplifies the unique chemistry attainable in mechanocatalytic reactions, compared to traditional thermocatalytic systems.

Finally, in Chapter 5, the mechanocatalytic hydrogenolysis of benzyl phenyl ether (BPE) over supported nickel catalysts is studied as a model system for lignin depolymerization. The reaction network observed during hydrogenolysis aligned closely with the reactivity of BPE in thermal reactions. Milling plays a key role in performing this reaction at ambient conditions by

liberating passivated nickel surfaces. During the hydrogenolysis reaction, catalyst deactivation and carbon deposition is observed, predominantly caused by the enhanced reactivity of the oxide support induced by milling. These results suggest that an improved catalyst should have a support less prone to fracture or be a non-supported metal to minimizing the formation of carbon deposits. Importantly, the chemistry necessary for advanced lignin valorization strategies, such as hydroprocessing or reductive catalytic fractionation, are feasible in mechanocatalytic reactors.

6.2 Recommendations for Future Work

6.2.1 Modeling Mechanocatalytic Reactors and Reactions

In Chapter 3, a model describing the reaction conditions during a ball-on-wall collision in a ball mill reactor was introduced. A major assumption of the model was that the collision could be described well by a head-on collision between the ball and a flat wall. However, glancing and rolling collision also make up a meaningful fraction of the impacts, especially in mills with different geometries (such as a planetary mill). Additional energy transfer experiments (ball drop experiments) could be performed to account for the different collision geometries (e.g., vertical drops on an angled plate or attaching the ball to a pendulum for glancing collisions or rolling the ball off a ramp to add rotation to the ball). The complexity of using larger mills with numerous balls may make direct characterization of the collision frequencies and qualities inhibitive, so future works should be coupled with additional computational approaches, like discrete element method (DEM) analysis. A calibrated DEM model would provide the necessary information on the distribution of collisions needed to design and bound the energy transfer experiments. Another difficulty for the model was determining what fraction of energy lost in the collision was converted to heat. While many studies have looked at different ways the energy can be partitioned, a comprehensive and quantitative study on this partition and systematic influences could not be

found. Such a study, particularly where the materials are varied as well, would be highly valuable for the accuracy of any future models.

The applicability of the hot spot model should also be expanded to describe mechanocatalytic reactions as well, with mechanocatalytic ammonia synthesis as the simplest first choice. In order to account for other means for the reaction, the formation and decay of hot spots could be quantified thermographically using a high-speed IR camera with an automated hammer set up. Infrared thermography has been successfully used to measure the temperature and energy distribution of impacts on composite materials[300-302] and energetic materials.[303] The progression of the hot spot temperature will be monitored as the heat distributes throughout the powder. Despite the high resolution of the IR camera, the thermography is expected to only provide course-grain information on the hot spot characteristics due to their small size and short duration. Thus, COMSOL should be used to infer higher resolution on the temperature profiles within the catalyst bed. For an initial assessment, the N_2 activation should be assumed to occur strictly mechanochemically during the collision while the hydrogenation reaction should be assumed to occur strictly thermochemically during the decay of the hot spot after the collision. The kinetics from these two half reactions will be incorporated into the hot spot model to determine the ammonia yield from a single collision. Additionally, potential discrepancies between the model and experimental results can provide additional insights to the roles of mechanically induced active sites.

6.2.2 Ammonia Synthesis

Chapter 4 demonstrated mechanocatalytic ammonia synthesis over titanium nitride as a proof of concept. The underlying chemical properties that control the activity of a mechanocatalyst are still unknown, so a follow up project should study additional transition metal nitrides,

specifically vanadium (V), zirconium (Zr), niobium (Nb), and molybdenum (Mo). The rate of mechanochemical nitridation of a metal is expected to be a key descriptor of the activity of the subsequent nitride for ammonia synthesis. An important metric as well to quantify will be the steady state rate for ammonia synthesis. This requires a new ball mill reactor capable of operating for extended times and means to continuously detect ammonia. Surveying these elements will provide initial trends and relationships between elemental/nitride properties and catalyst activity, which should allow for the rational design of potentially more active tertiary nitride catalysts. Additionally, molybdenum nitride is recognized as one of the best binary nitrides for thermal ammonia synthesis,[304] so comparing the relative activity of molybdenum nitride during mechanocatalytic and thermocatalytic reactions may provide deeper insights to the underlying mechanism of mechanocatalytic ammonia synthesis.

Another direction to focus the project on is to increase the sustainability of the process by utilizing water and air as primary reagents. The reactions were conducted using H_2, the production of which is dominant source of CO_2 emissions currently for ammonia synthesis.[305] H_2 could be produced on-site from water using electrolyzers, but the additional infrastructure will increase the cost and complexity of the process. The direct use of water as a reducing agent should first be explored. Thermal reactions with TiN showed ammonia formation when heated in pure Ar, which was attributed to the presence of water on the nitride surface (Appendix C.4.2). Another possibility is to operate with a dual catalyst system, where the water is mechanocatalytically split into H_2 and O_2 over a second catalyst. Single-pot systems like this have been used for the hydrogenation of numerous organic compounds, with Cr acting as the water-splitting catalyst and Ni acting as the hydrogenation catalyst.[276] The separation and purification of N_2 from air will also further increase the energy demand of the process, so replacing the N_2 with air is a logical next step. Avoiding the

use of purified H_2 and N_2 results in the presence of O_2 in the reactor, introducing the question of catalyst stability. For example, titanium nitride will begin to thermally oxidize to TiO_2, which is not active for ammonia synthesis, between 450 °C and 500 °C.[306-307] So, the kinetics of mechanochemical oxidation of nitrides and mediation strategies will most likely need to be explored too.

6.2.3 Lignin Depolymerization and Valorization

Chapter 5 discussed the mechanocatalytic hydrogenolysis of BPE, a model for the α-O-4 ether linkage found in native lignin. However, Chapter 2 clearly demonstrated that most ether linkages (β-O-4 and α-O-4 bonds) are lost during the fractionation of lignin. For this reason, follow up projects on mechanocatalytic depolymerization of lignin should be bifurcated: one focused on the reductive mechanocatalytic fractionation of lignocellulose and a second on the mechanocatalytic cleavage of model condensed moieties.

Reductive catalytic fractionation (RCF) relies on the combination of solvolysis of native, unfractionated lignin and reductive stabilization of reactive intermediates and can produce monomer yields between 40% and 60%, depending on the lignin source.[29] The chemistry needed for the latter step (hydrogenolysis, hydrodeoxygenation, hydrogenation) was demonstrated mechanocatalytically using BPE as a model system. Moving closer to real lignocellulosic biomass, initial studies should start with milled wood lignin (MWL), which preserves much of the native lignin structure, to introduce influences from polymeric material properties while avoiding the unnecessary complexity associated with the presence of cellulose and hemicellulose. Liquid assisted grinding (LAG) is a common technique in mechanochemistry and is the logical starting point for studying mechanochemical solvolysis. Even for direct hydrogenolysis, the presence of a small amount of solvent may be necessary to stabilize transition states or facilitate the interaction

between the lignin polymer and the catalyst. Depolymerization of the lignin can be quantified through three metrics: monomer yields (via GC or HPLC), β-O-4 reduction (via HSQC NMR spectroscopy), and molecular weight reduction (via GPC). Finally, results from Chapter 5 showed that non-active catalyst surface area contributes to significant carbon loss, so future experiments should focus on non-porous, non-supported metal catalysts in order to maximize the amount of reachable, active surface area.

While RCF can result in high mono-aromatic yields, approximately 50% of the aromatic rings remain part of an oligomer or a polymer. Additionally, many biorefining processes will not be compatible with a lignin-first approach and create a large supply of condensed, isolated lignin. Cleaving the condensed linkages in lignin will be necessary to achieve full lignin valorization, but breaking carbon-carbon bonds mechanocatalytically has not been extensively studied. Here, future work should first focus on demonstrating and understanding the depolymerization of well-defined carbon-chain polymers, such as polyolefins or polystyrene. Ruthenium based catalysts have been demonstrated to hydrogenlyze polyethylene (specifically over Ru/C)[308] and cleave carbon-carbon bonds in Kraft lignin and model dimers (over $Ru/NbOPO_4$),[309] so overlaps in the chemistries of the two systems should exist. Investigating well-defined polymers will make analysis of the products and reaction progress much less difficult, which will be important when probing such uncharted areas. In tandem and relying on similar chemistry, the cleavage of dimeric model compounds, such as 4,4'-biphenol (5-5 linkage), 2,4'-dihydroxydiphenylmethane, or bibenzyl (β-5 linkage), should be explored to understand how the different depolymerization approaches may translate to structures closer to lignin.

6.2.4 Mechanocatalytic Chemical Recycling of Plastics

The transition from a linear to a circular economy, based on reusing, recycling, and remanufacturing all material resources, has recently been the focus of much interest.[310] Recycling consumer plastics are a major hurdle to achieving a circular economy. Globally, 40 wt% of plastics are landfilled and 32 wt% enter the environment, while the consumption of plastics is projected to only grow in the coming years.[311] As discussed in Section 6.2.3, similarities in depolymerization chemistry are expected to exist between lignin and plastics, so utilizing mechanocatalysis should be explored as well as a means for efficient chemical recycling of plastics. Quantitative mechanochemical depolymerization of poly(ethylene terephthalate) (PET) has been demonstrated, but required stoichiometric consumption of NaOH.[312] Building on that study, future research should work to understand the influence of various milling parameters on the depolymerization kinetics. Demonstrating and exploring mechanocatalytic hydrolysis or alcoholysis on other polyesters and polyamides, most likely with lewis acid catalysts, would be important for creating a more industrially viable process. The hot spot temperatures described in Chapter 3 suggests that temperatures needed for the catalytic cracking of polyolefins (500 – 550 °C) may be achievable in mechanocatalytic systems. Here, future work should focus on understanding how material properties affect the energy transfer during a collision. Ultimately, these studies would both provide valuable applied insights for the chemical recycling of plastics and fundamental insights for the interactions between polymers and catalysts during ball milling.

APPENDIX A
SUPPLEMENTARY INFORMATION FOR CHAPTER 2

A.1 Compositional and Elemental Analysis

Table A1: Composition of Residual Sugars (in wt%) and Ash content (wt%).

Sample	Arabinan	Galactan	Glucan	Xylan	Mannan	Ash
SWK1	0.3	2.3	0.0	0.7	0.0	1.5
SWK2	0.3	2.0	0.0	0.6	0.0	0.6
SWK3	0.3	0.0	2.0	0.4	0.0	3.6
SWBuOH	0.0	0.0	0.5	0.0	0.0	0.1
HWK	0.0	0.1	0.1	0.1	0.0	0.0
HWSCW	0.0	0.0	4.4	0.0	0.0	0.9
HWSEW	0.0	0.1	2.3	1.4	0.0	1.4
HWBuOH	0.0	0.0	0.0	0.0	0.0	3.9

The CHNOS content (Table A2) of the lignin samples were similar, and in the ranges of previously reported values,[313-314] but samples from processes using sulfur chemicals (kraft samples and HWSEW) had higher contents of sulfur.

Table A2: CHNOS Elemental Composition (in wt%).

Sample	Carbon	Hydrogen	Nitrogen	Oxygen	Sulfur
SWK1	64.4	5.66	n.d[a]	28.1	1.77
SWK2	62.2	5.65	0.56	29.2	1.98
SWK3	64.3	5.73	n.d	27.7	1.94
SWBuOH	68.0	6.27	n.d	25.3	0.13
HWK	65.0	5.80	0.17	27.0	1.01
HWSCW	62.5	5.55	n.d	31.2	0.49
HWSEW	57.6	5.39	0.35	33.8	2.13
HWBuOH	63.7	6.41	3.67	24.5	0.53

[a] *n.d. = not detected*

Table A3: Elemental composition from PIXE analysis (in ppm). Cells are shaded linearly from red (negative) to green (positive) as distance from the mean value, excluding outliers, grows.

	SWK1	SWK2	SWK3	SWBuOH	HWK	HWSCW	HWSEW	HWBuOH
Sulfur	12590.0	12510.0	20060.0	162.3	10450.0	165.8	15770.0	4380.0
Sodium	1340.0	7140.0	434.4	0.0	8720.0	339.9	670.3	714.4
Magnesium	240.5	276.4	202.1	0.0	3080.0	149.5	251.3	380.3
Aluminum	124.0	206.4	64.4	455.8	239.2	133.9	98.2	57.7
Silicon	200.6	360.7	146.7	0.0	1960.0	493.0	156.0	0.0
Phosphorus	0.0	0.0	0.0	0.0	251.3	0.0	0.0	619.5
Chlorine	0.0	169.9	0.0	35.3	0.0	0.0	0.0	4010.0
Potassium	58.0	449.3	44.7	37.5	1500.0	31.9	507.9	3850.0
Calcium	28.9	194.2	97.0	22.1	1600.0	479.5	959.5	237.9
Titanium	0.0	0.0	0.0	0.0	0.0	4.9	0.0	0.0
Chromium	0.0	0.0	13.8	0.0	0.0	15.9	119.7	0.0
Manganese	13.4	24.8	9.4	0.0	271.7	0.0	65.5	0.0
Iron	30.3	32.8	81.8	76.5	75.4	176.3	967.1	210.4
Cobalt	0.0	0.0	0.0	0.0	0.0	8.4	0.0	0.0
Nickel	0.0	0.0	12.7	7.5	1.5	11.0	114.3	15.4
Copper	8.8	0.0	7.9	0.0	1.7	2.9	50.6	22.2
Zinc	17.1	10.8	5.6	1.8	6.2	0.0	46.9	35.3
Tungsten	0.0	0.0	0.0	0.0	0.0	27.9	0.0	0.0
Selenium	148.3	0.0	0.0	0.0	0.0	0.0	0.0	0.0
Strontium	0.0	0.0	0.0	0.0	0.0	0.0	8.1	0.0
Molybdenum	0.0	0.0	19.4	0.0	0.0	0.0	48.7	0.0
Rubidium	0.0	0.0	0.0	0.0	6.0	0.0	0.0	0.0
Vanadium	0.0	0.0	0.0	0.0	19.5	0.0	0.0	0.0
Bromine	0.0	0.0	0.0	0.0	2.1	0.0	0.0	11.8
Niobium	0.0	0.0	0.0	0.0	0.0	0.0	0.0	21.5

A.2 Gel Permeation Chromatography

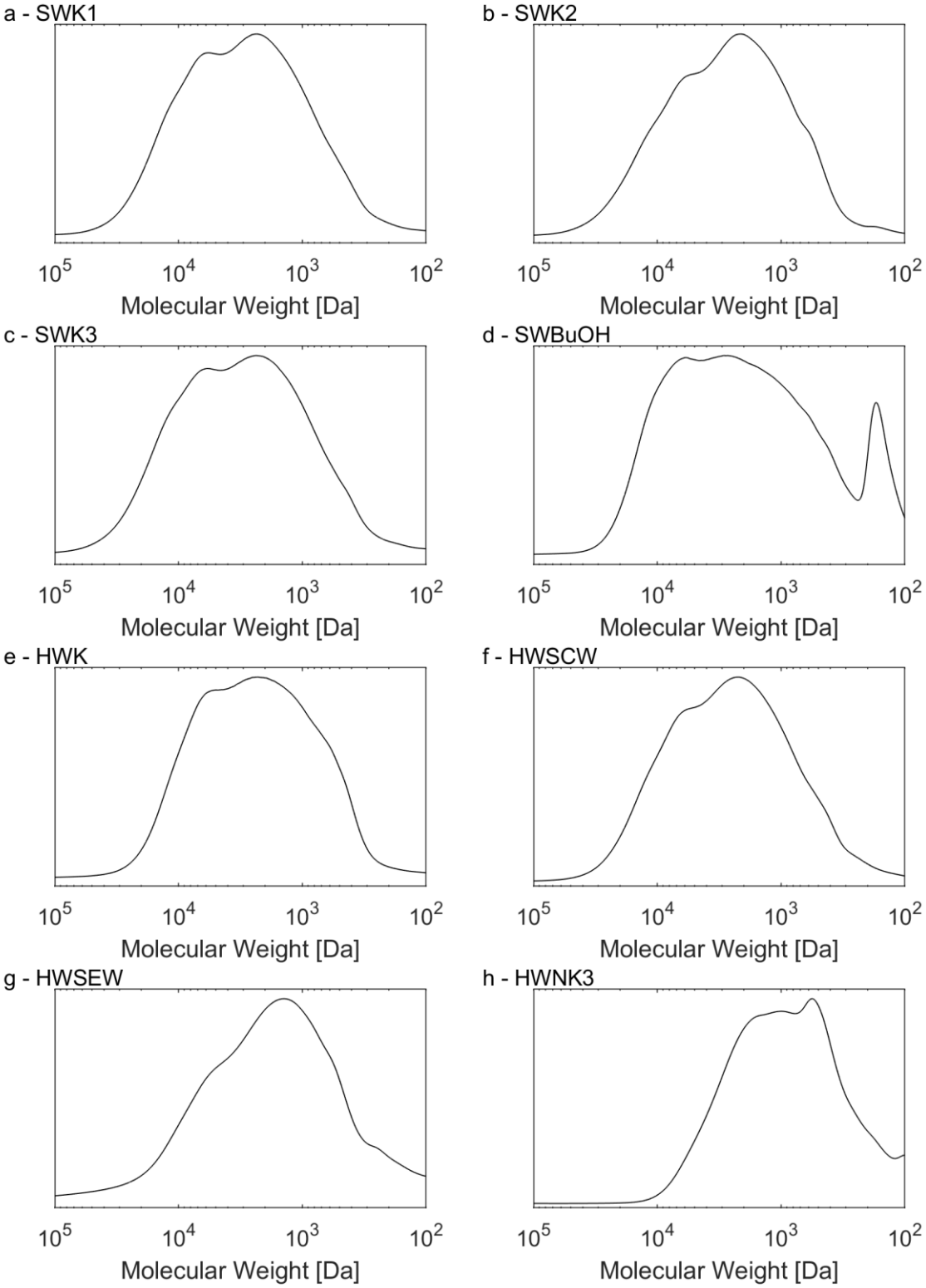

Figure A1: GPC traces for acetylbrominated lignin samples.

A.3 Quantitative ^{13}C NMR Spectroscopy

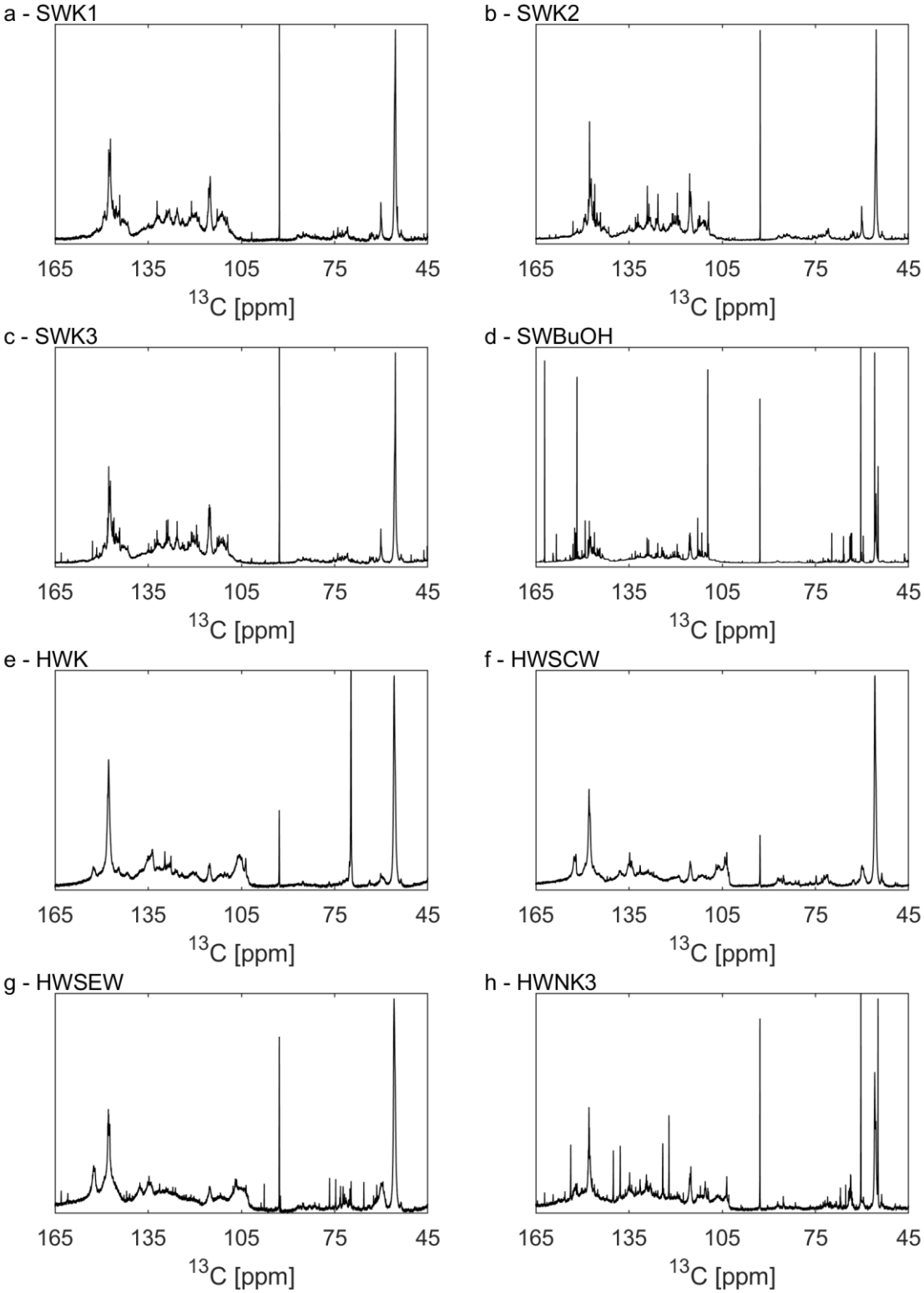

Figure A2: ^{13}C NMR Spectra for all lignin samples.

Table A4: Integral values of the ^{13}C NMR spectra. Integral values were normalized by defining the sum of the three aromatic regions as 6.

Sample	C_{ArO} [162 – 142 ppm]	C_{ArC} [142 – 125 ppm]	C_{ArH} [125 – 102 ppm]	C_{MeO} [58 – 54 ppm]
SWK1	1.94	1.79	2.27	0.91
SWK2	1.97	1.71	2.32	0.87
SWK3	1.80	1.84	2.36	0.85
SWBuOH	2.03	1.55	2.41	0.73
HWK	2.07	2.02	1.91	1.15
HWSCW	2.33	1.73	1.94	1.28
HWSEW	2.50	1.77	1.73	1.07
HWBuOH	2.10	1.91	1.99	0.74

A.4 2D HSQC NMR Spectroscopy

Table A5: Peak assignments of the HSQC NMR spectra.

δ_C [ppm]	δ_H [ppm]	Assignment
111.4	7.0	C_2/H_2 on G
115	6.7,6.94	C_5/H_5 on G
119.5	6.9	C_6/H_6 on G
103.3	6.6	C_2/H_2 and C_6/H_6 on S
106.5	7.0	C_2/H_2 and C_6/H_6 on Oxidized S
128.0	7.2	C_2/H_2 and C_6/H_6 on H
56.2	3.6	Methoxy Groups
70.9	4.71	$\beta O4_\alpha$ on G
71.8	4.83	$\beta O4_\alpha$ on S
83.4	4.27	$\beta O4_\beta$ on G
85.9	4.10	$\beta O4_\beta$ on S
82.9	4.48	$\beta O4_\beta$ on H
59.4	3.40, 3.72	$\beta O4_\gamma$
87.5	5.6	$\beta 5_\alpha$
53.1	3.43	$\beta 5_\beta$
62.6	3.67	$\beta 5_\gamma$
85.7	4.5	$\beta\beta_\alpha$
53.5	3.05	$\beta\beta_\beta$
71.0	3.81, 4.17	$\beta\beta_\gamma$

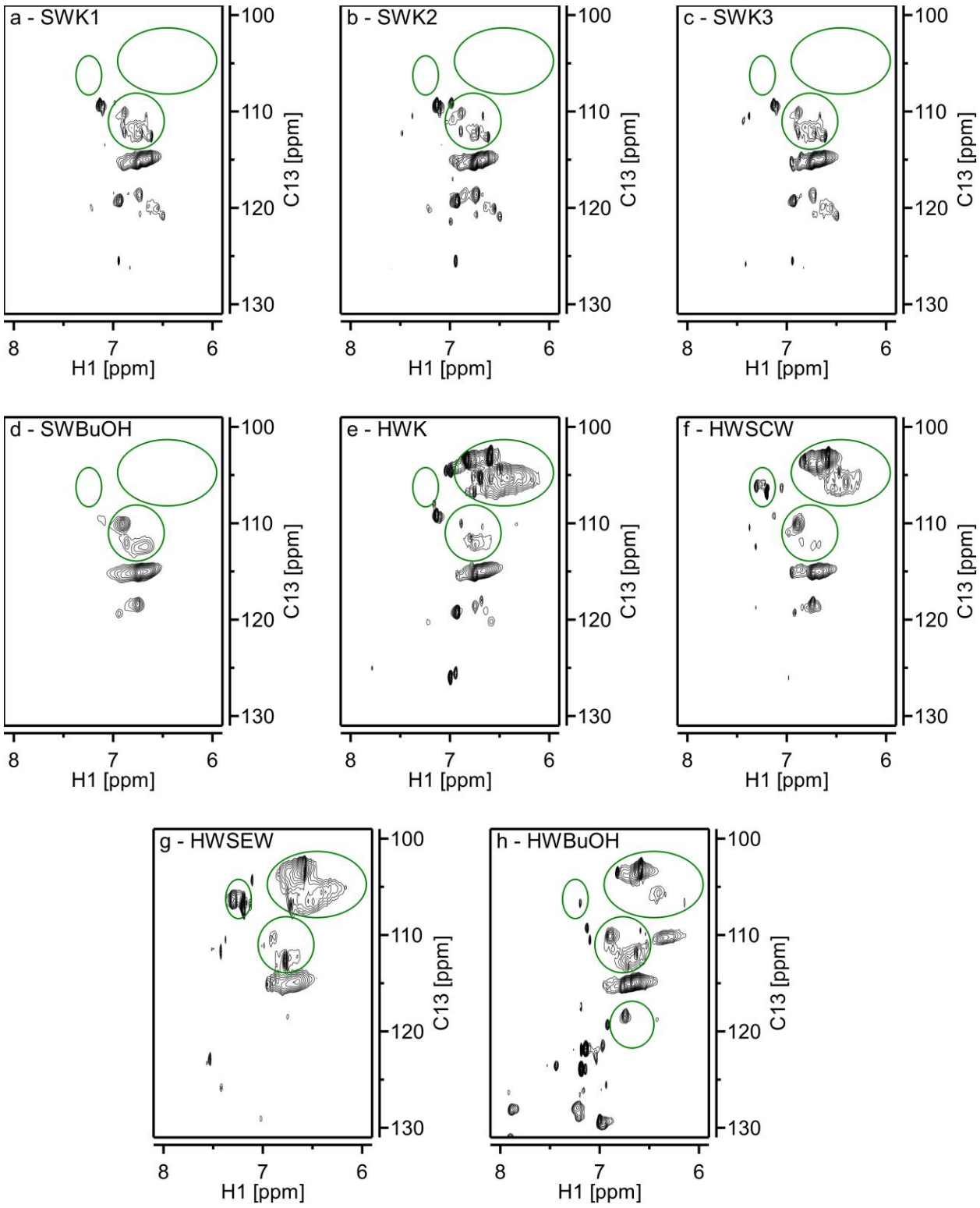

Figure A3: HSQC NMR spectra of the aromatic region for all lignin samples with integral boundaries.

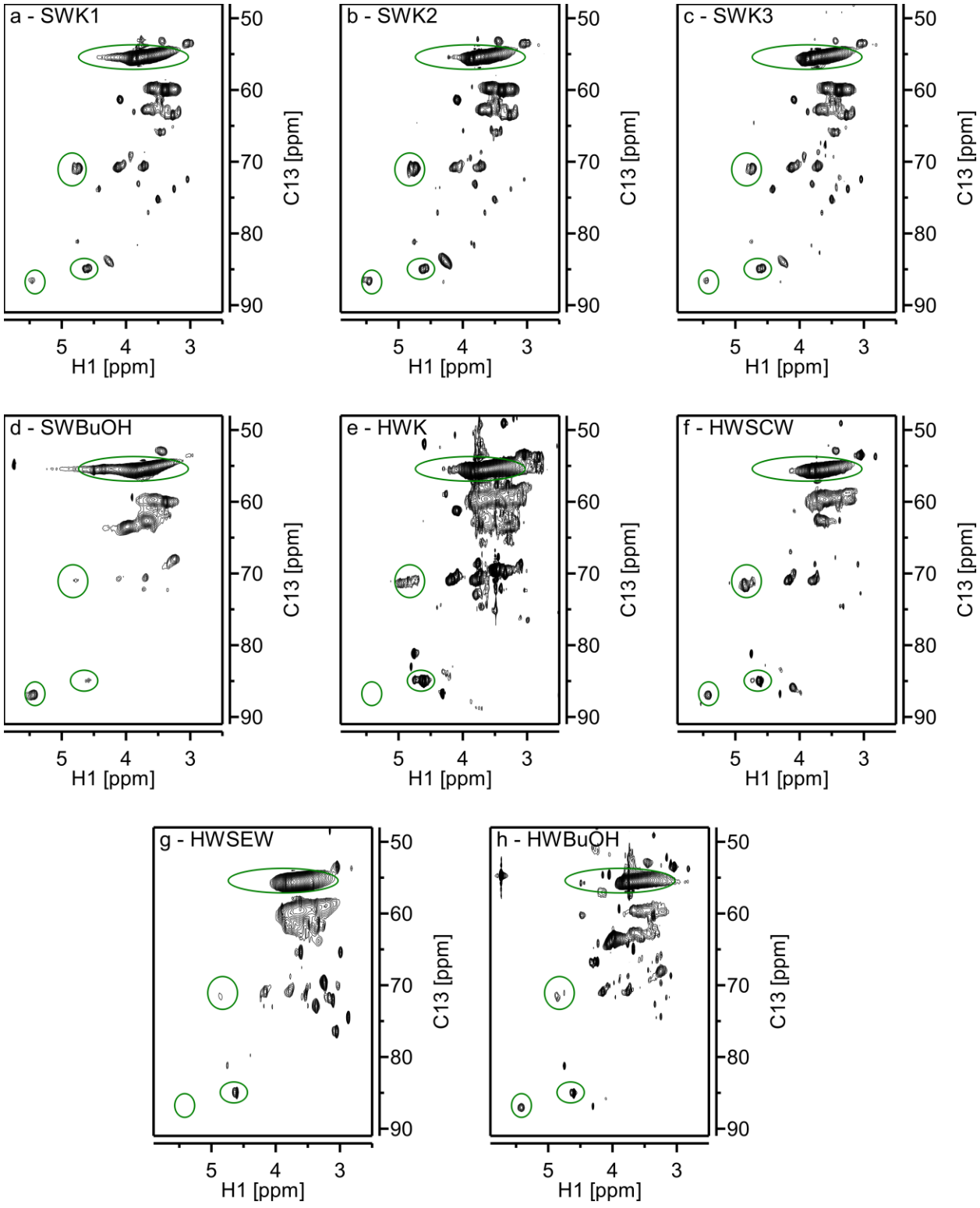

Figure A4: HSQC NMR spectra of the aliphatic region for all lignin samples with integral boundaries.

A.5 Theoretical Monomer Yield Calculations

Equations A1-3: Elemental Composition for the Empirical Monomeric Formula. Carbon, hydrogen, and oxygen weight percent determined from elemental analysis (Figure A2). Methoxy group content per aromatic (MeO^{Aro}) was determined from ^{13}C NMR (Table 3).

$$C^{Aro} \equiv 9 \tag{A1}$$

$$H^{Aro} = (C^{Aro} + MeO^{Aro}) \times \frac{H^{wt\%}}{\left(\frac{C^{wt\%}}{12}\right)} - (3 \times MeO^{Aro}) \tag{A2}$$

$$O^{Aro} = (C^{Aro} + MeO^{Aro}) \times \frac{\left(\frac{O^{wt\%}}{16}\right)}{\left(\frac{C^{wt\%}}{12}\right)} - MeO^{Aro} \tag{A3}$$

Equation A4: Monomeric Molar Mass.

$$Molar\ Mass\ \left[\frac{g}{mol}\right] = (C^{Aro} \times 12\ ) + (H^{Aro} \times 1) + (O^{Aro} \times 16) + (MeO^{Aro} \times 31) \tag{A4}$$

Equation A5: Degree of Polymerization. Number average molecular weight (M_N) determined by GPC (Table 2).

$$DoP = \frac{M_N}{Molar\ Mass} \tag{A5}$$

Equation A6: Fraction of Cleavable Bonds. βO4 content per aromatic ($\beta O4^{Aro}$) determined by HSQC NMR and ^{13}C NMR (Table 3).

$$F_{CB}\ [\%] = \frac{\beta O4^{Aro}}{\left(\frac{DoP-1}{DoP}\right)} \times 100 \tag{A6}$$

APPENDIX B
SUPPLEMENTARY INFORMATION FOR CHAPTER 3

Table B1: List of Nomenclature

C_p	Heat Capacity [J kg^{-1} K^{-1}]
C_{visc}	Coefficient of Viscosity [kg m$^{-1/2}$ s^{-1}]
D	Ball Deformation [m]
D_{max}	Maximum Ball Deformation [m]
dD/dt	Rate of Deformation [m s^{-1}]
E	Young's Modulus [Pa]
E_a	Activation Energy [J mol^{-1}]
E_E	Elastic Energy [J]
E_v	Dissipated Energy [J]
f_E	Restorative Force [N]
f_v	Dissipative Force [N]
f_{rate}	Reaction Rate Function [mol s^{-1} m^{-3}]
g	Gravitational Acceleration [m s^{-2}]
h	Heat Transfer Coefficient [W m^{-2} K^{-1}]
$\Delta_r H^0_T$	Enthalpy of Reaction [J mol^{-1}]
l	Powder Bed Height [m]
K	Effective Spring Constant [kg m$^{-1/2}$ s^{-2}]
k_{mt}	Effective Mass Transfer Coefficient [m^3 s^{-1}]
k_{rxn}	Pre-exponential Factor [s^{-1}]
m_{ball}	Mass of the Ball [kg]
m_{powder}	Mass of Collided Powder [kg]
M_{CaCO3}	Molar Mass of Calcium Carbonate [g mol^{-1}]
M_{CaO}	Molar Mass of Calcium Oxide [g mol^{-1}]
n_r	Moles of Reactant [mol]
p	Ball Position [m]
$\dot{p}$	Ball Velocity [m s^{-1}]
$\dot{p}_0$	Initial Ball Velocity [m s^{-1}]
$\ddot{p}$	Ball Acceleration [m s^{-2}]
p_{CO2}	Partial Pressure of CO_2 [atm]
p^*_{CO2}	Partial Pressure of CO_2 in Powder Bed [atm]
p^r_{CO2}	Partial Pressure of CO_2 in Bulk Reactor [atm]
Q_u	Useful Heat [J]
R_1	Gas Constant [J mol^{-1} K^{-1}]
R_2	Gas Constant [m^3 atm K^{-1} mol^{-1}]
R_{ball}	Ball Radius [m]
R_{def}	Radius of Deformation [m]
$Rate_{node}$	Nodal Reaction Rate [mol s^{-1}]
r_0	Carbonate Particle Size [m]
r_{node}	Nodal radial position [m]
Δr	Step Size in Radial Direction [m]
$\Delta_r S^0_T$	Entropy of Reaction [J mol^{-1} K^{-1}]
T	Temperature [K]
T_{node}	Nodal Temperature [K]
T_{rm}	Room Temperature [K]
T_{rxn}	Reaction Temperature
ΔT	Change in Temperature [K]
Δt	Time Step [s]
V^r	Volume of Reactor [m^3]
V^*	Void Space of Powder [m^3]
V_{node}	Nodal Volume
$\dot{v}$	Gas Volumetric Flow Rate [m^3 s^{-1}]
v_x	Velocity in x-direction [m s^{-1}]
v_{col}	Collision velocity [m s^{-1}]
Δz	Step Size in Vertical Direction [m]
γ	Pressure Conversion Factor [Pa atm^{-1}]
η_{total}	Total Energy Efficiency
$\eta_{thermal}$	Thermal Energy Efficiency
$\eta_{product}$	Product Efficiency
κ	Thermal conductivity [W m^{-1} K^{-1}]
ν	Poisson's Ratio
ξ	Extent of Reaction [mol]
ξ_{node}	Nodal Extent of Reaction [mol]
ξ_{col}	Extent of Reaction per Collision [mol]
ξ_{50ms}	Extent of Reaction at 50 milliseconds [mol]
ρ	Density [kg m^{-3}]
σ	Intermediate Material Property Parameter
φ	Thermal Dissipation Factor

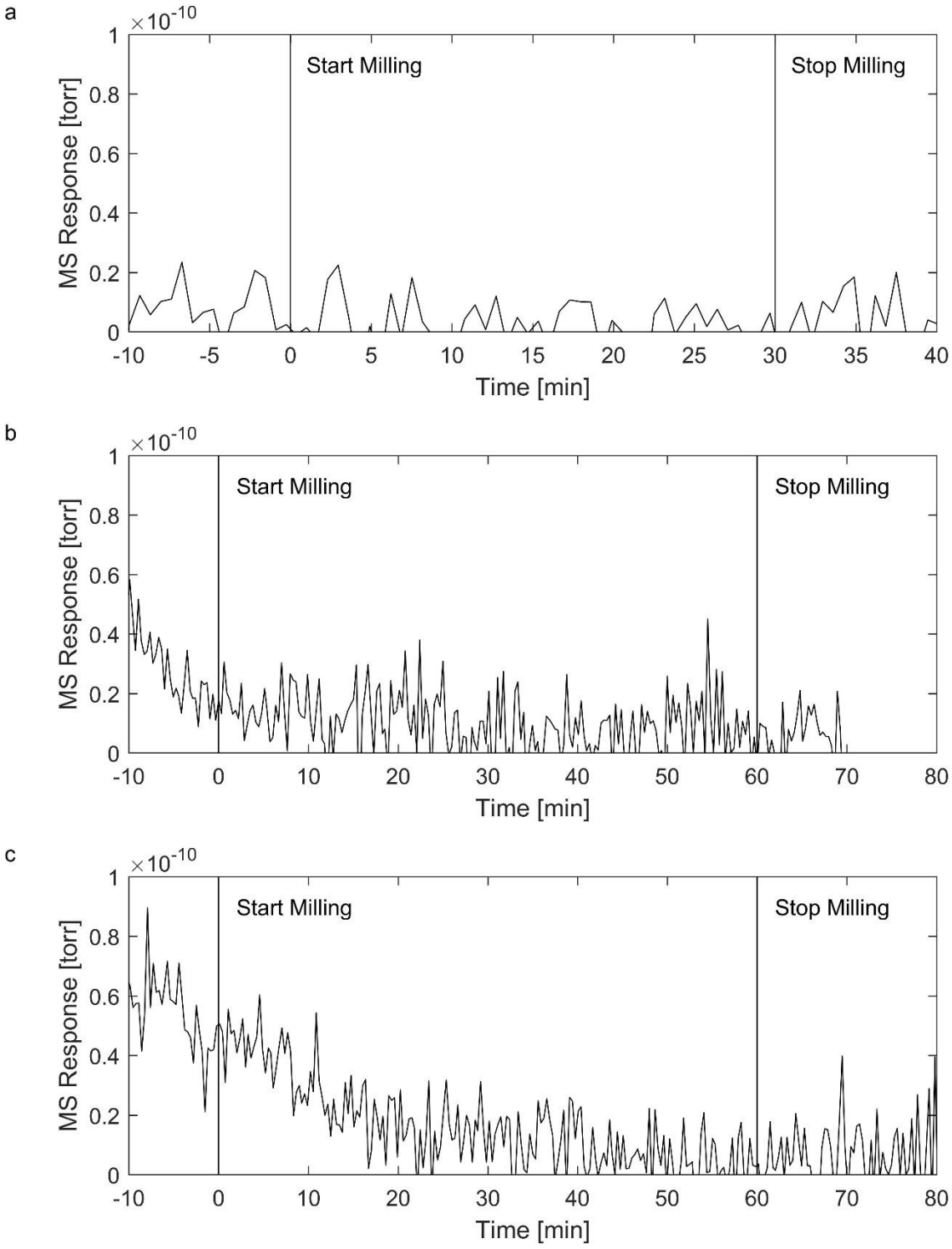

Figure B1: CO_2 response during milling of (a) SiO_2, (b) CaO, and (c) Na_2CO_3 at 30 Hz.

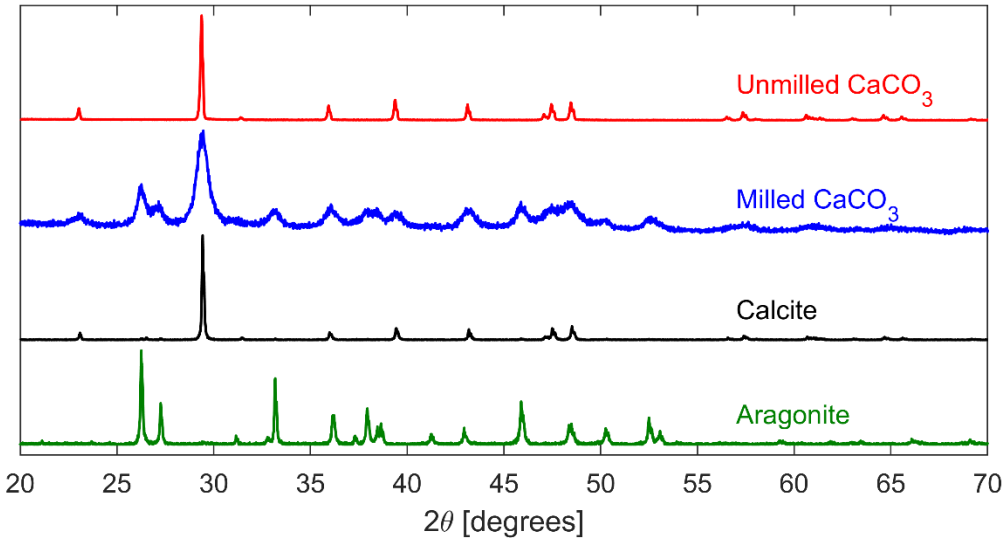

Figure B2: X-ray diffractograms of the unmilled calcium carbonate (red), calcium carbonate milled for about six hours under varying milling frequencies (blue), standard calcite[a] (black), and standard aragonite[b] (green). The milled calcium carbonate is from the same experiment depicted in Figure 12.
[a] http://rruff.info/Calcite/R040170; [b] https://rruff.info/Aragonite/R040078

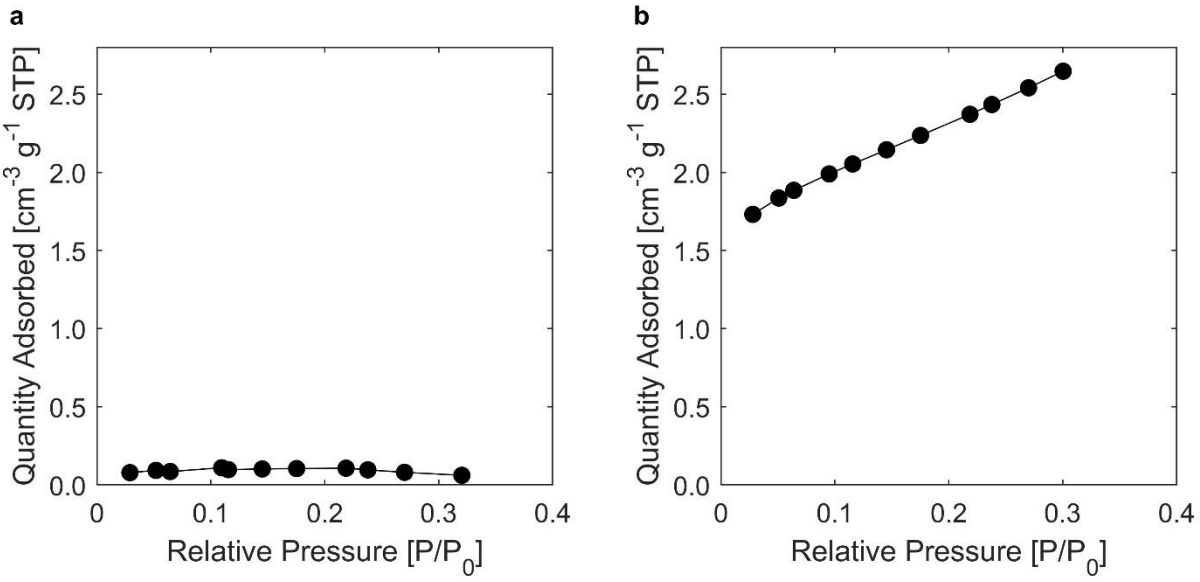

Figure B3: N_2 physisorption isotherm used to calculate BET surface area for (a) untreated calcium carbonate and (b) calcium carbonate milled for six hours.

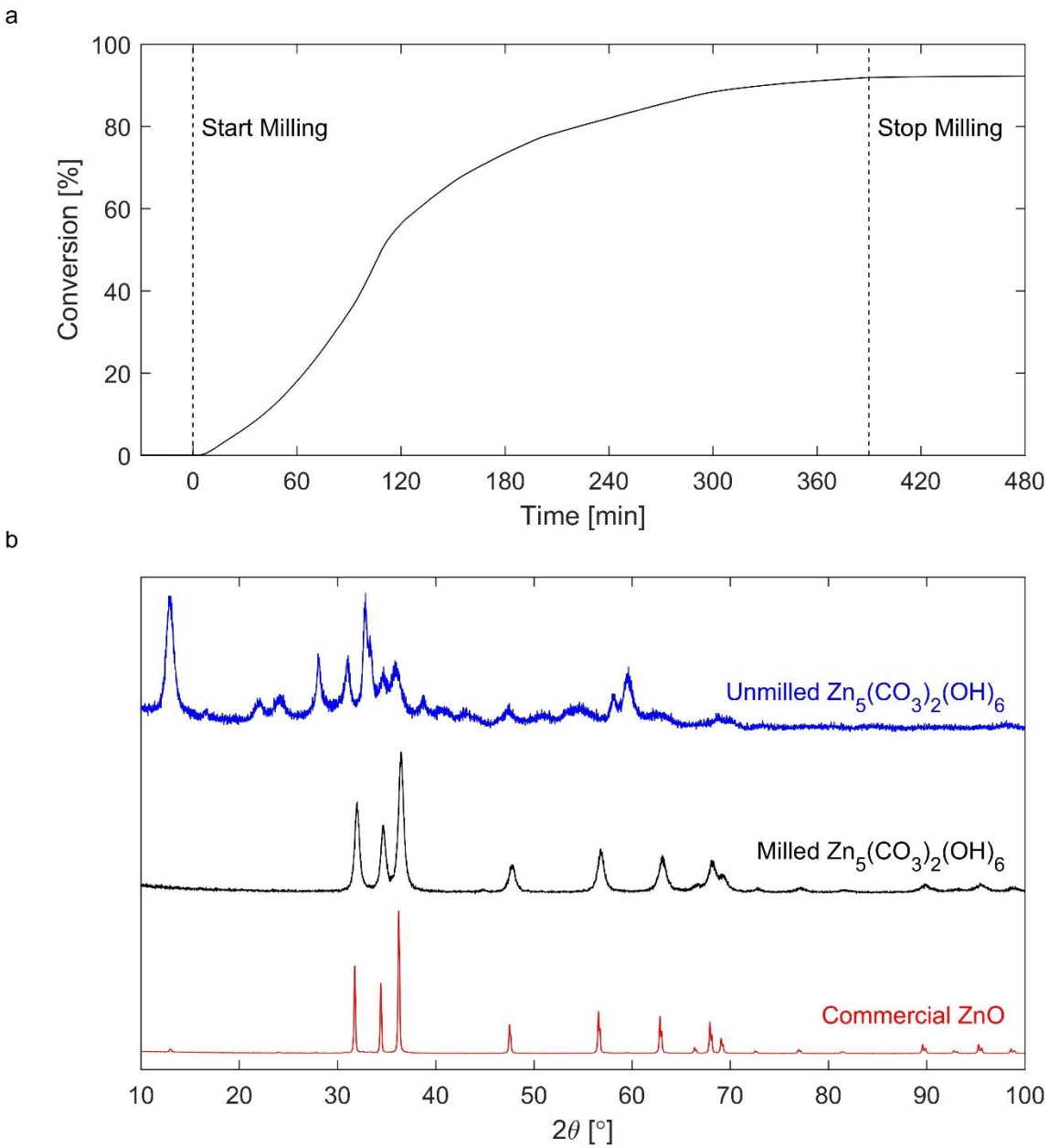

Figure B4: (a) Conversion of $Zn_5(CO_3)_2(OH)_6$ during milling at 30 Hz based on measured CO_2 rates. (b) XRD patterns for unmilled $Zn_5(CO_3)_2(OH)_2$, milled $Zn_5(CO_3)_2(OH)_2$ after 6.5 hours, and ZnO.

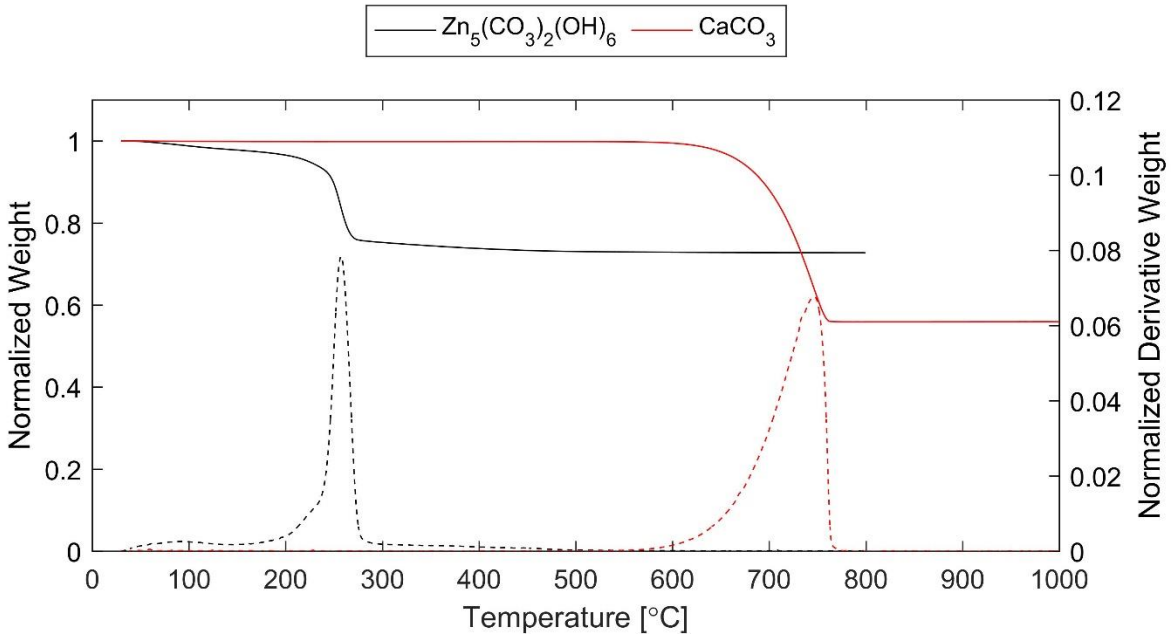

Figure B5: Normalized weight loss curve (solid) and derivative weight loss (dashed) for $Zn_5(CO_3)_2(OH)_2$ (black) and $CaCO_3$ (red) during TGA (ramp rate: 10 °C/min. gas flow: 50 sccm N_2). After ramping, temperature was held at 800 °C for 1 hour for $Zn5(CO_3)_2(OH)_6$ and 1000 °C for 1 hour for $CaCO_3$.

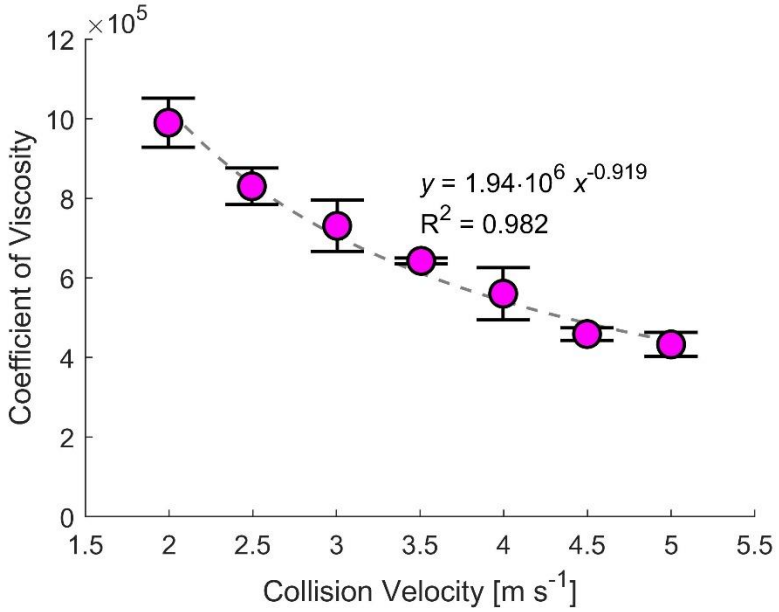

Figure B6: Results of ball drop and determination of the Coefficient of Viscosity as a function of impact velocity. The curve was fit with a power function.

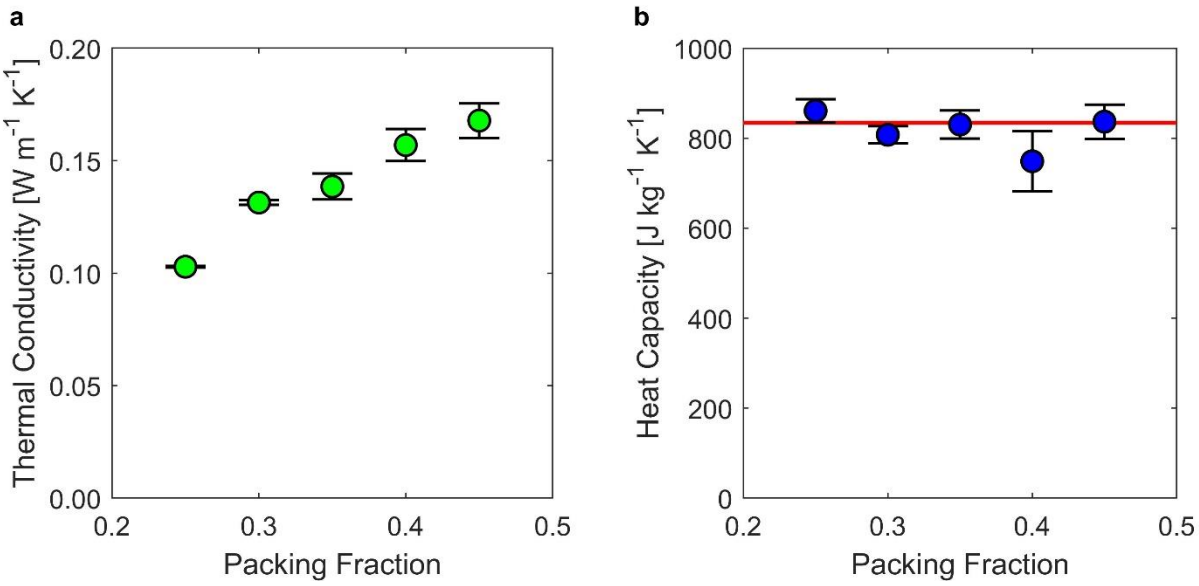

Figure B7: (a) Thermal diffusivity and (b) heat capacity of calcium carbonate powder bed as a function of packing density as determined by hot disk experiments. The literature value for the bulk heat capacity of calcium carbonate is shown at the red line.

APPENDIX C
SUPPLEMENTARY INFORMATION FOR CHAPTER 4

C.1 Detection and Quantification of Mechanochemical Ammonia

C.1.1 Colorimetry

The Berthelot reaction was utilized as a qualitative ammonia indication (Figure C1). No ammonia was detected (yellow solution) on the unmilled Ti (Table C1, Entry C-5) nor Ti milled in Ar for 6 h (Table C1, Entry C-6). Ammonia was detected (green solution) on the Ti milled in N_2 and H_2 (Table C1, Entry Ti-6).

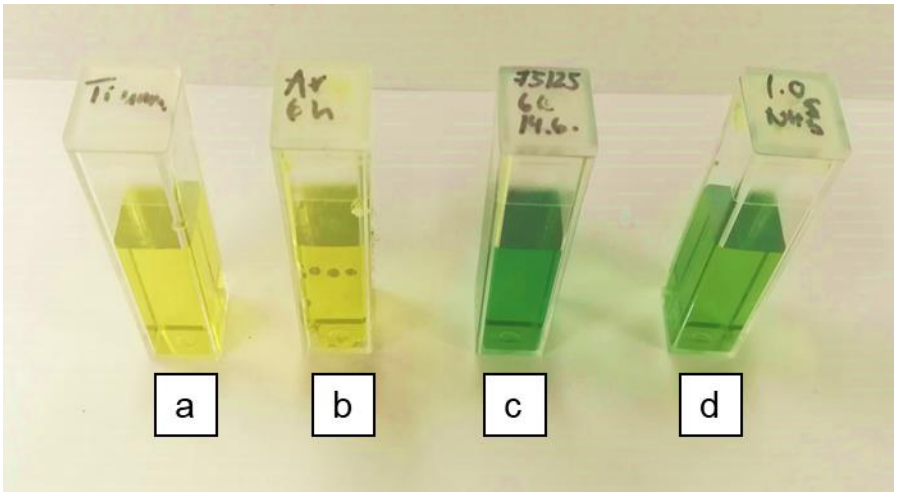

Figure C1: Use of Berthelot reaction as a qualitative analysis method. Color change from yellow to green indicates ammonia presence. (a) unmilled Ti (Experiment C-4), (b) Ti milled in Ar (Experiment C-6), (c) Ti milled in N_2 and H_2 (Experiment Ti-6), (d) 1 mg g^{-1} NH_3 standard (Hach company).

C.1.2 Mass Spectrometry

C.1.2.1 Determining Ionization Energy

Under typical operating conditions (ionization energy = 70 eV), a mass spectrometer will ionize and fragment water into *m/z* = 18 (H_2O), *m/z* = 17 (OH), and *m/z* = 16 (O). Similarly, ammonia will be ionized and fragmented to *m/z* = 17 (NH_3) and *m/z* = 16 (NH_2), resulting in overlapping signals from these two species. To deconvolute the signals, the ionization energy of

the mass spectrometer was decreased in order to not fragment the water. While sampling the headspace of pure water and aqueous ammonia (~30% NH_3, Sigma Aldrich), the mass spectrometer signal was recorded while scanning between masses *m/z* = 15 and *m/z* = 19 and ionization energies between 12 eV and 30 eV (Figure C2a-b). An ionization energy of 19 eV was selected, based on Figure C2c-d, in order to minimize the contribution from water and maximize the contribution from ammonia in signal *m/z* = 17.

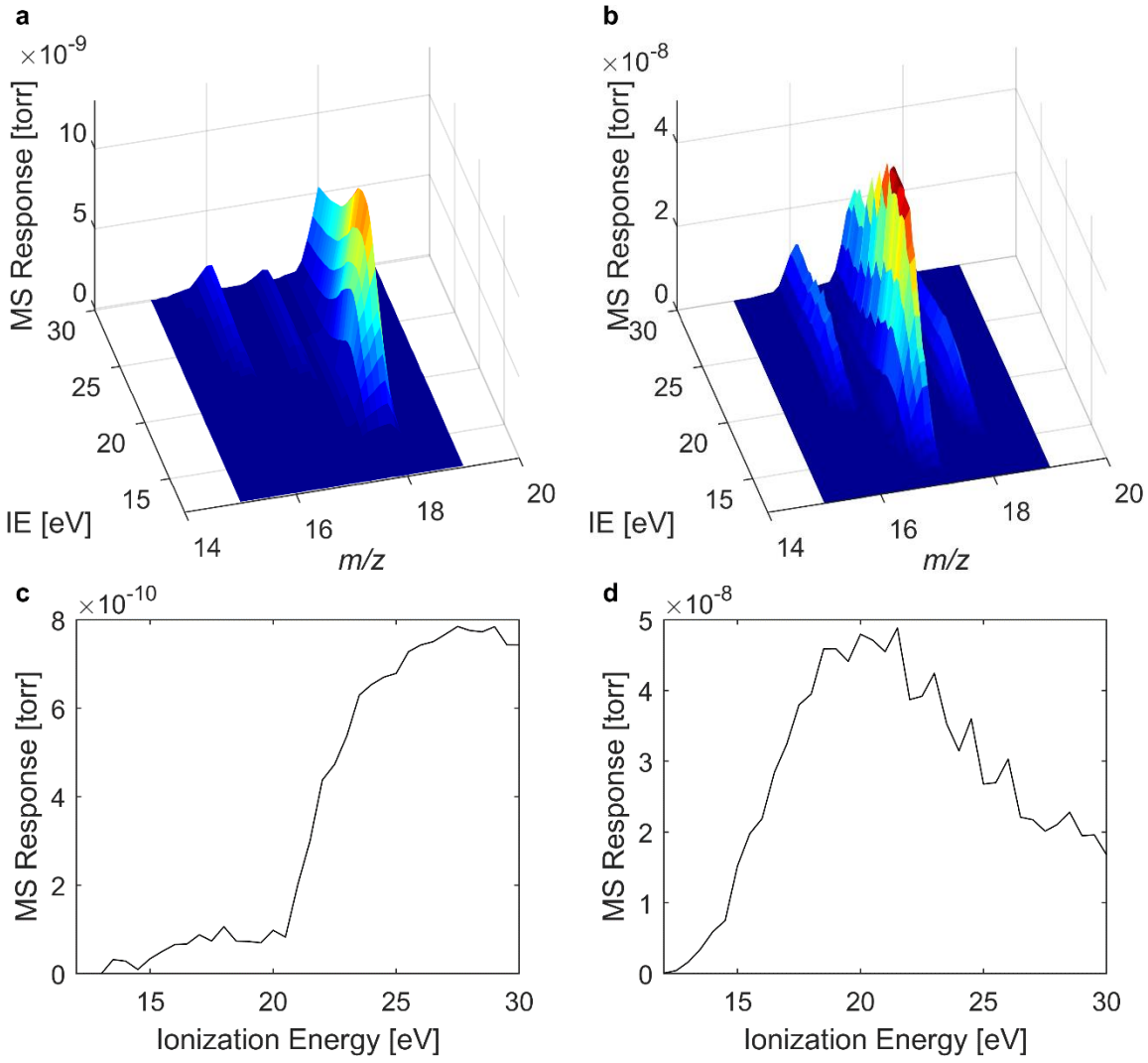

Figure C2: Mass spectrometry responses of masses from m/z = 15 to m/z = 19 and ionization energies from 12 eV to 30 eV while sampling over (a) pure water and (b) aqueous ammonia. The response profile of m/z = 17 from 12 eV to 30 eV while sampling over (c) pure water and (d) aqueous ammonia. IE = ionization energy.

C.1.2.2 Correcting for Influence of Hydrogen on the MS Signal

The presence of hydrogen in influences the background level for the *m/z* = 17 signal. Figure C3a shows the plot of the *m/z* = 17 signal versus the *m/z* = 2 signal in the presence of hydrogen and without ammonia. From this, a linear correction factor can be used to correct the ammonia signal in the presence of hydrogen. Figure C3b-d shows the full *m/z* = 2, *m/z* = 17, and correct *m/z* = 17 signal from the experiment from Figure 22. The jump in the *m/z* = 17 between 15 h and 40 h is clearly an artifact from the presence of hydrogen.

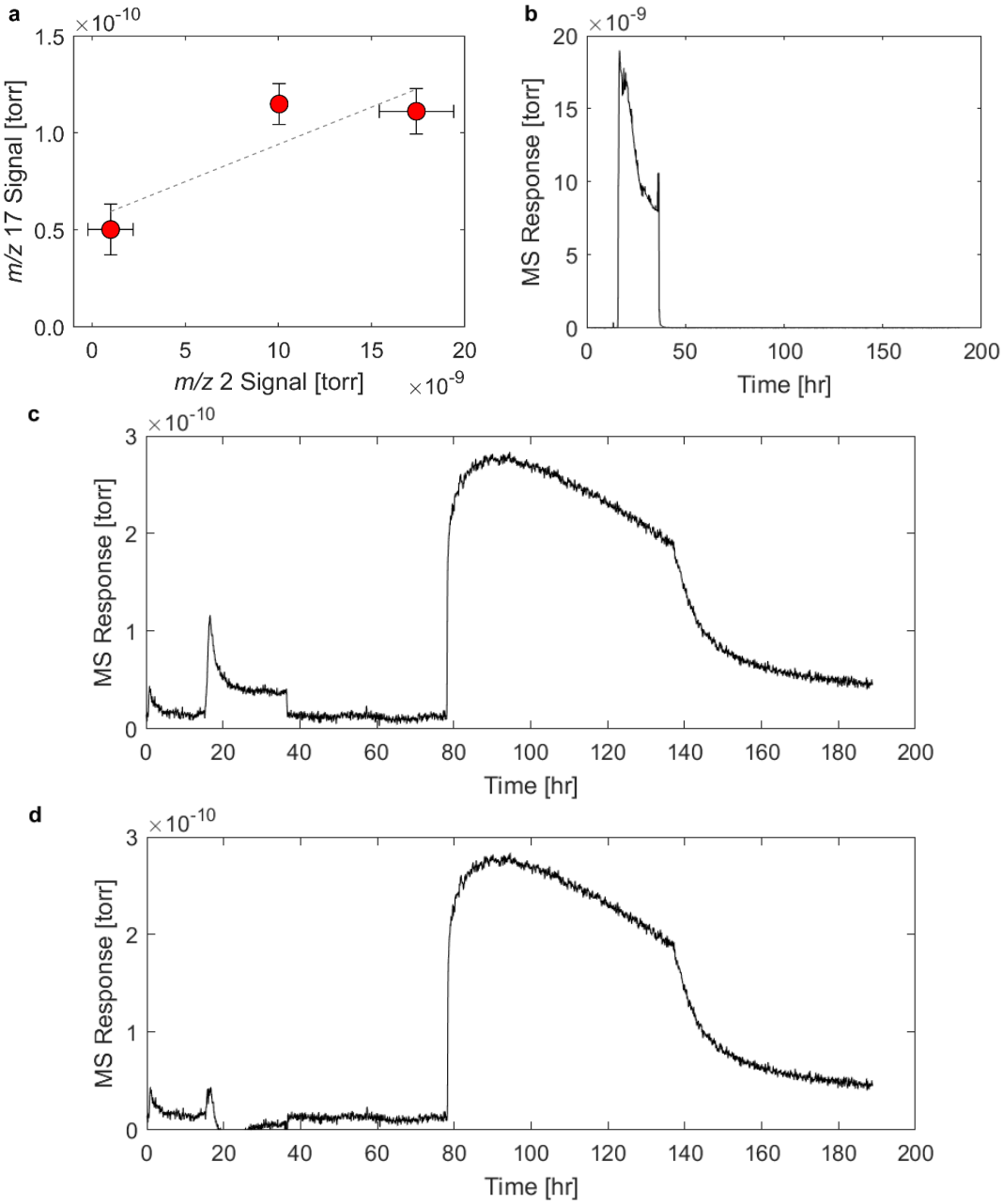

Figure C3: Hydrogen correction for ammonia MS signal. (a) Plot of m/z = 17 vs. m/z = 2 in the presence of hydrogen and without ammonia. The full mass spectrometer responses (smoothed, 3 point average) for (b) m/z = 2 and (c) m/z = 17 during the experiment described in Figure 22. (d) m/z = 17 response after correcting for the influence of hydrogen on the background signal.

C.1.2.3 Origin of the Delayed Ammonia Detection

The nearly 60 h delay between the formation of the ammonia and the eventual detection in the MS is proposed to occur primarily through an adsorption/desorption processes as the ammonia

travels away from the catalyst powder and through the reactor and effluent tubing. During and after milling, most of the catalyst remains caked onto the walls of the vessel, forming a dense powder bed (Figure C4). Unlike a traditional flow reactor where the carrier gas flows through the catalyst bed, the carrier gas in the vessel flows tangentially across the top of the catalyst bed, resulting in little flow within the bed. As such, the movement of ammonia is expected to be largely driven by diffusion, with a directional bias provided by the carrier gas. The long timescale of this process is understood through the strength of adsorption of the ammonia on the TiN surface. TPD experiments showed that ammonia desorbs around 150 °C (Appendix C.4.1). Since the ammonia has an affinity for the catalyst surface, it readsorbs while diffusing through the powder. As such, detectable amounts of ammonia do not leave the vessel until the catalyst nearest the gas exit becomes saturated. Additionally, the effluent tubing is most likely lined with fine catalyst powder that escapes during milling. The ammonia will again adsorb onto the powder and possibly the walls of the steel tubes themselves due to the low concentrations resulting in a concentration front that propagates through the tubing due to on an adsorption-based surface diffusion, providing the sharp chromatographic-like breakthrough after ~58 h. Importantly, despite possible explanations for the cause of the delay, the experiment demonstrates an orthogonal detection of ammonia.

Figure C4: Photos of the milling vessel after reaction with the Ti powder caked on the walls of the vessel.

C.1.3 Olfactory

After reaction, the ~1.98 g of catalyst not washed for IC were stored in sealed 20 mL borosilicate glass vials. After the gas phase inside the vial equilibrated (>1 week), samples milled in reactive conditions gave off a distinct ammonia smell, whereas fresh TiN and Ti as well as control samples did not smell like ammonia. Ammonia has an odor detection limit of about 50 ppm.[315]

C.1.4 Ion Chromatography and Control Experiments

The traces as measured by ion chromatography are shown in Figure C5 for the sample reacted for 12 h (Ti-8) and the unmilled titanium hydride (TiH_2-1). The absence of the smaller peak around 5.5 min in the hydride sample indicates no ammonia contamination. The peak that elutes at around 5 min results from sodium from the glassware that was used during the washing procedure.

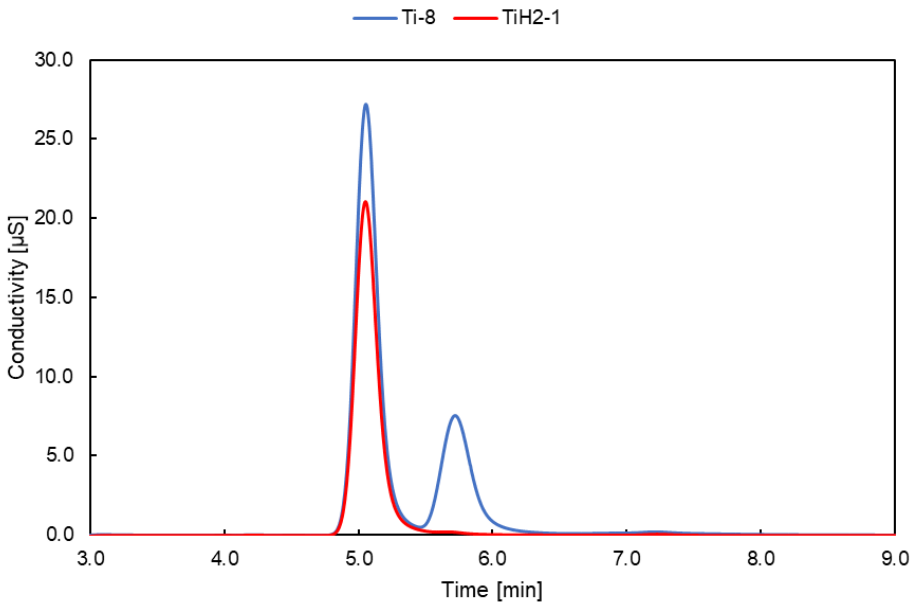

Figure C5: IC traces for the sample 12 h sample (Ti-8) and the unmilled TiH_2 (TiH_2-1). The peak around 5 min results from sodium from the glassware, the peak around 5.5 min from ammonia.

Table C1 summarizes the quantification of the IC analysis shown in Figure 2 a to c in the main article. The control experiments (Table C1 , C-7 and C-8) were performed to check for ammonia impurities from the catalyst washing procedure, namely from the glass vial for sample handling, stir bar, DI water, syringe filter and syringe, IC vial and the IC column. For this, water without catalyst was handled as described in Section 4.2.6. IC analysis of pure DI water did not indicate residual ammonia contamination. Control experiments with unmilled Ti and TiN powder were performed to check for initial contamination with ammonia, but both indicated negligible ammonia quantities. The stability of TiN in water was determined not to be a conflating issue since the ammonia content from TiN stirred in water for 9 days (C-9) was still an order of magnitude smaller than the ammonia reaction samples. For experiment C-10, titanium powder was loaded into the ball mill and exposed for 6 h to an Ar stream without turning on the mill. For experiment C-6, the conditions were the same as in C-9, but the mill was turned on (30 Hz). Experiments TiN-1 and TiN-2 were conducted by milling TiN, and experiments Ti-1 to Ti-9 by milling Ti metal. For experiments Ti-1 to Ti-5, the titanium was first milled in pure N_2 for between 1.5 h and 4.5 h, followed by milling in pure H_2 for between 1.5 h and 4.5 h. Titanium in experiments Ti-6 to Ti-9 were milled in a mixture of N_2 and H_2.

Table C1: Summary of the reactivity experiment results for Ti, TiN, TiH_2, and the control experiments (C-1 – C-12).

Experiment	Material	Frequency [Hz]	Experimental Conditions	Ammonia Yields [mg g^{-1}][a]
C-1	Fe	25	3 h in H_2 (5 sccm) + N_2 (25 sccm) + Ar (5 sccm)	n.d.[b]
C-2	Fe_3O_4	25	9 h in H_2 (5 sccm) + N_2 (25 sccm) + Ar (5 sccm)	n.d.
C-3	TiO_2	25	4.5 h in H_2 (5 sccm) + N_2 (25 sccm) + Ar (5 sccm)	n.d.
C-4	TiN	-	Unreacted[c]	0.005
C-5	Ti	-	Unreacted[c]	n.d.
C-6	Ti	30	6 h in Ar (15 sccm)	n.d.
C-7	-	-	Contamination from DI water, unreacted[d]	n.d.
C-8	-	-	Contamination from catalyst washing procedure, unreacted[e]	n.d.
C-9	TiN	0	TiN stored in water for 9 days	0.025
C-10	Ti	0	6 h in Ar (15 sccm)	n.d.
TiN-1	TiN	30	6 h in H_2 (15 sccm)	0.502 (±0.078)[f]
TiN-2	TiN	30	6 h in H_2 (7.55 sccm) + N_2 (7.5 sccm)	2.154 (±0.396)
Ti-1	Ti	30	4.5 h in N_2 (15 sccm) then 1.5 h in H_2 (15 sccm)	0.247 (±0.108)
Ti-2	Ti	30	4.5 h in N_2 (15 sccm) then 3 h in H_2 (15 sccm)	0.347 (±0.148)
Ti-3	Ti	30	4.5 h in N_2 (15 sccm) then 4.5 h in H_2 (15 sccm)	0.266 (±0.063)
Ti-3b	Ti	30	4.5 h in N_2 (15 sccm), purge with Ar (15 sccm) without milling, then mill 4.5 h in H_2 (15 sccm)	0.440
Ti-4	Ti	30	1.5 h in N_2 (15 sccm) then 4.5 h in H_2 (15 sccm)	0.021 (±0.030)
Ti-5	Ti	30	3 h in N_2 (15 sccm) then 4.5 h in H_2 (15 sccm)	0.296 (±0.172)
Ti-6	Ti	30	6 h in N_2 (7.5 sccm) + H_2 (7.5 sccm)	0.490 (±0.091)
Ti-7	Ti	30	9 h in N_2 (7.5 sccm) + H_2 (7.5 sccm)	1.029 (±0.398)
Ti-8	Ti	30	12 h in N_2 (7.5 sccm) + H_2 (7.5 sccm)	2.556 (±0.403)
Ti-9	Ti	30	6 h in N_2 (11.25 sccm) + H_2 (3.75 sccm)	0.662 (±0.215)
TiH_2-1	TiH_2	-	Unreacted[c]	n.d.

[a] Average yield as determined by IC (based on mass of catalyst after the reaction); [b] n.d. = not detected with IC; [c] Unreacted Ti, TiN, and TiH_2 were treated the same way as the reacted samples to check for impurities on the catalyst surface prior to reaction.; [d] Pure DI water was analyzed with IC; [e] Pure DI water was treated the same as catalyst washing water to check for contamination during the washing process; [f] Standard deviation based on the three runs

The reaction of TiH_2 with N_2 (Sample TiH_2-2) did produce a significant amount of ammonia. Importantly though, the TiH_2 was converted to TiN during this reaction (Appendix C.2.3). Some of the ammonia is expected to be formed as a direct byproduct of the conversion of TiH_2 to TiN. Additionally, H_2 was also expected to be a byproduct, indicating that ammonia formation may be a catalytic reaction over the newly formed TiN.

C.2 Catalyst Characterization

C.2.1 X-ray Diffraction for Ti milled in Argon

XRD was performed with Ti milled for 1, 2, and 6 h in Ar (Figure C6) to show that the TiN formation is not induced by reaction with N_2 in air by sample handling after the reaction. The XRD in Figure C6 shows that the sample remain pure Ti and no reaction with ambient N_2 occurs.

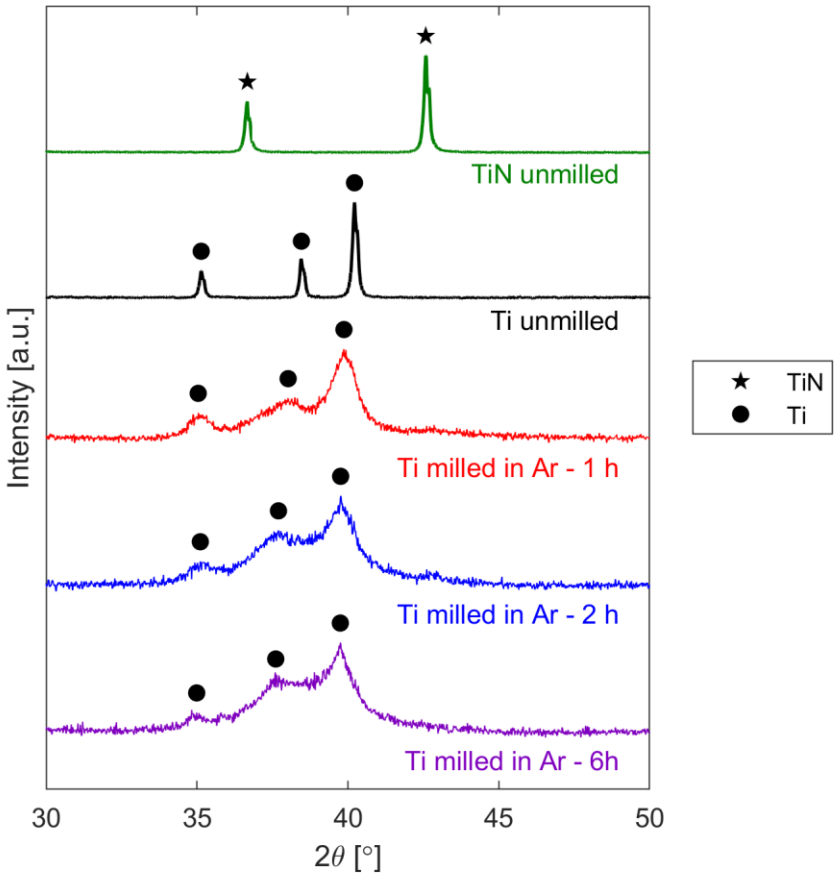

Figure C6: XRD for control experiments of Ti milled in Ar. X-Ray diffractograms for unmilled TiN (green), unmilled Ti (black), and Ti milled samples for 1 h (red), 2 h (blue) and 6 h (purple) at 30 Hz in 15 sccm pure Argon. Black stars indicate TiN associated peaks, black circles indicate Ti associated peaks.

C.2.2 XPS of Milled Ti

X-ray photoelectron spectroscopy (XPS) was performed on Ti milled in Ar for 6 h and Ti milled in N_2 for 6 h (Figure C7) to check for potential contamination of Fe from the milling vessel. No Fe was detected in either sample (binding energies ~ 700 – 750 eV, as indicated with the dashed line). The limit of detection for the instrument is ~1 mol%. The presence of oxygen is due surface oxidation of the sample when exposed to air after the reaction.

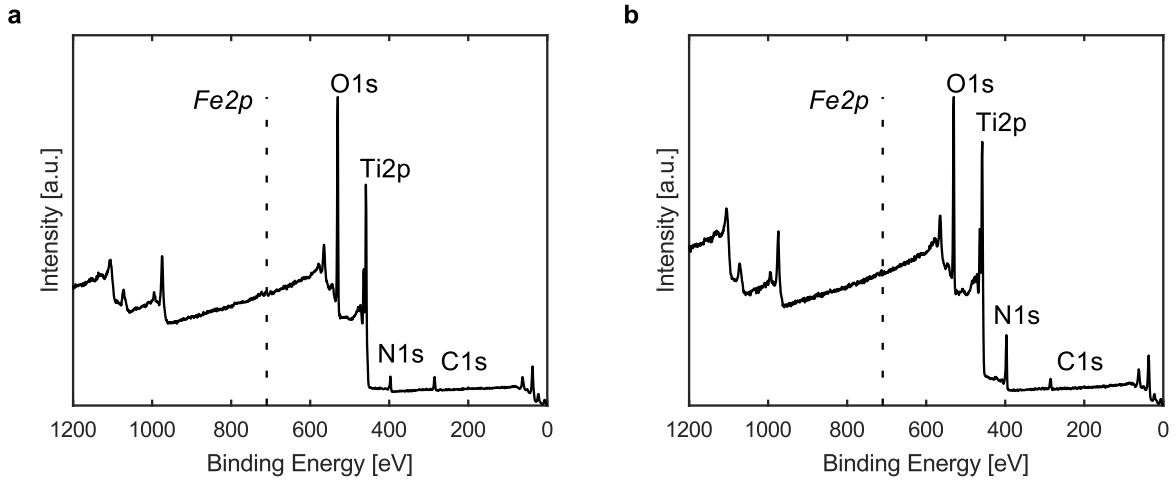

Figure C7: XPS spectra for titanium milled in (a) Ar and in (b) N_2. Milling was performed at 30 Hz for 6 h in a gas flow of 15 sccm for both samples. Peak assignment were determined by the XPS instrument software (Avantage software package v.5.957 by Thermo Scientific).

C.2.3 Formation of Titanium Hydride

XANES spectra were also collected for titanium hydride, titanium powder milled in hydrogen, and titanium powder milled under reactive conditions (nitrogen and hydrogen) (Figure C8). The titanium powder milled in hydrogen clearly showed titanium hydride characteristics, especially in the edge features, supporting the formation of titanium hydride during milling in the presence of N_2 and H_2. Linear combination fitting with the spectra of titanium milled in just nitrogen and titanium milled in just hydrogen was used to approximate composition of nitride and hydride in the titanium samples milled in reactive conditions (Figure C9). From this, the titanium milled a 1:1 N_2:H_2 mixture consisted of 68% nitride and 29% hydride, while the titanium milled in a 3:1 N_2:H_2 mixture was 74% nitride and 23% hydride. The weights were not constrained to add up to 100%.

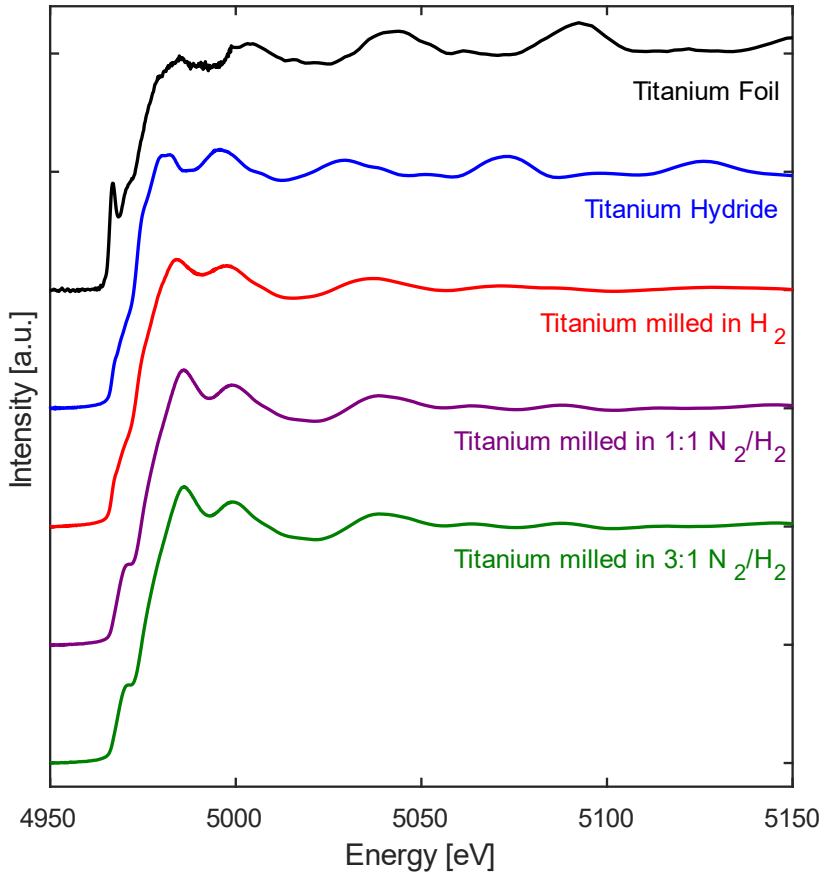

Figure C8: X-ray absorption spectra for the Ti K-Edge for titanium hydride formation. Titanium foil (black), titanium hydride (blue), titanium powder milled in hydrogen (red), titanium powder milled in a 1:1 N_2:H_2 mixture of nitrogen and hydrogen (purple), and titanium powder milled in a 3:1 N_2:H_2 mixture of nitrogen and hydrogen (green).

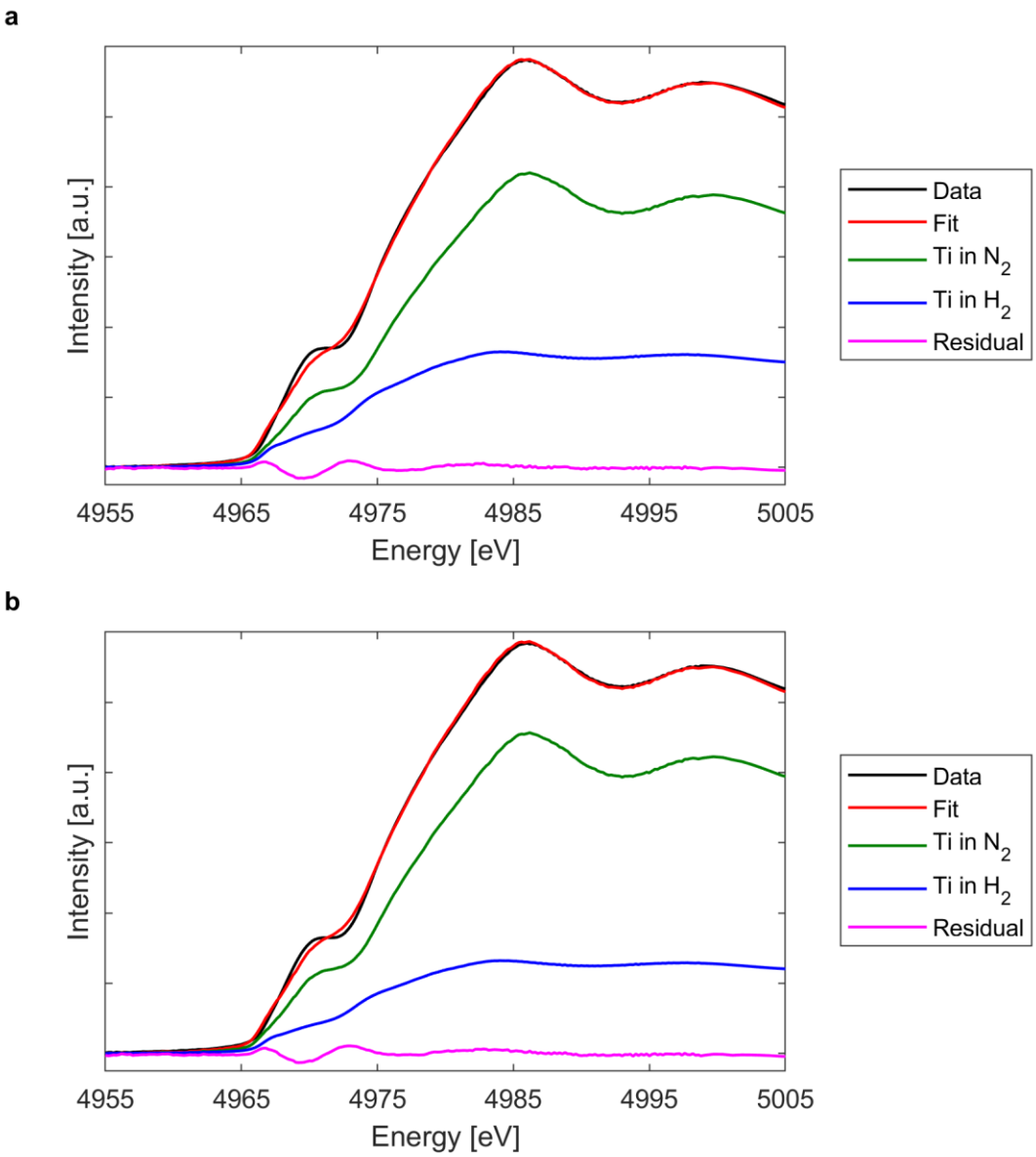

Figure C9: Linear fitting of mechanochemical synthesized TiN and TiH_2 to Ti milled in N_2 and H_2. XANES spectra of (a) titanium milled in a 1:1 N_2:H_2 mixture and (b) titanium milled in a 3:1 N_2:H_2 mixture (black). Linear combination fitting (red) was performed with XANES data from titanium milled in pure N_2 (green) and titanium milled in pure H_2 (blue). Purple marks the residual of the fit.

The ability to synthesize titanium hydride by ball milling titanium in H_2 is an established phenomenon.[316] XRD confirmed the synthesis of titanium hydride (TiH_2) from titanium metal via milling in H_2 using the current experimental set-up (Figure C10). The hydridation reaction also seems to occur much more rapidly than the nitridation reaction (1.5 h compared to 4.5 h). The

presence of TiN peaks in the diffractogram of Ti milled in H_2 may have resulted from residual N_2 in the vessel or the tubing when milling began. Commercial TiH_2 milled in N_2 for 6 h was nearly completely converted to TiN. However, the TiN milled in H_2 and in an N_2 and H_2 mixture showed no presence of a hydride phase. So, when Ti is milled in N_2 and H_2, TiH_2 is expected to form initially, but then react with N_2 to form TiN at extended reaction times. Additionally, the stability of TiN over TiH_2 suggests that ammonia synthesis via a TiN mechanism should dominate (Figure 23b).

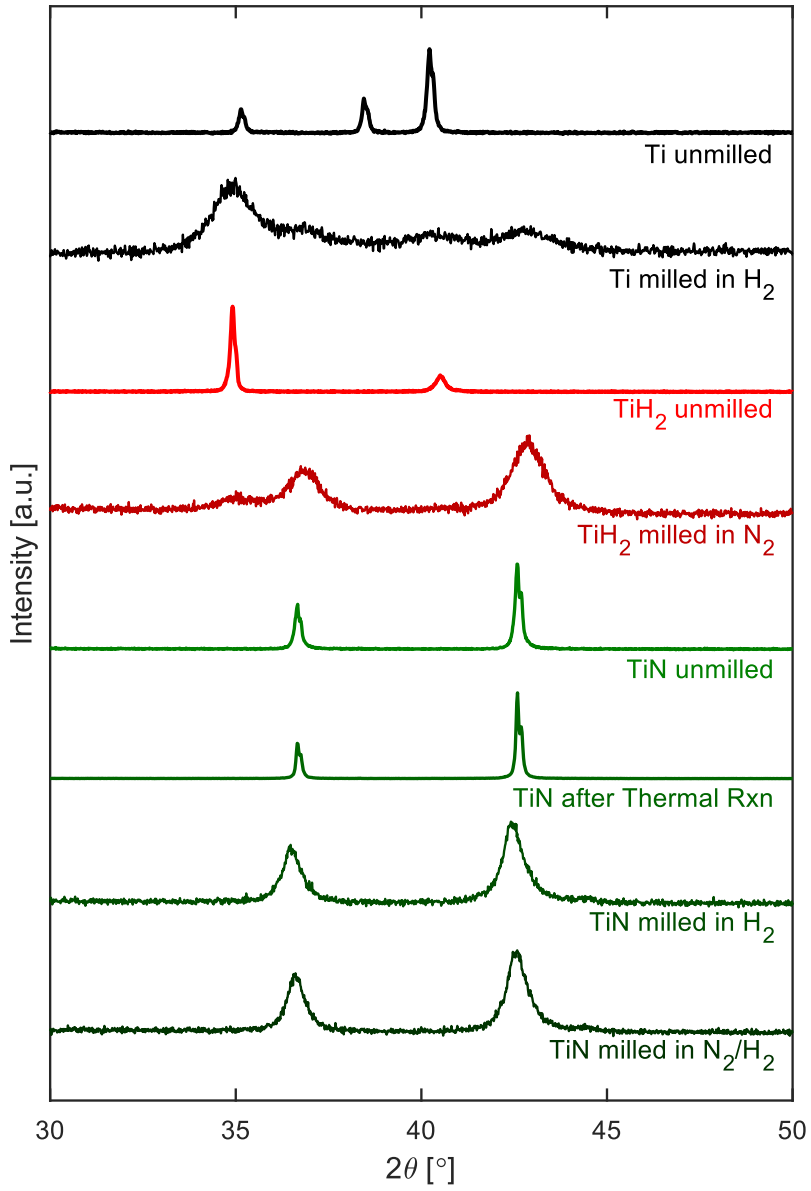

Figure C10: X-ray diffractograms of unmilled Ti powder, Ti milled in H_2 for 1.5 h, unmilled TiH_2 powder, TiH_2 milled in N_2 for 6 h, unmilled TiN powder, TiN after thermal reaction, TiN milled in H_2 for 4.5 h, and TiN milled in N_2 and H_2 for 4.5 hr.

C.3 Thermodynamics of the Local Reaction

C.3.1 Local Ammonia Formation Rate

The overall catalytic ammonia rate can be approximated by taking the slope of a linear fit for the yields of Ti milled in N_2 and H_2 (1:1 v/v) for 6 h, 9 (Table C1, Ti-6 to Ti-8).

$$Overall\ Rate = 5.62 \cdot 10^{-6} \frac{mmol_{NH_3}}{g_{TiN} \cdot s} \quad \text{(C1)}$$

While each experiment started with 2.0 g Ti, after being converted to TiN during milling, the actual total mass of catalyst in the system is assumed to be 2.59 g TiN. In combination with the assumption that there are two collisions per cycle (30 Hz → 60 collisions s^{-1}), a yield per collision can be calculated.

$$2.0\ g\ Ti \times \frac{61.9 \frac{g}{mol} TiN}{47.9 \frac{g}{mol} Ti} = 2.59\ g\ TiN \quad \text{(C2)}$$

$$Yield\ per\ Collision = \frac{5.62 \cdot 10^{-6} \frac{mmol_{NH_3}}{g_{TiN} \cdot s} \times 2.59\ g\ TiN}{60 \frac{collisions}{s}} = 2.42 \cdot 10^{-7} \frac{mmol_{NH_3}}{collision} \quad \text{(C3)}$$

In order to approximate the local reaction rate, the vessel and collision properties will be used from previous work (Section 3.5.1.1).[238]

$$Vessel\ Area: 4.3 \cdot 10^{-3}\ m^2$$

$$Collision\ Radius: 8.9 \cdot 10^{-4}\ m$$

$$Collision\ Area: 2.5 \cdot 10^{-6}\ m^2$$

As Figure C4 shows, the catalyst powder is approximately uniformly distributed on the vessel surface. Therefore, the fraction of collision area to the vessel area is the same as the collided (active) catalyst mass to the total mass. Similarly, the time the catalyst stays active will be similar to how long the material in our previous work stayed thermally active.[238]

$$Active\ Mass = 2.59\ g_{TiN} \times \frac{2.5 \cdot 10^{-6}\ m^2}{4.3 \cdot 10^{-3} m^2} = 1.47 \cdot 10^{-3}\ g_{TiN,Active} \quad \text{(C4)}$$

$$Active\ Time = 10^{-2} s$$

From these assumptions and the yield per collision, the local reaction rate can be calculated.

$$Local\ Reaction\ Rate = \frac{2.42 \cdot 10^{-7} \frac{mmol_{NH_3}}{collision}}{1.47 \cdot 10^{-3} \frac{g_{TiN,Active}}{collision} \times 10^{-2} s} = 1.64 \cdot 10^{-2}\ \frac{mmol_{NH_3}}{g_{TiN,Active} \cdot s} \quad \text{(C5)}$$

C.3.2 Consideration of Thermodynamics

Before assessing in which equilibrium regime the reaction lays, the equilibrium partial pressures between NH_3, N_2, and H_2 need to calculated for a given temperature (T).

$$\frac{1}{2} N_2 + \frac{3}{2} H_2 \rightarrow NH_3 \quad \text{(C6)}$$

$$\frac{P_{NH_3}}{P_{N_2}^{0.5} \times P_{H_2}^{1.5}} = K_{eq,T} = \exp\left(-\frac{\Delta G_{rxn,T}}{R \cdot T}\right) \quad \text{(C7)}$$

The Gibbs free energy of reaction at a given temperature was calculated using values and correlations from NIST, specifically for the $(H_T^o - H_{298}^o)$ and S_T^o terms.

$$\Delta G_{rxn,T}^o = \Delta H_{rxn,T}^o - T \Delta S_{rxn,T}^o \quad \text{(C8)}$$

$$\Delta G_{rxn,T}^o = \left(H_{NH_3,T}^o - H_{NH_3,298}^o\right) - \frac{1}{2}\left(H_{N_2,T}^o - H_{N_2,298}^o\right) - \frac{3}{2}\left(H_{H_2,T}^o - H_{H_2,298}^o\right)$$
$$-T\left(S_{NH_3,T}^o - \frac{1}{2} S_{N_2,T}^o - \frac{3}{2} S_{H_2,T}^o\right) + \Delta G_{rxn,298}^o + T_{298} \Delta S_{rxn,298}^o \quad \text{(C9)}$$

Next, the equilibrium partial pressure ratio is written in terms of the final NH_3 partial pressure, where $P_{N_2}^o$ and $P_{H_2}^o$ are the initial partial pressures of nitrogen and hydrogen and $y_{N_2}^o$ and $y_{H_2}^o$ are the initial mole fractions of nitrogen and hydrogen. The last two terms are necessary to account

for an open system where additional N_2 and H_2 make up the pressure decrease from the formation of NH_3. (The values for P^0_{N2} and P^0_{H2} come from the experimental conditions.)

$$K_{eq,T} = \frac{P_{NH_3,Equi}}{\left(P^o_{N_2} - \frac{1}{2}P_{NH_3,Equi} + y^o_{N_2}P_{NH_3,Equi}\right)^{0.5}\left(P^o_{H_2} - \frac{3}{2}P_{NH_3,Equi} + y^o_{H_2}P_{NH_3.Equi}\right)^{1.5}} \qquad \text{(C10)}$$

$$P^0_{N_2} = 0.5$$

$$P^0_{H_2} = 0.5$$

$$y_{NH_3,Equi} = \frac{P_{NH_3,Equi}}{P_{total}} \qquad \text{(C11)}$$

Next, a numerical root finding algorithm, in this case *fmincon* in Matlab, is used to calculate the equilibrium partial pressure (and mole fraction) of ammonia.

For determining the estimated mole fraction of ammonia, the quantity of ammonia is determined by the rate per collision and the volume of gas as the void space of the impacted catalyst. The packing fraction is assumed to be "random close-packed spheres".

$$Packing\ Fraction: 0.625\,\frac{m^3_{TiN}}{m^3}$$

$$Collided\ (Active)\ Mass: 1.14 \cdot 10^{-6}\ kg_{TiN}$$

$$Volume\ of\ TiN = 1.14 \cdot 10^{-6} kg_{TiN} \times \frac{m^3_{TiN}}{5400\ kg_{TiN}} = 2.11 \cdot 10^{-10}\ m^3_{TiN}$$

$$Volume\ of\ Void\ Space = \frac{2.11 \cdot 10^{-10}\ m^3_{TiN}}{0.625\,\frac{m^3_{TiN}}{m^3}} \times 0.375\,\frac{m^3_{void}}{m^3} = 1.3 \cdot 10^{-10} m^3_{void}$$

From here, the estimated mole fraction of ammonia can be calculated at a given temperature. The moles of ammonia is determined from the yield per collision.

$$y_{NH_3,Est} = \frac{2.42 \cdot 10^{-10}\ mol_{NH3}}{\left(\frac{101325\ Pa \times 1.3 \cdot 10^{-10}\ m^3}{8.314 \frac{m^3 \cdot Pa}{mol \cdot K} \times T}\right)} \quad \text{(C12)}$$

Figure 23a shows the mole fraction curves over a range of temperatures. The only feasible temperatures for a process where nitrogen is activated and ammonia is formed simultaneously are where $y_{NH_3,Equi}$ is greater than or equal to $y_{NH_3,Est}$ which has an upper limit of 230 °C, corresponding to an approximate mole fraction of 0.06. As shown below (Appendix C.4.2), TiN show has no measurable catalytic activity below 600 °C. Therefore, the most reasonable explanation is that the collision creates a dynamic environment where the N_2 dissociation and ammonia formation step occur is thermodynamically district conditions.

C.4 Detection of Thermal Ammonia

C.4.1 Ammonia Temperature Programmed Desorption on TiN

NH_3-TPD experiments were performed in order to get an information on the strength of ammonia binding on the TiN surface. Figure C11 shows peak desorption occurs around 150 °C. The low signal-to-noise-ratio prevented quantification of the adsorbed amount of ammonia with the current setup.

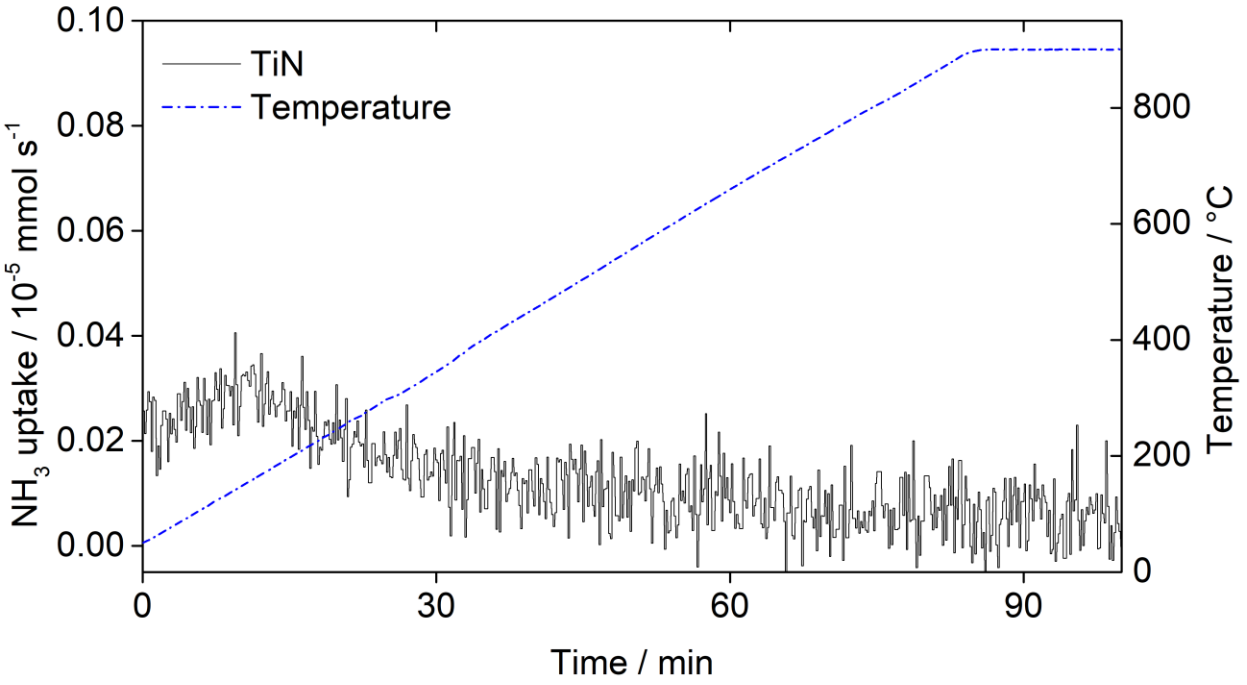

Figure C11: Ammonia TPD of Commercial Titanium Nitride. Fresh TiN was pretreated with N_2 at 600°C and then NH_3 in N_2 at room temperature was flushed over the catalyst. The TiN was then heated with an N_2 stream till 900 °C. Adsorbed ammonia was detected at 150 °

C.4.2 Thermal Reactivity and Catalytic Activity of TiN

The feasibility of TiN for gas phase ammonia synthesis was investigated first thermally. Experiments under constant argon (AirLiquide, 99.999%) atmosphere with a linear heating ramp show that small ammonia peaks appear at 230 °C and 700 °C (Figure C12). The initial ammonia production is attributed to the reaction of TiN with surface water, as evidenced by the run with only argon (green curve). The three runs in H_2 (AirLiquide, 99.999%) show approximately the same total amount of ammonia formation (red, black and purple curve). The TiN reheated in H_2 (blue curve) showed essentially no additional ammonia formation, suggesting depletion of the reactive nitride.

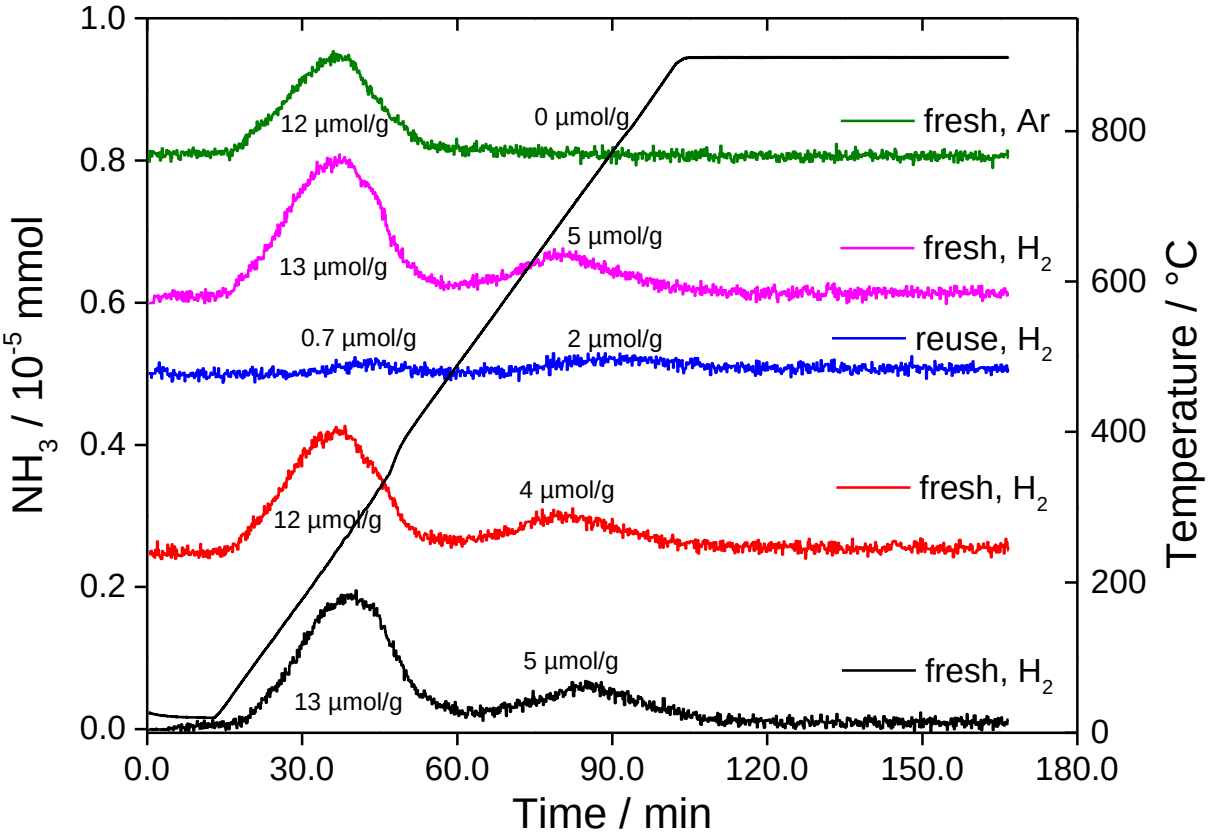

Figure C12: Thermal Reduction of TiN towards ammonia. Fresh TiN was investigated in a pure argon stream (green curve) and three times in a hydrogen stream (purple, red and black curve) to identify adsorbed catalytic active species at 230 °C and 700 °C. Reuse of a previous hydrogenated TiN (blue curve) show no more ammonia formation. The offset of the different profiles correlates to their corresponding baseline.

To gain more detailed insights into the difference between catalytic and thermally induced ammonia production, the temperature was increased stepwise from 600 °C to 900 °C (Figure C13). Comparing the ammonia yields from the pre-treated catalyst (in Ar at same temperature) and without any catalyst, it was obvious that TiN is responsible for a significantly increased ammonia production and also enables ammonia formation at slightly lower temperatures. Hence, TiN definitely enables a thermal catalytic reaction to produce ammonia from nitrogen (AirLiquide, 99.999%) and hydrogen. Notably, under these thermal conditions, the rate of ammonia production

is $5 \cdot 10^{-5}$ $mmol_{NH3}$ g^{-1}_{TiN} s^{-1}, whereas the local reaction rate via mechanocatalysis (Appendix C.3.1) is 10^{-2} $mmol_{NH3}$ g^{-1}_{TiN} s^{-1}, three orders of magnitude higher.

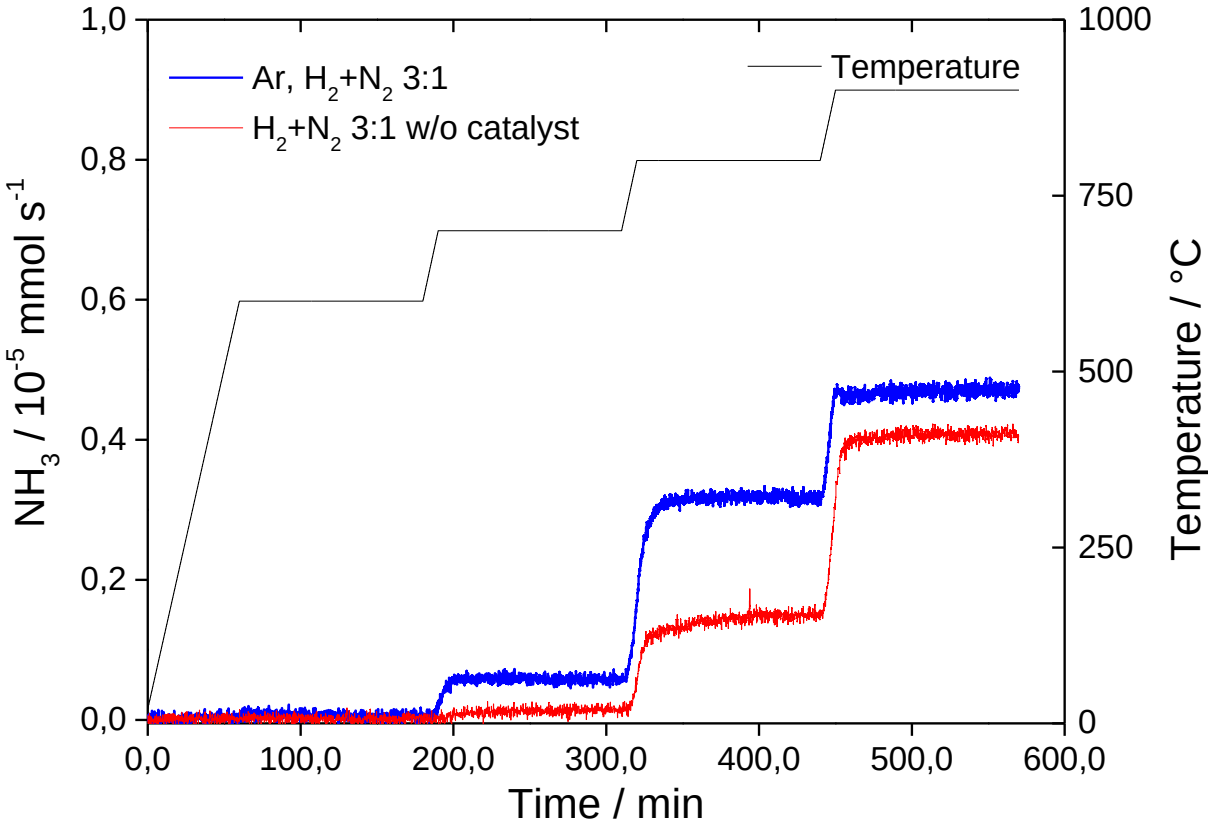

Figure C13: The stepwise increase of the temperature (black curve) without (red curve) and with TiN (blue curve) show an increased ammonia formation which is catalyzed by TiN. No ammonia formation is observed below 600 °C.

C.5 Energy Intensity and Preliminary Technoeconomic Calculations

C.5.1 Lab Scale Energy Efficiency

The lab scale energy efficiency of the process can be calculated using the total ammonia rate as determined in Appendix C.3.1, reaction time, and ball mill power rating.

$$Overall\ Rate: 5.62 \cdot 10^{-6} \frac{mmol_{NH_3}}{g_{TiN} \cdot s}$$

$$Catalyst\ Mass: 2.59\ g_{TiN}$$

$$Power\ Rating: 150\ W$$

$$Energy\ Efficiency = \frac{150\ W}{5.62 \cdot 10^{-6} \frac{mmol_{NH_3}}{g_{TiN} \cdot s} \times 2.59\ g_{TiN}} = 1.67 \cdot 10^7\ \frac{kJ}{mol} \sim 10^7\ \frac{kJ}{mol} \qquad \text{(C13)}$$

C.5.2 Preliminary Technoeconomic Analysis

Comer *et. al.* laid out several metrics to determine if a process could be feasible for distributed ammonia synthesis.[219] First, on average, farms consume $100\ \frac{kg_N}{hectare \cdot yr}$. For processes that will be solar powered, the power use should require only 1% of land dedicated to solar panels ($100\ \frac{m^2}{hectare}$), with an average solar flux of $200\ \frac{W}{m^2}$. This would require a solar energy efficiency of $8.83 \cdot 10^4\ \frac{kJ}{mol_N}$.

At lab scale, ammonia production would not be remotely economically viable. However, energy efficiency is expected to increase with larger ball mill,[317] so the specifications of a small industrial ball is used.[260]

$$Dimensions: 3ft\ diameter, 6\ ft\ length$$

$$Volume: 1.2\ m^3$$

$$Total\ Charge\ Loading: 50\%$$

$$Power\ Rating: 13.0\ kW$$

To get the total catalyst loading in the ball mill, both the balls and the catalyst powder as assumed to have packing fractions of "randomly close-packed spheres" (0.625).

$$Total\ Charge\ Volume = 0.5 \times 1.2\ m^3 = 0.6\ m^3$$

$$Bulk\ TiN\ Density = 5400\ \frac{kg}{m^3} \times 0.625 = 3376\ \frac{kg}{m^3}$$

$$Bulk\ TiN\ Volume = 0.6\ m^3 \times (1 - 0.625) = 0.225\ m^3$$

$$Catalyst\ Mass = 0.225\ m^3 \times 3376 \frac{kg}{m^3} = 759\ kg \sim 10^3\ kg$$

If the overall ammonia production rate is assumed to be constant when the system is scaled up, the scaled-up energy efficiency can be calculated. The milled is assumed to be operated by solar power ($200 \frac{W}{m^2}$ solar radiation, 20% solar conversion efficiency),[219] and with an average daily operating time of $12 \frac{h}{day}$.

$$Electric\ Energy\ Efficiency\ (\eta_{el}) = \frac{1.30 \cdot 10^4\ W}{5.62 \cdot 10^{-6} \frac{mmol_{NH_3}}{g_{TiN} \cdot s} \times 7.59 \cdot 10^5\ g_{TiN}} = 3.06 \cdot 10^3 \frac{kJ}{mol} \sim 10^3 \frac{kJ}{mol} \quad \text{(C14)}$$

$$Solar\ Energy\ Efficiency\ (\eta_{sol}) = \frac{\eta_{el}}{0.2} = 1.53 \cdot 10^4 \frac{kJ}{mol} \sim 10^4 \frac{kJ}{mol} \quad \text{(C15)}$$

$$Operating\ Time = 12 \frac{h}{day} \times 3600 \frac{s}{h} \times 365 \frac{day}{yr} = 1.58 \cdot 10^7 \frac{s}{yr} \quad \text{(C16)}$$

$$Ammonia\ Production\ Rate = 5.62 \cdot 10^{-6} \frac{mmol_{NH_3}}{g_{TiN} \cdot s} \times 17.03 \frac{g_{NH_3}}{mol_{NH_3}} \times 7.59 \cdot 10^5\ g_{TiN} \times 1.58 \cdot 10^7 \frac{s}{yr} = 1146 \frac{kg_{NH_3}}{yr} \sim 10^3 \frac{kg_N}{yr} \quad \text{(C17)}$$

A typical solar panel (18 ft^2 ~ 1.67 m^2) can be expected to have a power output of 65 W (same $200 \frac{W}{m^2}$ solar radiation and 20% efficiency), so 200 solar panels (335 m^2) would be needed to power the mill. A mill of this size could be reasonably used to produce fixed nitrogen for a 10-hectare farm with just 0.34% of land dedicated to solar energy production.

APPENDIX D
SUPPLEMENTARY INFORMATION FOR CHAPTER 5

D.1 Fresh Catalyst Characterization

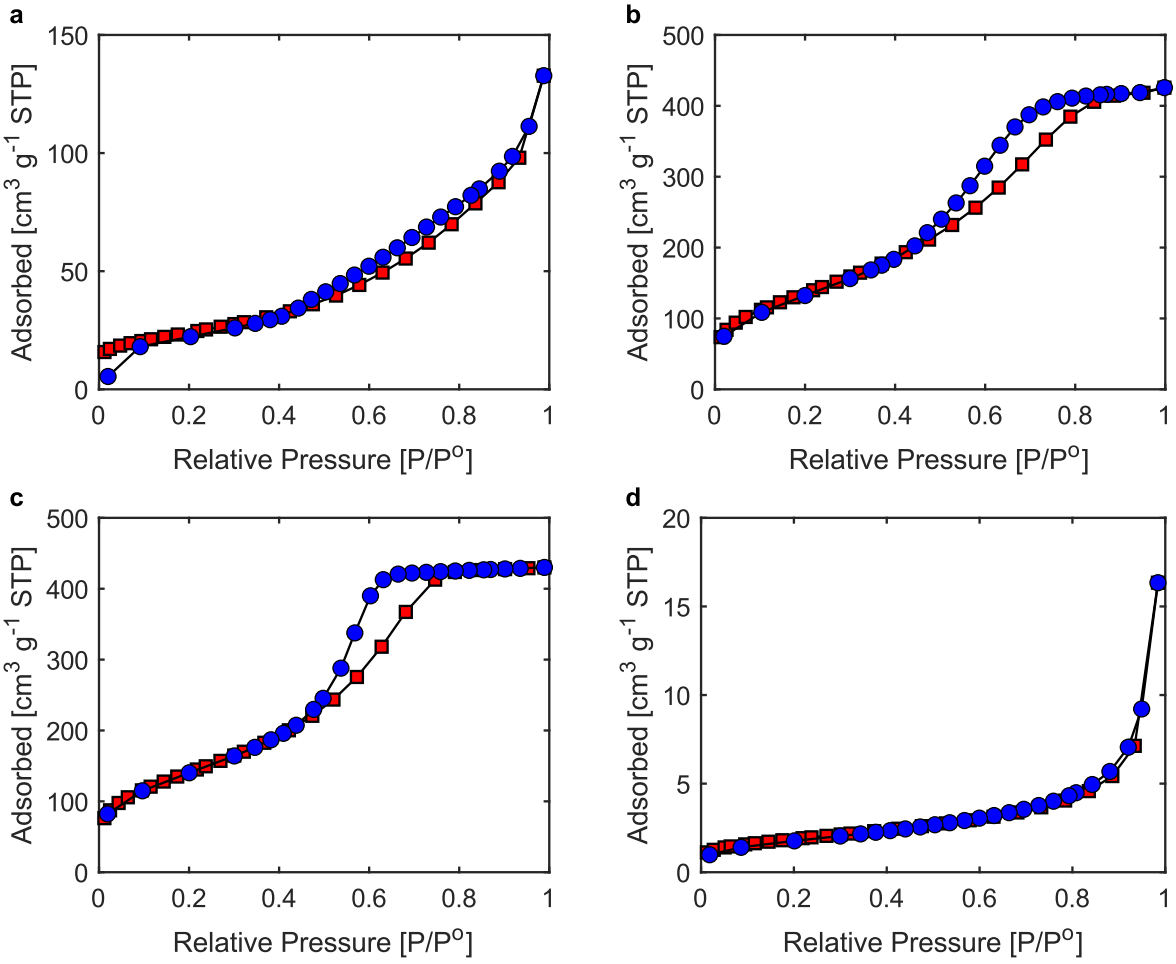

Figure D1: N_2 physisorption adsorption (red) and desorption (blue) isotherms.

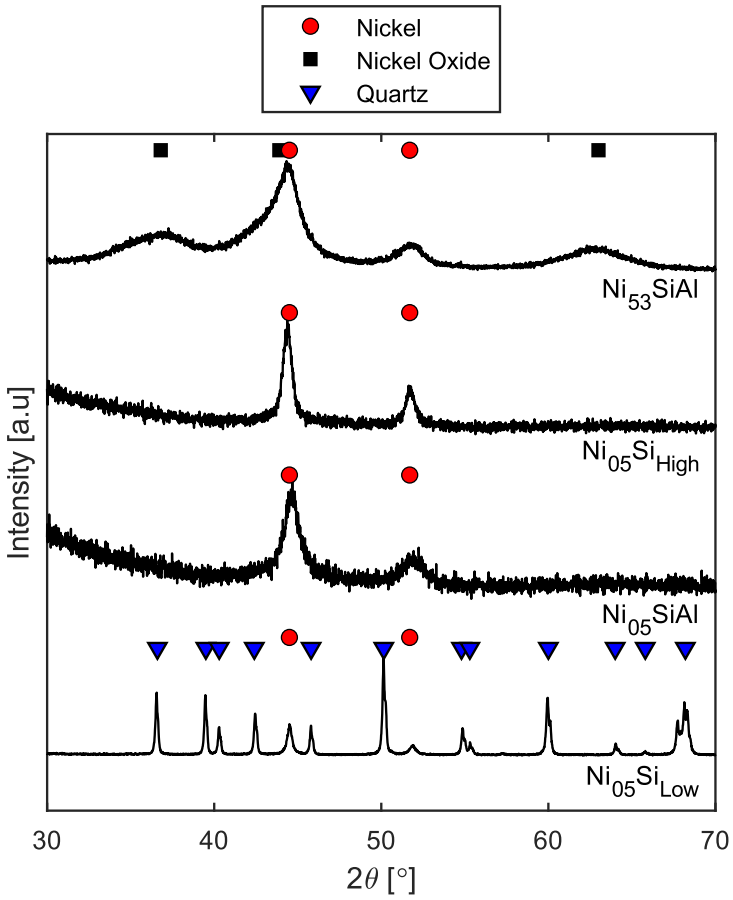

Figure D2: X-ray diffractograms of fresh catalysts.

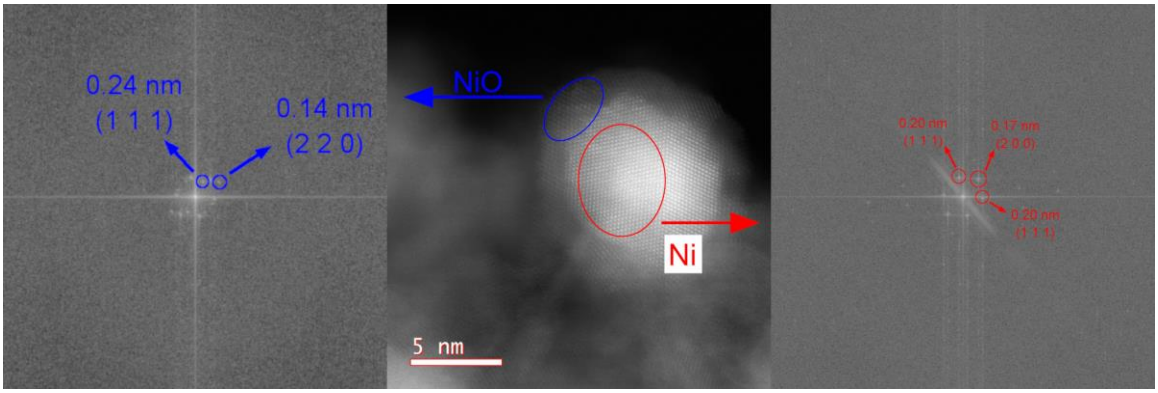

Figure D3: STEM image of a nickel particle on $Ni_{53}SiAl$ (center) with the FFT of the NiO outer layer (left) and the FFT of the Ni core (right).

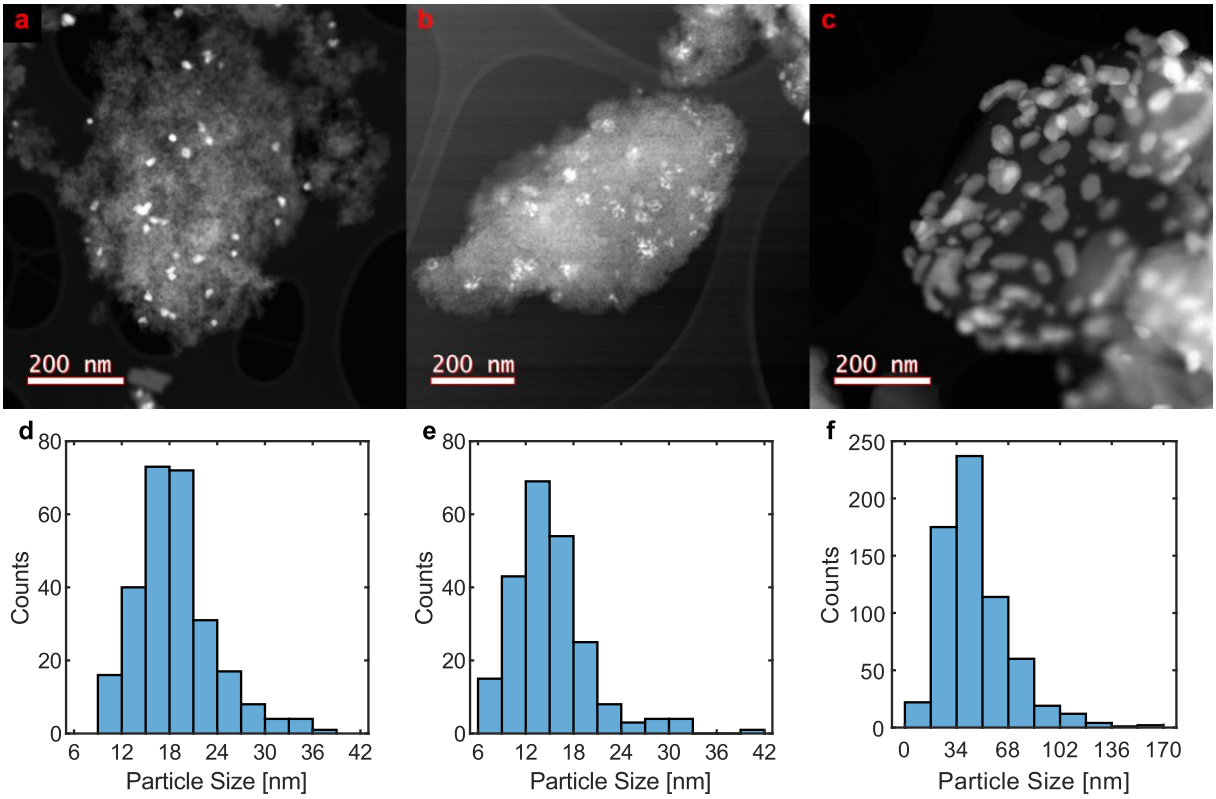

Figure D4: Example STEM images of (a) $Ni_{05}SiAl$, (b) $Ni_{05}Si_{High}$, and (c) $Ni_{05}Si_{Low}$ for particle size analysis and histograms of all measured particles for (d) $Ni_{05}SiAl$, (e) $Ni_{05}Si_{High}$, and (f) $Ni_{05}Si_{Low}$.

D.2 Mechanocatalytic Hydrogenolysis Reaction Results

Table D1: Full Results from Hydrogenolysis Reactions.

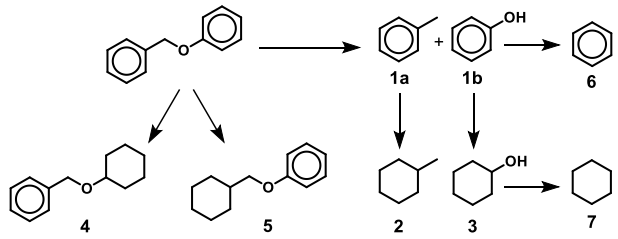

Entry	Catalyst	Milling Time [min]	BPE Conv. [%]	Yields [%]								Carbon Balance [%]
				1a	1b	2	3	4	5	6	7	
1	$Ni_{53}SiAl$	7.5	15.7	6.94	6.57	0	0	0	0.02	0	0	91.2
2	$Ni_{53}SiAl$	30	47.9	38.0	25.4	0.05	2.38	0.14	0.32	0	0	85.8
3	$Ni_{53}SiAl$	60	77.5	64.1	32.4	0.16	11.8	0.43	0.96	0.09	0	78.9
4	$Ni_{53}SiAl$ (Cycle 1)	120	99.6	88.2	30.4	0.13	28.34	0.36	0.89	0.22	0.08	76.5
5	$Ni_{53}SiAl$	180	99.9	89.6	17.3	0.12	42.1	0.11	0.57	0.26	0.18	76.7
6	$Ni_{53}SiAl$ (Cycle 2)	240	99.0	66.6	19.5	1.56	43.5	0.51	2.13	0.32	0.20	69.6
7	$Ni_{53}SiAl$ (Cycle 3)	240	65.1	28.1	12.2	0.42	10.8	1.19	3.15	0.36	0.18	65.4
8	$Ni_{05}SiAl$	180	76.5	5.77	5.89	0.08	0.62	0.10	0.63	0.44	0.37	23.5
9	$Ni_{05}Si_{High}$	180	82.2	8.96	8.35	0.05	1.46	0.06	0.43	0.41	0.17	28.0
10	$Ni_{05}Si_{Low}$	180	29.0	13.9	5.16	0.28	0.48	0.20	1.44	0.84	0.55	83.5

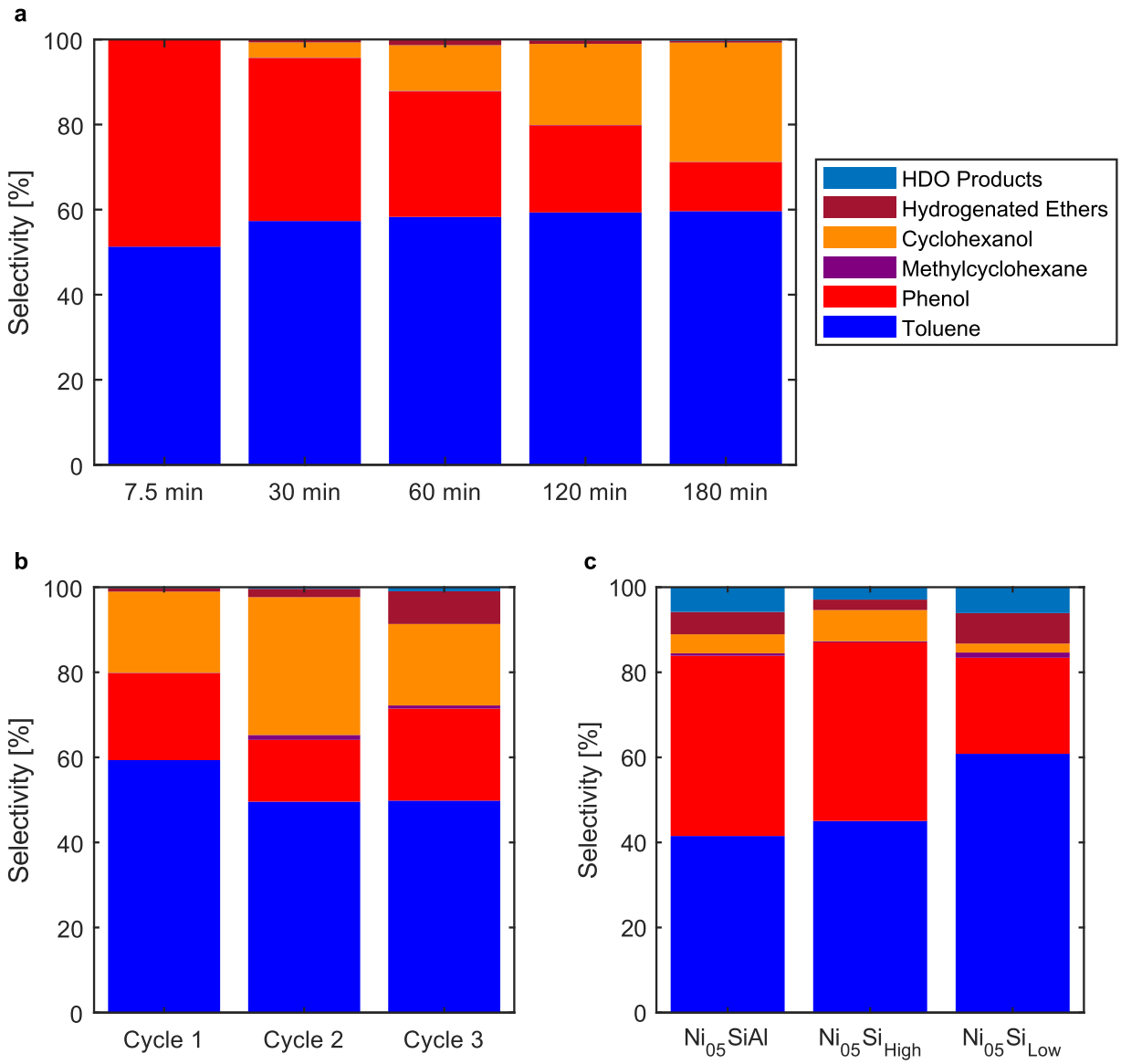

Figure D5: Product Selectivities from the hydrogenolysis reactions.

D.3 Spent $Ni_{53}SiAl$ Characterization

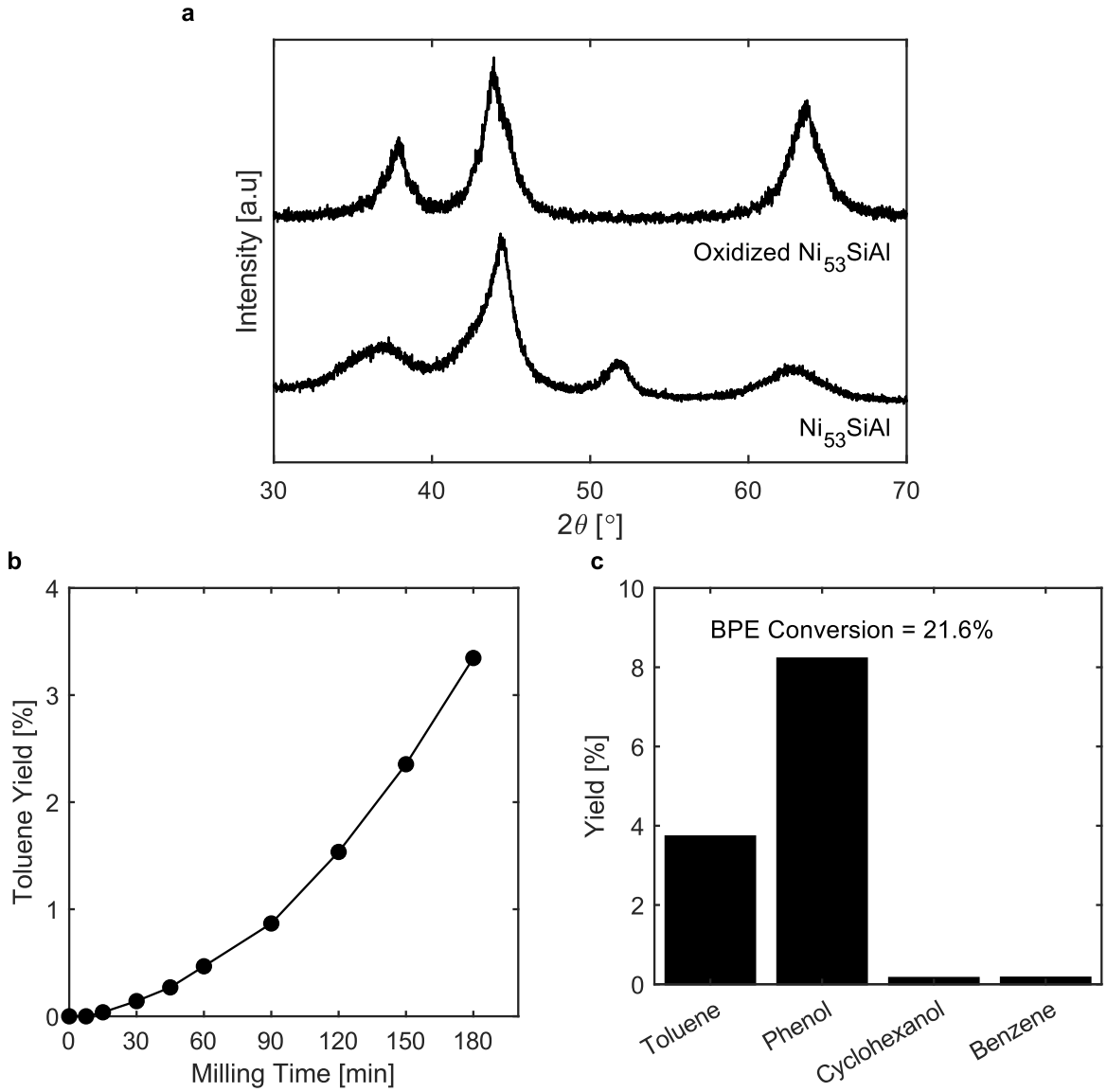

Figure D6: (a) X-ray diffractogram of fresh $Ni_{53}SiAl$ (bottom) and of oxidized $Ni_{53}SiAl$ (top). (b) Toluene yield and (c) full product profile during hydrogenolysis of BPE over oxidized $Ni_{53}SiAl$.

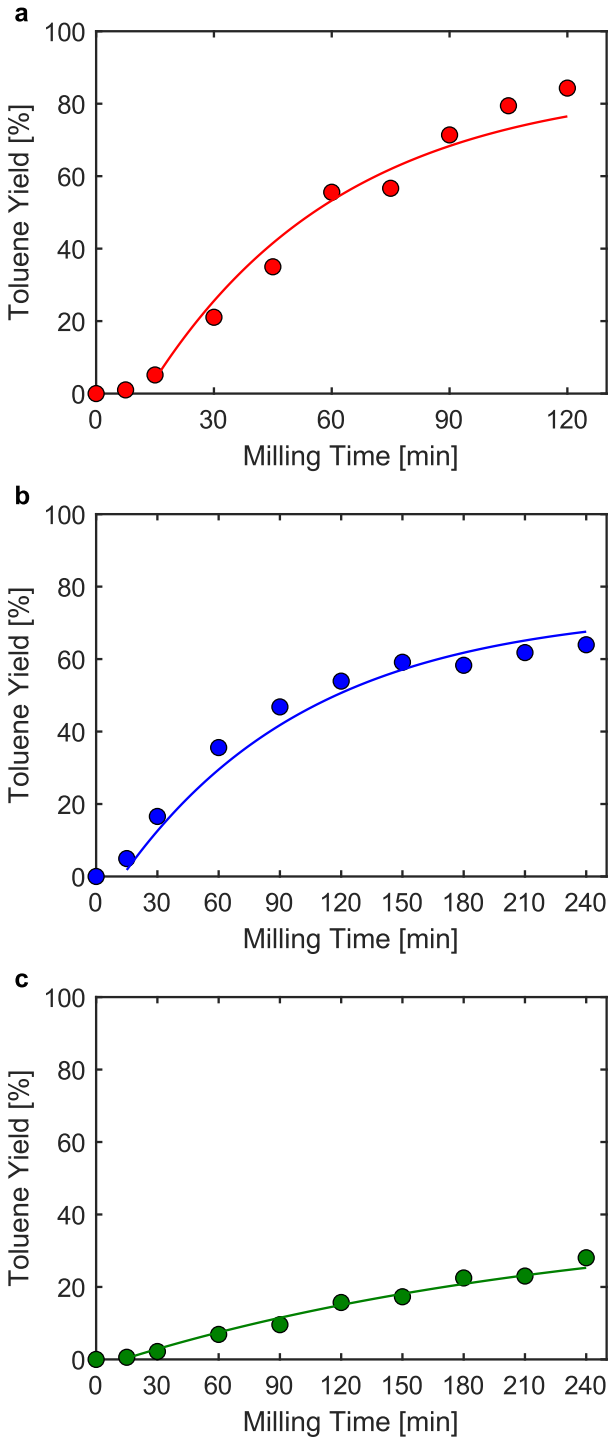

Figure D7: Independent fits for each cycle with $Ni_{53}SiAl$.

Table D2: Raman Band fitting of Spent $Ni_{53}SiAl$.

Raman Band [cm^{-1}]	2 h	6 h	10 h
G [1350]	45.56	44.99	48.13
D_1 [1580]	48.83	47.23	42.36
D_2 [1620]	5.61	7.79	9.51

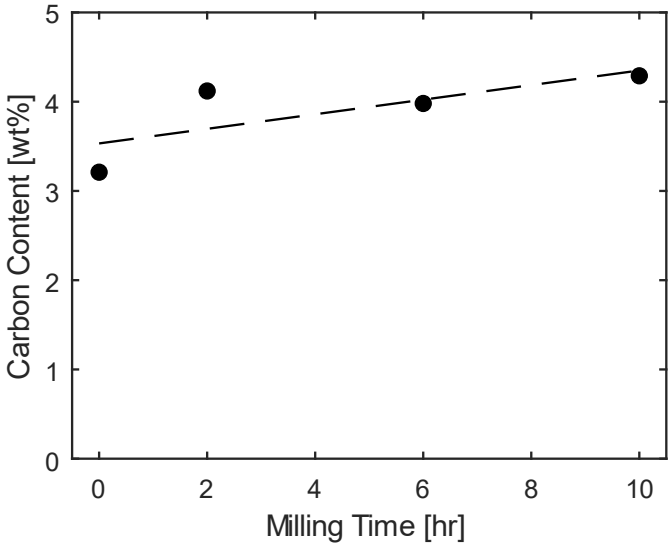

Figure D8: Carbon content of spent $Ni_{53}SiAl$ samples.

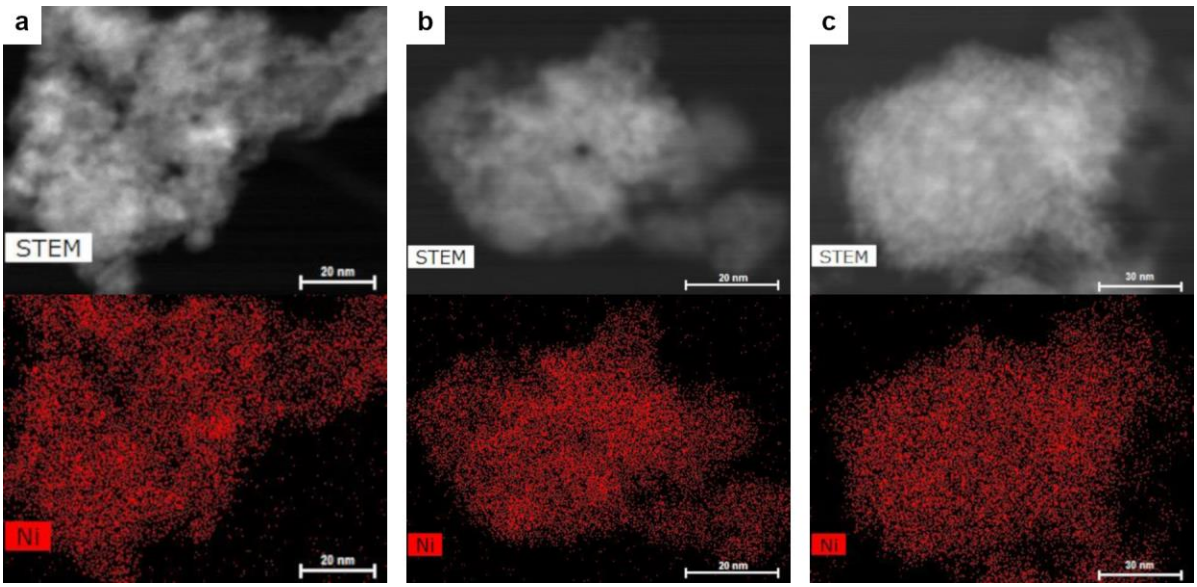

Figure D9: EDS mapping of $Ni_{53}SiAl$ after (a) Cycle 1, (b) Cycle 2, and (c) Cycle 3.

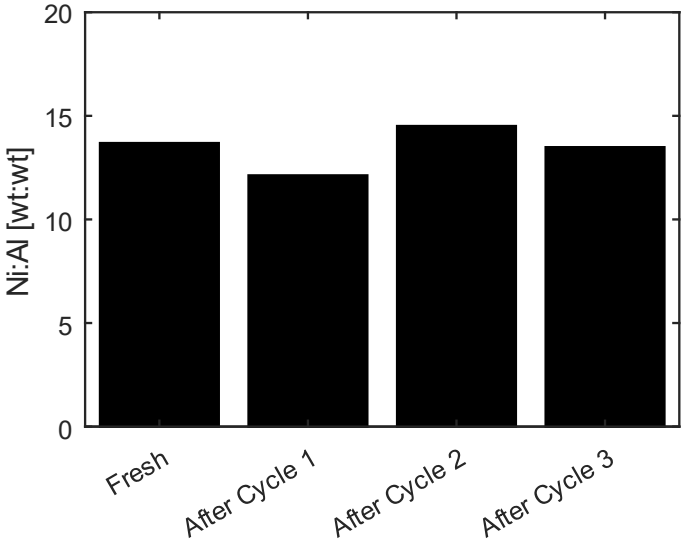

Figure D10: Ni:Al Ratio of spent $Ni_{53}SiAl$ as determined by ICP-OES.

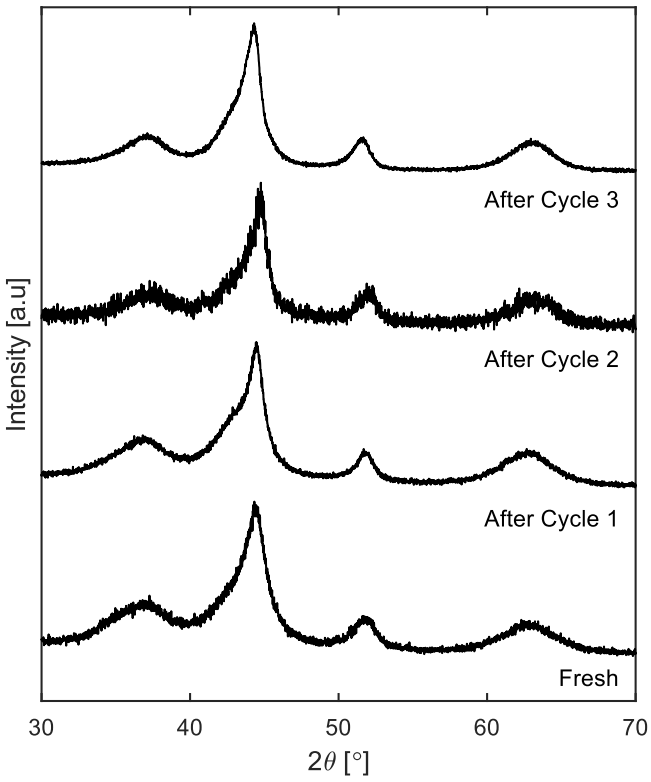

Figure D11: X-ray diffractograms of fresh and spent $Ni_{53}SiAl$ samples.

D.4 Spent Low Nickel Catalyst Characterization

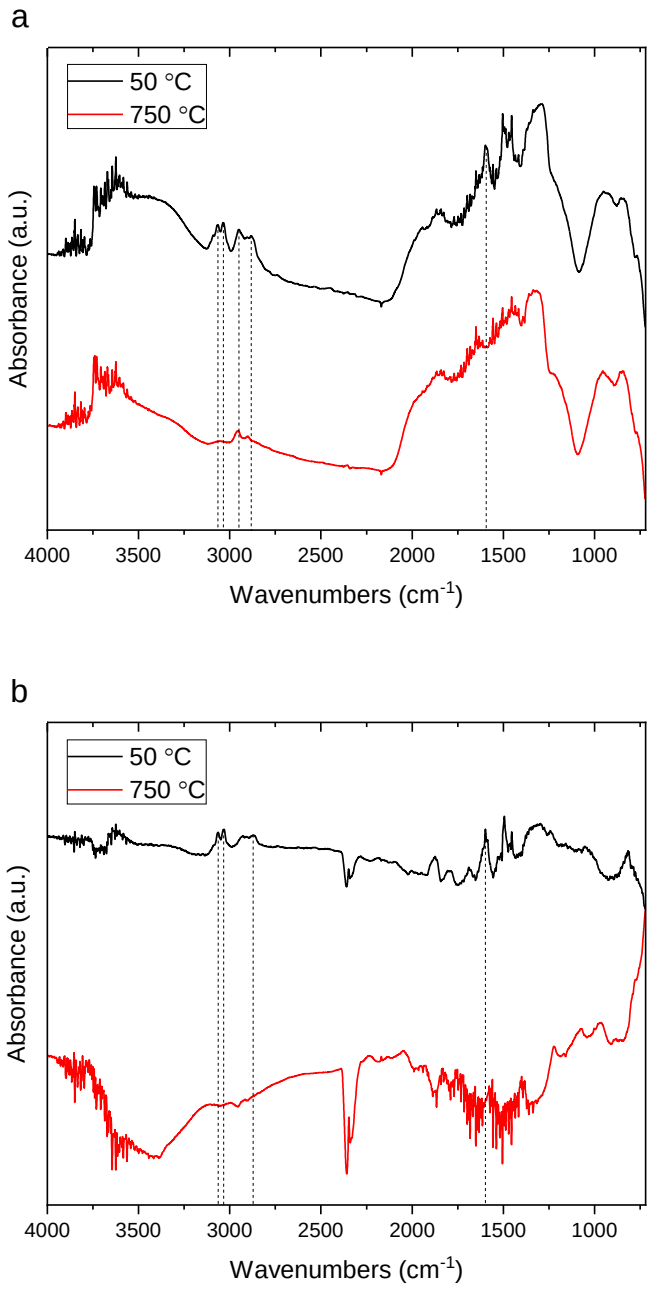

Figure D12: (a) DRIFTS spectra of $Ni_{05}Si_{High}$ with pre-adsorbed BPE at 50 ºC and after heating to 750 ºC for one hour in flow of 40 sccm N_2. (b) DRIFTS spectra of $Ni_{05}Si_{Low}$ with pre-adsorbed BPE at 50 ºC and after heating to 750 ºC for one hour in flow of 40 sccm N_2.

REFERENCES

1. Roosevelt, T., Productive Scientific Scholarship. *Science* **1917,** *45*, 7-12.

2. Monthly Energy Review April 2021. Energy, D. o., Ed. 2021.

3. Field, C. B.; Behrenfeld, M. J.; Randerson, J. T.; Falkowski, P., Primary production of the biosphere: integrating terrestrial and oceanic components. *Science* **1998,** *281*, 237-240.

4. Leffler, W. L., *Petroleum refining in nontechnical language*. PennWell Books, LLC: 2020.

5. Folkins, H. O., Benzene. In *Ullmann's Encyclopedia of Industrial Chemistry*, 2000.

6. Weber, M.; Weber, M.; Weber, V., Phenol. In *Ullmann's Encyclopedia of Industrial Chemistry*, 2020; pp 1-20.

7. Fiege, H.; Voges, H.-W.; Hamamoto, T.; Umemura, S.; Iwata, T.; Miki, H.; Fujita, Y.; Buysch, H.-J.; Garbe, D.; Paulus, W., Phenol Derivatives. In *Ullmann's Encyclopedia of Industrial Chemistry*, 2000.

8. Schutyser, W.; Renders, T.; Van den Bosch, S.; Koelewijn, S. F.; Beckham, G. T.; Sels, B. F., Chemicals from lignin: an interplay of lignocellulose fractionation, depolymerisation, and upgrading. *Chem. Soc. Rev.* **2018,** *47*, 852-908.

9. Rubin, E. M., Genomics of cellulosic biofuels. *Nature* **2008,** *454*, 841-845.

10. Corma, A.; Iborra, S.; Velty, A., Chemical routes for the transformation of biomass into chemicals. *Chem. Rev.* **2007,** *107*, 2411-2502.

11. Vanholme, R.; Demedts, B.; Morreel, K.; Ralph, J.; Boerjan, W., Lignin biosynthesis and structure. *Plant Physiol* **2010,** *153*, 895-905.

12. Ralph, J.; Lapierre, C.; Boerjan, W., Lignin structure and its engineering. *Curr. Opin. Biotechnol.* **2019,** *56*, 240-249.

13. Glasser, W. G.; Northey, R. A.; Schultz, T. P., *Lignin: historical, biological, and materials perspectives*. ACS Publications: 1999.

14. Saake, B.; Lehnen, R., Lignin. In *Ullmann's Encyclopedia of Industrial Chemistry*, 2007.

15. Aro, T.; Fatehi, P., Production and application of lignosulfonates and sulfonated lignin. *ChemSusChem* **2017,** *10*, 1861-1877.

16. Vishtal, A. G.; Kraslawski, A., Challenges in industrial applications of technical lignins. *BioResources* **2011,** *6*, 3547-3568.

17. Bomgardner, M., Following many routes to naturally derived vanillin. *Chem Eng News* **2014,** *92*, 14-15.

18. Fache, M.; Boutevin, B.; Caillol, S., Vanillin Production from Lignin and Its Use as a Renewable Chemical. *ACS Sustain. Chem. Eng.* **2016,** *4*, 35-46.

19. FAO Yearbook of Forest Products 1968. Nations, F. a. A. O. o. t. U., Ed. Rome, Italy, 1968.

20. FAO Yearbook of Frest PRoducts 2017. Nations, F. a. A. O. o. t. U., Ed. Rome, Italy, 2019.

21. Li, C. Z.; Zhao, X. C.; Wang, A. Q.; Huber, G. W.; Zhang, T., Catalytic Transformation of Lignin for the Production of Chemicals and Fuels. *Chem. Rev.* **2015,** *115*, 11559-11624.

22. Xu, C.; Ferdosian, F., Conversion of Lignin into Bio-Based Chemicals and Materials. Springer Berlin Heidelberg: Berlin, Heidelberg, 2017; pp 35-54.

23. Fache, M.; Boutevin, B.; Caillol, S., Vanillin Production from Lignin and Its Use as a Renewable Chemical. *ACS Sustain. Chem. Eng.* **2016,** *4*, 35-46.

24. Xu, C. P.; Arancon, R. A. D.; Labidi, J.; Luque, R., Lignin depolymerisation strategies: towards valuable chemicals and fuels. *Chem. Soc. Rev.* **2014,** *43*, 7485-7500.

25. Shuai, L.; Saha, B., Towards high-yield lignin monomer production. *Green Chem.* **2017,** *19*, 3752-3758.

26. Gratzl, J. S.; Chen, C.-L., Chemistry of Pulping: Lignin Reactions. In *Lignin: Historical, Biological, and Materials Perspectives*, American Chemical Society: 1999; Vol. 742, pp 392-421.

27. Abu-Omar, M. M.; Barta, K.; Beckham, G. T.; Luterbacher, J. S.; Ralph, J.; Rinaldi, R.; Román-Leshkov, Y.; Samec, J. S.; Sels, B. F.; Wang, F., Guidelines for performing lignin-first biorefining. *Energy Environ. Sci.* **2021,** *14*, 262-292.

28. Galkin, M. V.; Samec, J. S., Lignin valorization through catalytic lignocellulose fractionation: a fundamental platform for the future biorefinery. *ChemSusChem* **2016,** *9*, 1544-1558.

29. Renders, T.; Van den Bossche, G.; Vangeel, T.; Van Aelst, K.; Sels, B., Reductive catalytic fractionation: state of the art of the lignin-first biorefinery. *Curr. Opin. Biotechnol.* **2019,** *56*, 193-201.

30. Shuai, L.; Amiri, M. T.; Questell-Santiago, Y. M.; Heroguel, F.; Li, Y.; Kim, H.; Meilan, R.; Chapple, C.; Ralph, J.; Luterbacher, J. S., Formaldehyde stabilization facilitates lignin monomer production during biomass depolymerization. *Science* **2016,** *354*, 329-333.

31. Deuss, P. J.; Scott, M.; Tran, F.; Westwood, N. J.; de Vries, J. G.; Barta, K., Aromatic monomers by in situ conversion of reactive intermediates in the acid-catalyzed depolymerization of lignin. *J Am Chem Soc* **2015,** *137*, 7456-67.

32. Gomollón-Bel, F., Ten Chemical Innovations That Will Change Our World: IUPAC identifies emerging technologies in Chemistry with potential to make our planet more sustainable. *Chemistry International* **2019,** *41*, 12-17.

33. Ardila-Fierro, K. J.; Hernández, J. G., Sustainability Assessment of Mechanochemistry Using the Twelve Principles of Green Chemistry. *ChemSusChem* **2021**.

34. Baláž, P., Mechanochemistry in Minerals Engineering. In *Mechanochemistry in nanoscience and minerals engineering*, Springer: 2008; pp 257-296.

35. Lomovskiy, I.; Bychkov, A.; Lomovsky, O.; Skripkina, T., Mechanochemical and Size Reduction Machines for Biorefining. *Molecules* **2020,** *25*, 5345.

36. Andersen, J.; Mack, J., Mechanochemistry and organic synthesis: from mystical to practical. *Green Chem.* **2018,** *20*, 1435-1443.

37. Crawford, D. E.; Casaban, J., Recent developments in mechanochemical materials synthesis by extrusion. *Adv. Mater.* **2016,** *28*, 5747-5754.

38. James, S. L.; Adams, C. J.; Bolm, C.; Braga, D.; Collier, P.; Friščić, T.; Grepioni, F.; Harris, K. D.; Hyett, G.; Jones, W.; Krebs, A.; Mack, J.; Maini, L.; Orpen, A. G.; Parkin, I. P.; Shearouse, W. C.; Steed, J. W.; Waddell, D. C., Mechanochemistry: opportunities for new and cleaner synthesis. *Chem. Soc. Rev.* **2012,** *41*, 413-447.

39. Friscic, T.; Jones, W., Recent advances in understanding the mechanism of cocrystal formation via grinding. *Cryst. Growth Des.* **2009,** *9*, 1621-1637.

40. Amirjalayer, S.; Fuchs, H.; Marx, D., Understanding the Mechanocatalytic Conversion of Biomass: A Low-Energy One-Step Reaction Mechanism by Applying Mechanical Force. *Angew. Chem., Int. Edit.* **2019,** *58*, 5232-5235.

41. Delogu, F., Mechanochemical behavior of surface radicals in ground quartz. *J. Phys. Chem. C* **2011,** *115*, 21230-21235.

42. Immohr, S.; Felderhoff, M.; Weidenthaler, C.; Schüth, F., An orders-of-magnitude increase in the rate of the solid-catalyzed CO oxidation by in situ ball milling. *Angew. Chem., Int. Edit.* **2013,** *52*, 12688-12691.

43. Blair, R. G.; Hick, S. M.; Truitt, J. H., Solid Acid Catalyzed Hydrolysis of Cellulosic Materials. Google Patents: 2010.

44. Schell, D. J.; Harwood, C., Milling of Lignocellulosic Biomass - Results of Pilot-scale Testing. *Appl. Biochem. Biotechnol.* **1994,** *45-6*, 159-168.

45. Liu, S. B.; Okuyama, Y.; Tamura, M.; Nakagawa, Y.; Imai, A.; Tomishige, K., Production of Renewable Hexanols from Mechanocatalytically Depolymerized Cellulose by Using Ir-ReOx/SiO2 catalyst. *ChemSusChem* **2015,** *8*, 628-635.

46. Boissou, F.; Sayoud, N.; Vigier, K. D.; Barakat, A.; Marinkovic, S.; Estrine, B.; Jerome, F., Acid-Assisted Ball Milling of Cellulose as an Efficient Pretreatment Process for the Production of Butyl Glycosides. *ChemSusChem* **2015,** *8*, 3263-3269.

47. Almohalla, M.; Rodríguez-Ramos, I.; Ribeiro, L. S.; Órfão, J. J. M.; Pereira, M. F. R.; Guerrero-Ruiz, A., Cooperative action of heteropolyacids and carbon supported Ru catalysts for the conversion of cellulose. *Catal. Today* **2017**.

48. Dong, Y.; Haverinen, J.; Tuuttila, T.; Jaakkola, M.; Holm, J.; Leveque, J. M.; Lassi, U., Rapid one-step solvent-free acid-catalyzed mechanical depolymerization of pine sawdust to high-yield water-soluble sugars. *Biomass Bioenerg.* **2017,** *102*, 23-30.

49. Guo, X. J.; Xin, J. N.; Wolcott, M. P.; Zhang, J. W., Mechanochemical Oleation of Lignin Through Ball Milling and Properties of its Blends with PLA. *ChemistrySelect* **2016,** *1*, 3449-3454.

50. Kobayashi, H.; Techikawara, K.; Fukuoka, A., Hydrolytic hydrogenation of chitin to amino sugar alcohol. *Green Chem.* **2017**.

51. Li, L.; Yan, L.; Shen, F.; Qiu, M.; Qi, X., Mechanocatalytic Production of Lactic Acid from Glucose by Ball Milling. *Catalysts* **2017,** *7*, 170.

52. Blair, R. G.; Chagoya, K.; Biltek, S.; Jackson, S.; Sinclair, A.; Taraboletti, A.; Restrepo, D. T., The scalability in the mechanochemical syntheses of edge functionalized graphene materials and biomass-derived chemicals. *Faraday Discuss.* **2014,** *170*, 223-233.

53. Dabral, S.; Turberg, M.; Wanninger, A.; Bolm, C.; Hernandez, J. G., Mechanochemical Lignin-Mediated Strecker Reaction. *Molecules* **2017,** *22*, 10.

54. Zhang, Q. H.; Jerome, F., Mechanocatalytic Deconstruction of Cellulose: An Emerging Entry into Biorefinery. *ChemSusChem* **2013,** *6*, 2042-2044.

55. Jerome, F.; Chatel, G.; Vigier, K. D., Depolymerization of cellulose to processable glucans by non-thermal technologies. *Green Chem.* **2016,** *18*, 3903-3913.

56. Kaldstrom, M.; Meine, N.; Fares, C.; Rinaldi, R.; Schuth, F., Fractionation of `water-soluble lignocellulose' into C-5/C-6 sugars and sulfur-free lignins. *Green Chem.* **2014,** *16*, 2454-2462.

57. Schuth, F.; Rinaldi, R.; Meine, N.; Kaldstrom, M.; Hilgert, J.; Rechulski, M. D. K., Mechanocatalytic depolymerization of cellulose and raw biomass and downstream processing of the products. *Catal. Today* **2014,** *234*, 24-30.

58. Rechulski, M. D. K.; Kaldstrom, M.; Richter, U.; Schuth, F.; Rinaldi, R., Mechanocatalytic Depolymerization of Lignocellulose Performed on Hectogram and Kilogram Scales. *Ind. Eng. Chem. Res.* **2015,** *54*, 4581-4592.

59. Loustau-Cazalet, C.; Sambusiti, C.; Buche, P.; Solhy, A.; Bilal, E.; Larzek, M.; Barakat, A., Innovative Deconstruction of Biomass Induced by Dry Chemo-Mechanical Activation: Impact on Enzymatic Hydrolysis and Energy Efficiency. *ACS Sustain. Chem. Eng.* **2016,** *4*, 2689-2697.

60. Lee, D. Y.; Tachibana, S.; Sumimoto, M., Mechanochemistry of Lignin .2. Mechanochemical Reactions of Coniferyl Alcohol Methyl-ether. *Cell Chem. Technol.* **1988,** *22*, 201-210.

61. Lee, D. Y.; Sumimoto, M., Mechanochemistry of Lignin .3. Mechanochemical Reactions of Beta-O-4 Lignin Model Compounds. *Holzforschung* **1990,** *44*, 347-350.

62. Lee, D. Y.; Matsuoka, M.; Sumimoto, M., Mechanochemistry of Lignin .4. Mechanochemical Reactions of Phenylcoumaran Models. *Holzforschung* **1990,** *44*, 415-418.

63. Wu, Z. H.; Sumimoto, M.; Tanaka, H., Mechanochemistry of Lignin .16. Generation of Oxygen-Containing Radicals in the Aqueous-Media of Mechanical Pulping. *J. Wood Chem. Technol.* **1994,** *15*, 27-42.

64. Wu, Z. H.; Sumimoto, M.; Tanaka, H., Mechanochemistry of Lignin .17. Factors Influencing Mechanochemical Reactions of VEratrylglycerol-Beta-Syringaldehyde Ether. *Holzforschung* **1994,** *48*, 395-399.

65. Wu, Z. H.; Sumimoto, M.; Tanaka, H., Mechanochemistry of Lignin .18. A Novel-Approach to Improve Brightness Stability Of H2O2-bleached HIgh-yield Pulps by Addition of Radical Scavengers to the Pulping Process. *Holzforschung* **1994,** *48*, 400-404.

66. Kaldstrom, M.; Meine, N.; Fares, C.; Schuth, F.; Rinaldi, R., Deciphering 'water-soluble lignocellulose' obtained by mechanocatalysis: new insights into the chemical processes leading to deep depolymerization. *Green Chem.* **2014,** *16*, 3528-3538.

67. Yao, S. G.; Mobley, J. K.; Ralph, J.; Crocker, M.; Parkin, S.; Selegue, J. P.; Meier, M. S., Mechanochemical treatment facilitates two-step oxidative depolymerization of kraft lignin. *ACS Sustain. Chem. Eng.* **2018,** *6*, 5990-5998.

68. Kleine, T.; Buendia, J.; Bolm, C., Mechanochemical degradation of lignin and wood by solvent-free grinding in a reactive medium. *Green Chem.* **2013,** *15*, 160-166.

69. Brittain, A. D.; Chrisandina, N. J.; Cooper, R. E.; Buchanan, M.; Cort, J. R.; Olarte, M. V.; Sievers, C., Quenching of reactive intermediates during mechanochemical depolymerization of lignin. *Catal. Today* **2018,** *302*, 180-189.

70. Dabral, S.; Wotruba, H.; Hernandez, J. G.; Bolm, C., Mechanochemical Oxidation and Cleavage of Lignin β-O-4 Model Compounds and Lignin. *ACS Sustain. Chem. Eng.* **2018**, 3242-3254.

71. Li, C.; Zhao, X.; Wang, A.; Huber, G. W.; Zhang, T., Catalytic Transformation of Lignin for the Production of Chemicals and Fuels. *Chem. Rev.* **2015,** *115*, 11559-11624.

72. Rinaldi, R.; Jastrzebski, R.; Clough, M. T.; Ralph, J.; Kennema, M.; Bruijnincx, P. C.; Weckhuysen, B. M., Paving the Way for Lignin Valorisation: Recent Advances in Bioengineering, Biorefining and Catalysis. *Angew. Chem.-Int. Edit.* **2016,** *55*, 8164-8215.

73. Pandey, M. P.; Kim, C. S., Lignin Depolymerization and Conversion: A Review of Thermochemical Methods. *Chem. Eng. Technol.* **2011,** *34*, 29-41.

74. Davis, R.; Tao, L.; Tan, E.; Biddy, M.; Beckham, G.; Scarlata, C.; Jacobson, J.; Cafferty, K.; Ross, J.; Lukas, J. *Process design and economics for the conversion of lignocellulosic biomass to hydrocarbons: dilute-acid and enzymatic deconstruction of biomass to sugars and biological conversion of sugars to hydrocarbons*; National Renewable Energy Lab: Golden, CO, United States, 2013.

75. Bajwa, D.; Pourhashem, G.; Ullah, A.; Bajwa, S., A concise review of current lignin production, applications, products and their environmental impact. *Ind. Crop. Prod.* **2019,** *139*, 111526.

76. Tikka, P., *Chemical Pulping Part 2: Recovery of Chemical and Energy*. Paperi ja Puu Oy: 2008.

77. Kwok, T. T.; Bright, J. R.; Realff, M. J.; Bommarius, A. S., Pretreatment Efficacy and Lignin Solubility of Organic Solvents on Juvenile Slash Pine Chips for Lignin Value Prior to Pulping. *Bioresources* **2019,** *14*, 5988-6003.

78. Tomani, P., The lignoboost process. *Cell. Chem. Technol.* **2010,** *44*, 53-58.

79. Öhman, F.; Theliander, H.; Norgren, M.; Tomani, P.; Axegård, P. Method for separating lignin from a lignin containing liquid/slurry. EP1797236B1, June 15, 2011.

80. Hu, Z. J.; Du, X. Y.; Liu, J.; Chang, H. M.; Jameel, H., Structural Characterization of Pine Kraft Lignin: BioChoice Lignin vs Indulin AT. *J. Wood Chem. Technol.* **2016,** *36*, 432-446.

81. Gellerstedt, G.; Tomani, P.; Axegård, P.; Backlund, B., Lignin Recovery and Lignin-Based Products. In *Integrated Forest Biorefineries: Challenges and Opportunities*, The Royal Society of Chemistry: 2013; pp 180-210.

82. Klein-Marcuschamer, D.; Simmons, B. A.; Blanch, H. W., Techno-economic analysis of a lignocellulosic ethanol biorefinery with ionic liquid pre-treatment. *Biofuels, Bioprod. Bioref.* **2011,** *5*, 562-569.

83. Manesh, A.; Guenther, J. H.; Zoborowski, E. G.; Braenner, W.; Manesh, M. A.; Hawk, L. J. Oxygen assisted organosolv process, system and method for delignification of lignocellulosic materials and lignin recovery. US9382283B2, July 05, 2016.

84. Retsina, T.; Pylkkanen, V. Method for the production of fermentable sugars and cellulose from lignocellulosic material. US8030039B1, October 04, 2011.

85. Kadam, K.; Simard, M. A.; Champagne, A. T. Lignin production from lignocellulosic biomass. US8840995B2, September 23, 2014.

86. Holladay, J. E.; White, J. F.; Bozell, J. J.; Johnson, D. *Top value-added chemicals from biomass-Volume II—Results of screening for potential candidates from biorefinery lignin*; Pacific Northwest National Lab: Richland, WA, United States, 2007.

87. Phongpreecha, T.; Hool, N. C.; Stoklosa, R. J.; Klett, A. S.; Foster, C. E.; Bhalla, A.; Holmes, D.; Thies, M. C.; Hodge, D. B., Predicting lignin depolymerization yields from quantifiable properties using fractionated biorefinery lignins. *Green Chem* **2017,** *19*, 5131-5143.

88. Chen, C.; Jin, D. X.; Ouyang, X. P.; Zhao, L. S.; Qiu, X. Q.; Wang, F. R., Effect of structural characteristics on the depolymerization of lignin into phenolic monomers. *Fuel* **2018,** *223*, 366-372.

89. Zhu, W. Z.; Theliander, H., Precipitation of Lignin from Softwood Black Liquor: An Investigation of the Equilibrium and Molecular Properties of Lignin. *BioResources* **2015,** *10*, 1696-1714.

90. Sluiter, A.; Hames, B.; Ruiz, R.; Scarlata, C.; Sluiter, J.; Templeton, D.; Crocker, D., Determination of structural carbohydrates and lignin in biomass. *Laboratory analytical procedure* **2008,** *1617*, 1-16.

91. Dundy, M.; Stehr, E., Determination of Oxygen in Organic Materials by Modified Schütze-Unterzaucher Method. *Anal. Chem.* **1951,** *23*, 1408-1413.

92. Guerra, A.; Filpponen, I.; Lucia, L. A.; Argyropoulos, D. S., Comparative evaluation of three lignin isolation protocols for various wood species. *J. Agric. Food Chem.* **2006,** *54*, 9696-9705.

93. Crestini, C.; Lange, H.; Sette, M.; Argyropoulos, D. S., On the structure of softwood kraft lignin. *Green Chem.* **2017,** *19*, 4104-4121.

94. Mansfield, S. D.; Kim, H.; Lu, F.; Ralph, J., Whole plant cell wall characterization using solution-state 2D NMR. *Nat. Protoc.* **2012,** *7*, 1579-1589.

95. Capanema, E. A.; Balakshin, M. Y.; Kadla, J. F., A comprehensive approach for quantitative lignin characterization by NMR spectroscopy. *J. Agric. Food Chem.* **2004,** *52*, 1850-1860.

96. Capanema, E. A.; Balakshin, M. Y.; Kadla, J. F., Quantitative characterization of a hardwood milled wood lignin by nuclear magnetic resonance spectroscopy. *J. Agric. Food Chem.* **2005,** *53*, 9639-49.

97. Huang, F.; Singh, P. M.; Ragauskas, A. J., Characterization of milled wood lignin (MWL) in Loblolly pine stem wood, residue, and bark. *J. Agric. Food Chem.* **2011,** *59*, 12910-12916.

98. Balakshin, M. Y.; Capanema, E. A.; Santos, R. B.; Chang, H.-m.; Jameel, H., Structural analysis of hardwood native lignins by quantitative 13C NMR spectroscopy. *Holzforschung* **2016,** *70*, 95-108.

99. Lan, W.; Luterbacher, J. S., Preventing Lignin Condensation to Facilitate Aromatic Monomer Production. *Chimia (Aarau)* **2019,** *73*, 591-598.

100. Sjostrom, E., *Wood chemistry: fundamentals and applications*. Gulf Professional Publishing: 1993.

101. del Rio, J. C.; Rencoret, J.; Prinsen, P.; Martinez, A. T.; Ralph, J.; Gutierrez, A., Structural characterization of wheat straw lignin as revealed by analytical pyrolysis, 2D-NMR, and reductive cleavage methods. *J. Agric. Food Chem.* **2012,** *60*, 5922-5935.

102. Pinto, P. C. R.; da Silva, E. A. B.; Rodrigues, A. E., Insights into Oxidative Conversion of Lignin to High-Added-Value Phenolic Aldehydes. *Ind. Eng. Chem. Res.* **2011,** *50*, 741-748.

103. Erdocia, X.; Prado, R.; Corcuera, M. A.; Labidi, J., Base catalyzed depolymerization of lignin: Influence of organosolv lignin nature. *Biomass Bioenergy* **2014,** *66*, 379-386.

104. Guo, H.; Zhang, B.; Qi, Z.; Li, C.; Ji, J.; Dai, T.; Wang, A.; Zhang, T., Valorization of Lignin to Simple Phenolic Compounds over Tungsten Carbide: Impact of Lignin Structure. *ChemSusChem* **2017,** *10*, 523-532.

105. Feghali, E.; Carrot, G.; Thuery, P.; Genre, C.; Cantat, T., Convergent reductive depolymerization of wood lignin to isolated phenol derivatives by metal-free catalytic hydrosilylation. *Energy Environ. Sci.* **2015,** *8*, 2734-2743.

106. Amiri, M. T.; Bertella, S.; Questell-Santiago, Y. M.; Luterbacher, J. S., Establishing lignin structure-upgradeability relationships using quantitative 1 H–13 C heteronuclear single quantum coherence nuclear magnetic resonance (HSQC-NMR) spectroscopy. *Chem. Sci.* **2019,** *10*, 8135-8142.

107. Parthasarathi, R.; Romero, R. A.; Redondo, A.; Gnanakaran, S., Theoretical Study of the Remarkably Diverse Linkages in Lignin. *J. Phys. Chem. Lett.* **2011,** *2*, 2660-2666.

108. Liu, Q.; Wang, S.; Zheng, Y.; Luo, Z.; Cen, K., Mechanism study of wood lignin pyrolysis by using TG–FTIR analysis. *J. Anal. Appl. Pyrol.* **2008,** *82*, 170-177.

109. Yang, H. P.; Yan, R.; Chen, H. P.; Lee, D. H.; Zheng, C. G., Characteristics of hemicellulose, cellulose and lignin pyrolysis. *Fuel* **2007,** *86*, 1781-1788.

110. Zhao, J.; Xiuwen, W.; Hu, J.; Liu, Q.; Shen, D.; Xiao, R., Thermal degradation of softwood lignin and hardwood lignin by TG-FTIR and Py-GC/MS. *Polym. Degrad. Stabil.* **2014,** *108*, 133-138.

111. Yildiz, G.; Ronsse, F.; Venderbosch, R.; van Duren, R.; Kersten, S. R. A.; Prins, W., Effect of biomass ash in catalytic fast pyrolysis of pine wood. *Appl. Catal. B* **2015,** *168*, 203-211.

112. Shen, D.; Gu, S.; Luo, K.; Wang, S.; Fang, M., The pyrolytic degradation of wood-derived lignin from pulping process. *Bioresour. Technol.* **2010,** *101*, 6136-6146.

113. Takacs, L., The historical development of mechanochemistry. *Chem. Soc. Rev.* **2013,** *42*, 7649-7659.

114. Balaz, P.; Achimovicova, M.; Balaz, M.; Billik, P.; Cherkezova-Zheleva, Z.; Criado, J. M.; Delogu, F.; Dutkova, E.; Gaffet, E.; Gotor, F. J.; Kumar, R.; Mitov, I.; Rojac, T.; Senna, M.; Streletskii, A.; Wieczorek-Ciurowa, K., Hallmarks of mechanochemistry: from nanoparticles to technology. *Chem. Soc. Rev.* **2013,** *42*, 7571-637.

115. Zhang, Q.; Saito, F., Mechanochemical processing of celestine. *Chem. Eng. J.* **1997,** *66*, 79-82.

116. Mukasyan, A. S.; Khina, B. B.; Reeves, R. V.; Son, S. F., Mechanical activation and gasless explosion: Nanostructural aspects. *Chem. Eng. J.* **2011,** *174*, 677-686.

117. Lin, X.; Peng, P.; Guo, J.; Xiang, Z., Reaction milling for scalable synthesis of N, P-codoped covalent organic polymers for metal-free bifunctional electrocatalysts. *Chem. Eng. J.* **2019,** *358*, 427-434.

118. Lee, Y.-R.; Jang, M.-S.; Cho, H.-Y.; Kwon, H.-J.; Kim, S.; Ahn, W.-S., ZIF-8: A comparison of synthesis methods. *Chem. Eng. J.* **2015,** *271*, 276-280.

119. Li, Y.; Miao, J.; Sun, X.; Xiao, J.; Li, Y.; Wang, H.; Xia, Q.; Li, Z., Mechanochemical synthesis of Cu-BTC@GO with enhanced water stability and toluene adsorption capacity. *Chem. Eng. J.* **2016,** *298*, 191-197.

120. Verdoni, L. P.; Fink, M. J.; Mitchell, B. S., A fractionation process of mechanochemically synthesized blue-green luminescent alkyl-passivated silicon nanoparticles. *Chem. Eng. J.* **2011,** *172*, 591-600.

121. Li, J.; Nagamani, C.; Moore, J. S., Polymer mechanochemistry: from destructive to productive. *Acc. Chem. Res.* **2015,** *48*, 2181-90.

122. Zhang, W.; Wang, H.; Jun, H.; Yu, M.; Wang, F.; Zhou, L.; Yu, G., Acceleration and mechanistic studies of the mechanochemical dechlorination of HCB with iron powder and quartz sand. *Chem. Eng. J.* **2014,** *239*, 185-191.

123. Lu, S.; Huang, J.; Peng, Z.; Li, X.; Yan, J., Ball milling 2,4,6-trichlorophenol with calcium oxide: Dechlorination experiment and mechanism considerations. *Chem. Eng. J.* **2012,** *195-196*, 62-68.

124. Baláž, P.; Aláčová, A.; Briančin, J., Sensitivity of Freundlich equation constant 1/n for zinc sorption on changes induced in calcite by mechanical activation. *Chem. Eng. J.* **2005,** *114*, 115-121.

125. Stellacci, P.; Liberti, L.; Notarnicola, M.; Bishop, P. L., Valorization of coal fly ash by mechano-chemical activationPart I. Enhancing adsorption capacity. *Chem. Eng. J.* **2009,** *149*, 11-18.

126. Stellacci, P.; Liberti, L.; Notarnicola, M.; Bishop, P. L., Valorization of coal fly ash by mechano-chemical activationPart II. Enhancing pozzolanic reactivity. *Chem. Eng. J.* **2009,** *149*, 19-24.

127. Hick, S. M.; Griebel, C.; Restrepo, D. T.; Truitt, J. H.; Buker, E. J.; Bylda, C.; Blair, R. G., Mechanocatalysis for biomass-derived chemicals and fuels. *Green Chem.* **2010,** *12*, 468-474.

128. Kleine, T.; Buendia, J.; Bolm, C., Mechanochemical degradation of lignin and wood by solvent-free grinding in a reactive medium. *Green Chem.* **2013,** *15*, 160-166.

129. Schneider, L.; Haverinen, J.; Jaakkola, M.; Lassi, U., Pretreatment and fractionation of lignocellulosic barley straw by mechanocatalysis. *Chem. Eng. J.* **2017,** *327*, 898-905.

130. Hernandez, J. G.; Frings, M.; Bolm, C., Mechanochemical Enzymatic Kinetic Resolution of Secondary Alcohols under Ball-Milling Conditions. *ChemCatChem* **2016,** *8*, 1769-1772.

131. Hernandez, J. G.; Ardila-Fierro, K. J.; Crawford, D.; James, S. L.; Bolm, C., Mechanoenzymatic peptide and amide bond formation. *Green Chem.* **2017,** *19*, 2620-2625.

132. Schreyer, H.; Immohr, S.; Schüth, F., Oscillatory combustion of propene during in situ mechanical activation of solid catalysts. *J. Mater. Sci.* **2017,** *52*, 12021-12030.

133. Blair, R. G.; Chagoya, K.; Biltek, S.; Jackson, S.; Sinclair, A.; Taraboletti, A.; Restrepo, D. T., The scalability in the mechanochemical syntheses of edge functionalized graphene materials and biomass-derived chemicals. *Faraday Discuss.* **2014,** *170*, 223-33.

134. Delogu, F.; Mulas, G.; Schiffini, L.; Cocco, G., Mechanical work and conversion degree in mechanically induced processes. *Mat Sci Eng a-Struct* **2004,** *382*, 280-287.

135. Napolitano, E.; Mulas, G.; Enzo, S.; Delogu, F., Kinetics of mechanically induced anatase-to-rutile phase transformations under inelastic impact conditions. *Acta Materialia* **2010,** *58*, 3798-3804.

136. Garroni, S.; Takacs, L.; Leng, H. Y.; Delogu, F., Kinetics of the mechanochemical synthesis of alkaline-earth metal amides. *Chemical Physics Letters* **2014,** *608*, 80-83.

137. Butyagin, P., Mechanochemical synthesis: mechanical and chemical factors. *Journal of materials synthesis and processing* **2000,** *8*, 205-211.

138. Butyagin, P. Y.; Streletskii, A., The kinetics and energy balance of mechanochemical transformations. *Physics of the Solid State* **2005,** *47*, 856-862.

139. Colacino, E.; Carta, M.; Pia, G.; Porcheddu, A.; Ricci, P. C.; Delogu, F., Processing and Investigation Methods in Mechanochemical Kinetics. *ACS Omega* **2018,** *3*, 9196-9209.

140. Cagnetta, G.; Huang, J.; Wang, B.; Deng, S.; Yu, G., A comprehensive kinetic model for mechanochemical destruction of persistent organic pollutants. *Chem. Eng. J.* **2016,** *291*, 30-38.

141. Delogu, F.; Schiffini, L.; Cocco, G., The invariant laws of the amorphization processes by mechanical alloying - I. Experimental findings. *Philos. Mag. A* **2001,** *81*, 1917-1937.

142. Halasz, I.; Friscic, T.; Kimber, S. A.; Uzarevic, K.; Puskaric, A.; Mottillo, C.; Julien, P.; Strukil, V.; Honkimaki, V.; Dinnebier, R. E., Quantitative in situ and real-time monitoring of mechanochemical reactions. *Faraday Discuss.* **2014,** *170*, 203-21.

143. Ma, X.; Yuan, W.; Bell, S. E.; James, S. L., Better understanding of mechanochemical reactions: Raman monitoring reveals surprisingly simple 'pseudo-fluid'model for a ball milling reaction. *Chem. Comm.* **2014,** *50*, 1585-1587.

144. Michalchuk, A. A.; Tumanov, I. A.; Konar, S.; Kimber, S. A.; Pulham, C. R.; Boldyreva, E. V., Challenges of Mechanochemistry: Is In Situ Real-Time Quantitative Phase Analysis Always Reliable? A Case Study of Organic Salt Formation. *Advanced Science* **2017,** *4*, 1700132.

145. Bab, M. A.; Mendoza-Zélis, L., A model for the kinetics of mechanically assisted gas–solid reactions. *Scr. Mater.* **2004,** *50*, 99-104.

146. Fischer, F.; Wenzel, K. J.; Rademann, K.; Emmerling, F., Quantitative determination of activation energies in mechanochemical reactions. *Phys. Chem. Chem. Phys.* **2016,** *18*, 23320-5.

147. Delogu, F.; Takacs, L., Information on the mechanism of mechanochemical reaction from detailed studies of the reaction kinetics. *J. Mater. Sci.* **2018,** *53*, 13331-13342.

148. Davis, R. M.; McDermott, B.; Koch, C. C., Mechanical alloying of brittle materials. *Metall. Trans. A* **1988,** *19*, 2867-2874.

149. Maurice, D. R.; Courtney, T., The physics of mechanical alloying: a first report. *Metall. Trans. A* **1990,** *21*, 289-303.

150. Burgio, N.; Iasonna, A.; Magini, M.; Martelli, S.; Padella, F., Mechanical alloying of the Fe−Zr system. Correlation between input energy and end products. *Nuovo Cimento D* **1991,** *13*, 459-476.

151. Kessler, M.; Woodward, R.; Wong, N.; Rinaldi, R., Kinematic Modelling of Mechanocatalytic Depolymerization of α-Cellulose and Beechwood. *ChemSusChem* **2018,** *11*, 552-561.

152. Hashimoto, H.; Watanabe, R., Model Simulation of Energy Consumption during Vibratory Ball Milling of Metal Powder. *Mater. Tran. JIM* **1990,** *31*, 219-224.

153. Wu, Y.-Q.; Huang, F.-L., A microscopic model for predicting hot-spot ignition of granular energetic crystals in response to drop-weight impacts. *Mech. Mater.* **2011,** *43*, 835-852.

154. Urakaev, F. K., Mechanochemical synthesis of nanoparticles by a dilution method: derivation of kinetic equations. *Mendeleev Commun.* **2012,** *22*, 103-105.

155. Delogu, F., A combined experimental and numerical approach to the kinetics of mechanically induced phase transformations. *Acta Mater.* **2008,** *56*, 905-912.

156. Urakaev, F. K.; Boldyrev, V., Mechanism and kinetics of mechanochemical processes in comminuting devices: 1. Theory. *Powder Technology* **2000,** *107*, 93-107.

157. Urakaev, F. K.; Boldyrev, V., Mechanism and kinetics of mechanochemical processes in comminuting devices: 2. Applications of the theory. Experiment. *Powder Technology* **2000,** *107*, 197-206.

158. Bowden, F.; Yoffe, A., *Initiation and growth of explosion in liquids and solids*. Cambridge University Press: 1952.

159. Bowden, F. P.; Yoffe, A. D., *Fast reactions in solids*. Butterworth's Scientific Publications: 1958.

160. Thiessen PA, M. K.; Heinicke, G., Grundlagen der Tribochemie. *Berlin: Academie-Verlag* **1967**.

161. Boldyrev, V. V.; Heinicke, G., Reaktionsursachen in der Tribochemie. *Z. Chem.* **1979,** *19*, 353-362.

162. Boldyrev, V., Experimental methods in the mechanochemistry of inorganic solids. In *Treatise on Materials Science & Technology*, Elsevier: 1983; Vol. 19, pp 185-223.

163. Sandusky, H. W.; Glancy, B. C.; CARLSON, D. W.; ELBAN, W. L.; ARMSTRONG, R. W., Relating deformation to hot spots in shock-loaded crystals of ammonium perchlorate. *Journal of Propulsion and Power* **1991,** *7*, 518-525.

164. Psakhie, S. G.; Zol'nikov, K.; Saraev, D. Y., Local structural instability and formation of hot spots in materials under mechanical loading. *Combustion, Explosion and Shock Waves* **1997,** *33*, 246-249.

165. Urakaev, F.; Takacs, L.; Soika, V.; Shevchenko, V. S.; Boldyrev, V. V., *The mechanisms of formation of "Hot Spots" in mechanochemical reactions between metals and sulfur*. 2001; Vol. 75, p 1997-2001.

166. Urakaev, F. K.; Shevchenko, V.; Boldyrev, V. In *Role of the heat of reaction in modeling mechanochemical processes*, Doklady Physical Chemistry, Springer: 2001; pp 59-61.

167. Urakaev, F. K., Simulation of mechanically induced self-propagating reactions: density of the heat source due to the enthalpy of reaction. *Combustion Science and Technology* **2013,** *185*, 723-734.

168. Fox, P. G., Mechanically initiated chemical reactions in solids. *J. Mater. Sci.* **1975,** *10*, 340-360.

169. Swallowe, G. M.; Field, J. E., The Ignition of a Thin Layer of Explosive by Impact; the Effect of Polymer Particles. *Proc. R. Soc. Lond. A* **1982,** *379*, 389-408.

170. Field, J. E.; Bourne, N. K.; Palmer, S. J. P.; Walley, S. M.; Smallwood, J. M., Hot-spot ignition mechanisms for explosives and propellants. *Philos. T. Roy. Soc. A* **1992,** *339*, 269-283.

171. Field, J. E., Hot spot ignition mechanisms for explosives. *Acc. Chem. Res.* **1992,** *25*, 489-496.

172. Dienes, J. K., Frictional hot-spots and propellant sensitivity. *Mater. Res. Soc. Symp. Proc.* **1983,** *24*, 373-381.

173. Bennett, J. G.; Haberman, K. S.; Johnson, J. N.; Asay, B. W., A constitutive model for the non-shock ignition and mechanical response of high explosives. *J. Mech. Phys. Solids* **1998,** *46*, 2303-2322.

174. Delogu, F.; Cocco, G., Weakness of the “hot spots” approach to the kinetics of mechanically induced phase transformations. *J. Alloys Compd.* **2008,** *465*, 540-546.

175. Andersen, J. M.; Mack, J., Decoupling the Arrhenius equation via mechanochemistry. *Chem. Sci.* **2017,** *8*, 5447-5453.

176. Andersen, J.; Mack, J., Insights into mechanochemical reactions at targetable and stable, sub-ambient temperatures. *Angew. Chem., Int. Ed.* **2018,** *57*, 13062-13065.

177. Urakaev, F. K.; Boldyrev, V.; Pozdnyakov, O.; Regel, V., Studying mechanism of mechanochemical decomposition of solid inorganic compounds. *Kinetika i Kataliz* **1977,** *18*, 350-358.

178. W. Boldyrew, W.; G. Awwakumow, E.; I. Strugowa, L.; Harenz, H.; Heinicke, G., Zur Tribochemischen Zersetzung von Alkali-Bromaten und-Nitraten. *Z. Anorg. Allg. Chem.* **1972,** *393*, 152-158.

179. Urakaev, F. K.; Boldyrev, V., Correlation between the yield of volatile products and the characteristics of the propagation of cracks in crystals. *Russian Journal of Physical Chemistry A* **2000,** *74*, 1339-1344.

180. Boldyrew, W. W., Der Mechanismus der tribochemischen Zerlegung anorganischer Salze. In *Zeitschrift für Physikalische Chemie*, 1975; Vol. 256O, p 342.

181. Boldyreva, E., Mechanochemistry of inorganic and organic systems: what is similar, what is different? *Chem Soc Rev* **2013,** *42*, 7719-38.

182. Hernandez, J. G.; Bolm, C., Altering Product Selectivity by Mechanochemistry. *J Org Chem* **2017,** *82*, 4007-4019.

183. Hopgood, H.; Mack, J., An Increased Understanding of Enolate Additions under Mechanochemical Conditions. *Molecules* **2017,** *22*, 696.

184. Brunauer, S.; Emmett, P. H.; Teller, E., Adsorption of gases in multimolecular layers. *Journal of the American chemical society* **1938,** *60*, 309-319.

185. Timoshenko, S.; Timoshenko, S.; Goodier, J. N., *Theory of Elasticity*. 2nd ed.; McGraw-Hill Book Co.: New York-Toronto-London, 1951.

186. Machado, M.; Moreira, P.; Flores, P.; Lankarani, H. M., Compliant contact force models in multibody dynamics: Evolution of the Hertz contact theory. *Mech. Mach. Theory* **2012,** *53*, 99-121.

187. Bassam, F.; York, P.; Rowe, R.; Roberts, R., Young's modulus of powders used as pharmaceutical excipients. *International journal of pharmaceutics* **1990,** *64*, 55-60.

188. Watanabe, R.; Hashimoto, H.; Lee, G. G., Computer Simulation of Milling Ball Motion in Mechanical Alloying. *Mater. Tran. JIM* **1995,** *36*, 102-109.

189. Whitelaw, J. H., Convective Heat Transfer. CRC Press, Boca Raton, Fla: 1997; p 237.

190. Ivanov, B. A.; Deutsch, A., The phase diagram of CaCO3 in relation to shock compression and decomposition. *Phys. Earth Planet. Inter.* **2002,** *129*, 131-143.

191. Benitez-Guerrero, M.; Valverde, J. M.; Perejon, A.; Sanchez-Jimenez, P. E.; Perez-Maqueda, L. A., Effect of milling mechanism on the CO2 capture performance of limestone in the Calcium Looping process. *Chem. Eng. J.* **2018,** *346*, 549-556.

192. Fox, P.; Soria-Ruiz, J., Fracture-induced thermal decomposition in brittle crystalline solids. *Proceedings of the Royal Society of London. A. Mathematical and Physical Sciences* **1970,** *317*, 79-90.

193. Urakaev, F. K.; Boldyrev, V., Kinetics of gas evolution during the cleavage and grinding of calcite monocrystals. *Russian Journal of Physical Chemistry A* **2000,** *74*, 1334-1338.

194. L'vov, B. V.; Ugolkov, V. L., Peculiarities of CaCO3, SrCO3 and BaCO3 decomposition in CO2 as a proof of their primary dissociative evaporation. *Thermochim. Acta* **2004,** *410*, 47-55.

195. Presley, M. A.; Christensen, P. R., Thermal conductivity measurements of particulate materials 1. A review. *J. Geophys. Res. E* **1997,** *102*, 6535-6549.

196. Presley, M. A.; Christensen, P. R., Thermal conductivity measurements of particulate materials 2. Results. *J. Geophys. Res. E* **1997,** *102*, 6551-6566.

197. Heat Capacity Of Selected Solids. In *CRC Handbook of Chemistry and Physics, 99th Edition (Internet Version 2018)*, CRC Press/Taylor & Francis: Boca Raton, FL.

198. Miller, P. J.; Coffey, C. S.; DeVost, V. F., Heating in crystalline solids due to rapid deformation. *J. Appl. Phys.* **1986,** *59*, 913-916.

199. Bhattacharya, A. K.; Arzt, E., Temperature rise during mechanical alloying. *Scr. Metall. Mater.* **1992,** *27*, 749-754.

200. Joardar, J.; Pabi, S. K.; Murty, B. S., Estimation of entrapped powder temperature during mechanical alloying. *Scr. Mater.* **2004,** *50*, 1199-1202.

201. Thermal Conductivity Of Crystalline Dielectrics. In *CRC Handbook of Chemistry and Physics, 99th Edition (Internet Version 2018)*, Rumble, J. R., Ed. RC Press/Taylor & Francis: Boca Raton, FL.

202. Potapov, A. V.; Campbell, C. S., The breakage induced by a single grinding ball dropped onto a randomly packed particle bed. *Powder. Technol.* **2000,** *107*, 108-117.

203. Marino-Salguero, J.; Jorge, J.; Menendez-Aguado, J. M.; Alvarez-Rodriguez, B.; de Felipe, J. J., Heat generation model in the ball-milling process of a tantalum ore. *Miner. Metall. Proc.* **2017,** *34*, 10-19.

204. Eckert, R.; Felderhoff, M.; Schüth, F., Preferential Carbon Monoxide Oxidation over Copper-Based Catalysts under In Situ Ball Milling. *Angew. Chem., Int. Ed.* **2017,** *56*, 2445-2448.

205. Takacs, L.; McHenry, J. S., Temperature of the milling balls in shaker and planetary mills. *J. Mater. Sci.* **2006,** *41*, 5246-5249.

206. Schmidt, R.; Martin Scholze, H.; Stolle, A., Temperature progression in a mixer ball mill. *Int. J. Ind. Chem.* **2016,** *7*, 181-186.

207. Kulla, H.; Wilke, M.; Fischer, F.; Röllig, M.; Maierhofer, C.; Emmerling, F., Warming up for mechanosynthesis–temperature development in ball mills during synthesis. *Chemical Communications* **2017,** *53*, 1664-1667.

208. Kulla, H.; Haferkamp, S.; Akhmetova, I.; Röllig, M.; Maierhofer, C.; Rademann, K.; Emmerling, F., In Situ Investigations of Mechanochemical One-Pot Syntheses. *Angew. Chem., Int. Edit.* **2018,** *57*, 5930-5933.

209. Butyagin, P. Y.; Pavlichev, I. K., Determination of energy yield of mechanochemical reactions. *React. Solid.* **1986,** *1*, 361-372.

210. Takacs, L.; Šepelák, V., Quantitative comparison of the efficiency of mechanochemical reactors. *J. Mater. Sci.* **2004,** *39*, 5487-5489.

211. Bruckmann, A.; Krebs, A.; Bolm, C., Organocatalytic reactions: effects of ball milling, microwave and ultrasound irradiation. *Green Chem.* **2008,** *10*, 1131-1141.

212. Politov, A.; Golyazimova, O., Increasing the energy yield of mechanochemical transformations: selected case studies. *Faraday Discuss.* **2014,** *170*, 345-56.

213. Smil, V., Detonator of the population explosion. *Nature* **1999,** *400*, 415.

214. Erisman, J. W.; Sutton, M. A.; Galloway, J.; Klimont, Z.; Winiwarter, W., How a century of ammonia synthesis changed the world. *Nat. Geosci.* **2008,** *1*, 636-639.

215. Appl, M., Ammonia. In *Ullmann's Encyclopedia of Industrial Chemistry*, WILEY-VCH Verlag GmbH & Co. KGaA: Weinheim, 2006.

216. McArthur, J. W.; McCord, G. C., Fertilizing growth: Agricultural inputs and their effects in economic development. *J. Dev. Econ.* **2017,** *127*, 133-152.

217. Medford, A. J.; Hatzell, M. C., Photon-Driven Nitrogen Fixation: Current Progress, Thermodynamic Considerations, and Future Outlook. *ACS Catal.* **2017,** *7*, 2624-2643.

218. Minteer, S. D.; Christopher, P.; Linic, S., Recent developments in nitrogen reduction catalysts: A virtual issue. *ACS Energy Lett.* **2018,** *4*, 163-166.

219. Comer, B. M.; Fuentes, P.; Dimkpa, C. O.; Liu, Y. H.; Fernandez, C. A.; Arora, P.; Realff, M.; Singh, U.; Hatzell, M. C.; Medford, A. J., Prospects and Challenges for Solar Fertilizers. *Joule* **2019,** *3*, 1578-1605.

220. Schiffer, Z. J.; Manthiram, K., Electrification and decarbonization of the chemical industry. *Joule* **2017,** *1*, 10-14.

221. Deng, J.; Iñiguez, J. A.; Liu, C., Electrocatalytic nitrogen reduction at low temperature. *Joule* **2018,** *2*, 846-856.

222. Suryanto, B. H.; Kang, C. S.; Wang, D.; Xiao, C.; Zhou, F.; Azofra, L. M.; Cavallo, L.; Zhang, X.; MacFarlane, D. R., Rational electrode–electrolyte design for efficient ammonia electrosynthesis under ambient conditions. *ACS Energy Lett.* **2018,** *3*, 1219-1224.

223. Schrauzer, G. N.; Guth, T. D., Photolysis of Water and Photoreduction of Nitrogen on Titanium Dioxide. *J. Am. Chem. Soc.* **1977,** *99*, 7189-7193.

224. Comer, B. M.; Liu, Y.-H.; Dixit, M. B.; Hatzell, K. B.; Ye, Y.; Crumlin, E. J.; Hatzell, M. C.; Medford, A. J., The Role of Adventitious Carbon on Photocatalytic Nitrogen Fixation by Titania. *J. Am. Chem. Soc.* **2018,** *140*, 15157–15160.

225. Liu, Y.-H.; Vu, M. H.; Lim, J.; Do, T.-O.; Hatzell, M. C., Influence of carbonaceous species on aqueous photo-catalytic nitrogen fixation by titania. *Faraday Discuss.* **2019,** *215*, 379-392.

226. Mehta, P.; Barboun, P.; Herrera, F. A.; Kim, J.; Rumbach, P.; Go, D. B.; Hicks, J. C.; Schneider, W. F., Overcoming ammonia synthesis scaling relations with plasma-enabled catalysis. *Nat. Catal.* **2018,** *1*, 269-275.

227. Mehta, P.; Barboun, P.; Go, D. B.; Hicks, J. C.; Schneider, W. F., Catalysis enabled by plasma activation of strong chemical bonds: A review. *ACS Energy Lett.* **2019,** *4*, 1115-1133.

228. Michalsky, R.; Avram, A. M.; Peterson, B. A.; Pfromm, P. H.; Peterson, A. A., Chemical looping of metal nitride catalysts: low-pressure ammonia synthesis for energy storage. *Chem. Sci.* **2015,** *6*, 3965-3974.

229. Laassiri, S.; Zeinalipour-Yazdi, C. D.; Catlow, C. R. A.; Hargreaves, J. S. J., The potential of manganese nitride based materials as nitrogen transfer reagents for nitrogen chemical looping. *Appl. Catal. B* **2018,** *223*, 60-66.

230. Swearer, D. F.; Knowles, N. R.; Everitt, H. O.; Halas, N. J., Light-Driven Chemical Looping for Ammonia Synthesis. *ACS Energy Lett.* **2019,** *4*, 1505-1512.

231. Friščić, T.; Mottillo, C.; Titi, H. M., Mechanochemistry for synthesis. *Angew. Chem., Int. Edit.* **2020,** *59*, 1018-1029.

232. Hernández, J. G.; Friščić, T., Metal-catalyzed organic reactions using mechanochemistry. *Tetrahedron Lett.* **2015,** *56*, 4253-4265.

233. Uzarevic, K.; Halasz, I.; Friščić, T., Real-Time and In Situ Monitoring of Mechanochemical Reactions: A New Playground for All Chemists. *J. Phys. Chem. Lett.* **2015,** *6*, 4129-4140.

234. Weidenthaler, C.; Pommerin, A.; Felderhoff, M.; Sun, W.; Wolverton, C.; Bogdanovic, B.; Schüth, F., Complex rare-earth aluminum hydrides: Mechanochemical preparation, crystal structure and potential for hydrogen storage. *J. Am. Chem. Soc.* **2009,** *131*, 16735-16743.

235. Bolm, C.; Hernández, J. G., Mechanochemistry of gaseous reactants. *Angew. Chem., Int. Edit.* **2018,** *58*, 3285-3299.

236. Bilke, M.; Losch, P.; Vozniuk, O.; Bodach, A.; Schüth, F., Methane to Chloromethane by Mechanochemical Activation: A Selective Radical Pathway. *J. Am. Chem. Soc.* **2019,** *141*, 11212-11218.

237. Meine, N.; Rinaldi, R.; Schüth, F., Solvent-free catalytic depolymerization of cellulose to water-soluble oligosaccharides. *ChemSusChem* **2012,** *5*, 1449-1454.

238. Tricker, A. W.; Samaras, G.; Hebisch, K. L.; Realff, M. J.; Sievers, C., Hot spot generation, reactivity, and decay in mechanochemical reactors. *Chem. Eng. J.* **2020,** *382*, 122954.

239. Suryanarayana, C., Mechanical alloying and milling. *Prog. Mater. Sci.* **2001,** *46*, 1-184.

240. Calka, A., Formation of titanium and zirconium nitrides by mechanical alloying. *Appl. Phys. Lett.* **1991,** *59*, 1568-1569.

241. Ogino, Y.; Yamasaki, T.; Atzumi, N.; Yoshioka, K., Nitriding of Transition-Metal Powders by Ball-Milling in Nitrogen Gas. *Mater. Trans. JIM* **1993,** *34*, 1212-1216.

242. Han, G.-F.; Shi, X.-M.; Kim, S.-J.; Kim, J.; Jeon, J.-P.; Noh, H.-J.; Im, Y.-K.; Li, F.; Uhm, Y. R.; Kim, C. S., Dissociating stable nitrogen molecules under mild conditions by cyclic strain engineering. *Sci. Adv.* **2019,** *5*, eaax8275.

243. Heinicke, G.; Meyer, K.; Senzky, U., Die Bildung Von Ammoniak Aus Den Elementen Durch Mechanische Beanspruchung Des Katalysators. *Z. Anorg. Allg. Chem.* **1961,** *312*, 180-185.

244. Thiessen, P. A.; Heinicke, G.; Bock, N., Zur tribochemischen NH_3-Bildung und deren Sensibilisierung durch Wasser. *Z. Chem.* **1974,** *14*, 76.

245. Krom, M. D., Spectrophotometric determination of ammonia: a study of a modified Berthelot reaction using salicylate and dichloroisocyanurate. *Analyst* **1980,** *105*, 305-316.

246. Shi, M. M.; Bao, D.; Wulan, B. R.; Li, Y. H.; Zhang, Y. F.; Yan, J. M.; Jiang, Q., Au Sub-Nanoclusters on TiO2 toward Highly Efficient and Selective Electrocatalyst for N2 Conversion to NH3 at Ambient Conditions. *Adv. Mater.* **2017,** *29*, 1606550.

247. Bearden, J. A.; Burr, A. F., Reevaluation of X-Ray Atomic Energy Levels. *Rev. Mod. Phys.* **1967,** *39*, 125-142.

248. Hargreaves, J., Nitrides as ammonia synthesis catalysts and as potential nitrogen transfer reagents. *Appl. Petrochem. Res.* **2014,** *4*, 3-10.

249. Abghoui, Y.; Garden, A. L.; Howalt, J. G.; Vegge, T.; Skúlason, E., Electroreduction of N2 to ammonia at ambient conditions on mononitrides of Zr, Nb, Cr, and V: A DFT guide for experiments. *ACS Catal.* **2016,** *6*, 635-646.

250. Ardagh, M. A.; Abdelrahman, O. A.; Dauenhauer, P. J., Principles of Dynamic Heterogeneous Catalysis: Surface Resonance and Turnover Frequency Response. *ACS Catal.* **2019,** *9*, 6929-6937.

251. Chin, Z. H.; Perng, T. P., In situ observation of combustion to form TiN during ball milling Ti in nitrogen. *Appl. Phys. Lett.* **1997,** *70*, 2380-2382.

252. Gotor, F. J.; Alcala, M. D.; Real, C.; Criado, J. M., Combustion synthesis of TiN induced by high-energy ball milling of Ti under nitrogen atmosphere. *J. Mater. Res.* **2002,** *17*, 1655-1663.

253. Oghenevweta, J.; Wexler, D.; Calka, A., Understanding reaction sequences and mechanisms during synthesis of nanocrystalline Ti 2 N and TiN via magnetically controlled ball milling of Ti in nitrogen. *J. Mater. Sci.* **2018,** *53*, 3064-3077.

254. Greenlee, L. F.; Renner, J. N.; Foster, S. L., The Use of Controls for Consistent and Accurate Measurements of Electrocatalytic Ammonia Synthesis from Dinitrogen. *ACS Catal.* **2018,** *8*, 7820-7827.

255. Andersen, S. Z.; Čolić, V.; Yang, S.; Schwalbe, J. A.; Nielander, A. C.; McEnaney, J. M.; Enemark-Rasmussen, K.; Baker, J. G.; Singh, A. R.; Rohr, B. A., A rigorous electrochemical ammonia synthesis protocol with quantitative isotope measurements. *Nature* **2019,** *570*, 504-508.

256. Kibsgaard, J.; Nørskov, J. K.; Chorkendorff, I., The difficulty of proving electrochemical ammonia synthesis. *ACS Energy Lett.* **2019,** *4*, 2986-2988.

257. Volpe, L.; Boudart, M., Ammonia synthesis on molybdenum nitride. *J. Phys. Chem.* **1986,** *90*, 4874-4877.

258. Mckay, D.; Hargreaves, J.; Rico, J.; Rivera, J.; Sun, X.-L., The influence of phase and morphology of molybdenum nitrides on ammonia synthesis activity and reduction characteristics. *J. Solid State Chem.* **2008,** *181*, 325-333.

259. Jacobsen, C. J. H.; Dahl, S.; Clausen, B. S.; Bahn, S.; Logadottir, A.; Nørskov, J. K., Catalyst Design by Interpolation in the Periodic Table: Bimetallic Ammonia Synthesis Catalysts. *J. Am. Chem. Soc.* **2001,** *123*, 8404-8405.

260. Michaud, D., Ball Mills. 911Metallurgist, 2017; Vol. 2020.

261. Olivos-Suarez, A. I.; Szécsényi, A. g.; Hensen, E. J.; Ruiz-Martinez, J.; Pidko, E. A.; Gascon, J., Strategies for the direct catalytic valorization of methane using heterogeneous catalysis: challenges and opportunities. *ACS Catal.* **2016,** *6*, 2965-2981.

262. Jocz, J. N.; Medford, A. J.; Sievers, C., Thermodynamic Limitations of the Catalyst Design Space for Methanol Production from Methane. *ChemCatChem* **2019,** *11*, 593-600.

263. Ratnasamy, C.; Wagner, J. P., Water gas shift catalysis. *Catal. Rev.* **2009,** *51*, 325-440.

264. Luo, H.; Abu-Omar, M. M., Chemicals From Lignin. In *Encyclopedia of Sustainable Technologies*, Abraham, M. A., Ed. Elsevier: Oxford, 2017; pp 573-585.

265. Boerjan, W.; Ralph, J.; Baucher, M., Lignin biosynthesis. *Annu. Rev. Plant Biol.* **2003,** *54*, 519-546.

266. Tricker, A. W.; Stellato, M. J.; Kwok, T. T.; Kruyer, N. S.; Wang, Z.; Nair, S.; Thomas, V. M.; Realff, M. J.; Bommarius, A. S.; Sievers, C., Similarities in Recalcitrant Structures of Industrial Non-kraft and Kraft Lignin. *ChemSusChem* **2020,** *13*, 4624 - 4632.

267. Cooreman, E.; Vangeel, T.; Van Aelst, K.; Van Aelst, J.; Lauwaert, J.; Thybaut, J. W.; Van den Bosch, S.; Sels, B. F., Perspective on overcoming scale-up hurdles for the reductive catalytic fractionation of lignocellulose biomass. *Ind. Eng. Chem. Res.* **2020,** *59*, 17035-17045.

268. Tricker, A. W.; Hebisch, K. L.; Buchmann, M.; Liu, Y.-H.; Rose, M.; Stavitski, E.; Medford, A. J.; Hatzell, M. C.; Sievers, C., Mechanocatalytic Ammonia Synthesis over TiN in Transient Microenvironments. *ACS Energy Lett.* **2020,** *5*, 3362-3367.

269. Kuga, S.; Wu, M., Mechanochemistry of cellulose. *Cellulose* **2019,** *26*, 215-225.

270. Heinicke, G.; Lischke, I., Wirksamkeit von Katalysatoren unter Bedingungen der mechanischen Bearbeitung. *Z. Chem.* **1963,** *3*, 355-356.

271. Bolm, C.; Hernandez, J. G., Mechanochemistry of Gaseous Reactants. *Angew. Chem., Int. Edit.* **2019,** *58*, 3285-3299.

272. Bolm, C.; Hernández, J. G., Mechanochemie gasförmiger Reaktanten. *Angewandte Chemie* **2019,** *131*, 3320-3335.

273. Mori, S.; Xu, W. C.; Ishidzuki, T.; Ogasawara, N.; Imai, J.; Kobayashi, K., Mechanochemical activation of catalysts for CO2 methanation. *Appl. Catal. A Gen.* **1996,** *137*, 255-268.

274. Yatagai, K.; Shishido, Y.; Gemma, R.; Boll, T.; Uchida, H.-H.; Oguri, K., Mechanochemical CO2 methanation over LaNi-based alloys. *Int. J. Hydrog. Energy* **2020,** *45*, 5264-5275.

275. Mulas, G.; Campesi, R.; Garroni, S.; Delogu, F.; Milanese, C., Hydrogenation of carbon monoxide over nanostructured systems: A mechanochemical approach. *Appl. Surf. Sci.* **2011,** *257*, 8165-8170.

276. Sawama, Y.; Kawajiri, T.; Niikawa, M.; Goto, R.; Yabe, Y.; Takahashi, T.; Marumoto, T.; Itoh, M.; Kimura, Y.; Monguchi, Y., Stainless-Steel Ball-Milling Method for Hydro-/Deutero-genation using H2O/D2O as a Hydrogen/Deuterium Source. *ChemSusChem* **2015,** *8*, 3773-3776.

277. Sawama, Y.; Yasukawa, N.; Ban, K.; Goto, R.; Niikawa, M.; Monguchi, Y.; Itoh, M.; Sajiki, H., Stainless steel-mediated hydrogen generation from alkanes and diethyl ether and its application for arene reduction. *Org. Lett.* **2018,** *20*, 2892-2896.

278. Nash, D. J.; Restrepo, D. T.; Parra, N. S.; Giesler, K. E.; Penabade, R. A.; Aminpour, M.; Le, D.; Li, Z.; Farha, O. K.; Harper, J. K., Heterogeneous metal-free hydrogenation over defect-laden hexagonal boron nitride. *ACS Omega* **2016,** *1*, 1343-1354.

279. Han, G.-F.; Li, F.; Chen, Z.-W.; Coppex, C.; Kim, S.-J.; Noh, H.-J.; Fu, Z.; Lu, Y.; Singh, C. V.; Siahrostami, S., Mechanochemistry for ammonia synthesis under mild conditions. *Nat. Nanotechnol.* **2021,** *16*, 325-330.

280. Qi, L.; Chamas, A.; Jones, Z. R.; Walter, E. D.; Hoyt, D. W.; Washton, N. M.; Scott, S. L., Unraveling the Dynamic Network in the Reactions of an Alkyl Aryl Ether Catalyzed by Ni/γ-Al2O3 in 2-Propanol. *J. Am. Chem. Soc.* **2019,** *141*, 17370-17381.

281. Duzee, E. M. v.; Adkins, H., Hydrogenation and hydrogenolysis of ethers. *J. Am. Chem. Soc.* **1935,** *57*, 147-151.

282. He, J.; Lu, L.; Zhao, C.; Mei, D.; Lercher, J. A., Mechanisms of catalytic cleavage of benzyl phenyl ether in aqueous and apolar phases. *J. Catal.* **2014,** *311*, 41-51.

283. He, J.; Zhao, C.; Lercher, J. A., Ni-catalyzed cleavage of aryl ethers in the aqueous phase. *J. Am. Chem. Soc.* **2012,** *134*, 20768-20775.

284. Jiang, L.; Guo, H.; Li, C.; Zhou, P.; Zhang, Z., Selective cleavage of lignin and lignin model compounds without external hydrogen, catalyzed by heterogeneous nickel catalysts. *Chem. Sci.* **2019,** *10*, 4458-4468.

285. Li, L.; Fan, H. J.; Hu, H. Q., A theoretical study on bond dissociation enthalpies of coal based model compounds. *Fuel* **2015,** *153*, 70-77.

286. Lupoi, J. S.; Singh, S.; Parthasarathi, R.; Simmons, B. A.; Henry, R. J., Recent innovations in analytical methods for the qualitative and quantitative assessment of lignin. *Renew. Sust. Energ. Rev.* **2015,** *49*, 871-906.

287. Zhao, C.; Kasakov, S.; He, J.; Lercher, J. A., Comparison of kinetics, activity and stability of Ni/HZSM-5 and Ni/Al2O3-HZSM-5 for phenol hydrodeoxygenation. *J. Catal.* **2012,** *296*, 12-23.

288. Güvenatam, B.; Heeres, E. H.; Pidko, E. A.; Hensen, E. J., Decomposition of lignin model compounds by Lewis acid catalysts in water and ethanol. *J. Mol. Catal. A Chem.* **2015,** *410*, 89-99.

289. Guvenatam, B.; Kursun, O.; Heeres, E. H. J.; Pidko, E. A.; Hensen, E. J. M., Hydrodeoxygenation of mono- and dimeric lignin model compounds on noble metal catalysts. *Catal. Today* **2014,** *233*, 83-91.

290. Sadezky, A.; Muckenhuber, H.; Grothe, H.; Niessner, R.; Pöschl, U., Raman microspectroscopy of soot and related carbonaceous materials: spectral analysis and structural information. *Carbon* **2005,** *43*, 1731-1742.

291. Xing, T.; Li, L. H.; Hou, L.; Hu, X.; Zhou, S.; Peter, R.; Petravic, M.; Chen, Y., Disorder in ball-milled graphite revealed by Raman spectroscopy. *Carbon* **2013,** *57*, 515-519.

292. Schaffer, H.; Chance, R.; Silbey, R.; Knoll, K.; Schrock, R., Conjugation length dependence of Raman scattering in a series of linear polyenes: Implications for polyacetylene. *J. Chem. Phys.* **1991,** *94*, 4161-4170.

293. Agarwal, U. P.; McSweeny, J. D.; Ralph, S. A., FT–Raman investigation of milled-wood lignins: softwood, hardwood, and chemically modified black spruce lignins. *J. Wood Chem. Technol.* **2011,** *31*, 324-344.

294. Madzharova, F.; Heiner, Z.; Kneipp, J., Surface-Enhanced Hyper Raman Spectra of Aromatic Thiols on Gold and Silver Nanoparticles. *J. Phys. Chem. C* **2020,** *124*, 6233-6241.

295. Bibby, D. M.; Howe, R. F.; McLellan, G. D., Coke formation in high-silica zeolites. *Appl. Catal. A Gen.* **1992,** *93*, 1-34.

296. Guisnet, M.; Magnoux, P., Organic chemistry of coke formation. *Appl. Catal. A Gen.* **2001,** *212*, 83-96.

297. Delogu, F., Hydrogen generation by mechanochemical reaction of quartz powders in water. *Int. J. Hydrog. Energy* **2011,** *36*, 15145-15152.

298. Innocenti, G.; Benkeser, D. J.; Dase, J. E.; Wirth, X.; Sievers, C.; Kurtis, K. E., Beneficiation of ponded coal ash through chemi-mechanical grinding. *Fuel* **2021,** *299*, 120892.

299. Kandziolka, M.; Kidder, M.; Gill, L.; Wu, Z.; Savara, A., Aromatic–hydroxyl interaction of an alpha-aryl ether lignin model-compound on SBA-15, present at pyrolysis temperatures. *Phys. Chem. Chem. Phys.* **2014,** *16*, 24188-24193.

300. Meola, C.; Carlomagno, G. M., Impact damage in GFRP: new insights with infrared thermography. *Composites Part A: Applied Science and Manufacturing* **2010,** *41*, 1839-1847.

301. Meola, C.; Boccardi, S.; Boffa, N.; Ricci, F.; Simeoli, G.; Russo, P.; Carlomagno, G., New perspectives on impact damaging of thermoset-and thermoplastic-matrix composites from thermographic images. *Composite Structures* **2016,** *152*, 746-754.

302. Li, Y.; Zhang, W.; Yang, Z.-w.; Zhang, J.-y.; Tao, S.-j., Low-velocity impact damage characterization of carbon fiber reinforced polymer (CFRP) using infrared thermography. *Infrared Physics & Technology* **2016,** *76*, 91-102.

303. Hunt, E. M.; Malcolm, S.; Jackson, M., High-Speed Study of Drop-Weight Impact Ignition of PBX 9501 Using Infrared Thermography. *International Scholarly Research Notices* **2011,** *2011*.

304. Alexander, A.-M.; Hargreaves, J. S. J., Alternative catalytic materials: carbides, nitrides, phosphides and amorphous boron alloys. *Chem. Soc. Rev.* **2010,** *39*, 4388-4401.

305. Wang, M.; Khan, M.; Mohsin, I.; Wicks, J.; Ip, A. H.; Sumon, K. Z.; Dinh, C. T.; Sargent, E. H.; Gates, I. D.; Kibria, M. G., Can Sustainable Ammonia Synthesis Pathways Compete with Fossil-fuel Based Haber-Bosch Processes? *Energy Environ. Sci.* **2021**.

306. Milošv, I.; Strehblow, H. H.; Navinšek, B.; Metikoš-Huković, M., Electrochemical and thermal oxidation of TiN coatings studied by XPS. *Surface and interface analysis* **1995,** *23*, 529-539.

307. Hou, X. M.; Hu, X. J.; Chou, K. C., Kinetics of thermal oxidation of titanium nitride powder at different oxidizing atmospheres. *Journal of the American Ceramic Society* **2011,** *94*, 570-575.

308. Rorrer, J. E.; Beckham, G. T.; Román-Leshkov, Y., Conversion of Polyolefin Waste to Liquid Alkanes with Ru-Based Catalysts under Mild Conditions. *JACS Au* **2020**.

309. Dong, L.; Lin, L.; Han, X.; Si, X.; Liu, X.; Guo, Y.; Lu, F.; Rudić, S.; Parker, S. F.; Yang, S., Breaking the limit of lignin monomer production via cleavage of interunit carbon–carbon linkages. *Chem* **2019,** *5*, 1521-1536.

310. Stahel, W. R., The circular economy. *Nature News* **2016,** *531*, 435.

311. Vollmer, I.; Jenks, M. J.; Roelands, M. C.; White, R. J.; van Harmelen, T.; de Wild, P.; van Der Laan, G. P.; Meirer, F.; Keurentjes, J. T.; Weckhuysen, B. M., Beyond mechanical recycling: Giving new life to plastic waste. *Angew. Chem., Int. Edit.* **2020,** *59*, 15402-15423.

312. Štrukil, V., Highly efficient solid-state hydrolysis of waste polyethylene terephthalate by mechanochemical milling and vapour-assisted aging. *ChemSusChem* **2021,** *14*, 330-338.

313. Jiang, X.; Savithri, D.; Du, X.; Pawar, S.; Jameel, H.; Chang, H.-m.; Zhou, X., Fractionation and characterization of kraft lignin by sequential precipitation with various organic solvents. *ACS Sustain. Chem. Eng.* **2016,** *5*, 835-842.

314. El Mansouri, N.-E.; Salvadó, J., Structural characterization of technical lignins for the production of adhesives: Application to lignosulfonate, kraft, soda-anthraquinone, organosolv and ethanol process lignins. *Ind. Crop. Prod.* **2006,** *24*, 8-16.

315. Ammonia, anhydrous. In *Chemical Hazards Response Information System : hazardous chemical data manual*, United States Department of Transportation, U. S. C. G., Ed. Washington, D.C., 1999.

316. Zhang, H.; Kisi, E. H., Formation of titanium hydride at room temperature by ball milling. *J. Phys. Condens. Matter.* **1997,** *9*, L185-L190.

317. Rechulski, M. D. K.; Kaldstrom, M.; Richter, U.; Schüth, F.; Rinaldi, R., Mechanocatalytic Depolymerization of Lignocellulose Performed on Hectogram and Kilogram Scales. *Ind. Eng. Chem. Res.* **2015,** *54*, 4581-4592.